



Universiteit
Leiden
The Netherlands

Optogenetic investigation of cardiac arrhythmia mechanisms

Feola, I.

Citation

Feola, I. (2018, December 11). *Optogenetic investigation of cardiac arrhythmia mechanisms*. Retrieved from <https://hdl.handle.net/1887/67391>

Version: Not Applicable (or Unknown)

License: [Licence agreement concerning inclusion of doctoral thesis in the Institutional Repository of the University of Leiden](#)

Downloaded from: <https://hdl.handle.net/1887/67391>

Note: To cite this publication please use the final published version (if applicable).

Cover Page



Universiteit Leiden



The following handle holds various files of this Leiden University dissertation:

<http://hdl.handle.net/1887/67391>

Author: Feola, I.

Title: Optogenetic investigation of cardiac arrhythmia mechanisms

Issue Date: 2018-12-11

**OPTOGENETIC INVESTIGATION OF CARDIAC
ARRHYTHMIA MECHANISMS**

Iolanda Feola

Colophon

The studies described in this thesis were performed at the Department of Cardiology of the Leiden University Medical Center, Leiden, The Netherlands.

ISBN: 978-94-6182-923-8

The research in this thesis was supported by funding from the Netherlands Organisation for Scientific Research (NWO, Vidi grant 91714336), Ammodo and the European Research Council (ERC, Starting grant 716509) to Dr. D.A. Pijnappels.

Copyright © Iolanda Feola

All rights reserved. No part of this book may be reproduced or transmitted in any form or by any means, without prior written permission of the author.

Cover: 'Bright and sweet experiments'. Heart cake, baking and decoration with fondant by Iolanda Feola. Final design by Arch. Irma Palumbo.

Layout and printing: Off Page, Amsterdam

OPTOGENETIC INVESTIGATION OF CARDIAC ARRHYTHMIA MECHANISMS

Proefschrift

ter verkrijging van
de graad van Doctor aan de Universiteit Leiden,
op gezag van Rector Magnificus prof.mr. C.J.J.M. Stolker,
volgens besluit van het College voor Promoties
te verdedigen op dinsdag 11 december 2018
klokke 11:15 uur

door
Iolanda Feola
geboren te Vallo della Lucania, Salerno, Italië
in 1987

PROMOTOR

Prof. dr. M.J. Schalijs

CO-PROMOTOR

Dr. D.A. Pijnappels

Dr. A.A.F. de Vries

LEDEN PROMOTIECOMMISSIE

Prof. dr. D.E. Atsma

Prof. dr. A. Panfilov

Prof. dr. K. Zeppenfeld

Prof. dr. B.J.J.M. Brundel

TABLE OF CONTENTS

Chapter 1	General introduction and outline of the thesis	9
Chapter 2	Optogenetic engineering of atrial cardiomyocytes <i>Methods Mol Biol</i> 2016; 1408:319-3121	21
Chapter 3	Localized optogenetic targeting of rotors in atrial cardiomyocyte monolayers <i>Circ Arrhythm Electrophysiol</i> 2017; 10:e005591	37
Appendix 1	Letter by Houston <i>et al</i> Regarding Article, “Localized Optogenetic Targeting of Rotors in Atrial Cardiomyocyte Monolayers” <i>Circ Arrhythm Electrophysiol.</i> 2018; 11:e006118	57
Appendix 2	Response by Feola <i>et al</i> to Letter Regarding Article, “Localized Optogenetic Targeting of Rotors in Atrial Cardiomyocyte Monolayers” <i>Circ Arrhythm Electrophysiol.</i> 2018; 11:e006130	63
Chapter 4	Optogenetics enables real-time spatiotemporal control over spiral wave dynamics in an excitable cardiac system <i>Elife</i> 2018; 7pii: e41076	69
Chapter 5	Optogenetic manipulation of anatomical reentry by light-guided generation of a reversible local conduction block <i>Cardiovasc Res</i> 2017; 113:354-366	93
Chapter 6	Optogenetically-induced microfoci of oxidative stress increase proarrhythmic risk <i>In preparation for submission</i>	127
Chapter 7	Summary, Conclusions and Future perspectives	159
Chapter 8	Samenvatting	167
	List of publications	172
	Acknowledgments	174
	Curriculum vitae	176



*Above all, don't fear difficult moments.
The best comes from them.
(Rita Levi Montalcini, 2009)*

To dad,
to my family,
who keeps my heart beating.



Chapter

GENERAL INTRODUCTION AND
OUTLINE OF THE THESIS

1



BACKGROUND

Heart rhythm disorders, also known as cardiac arrhythmias, are one of the major causes of morbidity and mortality in the world.^{1,2} Such disorders affect the mechanical function of the heart, which could lead to a suboptimal distribution of oxygenated blood, nutrients, and regulatory factors to other organs. The clinical management of cardiac arrhythmias relies on several anti-arrhythmic therapies, *e.g.* drugs, ablation, and device implantation that, unfortunately, are often unspecific, irreversible and/or traumatizing, respectively.³⁻⁷ Recently, to overcome these side effects, gene therapy has been introduced as an alternative option to treat cardiac arrhythmias. Its main advantage is, indeed, the possibility to modulate cardiac electrical function by specifically targeting the biological defect.^{8,9} In this way, gene therapy can allow for a specific treatment that is based on the arrhythmic mechanism. However, gene therapy alone is lacking the possibility to gain precise spatiotemporal and quantitative control over a certain target. Interestingly, more recently, such precise control could be achieved with an innovative strategy, called optogenetics. Here, gene therapy is combined with optics allowing expression of light-activatable proteins that are specifically activate and deactivate by simply turning light on and off, respectively.¹⁰ Among these proteins, there are, for instance, light-gated ion channels and light-gated pumps, which are normally expressed in algae and bacteria. Their transgene expression and light-activation may allow controlling of a specific biological function, like for instance the excitability of cardiac cells. In order to fully comprehend how optogenetics could be used to improve our understanding and thereby treatment and of cardiac arrhythmias, a concise description of the electrical function of the heart in healthy and diseased conditions is provided in the following paragraph.

Electrical function in healthy and diseased conditions

The heart is a fascinating organ characterized by several cell types, *e.g.* atrial and ventricles cardiomyocytes, sinoatrial cells, atrioventricular cells, Purkinje fibers, fibroblasts, smooth muscle cells, and endothelial cells, that all together ensure normal cardiac function, *i.e.* electrical activation initiation and propagation, followed by synchronized mechanical activation.¹¹ In healthy condition, the electrical activation of the heart originates in the sinoatrial node, where so-called pacemaker cells spontaneously give rise to an action potential. This action potential is the result of a chain reaction based on the opening and closing of proteins that are located in the sarcolemma of the cardiac cells. In particular, voltage-gated ion channels are the ones that have a key role in shaping an action potential.^{12,13} Those ion channels are pore-forming proteins that open and close in response to changes in the voltage and allow the selective passage of certain cations or anions according to their electrochemical gradient. This chain reaction is characterized by five phases. It starts with an initial depolarization that causes the physiological resting membrane potential to become less negative and activates the voltage-gated Na⁺ (sodium, inward current) channels if their threshold is overcome (phase 0, the upstroke). The consequent Na⁺ influx guides the rapid further depolarization of the sarcolemma that triggers the successive opening and closing of several Ca²⁺ (calcium, inward current) and K⁺ (potassium, outward

current) voltage-gated ion channels. First, the simultaneous inactivation of inward Na^+ current (I_{Na}) and activation of the transient outward K^+ current (I_{to}) guide the first repolarization of the membrane (phase 1, the early repolarization). Secondly, the balance between the inward currents (I_{CaL} and I_{NaL}) and outward currents (I_{Kur} , I_{Kr} , and I_{Ks}) results in the transient plateau in membrane voltage (phase 2, the plateau). Finally, the delayed outward rectifying currents (I_{Kr} and I_{Ks}), and the inward rectifying current (I_{K1}) guide the repolarization and (phase 3, rapid repolarization) restore the cardiac myocytes resting state (phase 4, restoration on resting membrane potential). In this last phase, ionic pumps, like $\text{Na}^+/\text{Ca}^{2+}$ exchanger also plays a role in the restoration of the resting state. An action potential propagates from the sinoatrial node to the cardiac myocytes of both atria.¹⁴ Next, the electrical activation will propagate through the atrioventricular node, where it will slow down to create the critical delay between atrial and ventricular contraction, which is needed to allow blood emptying from the atria. Finally, the electrical impulse activates the cardiomyocytes of the ventricles, from apex to base, through a specialized conduction network consisting of the His-bundle, left and right bundle branches and the Purkinje network. Such propagation between cardiac cells relies on intercellular channels called gap junctions. Gap junctions consist of six hexamers of proteins called connexins that form transmembrane hemichannels (connexons) which connect to connexons of neighboring cells allowing the diffusion of small ions and small molecules.^{15,16} Connexins can co-oligomerize with the same connexins and form homomeric connexons or with mixed connexins and form heteromeric connexons, although only certain combinations are permitted. The same is true for the connexon assembly.¹⁷ Gap junction expression is tissue-specific and the ventricles mainly express connexin43 and connexin45, whereas connexin40, connexin43, and connexin45 are found in the atria and conduction system.¹⁸

In summary, in normal and healthy conditions, an action potential originates from the cells at the sinus node and propagates from the atria to the ventricles, followed by their mechanical activation.

In diseased conditions, *e.g.* ischemic heart disease, cardiomyopathy, coronary artery disease, the initiation and propagation of an action potential may become disturbed, thereby leading to cardiac arrhythmias.¹² Cardiac arrhythmias can be subdivided into bradyarrhythmias or tachyarrhythmias (on which this thesis is focused on), when the heart rate is either too low or too high, respectively. Bradyarrhythmias arise when impulse generation at the sinus node is abnormally slow or atrioventricular conduction is impaired. Tachyarrhythmias, such as atrial tachycardia, atrial fibrillation, ventricular tachycardia, and ventricular fibrillation, can originate from (i) abnormal impulse generation leading to automaticity or triggered activity and/or (ii) disrupted propagation that results in reentrant activation.¹⁹

Automaticity can be caused by enhanced normal automaticity or abnormal automaticity. Enhanced normal automaticity occurs when pacemaker cells, like those localized in the sinus node, give rise to an increased number of action potentials in time, due to an increased rate of spontaneous diastolic depolarization of the transmembrane potential. In those cells, the so-called funny current, also known as pacemaker current, is thought to have a major role in such depolarization.²⁰

Abnormal automaticity, instead, originates from non-pacemaker cells when the resting potential is sufficient depolarized to induce spontaneous impulse initiation. Such automaticity can be caused by abnormal Ca^{2+} handling, activation, and inactivation of delayed rectifier I_k , and inward I_{Na} current through the $\text{Na}^+/\text{Ca}^{2+}$ exchanger.²¹

Triggered activity involves new impulse initiation that is caused by depolarizations that follow a preceding action potential. Such depolarizations are called afterdepolarization and can occur early during repolarization phase (early-afterdepolarizations, EADs), or late when the cells are back in their resting state (late-afterdepolarization, DADs).^{22,23} EADs arise when the repolarization, during phase 2 or 3, is overcome by a transient shift of the net current towards an inward direction. Phase-2 EADs are mainly caused by I_{Ca} , $\text{Na}^+/\text{Ca}^{2+}$ exchanger and late I_{Na} . Phase-3 EADs are, instead, caused by dysfunction of Na^+ channels, *e.g.* failure to inactivate, increase of its narrow window current, and an increase in their recovery from inactivation. DADs are usually dependent on Ca^{2+} overload in the cytoplasm. Such increase activates the $\text{Na}^+/\text{Ca}^{2+}$ exchanger and the Ca^{2+} ions activate chloride channels that lead to depolarizing oscillation of the membrane potential that eventually will trigger a new action potential.

Regarding disturbed propagation, reentrant arrhythmias occur when an impulse propagates and re-excite cardiac tissue, giving rise to repetitive cycles.²⁴ Reentrant activity can propagate around an anatomical obstacle or a functional core defining in this way anatomical or functional reentry, respectively.^{24,25} In an anatomically determined circuit, the wave-front and the wave-tail are separated by a zone of excitable tissue called, excitable gap. The inexcitable anatomical obstacles delineate a pathway that is fixed in length and location, giving rise to tachyarrhythmias that are characterized by a monomorphic electrocardiographic pattern. The initiation and maintenance of anatomical reentry rely on conduction velocity and refractory period, indicating that its extinction appears when the excitation wave-front encounters tissue that is not yet recovered. Functional reentry can acquire the form of a rotor that forms a dynamical organizing center supporting spiraling waves around an excitable, yet inexcited core. An important characteristic of such spiral waves is the phase singularity, where the wave-front and wave-tail meet each other. The wave-front is characterized by a curvature that progressively increases toward the core. At the phase singularity, the convex curvature reaches a critical value that makes it impossible for the activity to invade the core. A spiral wave can be stable or drift, meander and break-up giving rise to monomorphic or polymorphic electrograms, respectively. Such latter behavior can appear in the presence of heterogeneities, such as gradients in excitability and refractoriness.^{26,27} Furthermore, a reentrant wave can make alternate transition between functional and anatomical reentry by pinning to or unpinning from an anatomical obstruction.²⁸⁻³⁰ Such phenomenon, which depends on several factors (*e.g.* size of the obstacle and tissue excitability),^{29,30} highlights the difficulty in identifying which type of reentry drives cardiac arrhythmia at a given time and space.

Treatment of cardiac arrhythmias via gene therapy

As already mentioned, the available treatments for cardiac arrhythmias are far from optimal, often characterized by side effects such as limited specificity, pain, and permanent tissue

damage.³⁻⁷ Such limitations may be overcome by an alternative strategy, *i.e.* gene therapy. This strategy relies on three main strategies: gene transfer, gene silencing, and gene editing. Gene transfer aims to i) replace a missing or not functioning protein or ii) introduce a protein that is normally not expressed. Gene silencing, instead, is used to reduce the expression of a certain protein. Finally, gene editing aims to repair a DNA sequence to reconstitute its functionality.^{8,9} All gene therapy strategies need the selection of a vector and a delivery system. The vectors are needed to translocate genetic material into the targeted cells. Those vectors can be nonviral or viral. The nonviral vectors include plasmid DNA, which often forms complexes with other molecules that will improve the intracellular translocation.³¹ Several studies have indicated how the percentage of genetically modified cells would increase when instead viral vectors were used.³² Those viral vectors are viruses that have been mutated to inhibit their reproduction and the pathology associated with them. For the *in vivo* application adeno-associated viruses (AAV) seem to be the first choice.^{33,34} These vectors, indeed, allow long-term gene expression with limited immune reactions. Furthermore, their small diameter allows easier penetration through the cardiac tissue. However, they cannot be always used since they cannot incorporate a transgene higher than 4.6 kb. For the *in vitro* application, the choice often goes towards the application of lentiviral (LV) vectors. Those vectors are characterized by a positive sense single strand linear RNA molecules that are reverse transcribed into cDNA that will allow integration of the transgene into the host genomic material allowing long-term gene expression. However, this latter property might cause insertional mutagenesis.^{35,36}

The use of viral particles allowed genetic modification of large mammalian heart via myocardial injection, intracoronary perfusion, and atrial epicardial gene painting. Genetic interventions have been used, for instance, to suppress atrial fibrillation in pigs by kv11.1 channel inactivation, *i.e.* by prolonging the action potential duration and the effective refractory period. Such modification was achieved in two independent studies by epicardial gene painting or direct atrial injection, respectively.^{37,38} In another study, AF was suppressed by increasing the expression of connexins 40 and 43, therefore increasing the conduction velocity across the atria.^{39,40} Ventricular arrhythmias have been suppressed by gene therapy in rat and pig ischemic heart models. An ischemic event leads to a decreased level of ATP and, as a consequence, to a decreased activity of the ATP-dependent calcium pump, SERCA, leading to an increased Ca^{2+} intracellular concentration, which, as mentioned in the previous paragraph, can induce EADs. In these studies, the overexpression of such pump was able to reduce ventricular arrhythmias.^{41,42}

However, such genetic modifications are lacking the full control over their quantitative activation in space and time. Such control might be achieved thanks to optogenetics that combines optics and gene therapy.

Optogenetics

The term optogenetics, introduced for the first time by Deisseroth, refers to the combination of optical and genetic techniques. Such combination allows the expression of light-activatable proteins, named microbial rhodopsins, which activation can be precisely controlled in space,

time and quantity by light.¹⁰ Bacteriorhodopsins, halorhodopsins, and channelrhodopsins are the microbial rhodopsins that have been intensively used in the optogenetic field. These proteins are usually expressed in organisms such as archaeobacteria and algae, where they exploit different functions. These functions range from the conversion of light into chemical energy or the motile reorientation away or towards a light source.⁴³ Structurally, these proteins are characterized by seven transmembrane α -helices with the N- and C-terminus facing the extracellular or intracellular milieu, respectively. In all microbial rhodopsin a chromophore, *i.e.* all-trans-retinal, is attached by a Schiff base linkage to the ϵ -amino group of a Lysine side chain in the middle of the helix 7. The retinal Schiff base is usually protonated, thereby determining the protein absorption into the visible light spectrum. When instead the Schiff base is unprotonated the absorption is shifted in the UV region. Beside the Schiff base protonation, the absorption spectrum is also determined by the chromophore-protein interactions such as electrostatic interaction with charged and polar amino acids.⁴⁴ Functionally, these proteins are activated by light of a specific wavelength that will isomerize the retinal from all-trans to 13-cis. Such isomerization will change the conformation of the proteins and allow the preferential passage of certain ions. Upon a light pulse, each of these proteins is characterized by an initial current, I_{Peak} , which decays to a steady-state current, $I_{\text{Steady-state}}$. Relaxation from I_{Peak} to $I_{\text{Steady-state}}$ is commonly called desensitization. Finally, the off-kinetics are determined by the rate of channels closure at the end of the light pulse.⁴⁵ With the aim to control the membrane potential of excitable cells these proteins have been expressed in heterologous living cells and tissue. Channelrhodopsin-2 (Chr2) have been used to depolarize the membrane of cells while Halorhodopsins and Archeorhodopsins have been used to inhibit excitation by producing a hyperpolarizing current, based on chloride ions that are pumped in or protons that are pumped out, respectively.⁴⁶⁻⁴⁸ Over the years several Chr2 mutants have been generated with the aim to improve biophysical properties of the channels, like the ion selectivity, kinetics, spectrum response properties.⁴⁸ This now opens new and unique possibilities for cardiac arrhythmias research based on optical modulation of excitability with superb spatiotemporal resolution.

AIM OF THE THESIS AND SUMMARY

Therefore, the aim of this thesis is to employ the unique features of optogenetic for investigating the underlying mechanism of arrhythmia initiation, maintenance, and termination in order to identify novel biological anti-arrhythmic strategies. In **Chapter I** of this thesis a comprehensive description of rhythmic disturbances, gene therapy, and optogenetics is presented. In **Chapter II**, all the steps needed to successfully optogenetically modify atrial cardiomyocytes (aCMCs) are described, going from the isolation of native aCMCs, to the production of the LV particles, the use of the particle to optogenetically modify the aCMCs and finally the functional assay showing the possibility to pace those monolayers by light. In **Chapter III**, monolayers of aCMCs expressing the depolarizing tool CatCh (calcium translocating channelrhodopsin)⁴⁸ were used to investigate rotor termination by optogenetically blocking electrical activation at or near the rotor core region. The block at the rotor core region would mimic a new ablation strategy, that recently has been adopted in clinical settings, *i.e.* rotor guided ablation, and allow

1

to explore its mechanism of termination. In **Chapter IV**, the CatCh-expressing monolayers were used to investigate the possibility to optogenetically control the spatial and temporal dynamics of a spiral wave. In this study *in vitro* experiments were implemented by *in silico* experiments. In **Chapter V**, CatCh was expressed in neonatal ventricular tissue slices to investigate optogenetic termination of anatomical reentry. Finally, in **Chapter VI** we exploited a different optogenetic tool in combination with patterned illumination to quantitatively exert spatial and temporal control over the production of reactive oxygen species (ROS) in monolayers of neonatal rat ventricular myocytes (NRVMs). This combination allowed to assess ROS effects on arrhythmogenicity.

REFERENCES

1. Miyasaka Y, Barnes ME, Bailey KR, Cha SS, Gersh BJ, Seward JB, Tsang TS. Mortality trends in patients diagnosed with first atrial fibrillation: A 21-year community-based study. *Journal of the American College of Cardiology*. 2007; 49:986-992.
2. Zipes DP, Wellens HJ. Sudden cardiac death. *Circulation*. 1998; 98:2334-2351.
3. Connolly SJ, Camm AJ, Halperin JL, Joyner C, Alings M, Amerena J, Atar D, Avezum A, Blomstrom P, Borggrefe M, Budaj A, Chen SA, Ching CK, Commerford P, Dans A, Davy JM, Delacretaz E, Di Pasquale G, Diaz R, Dorian P, Flaker G, Golitsyn S, Gonzalez Hermosillo A, Granger CB, Heidbuchel H, Kautzner J, Kim JS, Lanan F, Lewis BS, Merino JL, Morillo C, Murin J, Narasimhan C, Paolasso E, Parkhomenko A, Peters NS, Sim KH, Stiles MK, Tanomsup S, Toivonen L, Tomcsanyi J, Torp-Pedersen C, Tse HF, Vardas P, Vinereanu D, Xavier D, Zhu J, Zhu JR, Baret-Cormel L, Weinling E, Staiger C, Yusuf S, Chrolavicius S, Afzal R, Hohnloser SH, Investigators P. Dronedronedrone in high-risk permanent atrial fibrillation. *The New England journal of medicine*. 2011; 365:2268-2276.
4. Echt DS, Liebson PR, Mitchell LB, Peters RW, Obias-Manno D, Barker AH, Arensberg D, Baker A, Friedman L, Greene HL, et al Mortality and morbidity in patients receiving encainide, flecainide, or placebo. The cardiac arrhythmia suppression trial. *The New England journal of medicine*. 1991; 324:781-788.
5. Spragg DD, Dalal D, Cheema A, Scherr D, Chilukuri K, Cheng A, Henrikson CA, Marine JE, Berger RD, Dong J, Calkins H. Complications of catheter ablation for atrial fibrillation: Incidence and predictors. *Journal of cardiovascular electrophysiology*. 2008;19:627-631.
6. Bohnen M, Stevenson WG, Tedrow UB, Michaud GF, John RM, Epstein LM, Albert CM, Koplman BA. Incidence and predictors of major complications from contemporary catheter ablation to treat cardiac arrhythmias. *Heart rhythm: the official journal of the Heart Rhythm Society*. 2011; 8:1661-1666.
7. Kamphuis HC, de Leeuw JR, Derksen R, Hauer RN, Winnubst JA. Implantable cardioverter defibrillator recipients: Quality of life in recipients with and without and shock delivery: A prospective study. *Europace: European pacing, arrhythmias, and cardiac electrophysiology: journal of the working groups on cardiac pacing, arrhythmias, and cardiac cellular electrophysiology of the European Society of Cardiology*. 2003; 5:381-389.
8. Lugenbiel P, Schweizer PA, Katus HA, et al Antiarrhythmic gene therapy – will biologics replace catheters, drugs, and devices? *Eur J Pharmacol*. 2016; 15:264-273.
9. Bongianino R, Bongianino R, Priori SG Gene therapy to treat cardiac arrhythmias. *Nat Rev Cardiol*. 2015; 12:531-546.
10. Boyden ES, Zhang F, Bamberg E, Nagel G, Deisseroth K. Millisecond-timescale, genetically targeted optical control of neural activity. *Nature Neurosci*. 2015; 8:1263-1268.
11. Xin M, Olson EN, Bassel-Duby R. Mending broken hearts: cardiac development as a basis for adult heart regeneration and repair. *Nat Rev Mol Cell Biol*. 2013; 14: 529-541.
12. Hodgkin AL, Huxley AF. Currents carried by sodium and potassium ions through the membrane of the giant axon of Loligo. *The Journal of physiology*. 1952; 116:449-472.
13. Roden DM, Balsler JR, George AL, Jr., Anderson ME. Cardiac ion channels. *Annual review of physiology*. 2002; 64:431-475.
14. Feher J. The Cardiac Action Potential. *Quantitative Human Physiology*. 2012, 458-466.
15. Caspar DL, Goodenough DA, Makowski L, Phillips WC. Gap junction structures. I. Correlated electron microscopy and x-ray diffraction. *The Journal of cell biology*. 1977; 74:605-628.
16. Makowski L, Caspar DL, Phillips WC, Goodenough DA. Gap junction structures.

- ii. Analysis of the x-ray diffraction data. *The Journal of cell biology*. 1977; 74:629-645.
17. Unwin PN, Zampighi G. Structure of the junction between communicating cells. *Nature*. 1980; 283:545-549.
 18. Davis LM, Kanter HL, Beyer EC, Saffitz JE. Distinct gap junction protein phenotypes in cardiac tissues with disparate conduction properties. *Journal of the American College of Cardiology*. 1994; 24:1124-1132.
 19. Pogwizd SM, Hoyt RH, Saffitz JE, Corr PB, Cox JL, Cain ME. Reentrant and focal mechanisms underlying ventricular tachycardia in the human heart. *Circulation*. 1992; 86:1872-1887.
 20. DiFrancesco D, Ojeda C. Properties of the current i_f in the sino-atrial node of the rabbit compared with those of the current i_k in Purkinje fibres. *The Journal of physiology*. 1980; 308:353-367.
 21. le Marec H, Dangman KH, Danilo P, Rosen MR. An evaluation of automaticity and triggered activity in the canine heart one to four days after myocardial infarction. *Circulation*. 1985; 71:1224-1236.
 22. Ming Z, Nordin C, Aronson RS. Role of l-type calcium channel window current in generating current-induced early afterdepolarizations. *Journal of cardiovascular electrophysiology*. 1994; 5:323-334.
 23. Katra RP, Laurita KR. Cellular mechanism of calcium-mediated triggered activity in the heart. *Circulation research*. 2005; 96:535- 542.
 24. Rotors and the Dynamics of Cardiac Fibrillation. *Circ Res*. 2013; 112:849-862.
 25. Fast VG, Kleber AG. Role of wavefront curvature in propagation of cardiac impulse. *Cardiovascular research*. 1997; 33:258-271.
 26. Pertsov AM, Davidenko JM, Salomonsz R, Baxter WT, Jalife J. Spiral waves of excitation underlie reentrant activity in isolated cardiac muscle. *Circ Res*. 1993; 72:631-50.
 27. Fast VG, Kleber AG. Role of wavefront curvature in propagation of cardiac impulse. *Cardiovasc Res*. 1997; 33:258-71.
 28. Cabo C, Pertsov AM, Davidenko JM, Baxter WT, Gray RA, Jalife J. Vortex shedding as a precursor of turbulent electrical activity in cardiac muscle. *Biophys J*. 1996; 70:1105-11.
 29. Lim ZY, Maskara B, Aguel F, Emokpae R, Jr., Tung L. Spiral wave attachment to millimeter-sized obstacles. *Circulation*. 2006; 114:2113-21.
 30. Ikeda T, Yashima M, Uchida T, Hough D, Fishbein MC, Mandel WJ, Chen PS, Karagueuzian HS. Attachment of meandering reentrant wave fronts to anatomic obstacles in the atrium. Role of the obstacle size. *Circ Res*. 1997; 81:753-64.
 31. Yin H, Kanasty RL, Eltoukhy AA, Vegas AJ, Dorkin JR, Anderson DG. Nonviral vectors for gene-based therapy. *Nat Rev Genet*. 2014; 15:541-555.
 32. Katz MG, Fargnoli AS, Williams RD, Bridges CR. Gene therapy delivery systems for enhancing viral and nonviral vectors for cardiac diseases: current concepts and future applications. *Hum Gene Ther*. 2013; 24:914-927.
 33. Prasad KM, Xu Y, Yang Z, Acton ST, French BARobust cardiomyocyte specific gene expression following systemic injection of AAV: in vivo gene delivery follows a Poisson distribution. *Gene Ther*. 2011; 18:43-52.
 34. Kotterman MA, Schaffer DV. Engineering adeno-associated viruses for clinical gene therapy. *Nat Rev Genet*. 2014; 15:445-451.
 35. Pluta K, Kacprzak MM. Use of HIV as a gene transfer vector. *Acta Biochim Pol*. 2009; 56:531-595.
 36. Pauwels K, Gijssbers R, Toelen J, Schambach A, Willard-Gallo K, Verheust C, Debyser Z, Herman P. State-of-the-art lentiviral vectors for research use: risk assessment and biosafety recommendations. *Curr Gene Ther*. 2009; 9:459-474.
 37. Amit G, Kikuchi K, Greener ID, Yang L, Novack V, Donahue JK. Selective molecular potassium channel blockade prevents atrial fibrillation. *Circulation*. 2010; 121:2263-2270.
 38. Soucek R, Thomas D, Kelemen K, Bikou O, Seyler C, Voss F, Becker R, Koenen M, Katus HA, Bauer A. Genetic suppression of atrial fibrillation using a dominant-

- negative ether-a-go-go-related gene mutant. *Heart Rhythm*. 2012; 9:265-272.
39. Igarashi T, Finet JE, Takeuchi A, Fujino Y, Strom M, Greener ID, Rosenbaum DS, Donahue JK. Connexin gene transfer preserves conduction velocity and prevents atrial fibrillation. *Circulation*. 2012; 125:216-225.
 40. Bikou O, Thomas D, Trappe K, Lugenbiel P, Kelemen K, Koch M, Soucek R, Voss F, Becker R, Katus HA, Bauer A. Connexin 43 gene therapy prevents persistent atrial fibrillation in a porcine model. *Cardiovasc. Res*. 2011; 92:218-225.
 41. Del Monte F, Lebeche D, Guerrero JL, Tsuji T, Doye AA, Gwathmey JK, Hajjar R.J. Abrogation of ventricular arrhythmias in a model of ischemia and reperfusion by targeting myocardial calcium cycling. *Proc. Natl. Acad. Sci. USA*. 2004; 101:5622-562.
 42. Prunier F, Kawase Y, Gianni D, Scapin C, Danik SB, Ellinor PT, Hajjar RJ, Del Monte F. Prevention of ventricular arrhythmias with sarcoplasmic reticulum Ca²⁺ATPase pump overexpression in a porcine model of ischemia reperfusion. *Circulation*. 2008; 118:614-624.
 43. Schneider F, Grimm C, Hegemann P. Biophysics of Channelrhodopsin. *Annual Review of Biophysics*. 2015; 44:167-186.
 44. Lórenz-Fonfría VA, Heberle J. Channelrhodopsin unchained: Structure and mechanism of a light-gated cation channel. *Biochimica et Biophysica Acta (BBA) – Bioenergetics*. 2014; 5:626-642.
 45. Berndt A, Prigge M, Gradmann D, Hegemann P. Two open states with progressive proton selectivities in the branched channelrhodopsin-2 photocycle. *Biophys. J*. 2010; 98:753–761.
 46. Entcheva E. Cardiac optogenetics. *Am J Physiol Heart Circ Physiol*. 2013; 304:1179-1191.
 47. Ambrosi CM, Klimas A, Yu J, Entcheva E. Cardiac applications of optogenetics. *Prog Biophys Mol Biol*. 2014; 115:294-304.
 48. Kleinlogel S, Feldbauer K, Dempski RE, Fotis H, Wood PG, Bamann C, Bamberg, E. Ultra light-sensitive and fast neuronal activation with the Ca(2)+-permeable channelrhodopsin CatCh. *Nat Neurosci*. 2011; 14:513-518.



Chapter

OPTOGENETIC ENGINEERING OF ATRIAL CARDIOMYOCYTES

Iolanda Feola, MSc; Alexander Teplenin, MSc;
Antoine A.F. de Vries, PhD; Daniël A. Pijnappels, PhD.

Laboratory of Experimental Cardiology, Department of Cardiology, Heart
Lung Center Leiden; Leiden University Medical Center, the Netherlands.

2

SUMMARY

2

Optogenetics is emerging in the cardiology field as a new strategy to explore biological functions through the use of light-sensitive proteins and dedicated light sources. For example, this technology allows modification of the electrophysiological properties of cardiac muscle cells with superb spatiotemporal resolution and quantitative control. In this paper, the optogenetic modification of atrial cardiomyocytes (aCMCs) from 2-day-old Wistar rats using lentiviral vector (LV) technology and the subsequent activation of the light-sensitive proteins (*i.e.* ion channels) through light-emitting diodes (LEDs) are described.

Keywords: Optogenetics, Atrial Cardiomyocytes, Lentiviral vectors, Optical mapping, Light-emitting diode (LED)

INTRODUCTION

Optogenetics is a new technology to control cellular function by a combination of genetic engineering and light application. Optogenetics has revolutionized neuroscience by offering the possibility to control at high spatial and temporal resolution various biological processes both *in vitro* and *in vivo*.¹ Despite these unique features, optogenetics has not yet been extensively explored in cardiac research. Nevertheless, several scientific contributions have shown how light-gated ion channels can modulate the transmembrane potential of cardiomyocytes giving rise to excitatory or inhibitory responses, controlled in time, space and magnitude.^{2,3} Channelrhodopsins are excitatory proteins that upon illumination can evoke an action potential (AP) in excitable cells due to the passive inward flow of positively charged ions.⁴ When instead light induces protons or potassium ions to leave the cell or chloride ions to enter the cell, cellular excitation is inhibited.⁵⁻⁹ Due to their specific properties, light-activated ion transporters may be very helpful to gain additional insight into the mechanisms underlying cardiac arrhythmias, which may inspire the exploration of new strategies for treating electrical disturbances in the heart. Besides via light-gated ion transporters, optogenetics offers many other possibilities to control cellular behavior, including transcription as well as intracellular and receptor signaling and could thereby further improve our understanding of cardiomyocyte biology and heart function.¹⁰⁻¹²

The following section describes how aCMCs, isolated from the hearts of 2-day-old Wistar rats, can be successfully optogenetically engineered by forced expression of a depolarizing optogenetic tool, *i.e.*, Ca²⁺-permeable channelrhodopsin (CatCh) following LV-mediated transgene delivery.¹³ In addition, details are provided on how to study the functional consequences of LED-mediated CatCh activation by optical voltage mapping. For example, exposure of CatCh-expressing aCMCs to 10-ms blue light pulses induces a photocurrent strong enough to evoke an action potential (AP) in these cells.¹⁴

MATERIALS

Reagents for isolating aCMCs

- Isoflurane.
- Fibronectin working solution (100 µg/ml): dilute the fibronectin stock solution 10 times with phosphate-buffered saline (PBS) and store at 4°C.
- Solution A: 0.02 g/l phenol red, 136 mM NaCl, 5 mM KCl, 0.2 mM Na₂HPO₄·2H₂O, 0.44 mM KH₂PO₄, 5.5 mM D-glucose and 20 mM HEPES-acid free. Adjust the pH to 7.4-7.5 by adding 5 M NaOH at 21°C. Sterilize by filtration through a 0.22 µm pore size cellulose acetate bottle top filter and store at 4°C.
- Solution B: 1 mM CaCl₂·2H₂O, 60 mM MgCl₂·6H₂O in Solution A. Store at -20°C.
- Solution C: DNase I solution. Mix 500 units of deoxyribonuclease with 800 µl Solution A. Store at -20°C.

- Dissociation medium: mix 90,000 units of collagenase type I (Worthington Biochemical, Lakewood, NJ, USA) with 200 ml of Solution A, 2 ml of solution B and 200 μ l of solution C. Sterilize by filtration through a 0.22 μ m pore size cellulose acetate bottle top filter and store at -20°C.
- Growth medium: mix 450 ml of 1 \times Ham's F10 nutrient mix with 10 ml of heat-inactivated fetal bovine serum (HI-FBS), 10 ml of heat-inactivated horse serum (HI-HS) and 10 ml of penicillin-streptomycin stock solution (5000 U/ml). Store at 4°C.
- Solution D: 2.8 M sodium ascorbate, 107 mM pyruvic acid, 500 mM D-glucose and 5.7% (w/v) bovine serum albumin (BSA).
- CMC medium: add 15 ml of solution D to 250 ml of Dulbecco's modified Eagle's medium (DMEM)-low glucose. Next, add 25 ml of 10 \times Ham's F10, 192.5 ml of sterile water, 4 ml of 7.5% sodium-bicarbonate, 0.305 ml of 0.2 M L-glutamine, and 10 ml of penicillin-streptomycin solution. Store at 4°C.
- Sterile glass beads, 6.7-7.3 mm ϕ .
- Mitomycin-C solution: dissolve 2 mg Mitomycin-C powder (from *Streptomyces caespitosus*) in 4 ml PBS. Sterilize by filtration through a 0.22 μ m pore size cellulose acetate syringe filter and store at 4°C.
- Round glass coverslips (15 mm ϕ).
- Primaria cell culture dishes (60 mm ϕ).
- Falcon 70 μ m mesh size cell strainers.
- Costar 24 well clear TC-treated multiple well plates.

Reagents for producing self-inactivating LVs (SIN-LVs)

- 293T cells.¹⁵
- SIN-LV shuttle plasmid pLV.MHCK7.CatCh~eYFP.WHVPRE and derivatives thereof.¹⁴
- SIN-LV packaging/helper plasmids psPAX2 and pLP/VSV-G.
- DMEM-high glucose (HG) + 10% FBS.
- DMEM-HG + 5% FBS + 25 mM HEPES-NaOH (pH 7.4).
- TrypLE Express.
- 150 mM sterile NaCl solution.
- 1 mg/ml PEI solution (pH 7.4): weigh 45 mg of linear polyethylenimine (Mw 25,000), add 100 μ l of 1M HCl and 40 ml of sterile water of 80°C. Shake vigorously to facilitate dissolution. Adjust the pH to 7.4 with 37% HCl. Increase the total volume to 45 ml with

sterile water. Sterilize by filtration through a 0.22 μm pore size cellulose acetate syringe filter and store in 1.8-ml aliquots at -80°C .

- 20% sucrose solution: weigh 100 g of sucrose and add 500 ml of $10\times$ PBS. Increase the volume to 500 ml with sterile water. Use a magnetic stirrer to facilitate dissolution. Sterilize by filtration through a 0.22 μm pore size cellulose acetate bottle top filter and store in 50-ml aliquots at 4°C .
- Polyallomer ultracentrifuge tubes for SW28 or SW32 rotor.
- Millex sterile 0.45 μm pore size syringe filters (33 mm \varnothing).
- BD Plastipak sterile 50-ml syringes with Luer Lock system.
- PBS-1% BSA: dissolve 1 g of BSA in 100 ml of PBS by gentle stirring with a magnetic stirrer. Sterilize by filtration through 0.22 μm pore size cellulose acetate syringe filters and store in 1.6-ml aliquots at 4°C .

Combination of LED and optical mapping system

- HEPES-buffered, phenol red-free DMEM/F12.
- Di-4-ANEPPS solution (1 mg/ml): dissolve 5 mg of di-4-ANEPPS powder in 5 ml sterile dimethyl sulfoxide (DMSO) and store in 500- μl aliquots at 4°C and protected from light.
- MiCAM ULTIMA-L imaging system (SciMedia, Costa Mesa, CA, USA).
- Excitation filter (530 nm pass, Semrock, Rochester, NY, USA).
- Dichroic mirror (520-560 nm reflect $>90\%$, >600 nm pass $>85\%$, Semrock).
- Emission filter (>590 nm pass, Semrock).
- 470-nm Rebel LED mounted on a 25 mm \varnothing round CoolBase (Luxeonstar, Brantford, Ontario, Canada).
- Plano-convex lens (1 inch \varnothing , 25.4 mm focal length) (Thorlabs, Munich, Germany).
- Stimulus generator STG2004 (Multichannel System, Reutlingen, Germany).
- Custom-made platinum electrode pair for bipolar point stimulation.
- Power meter PM100D (Thorlabs).
- Brain Vision Analyzer 1208 software (Brainvision, Tokyo, Japan).

METHODS

aCMC isolation and culture

Isolation of aCMCs

2

- Anaesthetize 2-day-old Wistar rats (n>50) via 4-5% isoflurane inhalation. Ensure adequate anaesthesia by checking the absence of reflexes.
- Rapidly excise the hearts and collect them in a plastic Petri dish containing \pm 10 ml ice-cold Solution A.
- Separate the atria from the ventricles (*see* Note 1).
- Remove Solution A until the bottom of the Petri dish just stays covered with fluid. Chop the atrial tissues in small pieces and rinse the tissue with 4 ml of Solution A to get rid of erythrocytes (*see* Note 2).
- Prepare 12 ml of an ice-cold 1:1 mixture of dissociation medium and Solution A (Solution E). Remove solution A as much as possible with a 1000- μ l pipetman and add 7 ml of Solution E to the Petri dish with atrial tissue pieces.
- Transfer the atrial tissue pieces in Solution E to a sterile 50-ml Erlenmeyer flask with screw cap containing sterile glass beads.
- Incubate under gentle agitation at 37°C for 35 min.
- Transfer the fully digested material (5 ml) to a sterile 15-ml polypropylene screw cap tube on ice and leave the undigested material (2 ml) in the Erlenmeyer flask.
- Add 4 ml of fresh Solution E to the Erlenmeyer flask and incubate once again under agitation at 37°C for 35 min.
- Transfer the content of the Erlenmeyer flask to the 15-ml tube with the remainder of the atrial digest and pellet the cells by centrifugation for 10 min at 150 \times g. Suspend the cell pellet in 12 ml of prewarmed growth medium. Equally divide the cell suspension over 4 Primaria cell culture dishes and incubate at 37°C in a humidified 95% air/5% CO₂ atmosphere (culture conditions) for 120 min to allow preferential attachment of non-cardiomyocytes (mainly cardiac fibroblasts).
- Pass the growth medium with the non-adhered cells (mainly cardiomyocytes) through a nylon cell strainer with a mesh size of 70 μ m to remove undigested tissue fragments and cell aggregates.
- Count and seed the cells on fibronectin-coated glass coverslips in 24-well cell culture plates. To obtain confluent aCMC monolayers seed 8 \times 10⁵ cells/well.

Preparation of fibronectin-coated glass coverslips

- Place a sterile glass coverslips on the bottom of each well of a 24-well cell culture plate.

- Add 300 μ l of fibronectin solution to each well.
- Incubate for 1 h under culture conditions.
- Collect the fibronectin solution (can be used 2 more times) and leave the coverslips to dry in the flow hood for about 60 min.

Antiproliferative treatment with mitomycin-C

- The day after isolation dilute the mitomycin-C solution 50 times in growth medium and add 300 μ l/well of a 24-well cell culture plate.¹⁶
- Incubate for 2 h under culture conditions.
- Rinse the cells twice with PBS.
- Add 1 ml of CMC medium + 5% HI-HS of 37°C/well and maintain the cells under culture conditions.
- Refresh the culture medium once a day.

Production of vesicular stomatitis virus G protein (VSV-G)-pseudotyped SIN-LVs

Seeding of 293T cells in 175-cm² cell culture flasks

- Use 293T cells of low passage number for LV production. Check the 293T cells using an inverted phase-contrast microscope. When the cultures are \pm 80% confluent, remove the medium and rinse each 175-cm² cell culture flask once with 10 ml PBS.
- Add 1.5 ml of TrypLE Express/flask and after 1 min incubation gently rock the flask to facilitate cell detachment. Once the cells have detached from the plastic support collect them in DMEM-HG + 10% FBS.
- Generate a single cell suspension by forcefully pipetting the cell suspension up and down 3-5 times to disrupt remaining cell clusters without destroying the cells (can be checked microscopically).
- Suspend 7×10^7 viable 293T cells in 85 ml DMEM-HG + 10% FBS and add 20 ml of the cell suspension to each 175-cm² cell culture flask (*i.e.*, 1.65×10^7 cells/flask). Make sure the cells become evenly spread over the plastic support (*see* Note 3).

Transfection of 293T cells

- The day after, before starting with the transfection make sure that the cells are \pm 60-70% confluent, evenly spread over the surface of the culture flasks and viable (*see* Note 4).
- Prepare the DNA/NaCl solution by diluting 154 μ g of plasmid DNA (molar ratio SIN-LV shuttle plasmid:psPAX2:pLP/VSV-G is 8:5:5) in 4.4 ml of 150 mM NaCl in a sterile 50-ml polypropylene screw cap tube (*see* Note 5). Add the DNA to the NaCl solution instead of

the other way around and mix by gentle vortexing. The cell type(s) in which and the level at which the transgene is expressed will be determined by the promoter that drives its expression (Figure 1).

- Prepare the PEI/NaCl solution by adding 504 μ l of 1 mg/ml PEI solution to 4296 μ l of 150 mM NaCl in a sterile 50-ml polypropylene screw cap tube. Mix the PEI with the NaCl solution by gentle vortexing.
- Add 4.4 ml of the PEI/NaCl solution to the DNA/NaCl solution in a dropwise fashion. Gently rock/swirl the tubes during the addition of the PEI solution. Homogenize the content of the tubes by vortexing for 10 s (*see Note 6*).
- Incubate the tubes for 15 min at RT to allow the formation of DNA/PEI complexes, and then add 2 ml of this transfection mixture to each flask. Move the flasks to completely mix the transfection mixture and culture medium.

Replacement of the transfection medium by DMEM-HG + 5% FBS + 25 mM HEPES-NaOH (pH 7.4)

- Replace the transfection medium in each of the 175-cm² cell culture flasks by 15 ml fresh DMEM-HG + 5% FBS + 25 mM HEPES-NaOH (pH 7.4) (*see Note 7*).

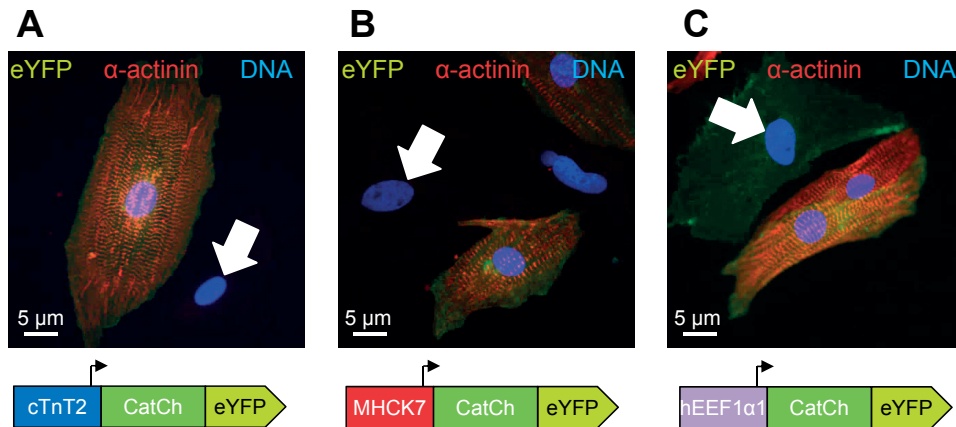


Figure 1. Immunocytochemical confirmation of aCMC-specific transgene expression. aCMC cultures were incubated with CatCh~eYFP-encoding SIN-LVs in which transgene expression was driven by (A) the striated muscle-specific MHCK7 promoter,²⁰ (B) the cardiomyocyte-specific chicken Tnnt2 promoter²¹ or (C) the ubiquitous human EEF1A1 promoter. The MHCK7 and Tnnt2 promoter give rise to transgene expression in α -actinin⁺ cells (*i.e.*, cardiomyocytes) only, while the promoter of the housekeeping gene EEF1A1 directs transgene expression in α -actinin⁺ cells as well as α -actinin⁻ cells (*i.e.*, cardiac fibroblasts [white arrows]). The blue fluorescence corresponds to cell nuclei stained with Hoechst 33342.

Harvesting of the culture supernatants and concentration/purification of the SIN-LV particles

- Before harvesting the LV particle-containing culture supernatants, \pm 36-48 h after transfection, check the transfection efficiency of the 293T cells using an inverted fluorescence microscope (Figure 2).
- Transfer the culture medium of each pair of two 175-cm² cell culture flasks to a sterile 50-ml polypropylene screw cap tube.
- Centrifuge the tubes for 10 min at 3,000 \times g and RT in a tabletop centrifuge.
- Push the cleared culture media through 0.45 μ m pore size polyethersulfone syringe filters and collect the filtrate in autoclaved 38.5-ml polyallomer ultracentrifuge tubes.
- Carefully move a 5-ml stripette containing 7 ml of 20% sucrose in PBS through the cell culture medium to the bottom of the ultracentrifuge tube and slowly release 5 ml of the sucrose solution to underlay the culture medium with a sucrose cushion.
- After taring with DMEM-HG + 5% FBS + 25 mM HEPES-NaOH (pH 7.4) spin the ultracentrifuge tubes for 2 h with slow acceleration and without braking at 15,000 revolutions/min and 4°C.
- Aspirate the supernatant and place the ultracentrifuge tube upside down on a piece of sterile filter paper to absorb the remaining supernatant.
- Add 400 μ l of ice-cold PBS-1% BSA to the LV particle-containing pellet in each ultracentrifuge tube.
- Place each ultracentrifuge tube in upright position in a 50-ml polypropylene screw cap tube and incubate overnight at 4°C in the cold room while shaking gently and with the cap closed.

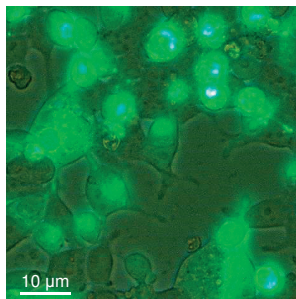


Figure 2. Fluoromicrograph of 293T cells 36 h after co-transfection with psPAX2, pLP/VSV-G and pLV.MHCK7.CatCh~eYFP.WHVPRE. LV yield strongly depends on the transfection efficiency, which should be >90%. The rounded shape of the cells is largely due to the cytotoxic effects associated with the accumulation and aggregation (brightly fluorescent perinuclear dots) of the CatCh~eYFP fusion protein in the LV producer cells.

Aliquoting of the concentrated SIN-LV suspensions

- Collect the SIN-LV suspensions in one of the ultracentrifuge tubes.
- Wash each ultracentrifuge tube with 100 μ l of ice-cold PBS-1% BSA and transfer the wash solution to the collection tube.
- Divide the supernatant on ice in 50-100 μ l aliquots using precooled 0.5-ml microtubes for storage at -80°C (*see* Note 8).

Transduction of aCMCs

Transduction

- Four days after aCMC isolation thaw the SIN-LV stock on ice and add the desired amount of SIN-LV particles to prewarmed CMC medium + 5% HI-HS.
- Gently mix to ensure homogenous distribution of SIN-LV particles and replace the culture medium with 400 μ l of inoculum/well of a 24-well cell culture plate (*see* Note 9).

Medium refreshment

- \pm 24 h after transduction aspirate the inoculum, wash the cells once with PBS and add 1 ml of prewarmed CMC medium + 5% HI-HS/well of a 24-well cell culture plate.

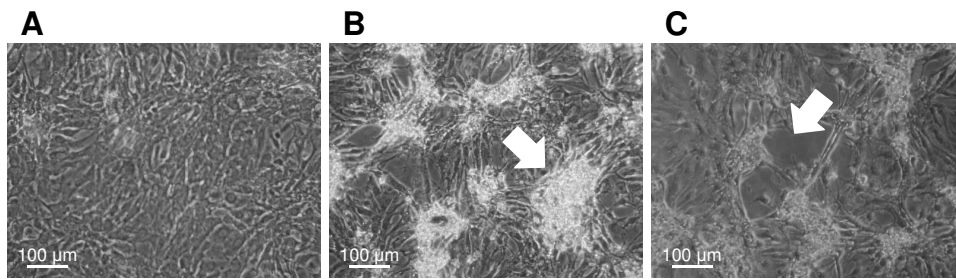
Light stimulation and optical voltage mapping

Preparation of the optical mapping system

- Place the plano-convex lens on top of the 470-nm LED.
- Align the LED assembly with the center of the MiCAM ULTIMA-L camera.
- Connect the lens-LED complex to the stimulus generator.

Preparation of aCMC cultures

- Check the aCMC monolayers for structural homogeneity, \pm 72 h after transduction, using an inverted phase-contrast microscope (*see* Note 10) (Figure 3).
- Check the aCMC monolayers for homogeneity of transgene expression by visualizing the enhanced yellow fluorescent protein tag fused to the channelrhodopsin with the aid of an inverted fluorescence microscope (*see* Note 11) (Figure 4).
- Prepare an 8 μ M di-4-ANEPPS solution in prewarmed DMEM/F12.
- Replace the CMC medium by 500 μ l of the potentiometric dye solution and incubate for 10 min under culture conditions.



2

Figure 3. Morphology of aCMC monolayers at day 9 after isolation. A, Non-interrupted, homogenous aCMC monolayer well suited form optical mapping studies. B, Inhomogenous aCMC monolayer containing star-shaped cell aggregates (white arrow). C, Non-continuous aCMC monolayer due to the presence of acellular areas (white arrow). Cultures (B) and (C) do not allow reliable acquisition of whole culture optical mapping data.

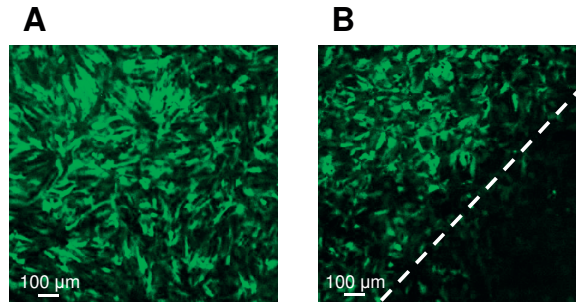


Figure 4. Fluoromicrograph of confluent aCMC cultures 3 days after transduction with LV.MHCK7. CatCh~eYFP.WHVPRE. A, Homogeneously transduced aCMC culture. B, Heterogeneously transduced aCMC culture. Only cultures showing (near-)quantitative transduction and homogenous transgene expression should be used for optical mapping experiments.

- Aspirate the di-4-ANEPPS solution and add 500 μ l DMEM/F12.
- Place the cells under the MiCAM ULTIMA-L camera.

Optical voltage mapping

- Focus the MiCAM ULTIMA-L camera and check for functional homogeneity by electrical point stimulation at a frequency of 1 Hz using 10-ms rectangular pulses of 8 V (*see* Note 12).
- While recording pace the cultures at a frequency of 1 Hz using 10-ms blue light pulses at the maximum current tolerated by the LED (*i.e.*, 700 mA) (Figure 5).

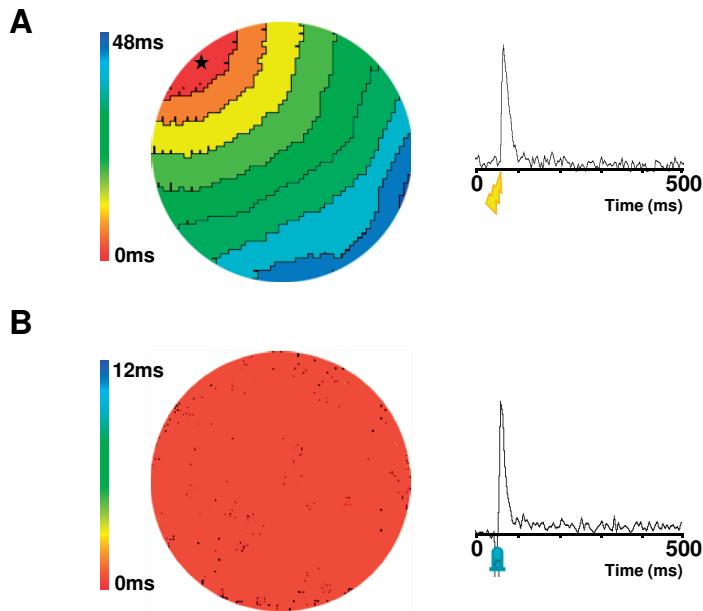


Figure 5. Activation maps (left) and optical signal traces (right) of CatCh-expressing aCMC monolayers following (A) electrical or (B) optical induction of APs. The activation map in (A) shows uniform convex AP propagation initiated at the bipolar pacing electrode (star). The activation map in (B) shows synchronous induction of APs in the entire monolayer following 10-ms exposure to 470-nm LED light (0.08 mW/mm² irradiance).

NOTES

1. Selective removal of the atria can be accomplished by placing an opened scissor tightly around the ventricles and gently moving the scissor upwards until the atria will fall on top of the blades of the scissor and can be cut off.
2. Standardization of the chopping procedure is complicated due to subtle differences in the technique used by individual researchers. Experience has taught us that both insufficient as well as excessive cutting strongly reduces cardiomyocyte yields.
3. Differences in 293T cell density within each culture flask or between culture flasks should be avoided by frequent homogenization of the cell suspension during the seeding procedure and by ensuring that the shelves of the CO₂ incubator are perfectly horizontal (check with a spirit level).
4. For LV production, only use 293T cells of low passage number (*i.e.*, <60). Furthermore, don't use 293T cells that have been seeded at too low a density, "over-trypsinized" or allowed to grow overconfluent.
5. The quality of the packing/helper construct and of the LV shuttle plasmid strongly influences LV yields. To achieve a high transfection efficiency, the plasmid DNA

- preparations should $\geq 95\%$ supercoiled as checked by agarose gel electrophoresis, have a low endotoxin content and contain minimal amounts of (in)organic contaminants.
6. The PEI/NaCl solution should be added to the DNA/NaCl solution instead of the other way around to ensure a high transfection efficiency.¹⁷
 7. 293T cells should be transfected at the right cell density (*i.e.*, subconfluency). If the cell cultures are already $\pm 60\text{-}70\%$ confluent in the morning of the day following seeding, the 293T cells should be transfected at that moment and refreshment of the transfection medium should be done in the late afternoon (*i.e.*, after 6-8 h).
 8. VSV-G-pseudotyped LV stocks can be repeatedly thawed and frozen without significant loss of functional titer provided that they are kept on ice/at 4°C during inoculum preparation.¹⁸
 9. The transduction efficiency of target cells by LVs is not only depending on the vector dose and infection period but also on the inoculum volume/vector concentration. To achieve the highest possible transduction efficiency, the inoculum volume should be kept as small as possible.¹⁹ However, the target cells should still be covered with sufficient culture medium to keep them healthy.
 10. The aCMC monolayers should not show acellular areas and/or star-shaped aggregated cell clusters.
 11. The aCMC monolayers should show homogenous transgene expression.
 12. The aCMC monolayers should not show spontaneous activity and areas of conduction slowing or block. Moreover, the monolayers should not show areas of significant optical signal prolongation.

ACKNOWLEDGMENT

This work was supported by a VIDI grant (91714336) from the Dutch Organization for Scientific Research (NWO) to Daniël Pijnappels. Antoine de Vries is a recipient of a Chinese Exchange Programme grant (10CDP007) from the Royal Netherlands Academy of Arts and Sciences (KNAW) and received additional support by ICIN-Netherlands Heart Institute.

REFERENCES

1. Boyden ES, Zhang F, Bamberg E, Nagel G, Deisseroth K. Millisecond-timescale, genetically targeted optical control of neural activity. *Nature Neurosci.* 2005; 8:1263–1268.
2. Entcheva E. Cardiac optogenetics. *Am J Physiol Heart Circ Physiol.* 2013; 304:1179-1191.
3. Bruegmann T, Malan D, Hesse M, Beiert T, Fuegemann CJ, Fleischmann BK, Sasse P. Optogenetic control of heart muscle in vitro and in vivo. *Nat Methods.* 2010; 7:897-900.
4. Nagel G, Szellas T, Huhn W, Kateriya S, Adeishvili N, Berthold P, Ollig D, Hegemann P, Bamberg E. Channelrhodopsin-2, a directly light-gated cation-selective membrane channel. *Proc Natl Acad Sci U S A.* 2003; 100:13940-13945.
5. Zhang F, Wang LP, Brauner M, Liewald JF, Kay K, Watzke N, Wood PG, Bamberg E, Nagel G, Gottschalk A, Deisseroth K. Multimodal fast optical interrogation of neural circuitry. *Nature.* 2007; 446:633–639.
6. Chow BY, Han X, Dobry AS, Qian X, Chuong AS, Li M, Henninger MA, Belfort GM, Lin Y, Monahan PE, Boyden ES. High-performance genetically targetable optical neural silencing by light-driven proton pumps. *Nature.* 2010; 463:98-102.
7. Cosentino C, Alberio L, Gazzarrini S, Aquila M, Romano E, Cermentati S, Zuccolini P, Petersen J, Beltrame M, Van Etten JL, Christie JM, Thiel G, Moroni A. Optogenetics Engineering of a light-gated potassium channel. *Science.* 2015; 348:707-710.
8. Wietek J, Wiegert JS, Adeishvili N, Schneider F, Watanabe H, Tsunoda SP, Vogt A, Elstner M, Oertner TG, Hegemann P. Conversion of channelrhodopsin into a light-gated chloride channel. *Science.* 2014; 344:409-412.
9. Berndt A, Lee SY, Ramakrishnan C, Deisseroth K. Structure-guided transformation of channelrhodopsin into a light-activated chloride channel. *Science.* 2014; 344:420-424.
10. Müller K, Naumann S, Weber W, Zurbriggen MD. Optogenetics for gene expression in mammalian cells. *Biol Chem.* 2015; 396:145-152.
11. Beyer HM, Naumann S, Weber W, and Radziwill G. Optogenetic control of signaling in mammalian cells. *Biotechnol J.* 2015; 10:273-283.
12. Zhang K, and Cui B. Optogenetic control of intracellular signaling pathways. *Trends Biotechnol.* 2015; 33:92-100.
13. Kleinlogel S, Feldbauer K, Dempski RE, Fotis H, Wood PG, Bamann C, Bamberg E. Ultra light-sensitive and fast neuronal activation with the Ca(2)+-permeable channelrhodopsin CatCh. *Nat Neurosci.* 2011; 14:513-518.
14. Bingen BO, Engels MC, Schaliij MJ, Jangsangthong W, Neshati Z, Feola I, Ypey DL, Askar SF, Panfilov AV, Pijnappels DA, de Vries AA. Light-induced termination of spiral wave arrhythmias by optogenetic engineering of atrial cardiomyocytes. *Cardiovasc Res.* 2014; 104:194–205.
15. DuBridge RB, Tang P, Hsia HC, Leong PM, Miller JH, Calos MP. Analysis of mutation in human cells by using an Epstein-Barr virus shuttle system. *Mol Cell Biol.* 1987; 7:379-387.
16. Askar SF, Ramkisoensing AA, Schaliij MJ, Bingen BO, Swildens J, van der Laarse A, de Vries AA, Ypey DL, Pijnappels DA. Antiproliferative treatment of myofibroblasts prevents arrhythmias in vitro by limiting myofibroblast-induced depolarization. *Cardiovasc Res.* 2011; 90:295-304.
17. Boussif O, Lezoualc'h F, Zanta MA, Mergny MD, Scherman D, Demeneix B, Behr JP. A versatile vector for gene and oligonucleotide transfer into cells in culture and in vivo: polyethylenimine. *Proc. Natl. Acad. Sci. U S A.* 1995; 92:7297–7301.
18. Higashikawa F, Chang L. Kinetic analyses of stability of simple and complex retroviral vectors. *Virology.* 2001; 280:124-131.
19. Zhang B, Metharom P, Jullie H, Ellem KA, Cleghorn G, West MJ, Wei MQ. The significance of controlled conditions in lentiviral vector titration and in the use of multiplicity of infection (MOI) for predicting gene transfer events. *Genet Vaccines Ther.* 2004; 2:6.
20. Salva MZ, Himeda CL, Tai PW, Nishiuchi E, Gregorevic P, Allen JM, Finn EE, Nguyen

Optogenetics and atrial cardiomyocytes

- QG, Blankinship MJ, Meuse L, Chamberlain JS, Hauschka SD. Design of tissue-specific regulatory cassettes for high-level rAAV-mediated expression in skeletal and cardiac muscle. *Mol Ther.* 2007; 15:320-9.
21. Prasad KM, Xu Y, Yang Z, Acton ST, French BA. Robust cardiomyocyte-specific gene expression following systemic injection of AAV: in vivo gene delivery follows a Poisson distribution. *Gene Ther.* 2011; 18:43-52.

2



Chapter

LOCALIZED OPTOGENETIC TARGETING OF ROTORS IN ATRIAL CARDIOMYOCYTE MONOLAYERS

Iolanda Feola¹, MSc; Linda Volkers¹, PhD;
Rupamanjari Majumder¹, PhD; Alexander Teplenin¹,
MSc; Martin J. Schalij¹, MD, PhD; Alexander V. Panfilov^{1,2}, PhD;
Antoine A.F. de Vries¹, PhD; Daniël A. Pijnappels¹, PhD.

¹ Laboratory of Experimental Cardiology, Department of Cardiology, Heart
Lung Center Leiden; Leiden University Medical Center, the Netherlands.

² Department of Physics and Astronomy, Ghent University, Ghent, Belgium.

3

ABSTRACT

Background

Recently, a new ablation strategy for atrial fibrillation (AF) has emerged, which involves the identification of rotors (*i.e.* local drivers) followed by the localized targeting of their core region by ablation. However, this concept has been subject to debate since the mode of arrhythmia termination remains poorly understood, as dedicated models and research tools are lacking. We took a unique optogenetic approach to induce and locally target a rotor in atrial monolayers.

3

Methods and Results

Neonatal rat atrial cardiomyocyte monolayers expressing a depolarizing light-gated ion channel (Ca^{2+} -translocating channelrhodopsin [CatCh]) were subjected to patterned illumination to induce a single, stable and centralized rotor by optical S1-S2 cross-field stimulation. Next, the core region of these rotors was specifically and precisely targeted by light to induce local conduction blocks of circular or linear shapes. Conduction blocks crossing the core region, but not reaching any unexcitable boundary, did not lead to termination. Instead, electrical waves started to propagate along the circumference of block, thereby maintaining reentrant activity, although at lower frequency. If, however, core-spanning lines of block reached at least one unexcitable boundary, reentrant activity was consistently terminated by wave collision. Lines of block away from the core region resulted merely in rotor destabilization (*i.e.* drifting).

Conclusions

Localized optogenetic targeting of rotors in atrial monolayers could lead to both stabilization and destabilization of reentrant activity. For termination, however, a line of block is required reaching from the core region to at least one unexcitable boundary. These findings may improve our understanding of the mechanisms involved in rotor-guided ablation.

Keywords

Ablation, atrial fibrillation, cardiomyocytes, optogenetics, optical mapping.

INTRODUCTION

Atrial fibrillation (AF) is the most common type of sustained cardiac arrhythmia, with so-called rotors as possible driving sources.¹⁻³ These rotors form dynamical organizing centers supporting self-sustained electrical waves spiralling around excitable, yet inexcited cores.⁴ AF can be terminated by the introduction of permanent tissue lesions, *i.e.* lines of conduction block, through catheter ablation therapy, which is now widely used for the treatment of both paroxysmal and persistent AF.^{5,6} These lesions either prevent AF by blocking electrical activation at specific sites to eliminate focal triggers, or terminate AF by interrupting the pathway of reentrant waves. The most common ablation strategy for preventing AF is anatomy-guided and concerns the electrical isolation of pulmonary veins, a known source of these focal triggers.⁷ This therapy results in an overall success rate of $\geq 80\%$ in paroxysmal AF patients. However, such anatomy-guided ablation is less successful in non-paroxysmal patients.⁸ Ablation of AF in these patients is a complex issue. Over the years many strategies for ablation were proposed, which, in addition to pulmonary vein isolation, included targeting of complex fractionated atrial electrograms and ganglionated plexi.⁹ Recently, a new ablation strategy for AF has emerged with the rotor itself as prime target. This strategy involves the identification of a rotor by computational mapping, followed by local ablation at its organizing center, or core region.^{10, 11} A number of clinical studies has indicated that such rotor-guided ablation could indeed terminate ongoing AF. Although this strategy has drawn a lot of attention, many of its fundamental aspects remain yet unexplored, including its mode of termination. Thus far, the effects of such precise local blocking of electrical propagation on rotor termination have only been studied in detail in computer models.¹²⁻¹⁵ Insights from biologically active cardiac tissue are still lacking because conventional research tools do not allow precise spatiotemporally controlled induction of block. We have been able to take this first step by using light-gated depolarizing ion channels and patterned illumination to create light-controlled conduction blocks in cardiac tissue of any size and shape and at any desired location. Through this method, called optogenetics, we could (i) induce a stable rotor at a pre-defined location in neonatal rat atrial cardiomyocyte (nraCMC) monolayers and (ii) investigate its termination by inducing local conduction blocks of different configurations including or excluding the rotor core.

MATERIALS AND METHODS

Cultures preparation

All animal experiments were reviewed and approved by the Animal Experiments Committee of the Leiden University Medical Center and conformed to the Guide for the Care and Use of Laboratory Animals as stated by the US National Institutes of Health.

Monolayer and low-density cultures of neonatal rat atrial cardiomyocytes (nraCMCs) were established as previously described.¹⁶ Briefly, 5% isoflurane was used to anesthetize 2-days-old Wistar rats. After rapid excision of the heart, the atria were carefully separated from the ventricles, then cut into small pieces and dissociated in a solution containing 450 U/ml collagenase type I (Worthington, Lakewood, NJ) and 18,75 Kunitz/ml DNase I (Sigma-Aldrich,

St. Louis, MO). The resulting cell suspension was transferred to Primaria-coated culture dishes (Becton Dickinson, Breda, the Netherlands) and incubated for 120 minutes in a humidified incubator at 37°C and 5% CO₂ to allow selective adhesion of non-nraCMCs. The non-attached cells (mainly nraCMCs) were filtered through a cell strainer (70 µm pore size; Corning Life Sciences, Amsterdam, the Netherlands) and seeded on round glass coverslips (15 mm diameter; Thermo Fisher Scientific Gerhard Menzel, Braunschweig, Germany) coated with fibronectin (100 µg/ml; Sigma-Aldrich). The cells were seeded at densities of 0.3-8×10⁵ cells/well of a 24-well culture plate (Corning Life Sciences) depending on the assay. To minimize proliferation of the remaining non-nraCMCs, the cultures were treated with Mitomycin-C (10 µg/ml; Sigma-Aldrich) for 2 hours.¹⁷ The cultures were incubated in an atmosphere of humidified 95% air- 5% CO₂ at 37°C. Culture medium was daily refreshed, and consisted of a 1:1 mixture of low-glucose Dulbecco's modified Eagle's medium (Thermo Fisher Scientific, Bleiswijk, the Netherlands) and Ham's F10 medium (MP Biomedicals, Santa Ana, CA) supplemented with 5% heat-inactivated horse serum (Thermo Fisher Scientific), 1× penicillin-streptomycin (Thermo Fisher Scientific), 2% bovine serum albumin (BSA) (Sigma-Aldrich) and sodium ascorbate (Sigma-Aldrich) to a final concentration of 0.4 mM.

Lentiviral (LV) vector production and transduction

LV particles encoding the L132C mutant of *Chlamydomonas reinhardtii* channelrhodopsin-2 (also known as Ca²⁺-translocating channelrhodopsin [CatCh]), were produced in 293T cells from LV shuttle plasmid pLV.GgTnnt2.CatCh~eYFP.WHVPRE, as detailed elsewhere.¹⁸ pLV.GgTnnt2.CatCh~eYFP.WHVPRE is a derivative of LV shuttle plasmid pLV.MHCK7. CatCh~eYFP.WHVPRE containing the chicken Tnnt2 promoter instead of the MHCK7 promoter in order to restrict transgene expression to cardiomyocytes. The LV particles were purified and concentrated by ultracentrifugation, suspended in phosphate-buffered saline (PBS) containing 1% BSA and stored at -80°C until use. At day 4 of culture, nraCMC monolayers were incubated for 20-24 h with LV particles at a dose resulting in homogeneous transduction of nearly 100% of the cells. Next, the cultures were washed once with PBS, given fresh culture medium and kept under culture conditions for 3-4 additional days. The transduction efficiency in the monolayer cultures was determined by visualization of the enhanced yellow fluorescent protein (eYFP) using a Nikon Eclipse 80i fluorescence microscope (Nikon Instruments Europe, Amstelveen, the Netherlands) after fixation of the cells with PBS/4% methanol-free formaldehyde (Thermo Fisher Scientific).

Immunocytology

Low-density nraCMC cultures (0.3×10⁵ cells/15-mm glass coverslip) were fixed in PBS/4% methanol-free formaldehyde (Thermo Fisher Scientific), permeabilized with PBS/0.1% Triton X-100 and stained with a primary antibody directed against sarcomeric α-actinin (mouse IgG1, clone EA-53; Sigma-Aldrich). Incubation with the primary antibody (1:200 dilution in PBS+0.1% donkey serum) was performed overnight at 4°C, while the corresponding Alexa

Fluor 568-conjugated secondary antibody (Life Technologies; 1:400 dilution) was allowed to bind for 3 hours at room temperature (RT). Nuclear counterstaining was performed at RT for 10 minutes with 10 $\mu\text{g}/\text{ml}$ Hoechst 33342 (Life Technologies) in PBS. After each processing step, cells were washed thrice with PBS. Coverslips were mounted in Vectashield mounting medium (Vector Laboratories, Burlingame, CA). Images were acquired with the Nikon Eclipse 80i fluorescence microscope. Immunostaining was performed on 3 independent cultures.

Optical mapping and optogenetic targeting

Optical voltage mapping was used to investigate the effects of local optogenetic targeting of rotors (*i.e.* induction of local conduction block) in CatCh-expressing nraCMC monolayers on day 7 of culture. Electrical activation was visualized using the voltage-sensitive dye di-4-ANBDQBS (52.5 μM final concentration; ITK diagnostics, Uithoorn, the Netherlands), which was excited by side illumination using a 150 W halogen light source (HL-151; SciMedia, Costa Mesa, CA) linked to a Semrock excitation filter (FF01-650/54-27, Semrock, Rochester, NY), while the emitted light was selected with an emission filter (pass >715 nm, FF01-715/LP-25, Semrock). Optical data were captured using a MiCAM ULTIMA-L imaging system (SciMedia) and analyzed with BrainVision Analyzer 1101 software (Brainvision, Tokyo, Japan). CatCh was locally activated by a patterned illumination device (Polygon400; Mightex Systems, Toronto, ON) that was connected to a 470-nm, high-power collimator light-emitting diode (LED) source (50 W, type-H, also from Mightex Systems), driven by a STG2004 stimulus generator (Multichannel Systems, Reutlingen, Germany). Accompanying PolyLite software (Mightex) was used to control the location and shape of the area of illumination, CatCh activation and conduction block. Light irradiance was measured using a PM100D optical power meter (Thorlabs, Munich, Germany). Before local optogenetic targeting, a single stable rotor was induced at the center of the monolayer by a light-based S1-S2 cross-field stimulation and monolayers were randomly assigned to either focal circular or linear configuration. Cycle length (CL) was determined as the time between 2 subsequent beats during sustained reentry. Action potential duration at 80% repolarization (APD_{80}) and conduction velocity (CV) during sustained reentry were spatial averages of three measurements per culture. Moreover, to minimize noise artifacts, a spatial averaging filter with 3×3 convolution kernel was used. Diastolic interval (DI) was defined as $\text{CL} - \text{APD}_{80}$, wavelength (λ) was expressed as $\text{CV} \times \text{APD}_{80}$. Cultures showing stable rotors for >6 s were exposed to different patterns of illumination for 250 and 500 ms at $0.3 \text{ mW}/\text{mm}^2$ to create local conduction blocks at the site of interest. Since during the light-on period a shift in the baseline signal was observed, a drift filter was applied to allow optical voltage trace data interpretation while the derivative filter was used to visualize electrical propagation.

Patch-clamp recordings

For patch experiments, isolated nraCMCs were bathed in modified Tyrode's solution containing 126 mM NaCl, 5.4 mM KCl, 1.8 mM CaCl_2 , 1 mM MgCl_2 , 11 mM glucose, 10 mM HEPES (pH adjusted to 7.4 with NaOH). Patch electrodes were pulled from borosilicate glass capillaries

and fire polished. Pipettes were fabricated with a P30 micropipet puller (Sutter Instruments, Novato, CA) and had a resistance of 2.4-3.0 M Ω when filled with the following solution: 80 mM L-aspartic acid potassium salt, 40 mM KCl, 8 mM NaCl 5.5 mM glucose, 5 mM HEPES, 1 mM MgCl₂, 4 mM Mg-ATP, 0.1 mM Na₃-GTP (pH adjusted to 7.2 with KOH). CatCh-expressing nraCMCs were identified via epifluorescence using an Axiovert 35 inverted phase-contrast and fluorescence microscope (Carl Zeiss, Sliedrecht, the Netherlands). For current clamp experiments, only eYFP-positive, contracting nraCMCs were measured. Optical stimulation of these cells was performed with light from an incorporated LED module (blue [470 nm] collimated LED for Zeiss Axioskop, 1000 mA, Thorlabs). Recordings were performed at room temperature (20-22°C) using the whole-cell voltage clamp configuration with an Axopatch 700B amplifier controlled by pCLAMP 10.3 (Axon Instruments, Union City, CA). Currents were acquired with a low-pass filter of 10 kHz and digitized at 20 kHz using a Digidata 1440A A-D converter (Axon instruments). Voltages were corrected for liquid junction potentials. Steady-state depolarized membrane potentials were determined at the end of the light pulses.

Statistical analysis

Optical voltage data were expressed as mean \pm SD. Comparison between 2 groups was performed with Student's t-test. Differences were considered statistically significant at $p < 0.05$. Statistical analyses were performed with GraphPad Prism 7.01 (GraphPad Software, La Jolla, CA) software.

Acquisition and analysis of patch clamp data were performed using Clampfit 10.3 (Axon instruments), Excel 2010 (Microsoft, Seattle, WA) and GraphPad Prism 7.01 software. Data are presented as mean \pm SEM.

RESULTS

CatCh expression and activation in nraCMCs

Immunocytological analysis of low-density nraCMC cultures transduced with LV.GgTnt2. CatCh-eYFP~WHVPRE (see vector map shown in Supplementary Figure 1A) showed that CatCh expression occurred only in nraCMCs, *i.e.* α -actinin⁺ cells (Figure 1A). To investigate the electrophysiological consequences of CatCh activation, whole-cell voltage- and current-clamp experiments were performed on single nraCMCs. Voltage-clamp recordings demonstrated that upon illumination with 470-nm light, at an intensity of 6 mW/mm² for 500 or 250 ms, a robust CatCh inward photocurrent was generated at resting membrane potentials of \sim -70 mV ($n=7$) (Figure 1B). More importantly, current-clamp experiments revealed the ability to induce prolonged depolarization by establishing a stable voltage plateau of -39 ± 4.9 and -41 ± 4.5 mV upon illumination for 250 and 500 ms, respectively ($n=6$; Figure 1C). The duration of the depolarized state was determined by the duration of the light pulses (Figure 1C). Taken together, these findings indicate that, given the significant upward shift in membrane potential upon illumination, electrical activation of nraCMCs could be blocked (*i.e.* the cells could be rendered temporary unexcitable) by prolonged activation of CatCh. Next, CatCh-expressing nraCMCs were used to create confluent monolayers (see Supplementary Figure 1B) to induce and target rotors.

Induction of a single stable rotor in nraCMC monolayers

With the aim to investigate the anti-arrhythmic effects of localized blocking of electrical activation near the rotor core region, a single and stable rotor was induced in nraCMC monolayers by a light-based S1-S2 cross-field stimulation (see Movie 1). Monolayers were optogenetically paced via patterned illumination of a 3-mm square area near the culture boundary using a brief light pulse (10 ms; 470 nm). The emerging S1 wave spread from the site of stimulation with a convex repolarization front.

3

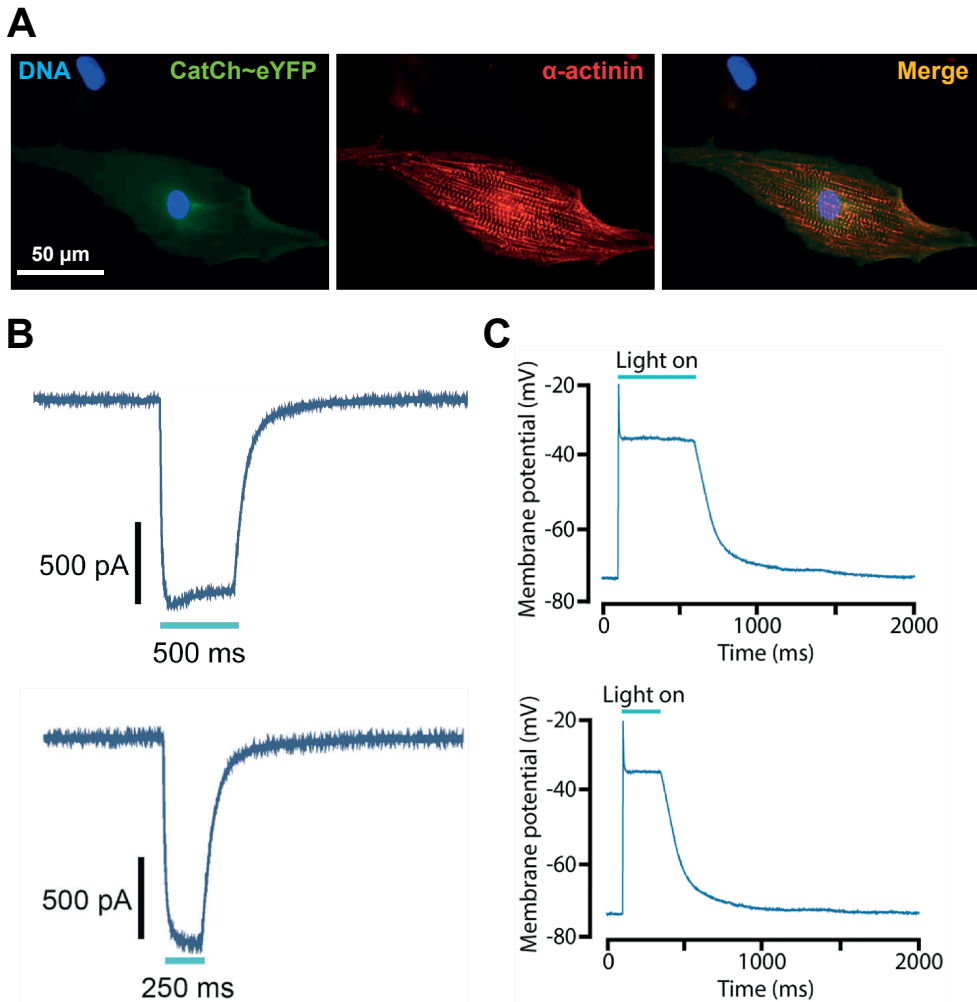


Figure 1. CatCh expression and activation in nraCMCs. **A**, Immunocytochemical staining of low-density CatCh-expressing nraCMC cultures for α -actinin⁺ (red), showing CatCh localization at the sarcolemma (green). **B**, Typical inward photocurrent evoked at a resting membrane potential of -70 mV by exposure of single CatCh-expressing nraCMCs to a 500- (top) or 250-ms (bottom) 470-nm light pulse ($n=7$). **C**, Representative membrane potential recordings of CatCh-expressing nraCMCs upon 470-nm light stimulation for 500- (top) or 250-ms (bottom), ($n=6$).

Circa 50 ± 10 ms later, a second light stimulus, S2 (20 ms; 470 nm), was applied to one half of the monolayer, perpendicular to the S1 repolarization front, such that, approximately one quarter of the culture remained excitable. This allowed the S2 stimulus to initiate a wave with a break at the interface between the excitable (non-illuminated, non-refractory) region and the temporary unexcitable (illuminated and therefore refractory) part of the monolayer (Figure 2A-B). With this protocol, a single rotor was induced in 100% of the monolayers (23 out of 23). Importantly, all these rotors were i) stable in time and space (see Figure 2B and C), and ii) centrally positioned in the monolayer (see Figure 2A and C). Thus, a robust *in vitro* model was created for studying the effects of local conduction blocks on atrial rotors in a unique and systematic manner.

Effects of core region targeting with circular conduction blocks

First, the effects of a circular conduction block at the site of the rotor core region were investigated. To this end, this region was targeted (*i.e.* focally illuminated; 470 nm, 0.3 mW/mm², 500 ms) with circular configurations of increasing diameter (3-, 6- or 12-mm, see Movies 2-4).

Upon local illumination, and therefore local activation of CatCh, two important simultaneously occurring phenomena could be observed: (i) emergence of a new electrical wave and (ii) formation of a functional conduction block (Figure 3A). During propagation, this new wave encountered both the activation and repolarization fronts of the existing rotor.

While its collision with the activation front of the existing rotor led to annihilation, interaction between the emergent wave and the repolarization front of this rotor led to the development of a new reentrant wave. This wave anchored to the illuminated area where a functional conduction

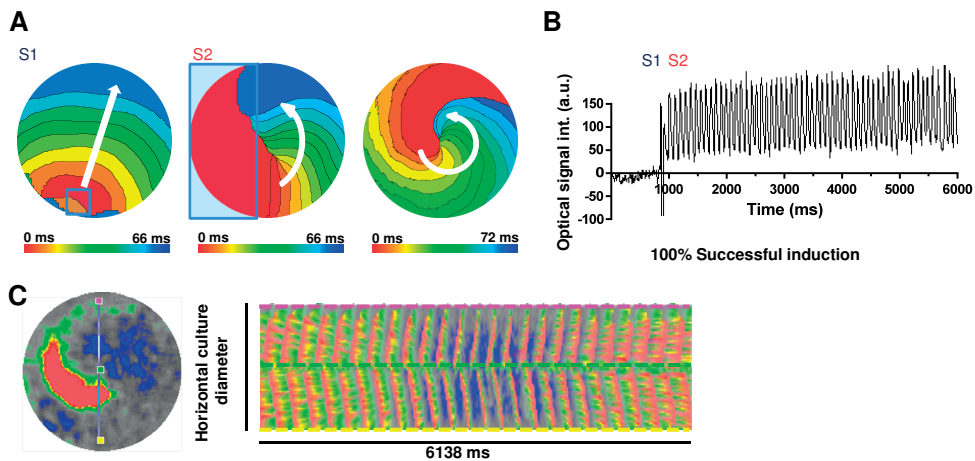


Figure 2. Optogenetic induction of a single, centralized and stable rotor. A and B, Representative activation maps (A) and optical trace (B) of a CatCh-expressing monolayer subjected to S1-S2 cross-field light stimulation to induce a single stable rotor at the center of the monolayer. C, Typical line scan analysis across a CatCh-expressing monolayer indicating that the rotor is stable in both space and time.

Optical ablation of rotors

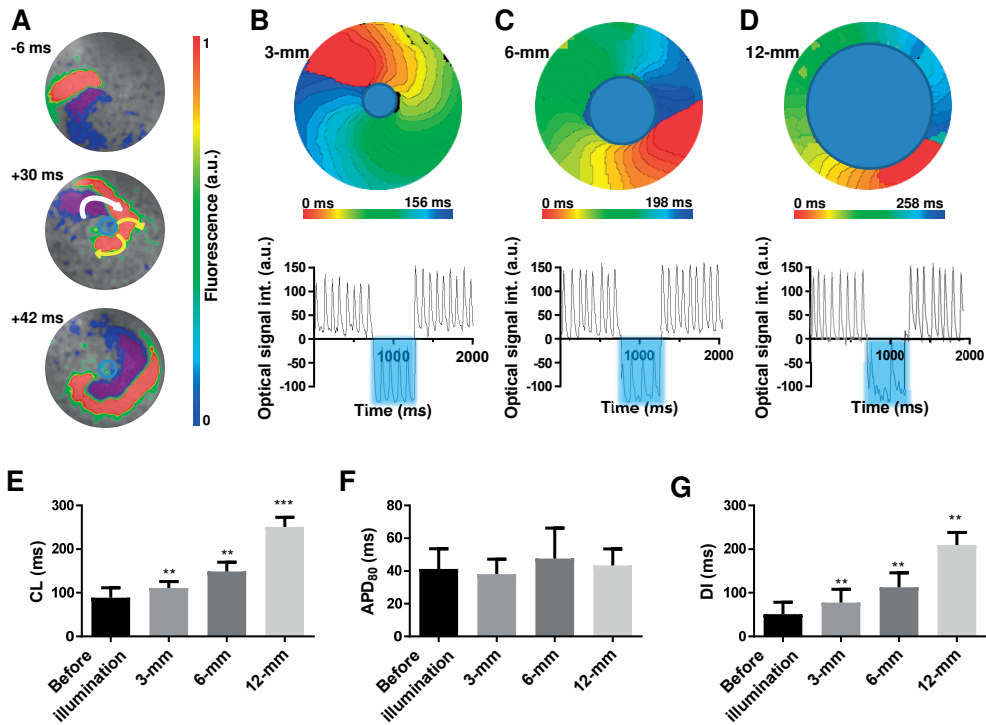


Figure 3. Effects of core region targeting with circular conduction blocks. A, Snapshots of optical signal before (upper panel) and during exposure (middle and bottom panel) to 470-nm light, showing the two typical phenomena occurring upon illumination: appearance of a new wave (indicated by yellow arrows) that interact with the existing reentrant wave (white arrows) and creation of a functional conduction block at the site of optical stimulation. B, C and D, Representative activation maps during 500-ms exposure to 470-nm light with centrally located circular shapes (blue shading) of 3- (B, top), 6- (C, top) or 12-mm in diameter (D, top). During illumination, the emerging wave anchors to the light-induced functional conduction block, thereby converting functional into anatomical reentrant activity. The corresponding optical signal traces recorded before, during and after light exposure are shown below the activation maps. E, F and G, Effect of circular conduction blocks (of 3-, 6- and 12-mm in diameter) at the rotor core region on (E) cycle length (CL), (F) action potential duration at 80% repolarization (APD₈₀), and (G) diastolic interval (DI). **P<0.01; ***P<0.001.

block was induced (Figure 3B, C, and D), thereby maintaining arrhythmic activity. Thus, instead of terminating the rotor, optogenetic targeting of the rotor core region converted functional into so-called anatomical reentry. Electrophysiological characterization of the electrical activity before and during illumination revealed a significant and diameter-dependent increase in CL ($CL_{bi}=82\pm 20$; $CL_{3-mm}=111.5\pm 14.5$; $CL_{6-mm}=149.5\pm 21$; $CL_{12-mm}=251\pm 22$; $P(CL_{bi} \text{ vs } CL_{3-6-12-mm}) < 0.01$; Figure 3E). APD₈₀ did not show any significant difference (Figure 3F). Finally, there was a significant and diameter-dependent prolongation of the DI ($DI_{bi}=49\pm 24$; $DI_{3-mm}=77\pm 30$; $DI_{6-mm}=113\pm 33$; $DI_{12-mm}=209\pm 28$; $P(DI_{bi} \text{ vs } DI_{3-6-12-mm}) < 0.01$; Figure 3G) (n=8).

Effects of core region targeting with linear conduction blocks

Next, the effects of a linear conduction block at the rotor core region were investigated. To this purpose, a focal and central line (1 × 8 mm) was illuminated crossing the core region but not reaching one of the unexcitable boundaries of the culture (Figure 4A). Again the emergent new waves interacted with the existing rotor and replaced it by a new electrical wave that anchored to the light-induced functional conduction block, thereby maintaining arrhythmic activity (Figure 4B-C and Movie 5). However, when the length of this illuminated line was increased to 16 mm to connect the core region with both unexcitable boundaries of the culture (Figure 5A), all rotors were terminated (15 out of 15; Figure 5B and Movie 6).

Mechanistically, the local block of electrical activation forced both the existing reentrant wave and the light-induced emergent wave to drift along the line of block and towards the unexcitable boundaries of the culture, where they collided and vanished (Figure 5C). On the contrary, no termination occurred when monolayer-spanning lines of block did not include the core region (Figure 6B and Movie 7).

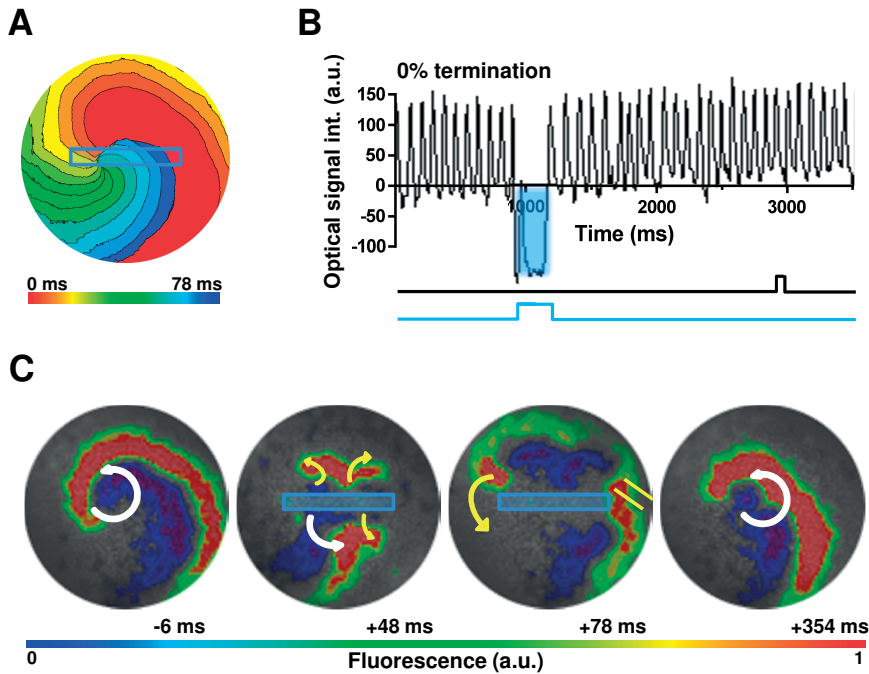


Figure 4. Effects of core region targeting with a linear conduction block not reaching any unexcitable boundaries. **A**, Activation map showing a single stable rotor and the area (blue shading) that will be exposed to light to induce a functional conduction block. **B**, Representative optical trace recorded before, during and after induction of conduction block by 250-ms exposure to 470-nm light. **C**, Snapshots of optical signal before and during light exposure showing unsuccessful rotor termination. The new waves (yellow arrows), emerge from the illuminated region and interact with the existing reentrant wave (white arrows), resulting in anchoring of a new wave to the light-induced conduction block, thereby maintaining arrhythmic activity.

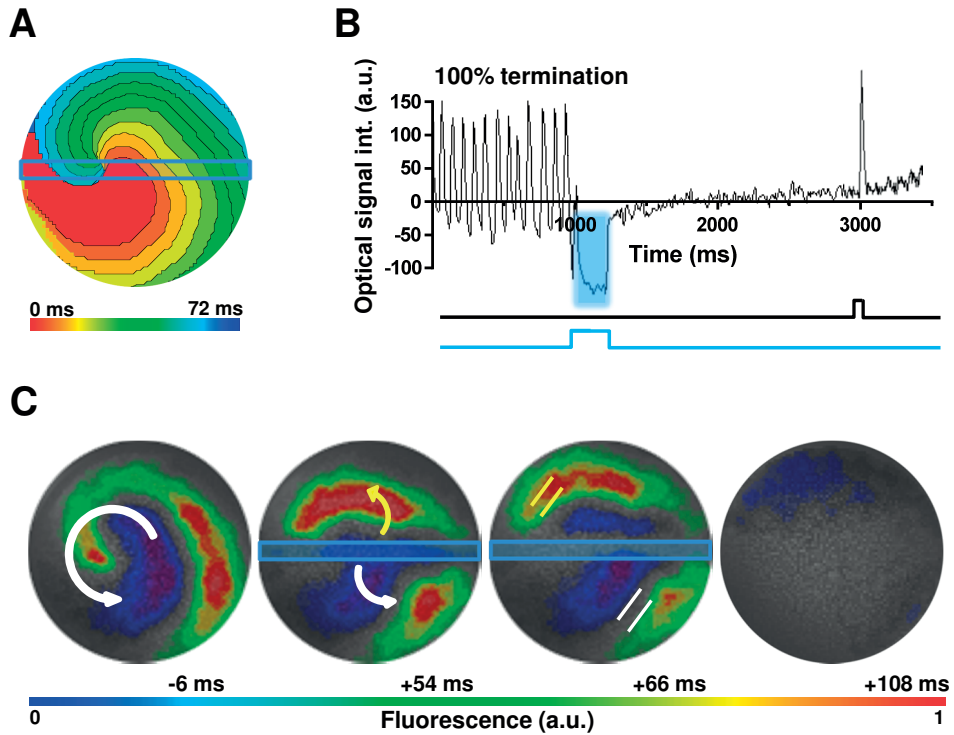


Figure 5. Effects of core region targeting with a linear conduction block reaching two opposite unexcitable boundaries. A, Activation map showing the position of the rotor core region and the area (blue shading) where light will be applied. B, Representative optical trace obtained before, during and after 250-ms exposure to 470-nm light. C, Snapshots of optical signal before and during light exposure showing successful rotor termination. Localized blocking of electric activity forces both the existing reentrant wave (in white arrows) and the light-induced emergent wave (yellow arrows) to drift toward the unexcitable boundaries in the culture, with which they collide.

In such cases, the emergent wave interfered with the existing rotor, leading to destabilization of its core. The rotor itself, however, survived and was attracted towards the site of optical stimulation (Figure 6C). Based on the success of the monolayer-spanning and rotor core-crossing linear configurations, we repeated the experiment with an illuminated line of 1×8 mm targeting the rotor core region and only one culture boundary (Figure 7A). Also with this configuration, rotor termination could be observed in 100% of the cases (Figure 7B and Movie8).

Both the original reentrant wave and the new wave followed the line of block and thereby collided with the unexcitable boundary of the culture and disappeared (Figure 7C).

In all cases, one electrical stimulus was applied 1.75 s after illumination (indicated by a black line) to confirm, in case of termination, the ability of the monolayers to be reactivated (Figure 5B and 7B).

Taken together these findings show that local targeting of a rotor without reaching to an unexcitable boundary, *i.e.* the creation of a circular or linear conduction block at the rotor

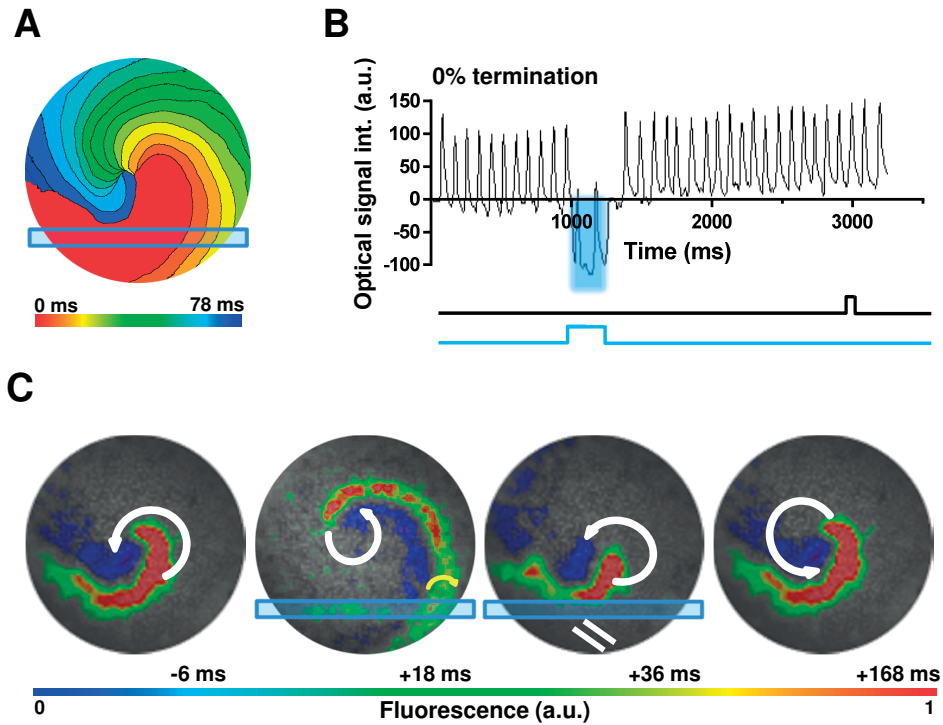


Figure 6. Effects of localized targeting away from the rotor core region with a linear conduction block reaching two opposite unexcitable boundaries. **A**, Activation map showing the location of the rotor core region with respect to the area (blue shading) that will be exposed to light. **B**, Representative optical traces registered before, during and after 250-ms exposure to 470-nm light. **C**, Snapshots of optical signal before and during light exposure showing unsuccessful rotor termination. The emergent wave (yellow arrows) interferes with the existing reentrant activity (in white arrows), leading to core destabilization and attraction towards the site of illumination, without causing arrhythmia termination.

core region in atrial CMC monolayers, does not lead to rotor termination. Instead, as long as the conduction block is present, the arrhythmic activity is maintained by so-called anatomical reentry albeit at a lower activation frequency. Here it is shown that for rotor termination by localized targeting, a line of conduction block should be created that is spanning from the rotor core region to at least one unexcitable boundary.

DISCUSSION

In this study, we investigated rotor termination in monolayers of nraCMCs by optogenetically blocking electrical activation at or near the rotor core region. Our findings reveal that an essential requirement for termination is the creation of a line of conduction block that is spanning from the rotor core region to at least one unexcitable boundary. Such localized targeting of the rotor forces the reentrant wave to propagate along the line of block to eventually collide into the unexcitable boundary, after which normal activation can regain.

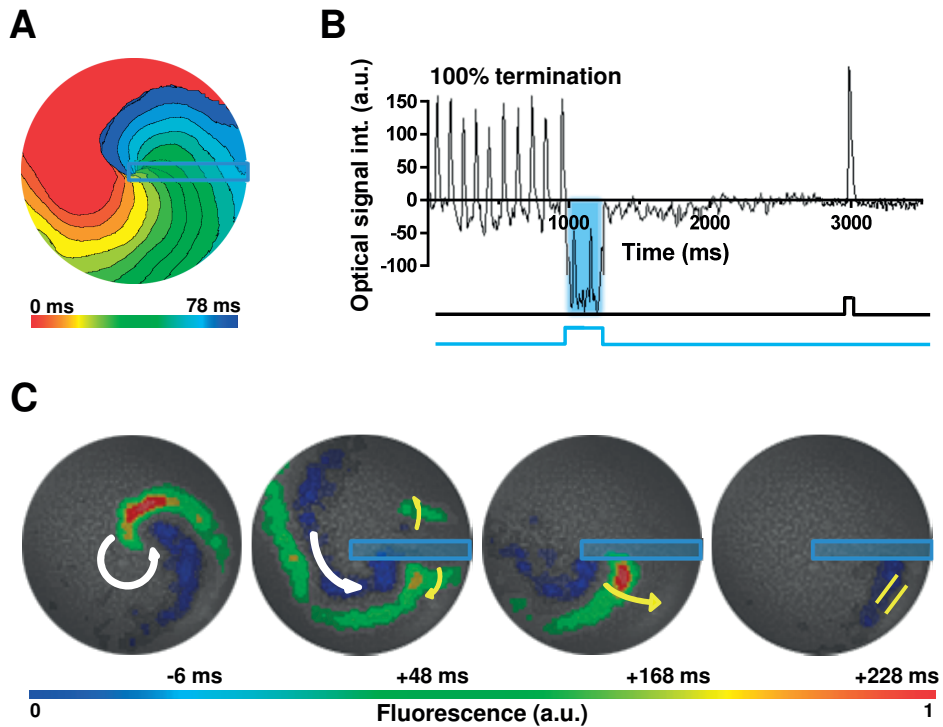


Figure 7. Effects of core region targeting with a linear conduction block reaching only one unexcitable boundary. A, Activation map showing the location of the core region of a single reentrant circuit and the location of the linear shape (blue shading) exposed to light. B, Optical traces recorded before, during and after 250-ms exposure to 470-nm light. C, Snapshots of optical signal before and during light exposure showing rotor termination. Both the original rotor (indicated by white arrows) and the new wave (in yellow arrows) follow the contour of the line where the conduction block is created, anchor and collide with the unexcitable boundary of the culture.

Optogenetic control of cardiac electrical function

In the past few years, optogenetics has emerged as a unique technology to modulate cardiac electrical function.^{16, 19-25} This technology relies on forced expression of light-sensitive proteins whose activity can be precisely controlled in time and space by illumination. Optogenetic modulation of heart function was first proven in zebrafish by the stimulation and inhibition of electrical activation via brief and prolonged illumination, respectively.¹⁹ Afterward, similar effects were also shown in rodent cardiomyocytes, both in monolayers and in intact hearts.²² Here, brief light exposure caused membrane depolarization at the site of illumination, creating a supra-threshold stimulus for excitation, leading to action potential initiation and subsequent propagation out of the illuminated area. In the present study, we made use of the unique features of optical stimulation and inhibition of electrical activation to induce a single stable rotor. This was achieved by combining patterned illumination with a light-based pacing strategy, adapted from the well-established *in silico* S1-S2 cross-field stimulation protocol. This not only allowed

us to predetermine the location of the rotor core region, but also enabled us to target the rotor core region at a spatiotemporal resolution that could not be reached prior to the introduction of optogenetics. The possibility to induce a single stable rotor *in vitro* via S1-S2 cross-field stimulation has been previously described by Lim *et al*, who instead relied on the use of custom-made electrodes.²⁶ Our approach has, however, several technical advantages compared to the electrode-based method since it (i) allows better monitoring via optical mapping, owing to the absence of visually obstructive electrodes, and (ii) is more flexible in inducing rotors of predetermined chirality, at the desired location within the culture.

Recently, in addition to optical pacing, the ability to optogenetically terminate ventricular tachyarrhythmias in whole rat and mouse hearts expressing light-gated ion channels has been demonstrated.²³⁻²⁵ Of those studies, Crocini *et al* used transgenic mice expressing *Chlamydomonas reinhardtii* channelrhodopsin-2 mutant H143R in the heart to investigate optogenetic induction of local conduction block for termination of ventricular tachycardia. Induction of 3 opposing lines of local block by patterned illumination resulted in arrhythmia termination with less energy than was required for arrhythmia termination by global illumination. In contrast to their more complex whole heart model, our 2D model and experimental setup allowed precise and predetermined optogenetic targeting of the actual arrhythmia driver, like induction of conduction block only in the core region of a rotor. Their study nevertheless confirms that local conduction blocks created by local activation of light-gated depolarizing ion channels allow termination of ongoing arrhythmias in the rodent heart.²⁵ Furthermore, optogenetic manipulation of anatomical reentry in ventricular tissue slices has been investigated in a previous study from our research group.²⁷ In this study, CatCh expression and its local activation, through patterned illumination, induced a local and reversible conduction block in the reentrant pathway, which allowed termination of reentrant activity.¹⁶ In another study, members of our research team have shown optogenetic termination of multiple reentrant circuits in monolayers of nraCMC cardiomyocytes by global activation of CatCh, which caused spiral wave drift and collisions. In the present study, we activated CatCh only locally in monolayers of nraCMC in order to investigate rotor termination by precise, spatially restricted optogenetic blocking of electrical activation at or near the rotor core region.

Optogenetic targeting of the rotor core region

One of our main motivations to study localized targeting of atrial rotors via the afore-mentioned approach was to improve our mechanistic understanding of so-called rotor-guided ablation. This ablation strategy involves the identification of the rotor core region by computational mapping, followed by targeted ablation of this particular site. Several recent clinical studies have indicated that such rotor-guided ablation could indeed favor termination of ongoing AF.^{10, 11, 13} However, the way by which the rotors are terminated remains poorly understood. This is partly due to a lack of dedicated research models and tools, especially regarding the precision by which a conduction block can be created in a certain shape at a particular location. In the present study, patterned illumination was used to activate CatCh with the aim to first induce a single

stable rotor, and then block electrical activation regionally in order to mimic the conduction block resulting from an ablation procedure. We used optogenetic induction of conduction block to tackle this issue of precision, and by doing so showed that localized targeting of the core region without reaching an unexcitable boundary does not terminate the arrhythmia. Computer simulations both support and contradict these findings. Likely due to the homogeneity of our monolayers, factors responsible for rotor drift and meandering were mostly absent resulting in highly stable rotors. These results are in line with *in silico* studies. In those studies, Spector *et al* and Carrick *et al* pointed out that the concept of using ablation to transect a spatially fixed reentrant pathway is understandable, but that creation of focal lesions targeting the rotor core region seems less obvious.^{12, 14} In contrast, a recent *in silico* study conducted by Rappel *et al* showed that focal ablation near the core region could indeed terminate a rotor if the cardiac tissue was affected by structural and functional heterogeneities.¹³ It may, therefore, be relevant to include such heterogeneities, like gradients in excitability and non-homogenous distribution of cardiac fibroblasts, in future optogenetic *in vitro* experiments to investigate their role in rotor termination by focal ablation. However, these heterogeneities will most likely also affect the stability of the rotor, both in time and space, which will no longer allow a precisely controlled and systematic study into localized targeting of rotors. In this context, our finding that linear blocks extending from the core region to at least one unexcitable boundary of homogeneous monolayers resulted in termination of all rotors is of particular interest. With the aim to optimize AF ablation efficacy, while limiting the tissue damage resulting from ablation, these results may help to further refine rotor-based ablation strategies.

In our study, the optogenetic induction of a conduction block to mimic the electrophysiological consequences of an ablation lesion, also resulted in the emergence of a new wave of excitation that played a crucial role in rotor termination by interfering with the existing reentrant wave and introducing new electrical activity into the monolayers. The clinical relevance of these ablation-induced waves remains yet to be clarified. Nevertheless, it is well known that ablation comes with cell death and could involve local thermic responses, which may cause transient and local membrane depolarization, causing ectopic activity.²⁸ Another interesting phenomenon that we observed in our experiments was the tendency of the light-induced functional conduction block to destabilize and attract nearby rotors. In these cases, the linear conduction block was established away from the core region of the rotor, which gradually drifted towards the area of conduction block although rotor termination did not occur. These findings are in line with the results of *in silico* studies by Defauw *et al*, who showed, by using the Ten Tusscher-Noble-Noble-Panfilov model for human ventricular tissue, that such interactions between the rotor core and the region of conduction block has important consequences for the dynamical behavior of the rotors and may result in their stabilization through conversion into anatomical reentry.²⁹ Regarding our results, more investigation is needed to determine whether and how localized targeting further away from the rotor core region may still lead to termination of arrhythmic activity.

Study limitations

The novel model presented in this study is a 2D model of atrial tachycardia based on a single stable rotor. This *in vitro* model obviously does not reproduce the structural and functional complexity of the intact heart and accompanying atrial arrhythmias, and therefore the results should be interpreted as such. Our model nonetheless did allow us to investigate the electrophysiological consequences of localized rotor targeting through optogenetic induction of conduction blocks, which now can be a stepping stone to future experiments on rotor targeting in more complex and realistic models of atrial tissue. Moreover, the temporary nature of the functional conduction block employed in this study does not allow investigating its role in preventing the formation of new rotors.

3

Conclusions

This study shows that localized targeting of rotors in atrial monolayers, by means of optogenetic induction of a conduction block at the site of the rotor core region, only leads to termination if the line of block reaches from the core region to at least one unexcitable boundary. Localized targeting with no involvement of such boundary merely forces the electrical waves to anchor to the conduction block, thereby sustaining arrhythmic activity based on anatomical reentry. These findings may therefore lead to a better understanding of the mechanisms involved in rotor destabilization and termination after localized ablation, and thus help to further improve AF ablation strategies.

ACKNOWLEDGMENTS

We thank Cindy Bart, Annemarie Kip and Serge A.I.P. Trines (Department of Cardiology, LUMC) for assistance with the animal experiments, LV production and constructive discussion, respectively.

FUNDING SOURCES

This work was supported by the Netherlands Organisation for Scientific Research (NWO, Vidi grant 91714336) and the European Research Council (ERC, Starting grant 716509, both to D.A.P.). Additional support was provided by Ammodo (to D.A.P. and A.A.F.d.V.).

DISCLOSURES

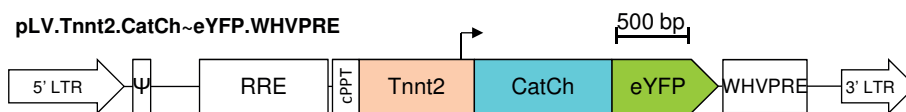
None.

REFERENCES

1. Chugh SS, Havmoeller R, Narayanan K, Singh D, Rienstra M, Benjamin EJ, Gillum RF, Kim YH, McAnulty JH, Jr., Zheng ZJ, Forouzanfar MH, Naghavi M, Mensah GA, Ezzati M, Murray CJ. Worldwide epidemiology of atrial fibrillation: a Global Burden of Disease 2010 Study. *Circulation*. 2014; 129:837-47.
2. Go AS, Hylek EM, Phillips KA, Chang Y, Henault LE, Selby JV, Singer DE. Prevalence of diagnosed atrial fibrillation in adults: national implications for rhythm management and stroke prevention: the AnTicoagulation and Risk Factors in Atrial Fibrillation (ATRIA) Study. *JAMA*. 2001; 285:2370-5.
3. Lloyd-Jones DM, Wang TJ, Leip EP, Larson MG, Levy D, Vasan RS, D'Agostino RB, Massaro JM, Beiser A, Wolf PA, Benjamin EJ. Lifetime risk for development of atrial fibrillation: the Framingham Heart Study. *Circulation*. 2004; 110:1042-6.
4. Pandit SV, Jalife J. Rotors and the dynamics of cardiac fibrillation. *Circ Res*. 2013; 112:849-62.
5. Mont L, Bisbal F, Hernandez-Madrid A, Perez-Castellano N, Vinolas X, Arenal A, Arribas F, Fernandez-Lozano I, Bodegas A, Cobos A, Matia R, Perez-Villacastin J, Guerra JM, Avila P, Lopez-Gil M, Castro V, Arana JI, Brugada J. Catheter ablation vs. antiarrhythmic drug treatment of persistent atrial fibrillation: a multicentre, randomized, controlled trial (SARA study). *Eur Heart J*. 2014; 35:501-7.
6. Pappone C, Augello G, Sala S, Gugliotta F, Vicedomini G, Gulletta S, Paglino G, Mazzone P, Sora N, Greiss I, Santagostino A, LiVolsi L, Pappone N, Radinovic A, Manguso F, Santinelli V. A randomized trial of circumferential pulmonary vein ablation versus antiarrhythmic drug therapy in paroxysmal atrial fibrillation: the APAF Study. *J Am Coll Cardiol*. 2006; 48:2340-7.
7. Pappone C, Oreto G, Rosanio S, Vicedomini G, Tocchi M, Gugliotta F, Salvati A, Dicandia C, Calabro MP, Mazzone P, Ficarra E, Di GC, Gulletta S, Nardi S, Santinelli V, Benussi S, Alfieri O. Atrial electroanatomic remodeling after circumferential radiofrequency pulmonary vein ablation: efficacy of an anatomic approach in a large cohort of patients with atrial fibrillation. *Circulation*. 2001; 104:2539-44.
8. Oral H, Pappone C, Chugh A, Good E, Bogun F, Pelosi F, Jr., Bates ER, Lehmann MH, Vicedomini G, Augello G, Agricola E, Sala S, Santinelli V, Morady F. Circumferential pulmonary-vein ablation for chronic atrial fibrillation. *N Engl J Med*. 2006; 354:934-41.
9. Kirchhof P, Calkins H. Catheter ablation in patients with persistent atrial fibrillation. *Eur Heart J*. 2017; 38:20-6.
10. Narayan SM, Krummen DE. Targeting Stable Rotors to Treat Atrial Fibrillation. *Arrhythm Electrophysiol Rev*. 2012; 1:34-8.
11. Narayan SM, Krummen DE, Shivkumar K, Clopton P, Rappel WJ, Miller JM. Treatment of atrial fibrillation by the ablation of localized sources: CONFIRM (Conventional Ablation for Atrial Fibrillation With or Without Focal Impulse and Rotor Modulation) trial. *J Am Coll Cardiol*. 2012; 60:628-36.
12. Carrick RT, Benson BE, Bates JH, Spector PS. Prospective, Tissue-Specific Optimization of Ablation for Multiwavelet Reentry: Predicting the Required Amount, Location, and Configuration of Lesions. *Circ Arrhythm Electrophysiol*. 2016;9.
13. Rappel WJ, Zaman JA, Narayan SM. Mechanisms for the Termination of Atrial Fibrillation by Localized Ablation: Computational and Clinical Studies. *Circ Arrhythm Electrophysiol*. 2015; 8:1325-33.
14. Spector PS, Correa de Sa DD, Tischler ES, Thompson NC, Habel N, Stinnett-Donnelly J, Benson BE, Bielau P, Bates JH. Ablation of multi-wavelet re-entry: general principles and in silico analyses. *Europace*. 2012; Suppl 5:v106-v111.
15. Ugarte JP, Tobon C, Orozco-Duque A, Becerra MA, Bustamante J. Effect of the electrograms density in detecting and ablating the tip of

- the rotor during chronic atrial fibrillation: an in silico study. *Europace*. 2015; 17 Suppl 2:ii97-104.
16. Bingen BO, Engels MC, Schalij MJ, Jangsongthong W, Neshati Z, Feola I, Ypey DL, Askar SF, Panfilov AV, Pijnappels DA, de Vries AA. Light-induced termination of spiral wave arrhythmias by optogenetic engineering of atrial cardiomyocytes. *Cardiovasc Res*. 2014; 104:194-205.
 17. Askar SF, Ramkisoensing AA, Schalij MJ, Bingen BO, Swildens J, van der Laarse A, Atsma DE, de Vries AA, Ypey DL, Pijnappels DA. Antiproliferative treatment of myofibroblasts prevents arrhythmias in vitro by limiting myofibroblast-induced depolarization. *Cardiovasc Res*. 2011; 90:295-304.
 18. Feola I, Teplenin A, de Vries AA, Pijnappels DA. Optogenetic Engineering of Atrial Cardiomyocytes. *Methods Mol Biol*. 2016; 1408:319-31.
 19. Arrenberg AB, Stainier DY, Baier H, Huisken J. Optogenetic control of cardiac function. *Science*. 2010; 330:971-4.
 20. Nussinovitch U, Gepstein L. Optogenetics for in vivo cardiac pacing and resynchronization therapies. *Nat Biotechnol*. 2015; 33:750-4.
 21. Nussinovitch U, Shinnawi R, Gepstein L. Modulation of cardiac tissue electrophysiological properties with light-sensitive proteins. *Cardiovasc Res*. 2014; 102:176-87.
 22. Bruegmann T, Malan D, Hesse M, Beiert T, Fuegemann CJ, Fleischmann BK, Sasse P. Optogenetic control of heart muscle in vitro and in vivo. *Nat Methods*. 2010; 7:897-900.
 23. Nyns EC, Kip A, Bart CI, Plomp JJ, Zeppenfeld K, Schalij MJ, de Vries AA, Pijnappels DA. Optogenetic termination of ventricular arrhythmias in the whole heart: towards biological cardiac rhythm management. *Eur Heart J*. 2017; 38:2132-2136.
 24. Bruegmann T, Boyle PM, Vogt CC, Karathanos TV, Arevalo HJ, Fleischmann BK, Trayanova NA, Sasse P. Optogenetic defibrillation terminates ventricular arrhythmia in mouse hearts and human simulations. *J Clin Invest*. 2016; 126:3894-904.
 25. Crocini C, Ferrantini C, Coppini R, Scardigli M, Yan P, Loew LM, Smith G, Cerbai E, Poggesi C, Pavone FS, Sacconi L. Optogenetics design of mechanistically-based stimulation patterns for cardiac defibrillation. *Sci Rep*. 2016; 6:35628.
 26. Lim ZY, Maskara B, Aguel F, Emokpae R, Jr, Tung L. Spiral wave attachment to millimeter-sized obstacles. *Circulation*. 2006; 114:2113-21.
 27. Watanabe M, Feola I, Majumder R, Jangsongthong W, Teplenin AS, Ypey DL, Schalij MJ, Zeppenfeld K, de Vries AA, Pijnappels DA. Optogenetic manipulation of anatomical re-entry by light-guided generation of a reversible local conduction block. *Cardiovasc Res*. 2017; 113:354-66.
 28. Nath S, Lynch C, III, Wayne JG, Haines DE. Cellular electrophysiological effects of hyperthermia on isolated guinea pig papillary muscle. Implications for catheter ablation. *Circulation*. 1993; 88:1826-31.
 29. Defauw A, Vandersickel N, Dawyndt P, Panfilov AV. Small size ionic heterogeneities in the human heart can attract rotors. *Am J Physiol Heart Circ Physiol*. 2014; 307:H1456-H1468.

SUPPLEMENTAL MATERIAL

A**B**

Supplementary figure 1. A, Structure of LV shuttle plasmid pLV.GgTnnt2.CatCh~eYFP.WHVPRE. B, Fluoromicrograph image of confluent Catch-expressing nraCMC monolayers showing homogenous transgene expression.

Movie 1. Induction of a single centralized stable rotor.

Movie 2. Effects of core region targeting with 3-mm circular conduction block.

Movie 3. Effects of core region targeting with 6-mm circular conduction block.

Movie 4. Effects of core region targeting with 12-mm circular conduction block.

Movie 5. Effects of core region targeting with a linear conduction block not reaching any unexcitable boundaries.

Movie 6. Effects of core region targeting with a linear conduction block reaching two opposite unexcitable boundaries.

Movie 7. Effects of localized targeting away from the rotor core region with a linear conduction block reaching two opposite unexcitable boundaries.

Movie 8. Effects of core region targeting with a linear conduction block reaching only one unexcitable boundary.

3



Appendix

LETTER BY HOUSTON *ET AL* REGARDING ARTICLE, “LOCALIZED OPTOGENETIC TARGETING OF ROTORS IN ATRIAL CARDIOMYOCYTE MONOLAYERS”

Charles Houston, MRes; Fu Siong Ng, MRCP, PhD;
Emmanuel Dupont, PhD

Myocardial Function, National Heart and Lung Institute, Imperial College
London, London, United Kingdom

1



TO THE EDITOR

We read with great interest the article by Feola and colleagues on investigating the mechanisms of rotor-guided ablation through optogenetic stimulation in monolayers of neonatal rat atrial cardiomyocytes.¹ The authors optically map single stable rotors which could be reliably initiated in their homogeneous monolayers, and report on the success rate of different light ablation approaches to terminate the rotors by localized conduction block.

We previously studied similar rotor activity using high spatiotemporal resolution optical mapping in monolayers of functionally homogeneous atrial murine cells (HL1-6 myocytes).² At similar mapping resolutions to this work, we also observe apparent spiral waves characteristic of rotor theory. Upon mapping the cores of our rotors at higher single-cell resolution (2.6x2.6µm per pixel), we found that the activity was instead driven by microreentry around lines of conduction block/slowing with lengths 200-800µm (<http://wwwf.imperial.ac.uk/imedia/content/view/6049>. Houston C, MRes, Dupont E, PhD, unpublished data, 2017). These lengths correlate with the regularity of the macro spiral wave, and contrast the view that the cores are round areas of excitable but unexcited cells as rotor theory postulates.³ Although a different functionally homogeneous biological model, we expect that similar microreentrant mechanisms drive the activity in this study.

The authors reported that their light-based S1-S2 protocol was reliable in initiating stable rotor activity at predetermined locations. Have the authors used their technique to study the core of rotors at higher resolution? In-silico studies of spiral waves in nraCMC monolayers suggest that microscopic heterogeneity is necessary for stable rotors.⁴ Our results similarly suggest that microscopic heterogeneity in electrical coupling or cell volume may lead to particular sites being susceptible to microreentry. If this is the case, we would expect rotors to reappear in the same location and with similar dynamics following termination. Was an attempt made to reinitiate a rotor using the same protocol following previous rotor termination? Do new rotors present the same spatial and temporal characteristics observed prior to termination?

Lastly, we would like to commend the authors for using a two-dimensional model of reduced complexity in studying the mechanisms of rotor-guided ablation; we fully support the application of biological models in laying foundations for future research across the translational spectrum.

DISCLOSURES

None.

REFERENCES

1. Feola I, Volkens L, Majumder R, Teplenin A, Schalij MJ, Panfilov AV, de Vries AAF, Pijnappels DA. Localized Optogenetic Targeting of Rotors in Atrial Cardiomyocyte Monolayers. *Circ Arrhythm Electrophysiol.* 2017;10:e005591.
2. Dias P, Desplantez T, El-Harasis MA, Chowdhury RA, Ullrich ND, Cabestrero de Diego A, Peters NS, Severs NJ, MacLeod KT, Dupont E. Characterisation of connexin expression and electrophysiological properties in stable clones of the HL-1 myocyte cell line. *PLoS ONE.* 2014;9:e90266.
3. Pandit SV, Jalife J. Rotors and the Dynamics of Cardiac Fibrillation. *Circ Res.* 2013;112:849–862.
4. Majumder R, Jangsangthong W, Feola I, Ypey DL, Pijnappels DA, Panfilov AV. A Mathematical Model of Neonatal Rat Atrial Monolayers with Constitutively Active Acetylcholine-Mediated K⁺ Current. *PLoS Computational Biology.* 2016;12:e1004946– e1004946.





Appendix

RESPONSE BY FEOLA *ET AL* TO LETTER REGARDING ARTICLE, “LOCALIZED OPTOGENETIC TARGETING OF ROTORS IN ATRIAL CARDIOMYOCYTE MONOLAYERS”

Iolanda Feola¹, MSc; Linda Volkers¹, PhD;
Rupamanjari Majumder¹, PhD; Alexander Teplenin¹, MSc;
Martin J. Schalij¹, MD, PhD; Alexander V. Panfilov^{1,2}, PhD;
Antoine A.F. de Vries¹, PhD; Daniël A. Pijnappels¹, PhD.

¹ Laboratory of Experimental Cardiology, Department of Cardiology, Heart Lung Center Leiden; Leiden University Medical Center, the Netherlands.

² Department of Physics and Astronomy, Ghent University, Ghent, Belgium.

2



IN RESPONSE

We thank Houston *et al* for their interest in our study. In their letter, they raise the question whether the rotors and accompanied spiral waves observed in our study represent microreentrant circuits anchored to lines of conduction block/slowing (*i.e.* anatomical reentry), instead of reentrant activity around an unexcited, yet excitable core region (*i.e.* functional reentry). Their comment is based on a movie published on their website, showing high-resolution mapping, in an HL-1 culture, of reentrant activity that seems anchored to microregions of conduction abnormalities. Although appraisal of these data is difficult without a detailed description of methods and results, we still would like to add our thoughts about the distinction between functional and anatomical reentry on a cellular level. Heterogeneities, such as gradients in excitability, refractoriness, and nonhomogeneous distribution of cardiac fibroblasts may have a destabilizing effect on functional reentry by contributing to drift, meandering, and breakup of spiral waves.^{1,2} Furthermore, reentrant activity may undergo alternating transitions between functional and anatomical reentry by pinning to or unpinning from an anatomical obstruction.³⁻⁶ These transitions depend on several factors (*e.g.* size of the obstacle and tissue excitability)^{5,6} and highlight the difficulty to determine which type of reentry underlies arrhythmic activity at a given location and time. To deal with the complex dynamic nature of reentrant activity, we used confluent monolayers of optogenetically modified neonatal rat atrial cardiomyocytes and patterned illumination to induce and target a single stable rotor. The resolution of optical voltage mapping allowed us to visualize electrical activity in the entire monolayer and to investigate the effects of rotor targeting by light-controlled induction of conduction blocks once a rotor had been established at a predefined location through light-based cross-field stimulation.⁷

Although any involvement of microreentry cannot be ruled out completely, we found evidence that rotor stability was related to the absence of the aforementioned heterogeneities. Our cultures showed uniform and fast activation with little dispersion in action potential duration on 1-Hz electric stimulation. Moreover, by changing the timing and location of the second light stimulus, stable rotors at different, yet predefined locations could be induced. Finally, we found spiral wave drifting by creating a line of block away from the core region, followed by post-illumination rotor stabilization. Such drifting was also evident in other cases where light-induced conduction block did not cause effective reentry termination. The reentrant wave described by Houston *et al* was able to follow a path of block, despite the poor excitability and coupling of the medium, because of the permanent expression of the oncogenic SV40-LT-ag (simian virus 40-large T-antigen) in HL-1 cells (*e.g.* conduction velocity of 4.1 ± 0.1 cm/s)^{8,9} and the sharp corners (*e.g.* U-turns) in the trajectory. These conditions would normally favor unpinning and subsequent transition into functional reentry, sparking curiosity about the underlying biophysical mechanism(s).^{3,4}

Clinically, it remains to be determined whether and how a strict distinction between functional and anatomical reentry, on a cellular level, could further improve the treatment of reentry-driven arrhythmias.¹⁰ We encourage the authors to publish an in-depth study on microreentry dynamics in HL-1 cultures.

DISCLOSURES

None.

3

REFERENCES

1. Pertsov AM, Davidenko JM, Salomonsz R, Baxter WT, Jalife J. Spiral waves of excitation underlie reentrant activity in isolated cardiac muscle. *Circ Res.* 1993;72:631–650.
2. Fast VG, Kléber AG. Role of wavefront curvature in propagation of cardiac impulse. *Cardiovasc Res.* 1997;33:258–271.
3. Pandit SV, Jalife J. Rotors and the dynamics of cardiac fibrillation. *Circ Res.* 2013;112:849–862.
4. Cabo C, Pertsov AM, Davidenko JM, Baxter WT, Gray RA, Jalife J. Vortex shedding as a precursor of turbulent electrical activity in cardiac muscle. *Biophys J.* 1996;70:1105–1111.
5. Lim ZY, Maskara B, Aguel F, Emokpae R Jr, Tung L. Spiral wave attachment to millimeter-sized obstacles. *Circulation.* 2006;114:2113–2121.
6. Ikeda T, Yashima M, Uchida T, Hough D, Fishbein MC, Mandel WJ, Chen PS, Karagueuzian HS. Attachment of meandering reentrant wave fronts to anatomic obstacles in the atrium. Role of the obstacle size. *Circ Res.* 1997;81:753–764.
7. Feola I, Volkers L, Majumder R, Teplenin A, Schalij MJ, Panfilov AV, de Vries AAF, Pijnappels DA. Localized optogenetic targeting of rotors in atrial cardiomyocyte monolayers. *Circ Arrhythm Electrophysiol.* 2017;10:e005591.
8. Dias P, Desplantez T, El-Harasis MA, Chowdhury RA, Ullrich ND, Cabestrero de Diego A, Peters NS, Severs NJ, MacLeod KT, Dupont E. Characterisation of connexin expression and electrophysiological properties in stable clones of the HL-1 myocyte cell line. *PLoS One.* 2014;9:e90266.
9. Claycomb WC, Lanson NA Jr, Stallworth BS, Egeland DB, Delcarpio JB, Bahinski A, Izzo NJ Jr. HL-1 cells: a cardiac muscle cell line that contracts and retains phenotypic characteristics of the adult cardiomyocyte. *Proc Natl Acad Sci USA.* 1998;95:2979–2984.
10. Nattel S, Xiong F, Aguilar M. Demystifying rotors and their place in clinical translation of atrial fibrillation mechanisms. *Nat Rev Cardiol.* 2017;14:509–520.



Chapter

OPTOGENETICS ENABLES REAL-TIME SPATIOTEMPORAL CONTROL OVER SPIRAL WAVE DYNAMICS IN AN EXCITABLE CARDIAC SYSTEM

Rupamanjari Majumder^{*1}, PhD; Iolanda Feola^{*1}, MSc;
Alexander Teplenin¹, MSc; Antoine A.F. de Vries¹, PhD;
Alexander V. Panfilov^{1,2}, PhD; Daniël A Pijnappels¹, PhD.

¹Laboratory of Experimental Cardiology, Department of Cardiology, Heart Lung Center Leiden; Leiden University Medical Center, the Netherlands.

²Department of Physics and Astronomy, Ghent University, Ghent, Belgium.

**equal contribution*

4

ABSTRACT

Propagation of non-linear waves is key to the functioning of diverse biological systems. Such waves can organize into spirals, rotating around a core, whose properties determine the overall wave dynamics. Theoretically, manipulation of a spiral wave core should lead to full spatiotemporal control over its dynamics. However, this theory lacks supportive evidence (even at a conceptual level), making it thus a long-standing hypothesis. Here, we propose a new phenomenological concept that involves artificially dragging spiral waves by their cores, to prove the aforementioned hypothesis *in silico*, with subsequent *in vitro* validation in optogenetically modified monolayers of rat atrial cardiomyocytes. We thereby connect previously established, but unrelated concepts of spiral wave attraction, anchoring and unpinning to demonstrate that core manipulation, through controlled displacement of heterogeneities in excitable media, allows forced movement of spiral waves along pre-defined trajectories. Consequently, we impose real-time spatiotemporal control over spiral wave dynamics in a biological system.

4

eLife digest

From a spinning galaxy to a swarm of honeybees, rotating spirals are widespread in nature. Even within the muscles of the heart, waves of electrical activity sometimes rotate spirally, leading to irregular heart rhythms or arrhythmia – a condition that can be fatal.

Irrespective of where they occur, spiral waves organize around a center or core with different biophysical properties compared to the rest of the medium. The properties of the core determine the overall dynamics of the spiral. This means that, theoretically, it should be possible to completely control a spiral wave just by manipulating its core.

Now, Majumder, Feola *et al* have tested this long-standing hypothesis using a combination of computer modeling and experiments with single layers of rat heart cells grown in a laboratory. First, the heart cells were genetically modified so that their electrical properties could be altered with light; in other words, the cells were put under optical control. Next, by using a narrow beam of light, Majumder, Feola *et al* precisely controlled the electrical properties of a small number of cells, which then attracted and supported a rotating spiral wave by acting as its new core. Moving the light beam allowed the core of the spiral wave to be shifted too, meaning the spiral wave could now be steered along any desired path in the cell layer.

Majumder, Feola *et al* hope that these underlying principles may one day provide the basis of new treatments for irregular heartbeats that are more effective and less damaging to the heart than existing options. Yet first, more work is needed to translate these findings from single layers of cells to actual hearts.

INTRODUCTION

Self-organization of macroscopic structures through atomic, molecular or cellular interactions is characteristic of many non-equilibrium systems. Such emergent dynamic ordering often reveals fundamental universalities.¹ One example is the occurrence of rotating spiral waves. Spiral waves are found in diverse natural systems: from active galaxies,² to simple oscillatory chemical reactions,^{3,4} to social waves in colonies of giant honey bees,⁵ to Min protein gradients in bacterial cell division,⁶ and to the formation of vortices in fluids flowing past obstacles.⁷ While being beneficial to some systems, for example slime molds, where they guide morphogenesis, such activity has detrimental consequences for other systems including the heart, where they underlie lethal cardiac arrhythmias.⁸ Understanding the dynamics of spiral waves in order to establish functional control over a system, has intrigued researchers for many decades. It has been reported that irrespective of the nature of the excitable medium, spiral wave activity organizes around an unexcitable center (core), whose properties determine its overall dynamics.^{9,10} Theorists attribute such particle-like behavior of a spiral wave to an underlying topological charge, which controls its short-range interaction, annihilation, and the ability to form intricate bound states with other spirals.¹¹⁻¹³

Rotational activity similar to spiral waves can also occur around small structural or functional heterogeneities (e.g. areas of conduction block). In this case, the dynamics of the rotating wave and its spatial position are determined by the location and properties of the heterogeneity. Thus, in theory, by controlling the position and size of spiral wave cores, one can precisely and directly control the dynamics of spiral waves in general. In order to achieve such control, it is therefore logical, to consider as a first step, possible core-targeting via the conversion of a free spiral wave to an anchored rotational activity. To this end, a detailed mechanistic study was performed by Steinbock *et al*,¹⁴ who demonstrated the possibility to forcibly anchor meandering spiral waves in an excitable light-sensitive Belousov-Zhabotinsky (BZ) reaction system. Furthermore, Ke *et al*¹⁵ demonstrated in a three-dimensional BZ reaction setting, that forced anchoring of scroll waves to thin glass rods, followed by subsequent movement of the rods themselves, could enable scroll wave relocation. On a broader perspective, this could have significant meaning for the heart, where controlling the dynamics of scroll waves could add to the treatment of cardiac arrhythmias sustained by such waves.

In cardiac tissue, the analogs of a classical spiral wave and a wave rotating around a heterogeneity, are, respectively, functional and anatomical reentry, both of which are recognized as drivers of arrhythmias. Interestingly, functional and anatomical reentrant waves are closely related to each other. Seminal findings by Davidenko *et al*¹⁶ demonstrated that a drifting spiral wave could anchor to an obstacle and thereby make a transition from functional to anatomical reentry. Conversely, Ripplinger *et al*¹⁷ showed that small electric shocks could unpin a reentrant wave rotating around an obstacle, bringing about the reverse transition from anatomical to functional reentry. Nakouzi *et al*¹⁸ and Zykov *et al*¹⁹ demonstrated that the transitions between anchored and free spiral states may be accompanied by hysteresis near the heterogeneities. Furthermore, Defauw *et al*²⁰ showed that small-sized anatomical heterogeneities could attract

spiral waves from a close distance, and even lead to their termination if located near an unexcitable boundary. However, to date, all studies dedicated to spiral wave attraction and anchoring involved the presence of anatomically predefined, permanent heterogeneities, or continuous-in-time processes, thereby making it impossible to manipulate spiral wave cores in a flexible, systematic and dynamical manner. In the present study, we propose a new phenomenological concept to demonstrate real-time spatiotemporal control over spiral wave dynamics through discrete, systematic, manipulation of spiral wave cores in a spatially extended biological medium, that is cardiac tissue. We establish such control through optogenetics,²¹⁻²⁴ which allows the creation of spatially and temporally predefined heterogeneities at superb resolution at any location within an excitable medium. Previous studies for example by Arrenberg *et al.*;²⁵ Bruegmann *et al.*;²⁶ Jia *et al.*;²⁷ Bingen *et al.*;²⁸ Entcheva and Bub²⁹ and Burton *et al.*,³⁰ demonstrate the power of optogenetics in cardiac systems. Thus, the same technology was chosen to strategically exploit fundamental dynamical properties of spiral waves, like attraction, anchoring and unpinning, to discretely and effectively steer spiral wave cores along any desired path within an excitable monolayer of cardiac cells. These findings are highly relevant for understanding non-linear wave dynamics and pattern formation in excitable biological media, as they enable, for the first time, real-time discrete dynamic control over processes that are associated with self-sustained spiraling phenomena, for example reentrant electrical activity, cAMP cycles and movement of cytosolic free Ca²⁺, to name a few. In particular, in the heart, tight control of spiral waves may allow restoration of normal wave propagation.

RESULTS

Self-sustained spiral waves can be actively generated in most natural excitable media. In this study, we induced spiral waves of period 60 ± 5 ms *in silico* and of period 63 ± 11 ms *in vitro* in confluent monolayers of optogenetically modified neonatal rat atrial cardiomyocytes (see Materials and methods for details). Targeted application of light to the monolayers led to the sequential occurrence of two events: (i) creation of a spatially predefined temporal heterogeneity (*i.e.* a reversible conduction block) near the core of a spiral wave, and (ii) emergence of a wave from the spot of illumination. In a previous study,³¹ we demonstrated the possibility to create such a temporal heterogeneity with optical control over the size, location and duration of the block. Here, we show how creation of a light-induced block close to the core of a spiral wave, can attract the spiral wave tip, causing it to eventually anchor to the block. Subsequent movement of the light spot to different locations within the monolayer, results in dragging of the spiral wave along a predefined pathway of illumination, thereby giving rise to, what we call Attract-Anchor-Drag-based (AAD) control. Figure 1A illustrates a schematic diagram of the experimental setup that we used for our *in vitro* studies, whereas the sequence of light patterns used for real-time AAD control is described in Figure 1B. Figure 1 (C1-4) and 1(D1-4) show representative examples of AAD control of spiral wave dynamics *in silico* and *in vitro*, respectively, where the spiral wave core is dragged along a predefined 9-step triangular path (see also Movie 1). Our results demonstrate the possibility to capture a spiral wave, to manipulate its trajectory in

a spatiotemporally precise manner (Figures 1 C2–3 and D2 , and, finally, to release it in order to rotate freely again (Figure 1 C4, D4). Thus, we prove that it is indeed possible to directly and precisely manipulate the spatial location of a stable spiral wave core, and thereby overcome the constraints imposed by internal and external factors that shape the natural meander and drift trajectories. Such control is very important because it provides a direct and effective handle over the spatiotemporal patterning of the system, which would affect its general functionality. Natural systems currently suffer from the lack of such a handle.^{32,33} Spiral wave dragging seeks to fill this lacuna at the simplest level.

An immediate application of such a process, that follows dynamic manipulation of spiral waves, involves using this technique to terminate complex spiral wave activity. We first focus on removing a single spiral wave *in silico* (Figures 2 A1–5; see also Movie 2). With a five-step drag sequence of circular light spots of 0.275 cm diameter and 250 ms illumination time per spot, we demonstrate the possibility to remove a spiral wave from a monolayer, by capturing its core somewhere near the middle of the simulation domain and subsequently dragging it all the way to the unexcitable boundary on the left, causing the phase singularity to collide with the border and annihilate. The representative trajectory of the spiral wave, as it is dragged to termination, is shown in Figure 2 (A2-4) with dashed red lines. The direction of movement of the spiral is indicated in each frame with red arrows. Inspired by the outcome of our *in silico* experiments, we tested the same principle *in vitro*, with a five-step drag sequence of circular light spots with

4

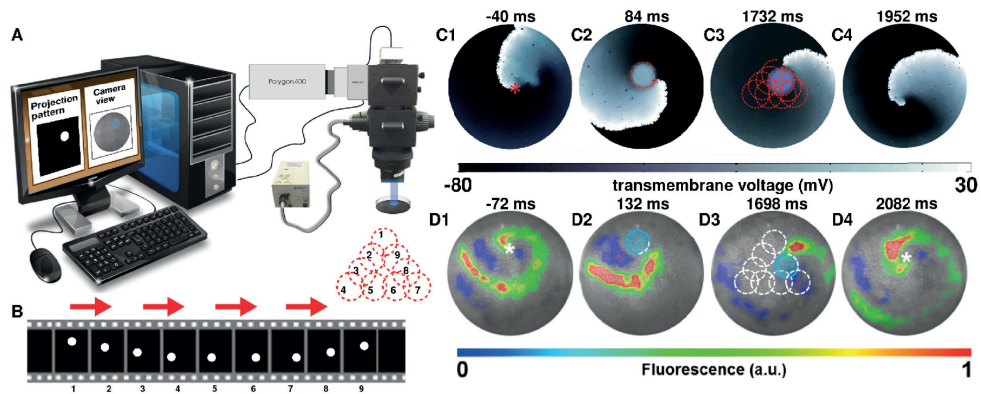


Figure 1. Attract-Anchor-Drag (AAD) control of a spiral wave core along a triangular trajectory. A, Schematic diagram of our *in vitro* setup, showing how we project light patterns on an optogenetically modified monolayer. B, The sequence of light spots that constitute the desired triangular trajectory of the spiral core. C1–C4, *In silico* AAD control data recorded at subsequent times. D1–D4, *In vitro* corroboration of our *in silico* findings (n=9). In panels (C) and (D), the current location of the applied light spot is indicated with a filled blue circle, whereas, the schematic movement of the tip of the spiral wave, as it is anchored to the location of the light spot at previous time points, is indicated in each frame by means of dashed red (*in silico*) and white (*in vitro*) lines. The location of the phase singularity of the spiral wave is marked in the first and last frame of panels (C) and (D) with a red (*in silico*) or white (*in vitro*) asterisk. a.u., arbitrary units. A movie demonstrating the process of dragging a spiral wave core along a triangular trajectory is presented in Movie 1.

similar characteristics as those applied *in silico*. Our *in vitro* findings corroborate the *in silico* results (Figures 2 B1–5; see also Movie 2). The representative trajectory of this spiral wave, as it is dragged to termination, is shown in Figure 2 (B2–4) with dashed white lines. In each frame of Figure 2, the location of the light spot is marked with a transparent blue circle.

Having proven the possibility to drag single spiral waves to inexcitable tissue borders in favor of termination, we attempt to develop an in-depth qualitative understanding of the parameters that play a crucial role in the dragging process. We focus on the previously described case: linear 5-step dragging from the center of the simulation domain to a point on the periphery, with continuous illumination, and start by investigating the dependence of the probability of successful dragging (P_{drag}), on the diameter (d) of a continuously illuminated moving spot (*i.e.* without a finite time gap between successive applications of light). Our study reveals a positive correlation between P and d . At $d \leq 3$ mm, the minimum time (τ_{min}) required for relocation of a spiral wave to the next position decreases abruptly with increasing of d . However, at $d > 3$ mm, τ_{min} decreases slowly, trending towards a possible saturation value. These results are illustrated in Figure 3.

4

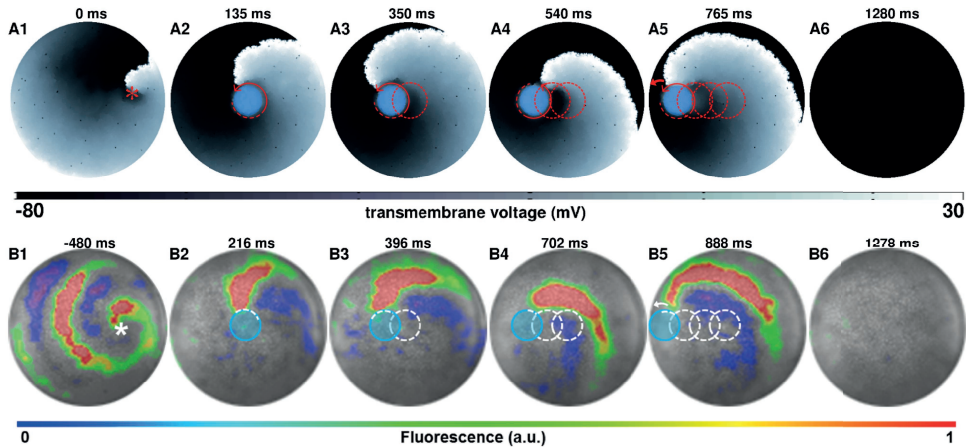
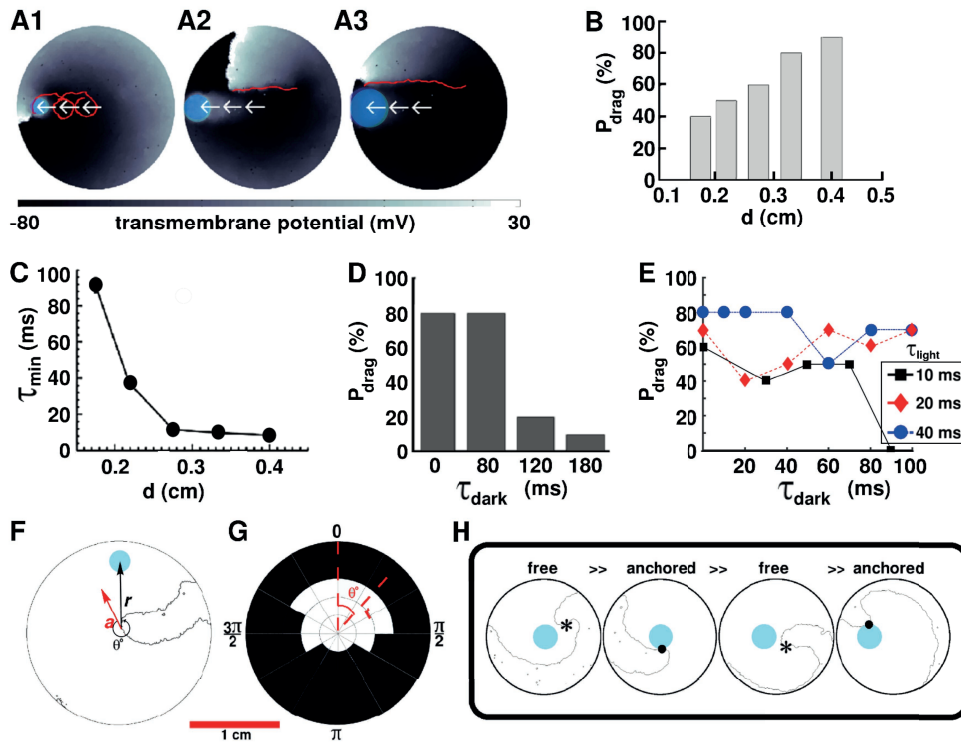


Figure 2. AAD control of a spiral wave core in favor of termination. The upper panel (A1–A6) shows successful removal of a spiral wave *in silico*, by capturing its core from the center of the simulation domain, and dragging it to the left boundary in a stepwise fashion ($\tau_{light}=250$ ms and $\tau_{dark}=1$ ms per spot, period of the reentry around the spot is 78 ± 2 ms). The lower panel (B1–B6) shows *in vitro* proof of the results presented in panel (A) ($n=9$). For each light spot, the current location of the applied light spot is indicated with a filled blue circle ($\tau_{light}=250$ ms and $\tau_{dark}=15$ ms, period of the reentry around the spot is 90 ± 12 ms). The schematic movement of the tip of the spiral wave, as it is anchored to the location of the light spot at previous time points, is indicated in each frame by means of dashed red (*in silico*) and white (*in vitro*) lines. The location of the phase singularity of the spiral wave is marked in the first frame of each panel with a red (*in silico*) or white (*in vitro*) asterisk. a.u., arbitrary units. A movie demonstrating the complete process of dragging a spiral wave core from the center of the monolayer to the left border, causing its termination, is presented in Movie 2. (Time $t=0$ ms denotes the moment when the light is applied).

Optogenetic control over spiral wave dynamics



4

Figure 3. AAD control by continuous illumination of circular light spots of different sizes and durations. Panel A shows representative dragging events as a spiral wave core is relocated from the center of the simulation domain to the periphery, with light spots of diameter $d=0.175, 0.275$ and 0.4 cm, respectively. In each case the real trajectories of the spiral tip is marked with solid red lines on top of the voltage map. When d is large, the spiral tip exhibits a tendency to move along a linear path, as opposed to the cycloidal trajectory at small d . With $d=0.275$ cm, (B) probability of successful dragging (P_{drag}) increases, and (C) spiral core relocation time (τ_{min}) decreases, with increasing d . In each of the aforementioned cases, the dragging process is illustrated with zero dark interval (τ_{dark}) and minimal light interval (τ_{light}). D, With finite non-zero τ_{dark} , P_{drag} increases with shortening of τ_{dark} , for light stimulation of a fixed cycle length (200 ms). E, Dependence of P_{drag} on τ_{dark} for 3 different light intervals (τ_{light}). F, Schematic representation of the drag angle θ and the distance (r) between the starting location of the spiral tip and the location of the applied light spot. G, Distribution of P_{drag} at different θ and r , thresholded at 50%. H, AAD control is effectuated by alternate transitions between functional (free wave) and anatomical (anchored wave) reentry. The phase singularity of the free spiral is marked with a black asterisk, whereas, the point of attachment of the anchored wave to the heterogeneity is marked with a black dot.

Traces of the spiral tip trajectory (indicated by means of red lines on top of a representative frame depicted in Figure 3 A1–A3) demonstrate that the ease with which a spiral core can be dragged, from the center of the domain to a border, increases with increasing d . At small d , the spiral tip is dragged along a cycloidal path, in which, the diameter of the loop is $O(d)$. As d increases, the spiral tends to translate linearly, without executing rotational movement about the core.

To investigate the conditions that allow spiral wave dragging with discrete light pulses, we apply a series of circular light spots of duration τ_{light} . These spots appear sequentially in time, and are physically separated in space, with gradually decreasing distance from the boundary. For simplicity, we apply all spots along the same line, drawn from the center of the simulation domain to the boundary. We define the time gap between successive light pulses (when the light is off everywhere) as the dark interval τ_{dark} . Thus, effectively, our optical stimulation protocol is periodic in time (with period $\tau_{light} + \tau_{dark}$), but not in space. We perform two sets of studies for the case of linear dragging. In the first set, we fix $\tau_{light} + \tau_{dark}$ at 200 ms and tune τ_{dark} . In the second set, we fix τ_{light} (3 different values) and tune τ_{dark} . Our results indeed demonstrate the occurrence of AAD control with discrete illumination ($\tau_{dark} = 0$ ms). Figure 3 D shows, for example, that at $\tau_{dark} = 0, 80, 120,$ and 180 ms, respectively, P_{drag} decreases from 80% to 20% to 10%. Interestingly, $\tau_{dark} = 80$ ms appears to be as effective as continuous illumination ($\tau_{dark} = 0$ ms, Figure 3 D). Thus, our findings confirm that, for a fixed cycle length of optical stimulation by a spot of light of diameter $d = 0.275$ cm, P_{drag} increases with decreasing τ_{dark} .

If, however, we tune to explore the dependence of P_{drag} on τ_{light} at flexible cycle lengths, there is no clear relationship between P_{drag} and τ_{light} (Figure 3E), despite an increase in the ease of attraction of the spiral tip towards the illuminated spot at short τ_{dark} . In general, $\tau_{light} \simeq O(0.1 \tau_{dark})$ does not lead to effective AAD control, whereas, $\tau_{light} \simeq O(10 \tau_{dark})$ ($\tau_{dark} \neq 0$) does, however, exceptional cases also exist. For example, (i) P_{drag} can be large (*i.e.* 70%) when a short light pulse ($\tau_{light} = 20$ ms) is followed by a long dark interval ($\tau_{dark} = 100$ ms); and, (ii) combinations of abbreviated τ_{light} and τ_{dark} (*i.e.* $\tau_{light} = 20$ ms, $\tau_{dark} = 20$ ms) can lead to lower P_{drag} than pulse combinations with shorter or longer τ_{dark} .

We find that the probability of attraction also depends on the phase of the spiral wave rotation at the moment of light exposure. This dependence, in simple terms, can be quantified as dependence on the angle between the vector along the instantaneous direction of motion of the spiral tip \vec{a} and the vector \vec{r} of the displacement of the center of the circular light spot, in polar coordinate system. This is illustrated in Figure 3F. Our results demonstrate that spiral wave dragging occurs most efficiently if the spot of light is applied sufficiently close to the location of the spiral tip and within an angular spread of $\Delta\theta_X$ in the direction of drift of the spiral core (Figure 3G). Here, X denotes the cutoff probability for the occurrence of dragging, *i.e.* $\Delta\theta_{50\%}$ refers to an angular spread of $\Delta\theta$ for which $P_{drag} \geq 50\%$. A spiral wave cannot be dragged when $r > 5.63$ mm. When $4.7 \text{ mm} < r < 5.63 \text{ mm}$, $\Delta\theta_{50\%} = 150^\circ$. P_{drag} increases to 240° when $3.44 \text{ mm} < r < 4.7 \text{ mm}$, and to 360° when $r < 3.44 \text{ mm}$. Furthermore, to develop a detailed understanding of the physical mechanisms involved in spiral wave dragging, the nature of the process itself is analyzed. Our *in silico* findings indicate that successful control necessitates the spiral wave to make alternate transitions between functional (free) and anatomical (anchored) types of reentry. When a spot of light is applied reasonably close to the core of a spiral wave, within the allowed $\Delta\theta$, it creates a region of light-induced depolarization that attracts and anchors the core of the free spiral, thereby effectuating a transition from functional to anatomical reentry. When the light spot is now moved to a different location, still within the basin of attraction of the first light spot, the previously depolarized region recovers, forcing the anchored spiral to

unpin and make a reverse transition to functional reentry. The larger the value of τ_{dark} , the more visible the transition. Finally, at the new location of the light spot, a zone of depolarization is created, which either attracts and anchors the spiral tip, or produces a new wave of excitation that replaces the existing spiral wave with a new one, still followed by attraction and anchoring. A sequence of *in silico* voltage maps in support of the proposed mechanism, is shown in Figure 3H.

With a detailed understanding of the parameters involved in the process of spiral wave dragging, we explore the possibility to apply this phenomenon to tackle more challenging problems, such as, termination of complex patterns of reentry. We specifically target two patterns: (i) figure-of-eight type reentry, and (ii) reentry characterized by multiple spiral waves, *i.e.* multiple phase singularities. *In silico*, we find that figure-of-eight type reentry can be removed efficiently by dragging the cores of both spiral waves towards each other, till their phase singularities collide, leading to self-annihilation. Figure 4(A1-6) (see also Movie 3) show subsequent steps in the process of removal of a figure of-eight type reentry via AAD control, when the reentry pattern comprises two spirals of opposite chirality, rotating in phase with each other.

4

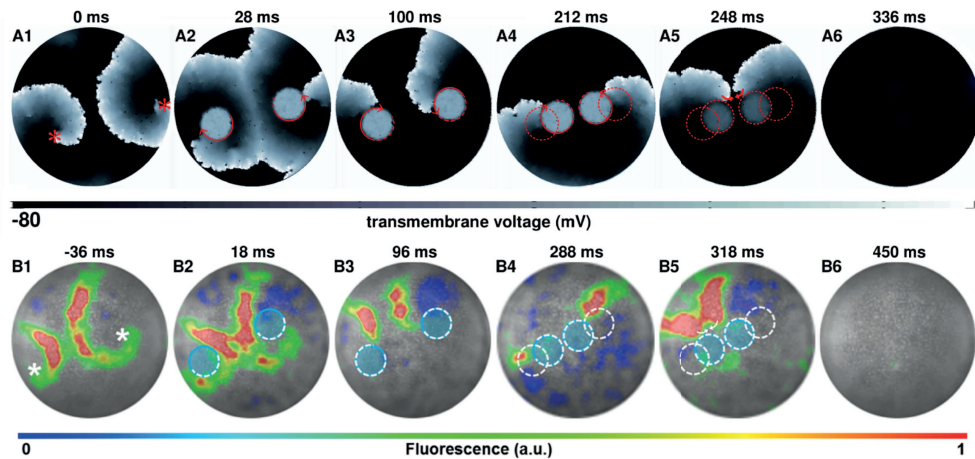


Figure 4. AAD control of a pair of spiral wave cores in favor of termination of figure-of-eight-type reentry. The upper panel (A1-A6) shows representative *in silico* voltage maps of the drag-to-termination process, at subsequent times. The lower panel (B1-B6) provides *in vitro* confirmation of the findings presented in panel (A) ($n=6$). In each case, the locations of the phase singularities are marked on the first frame of each panel with a red (*in silico*) or a white (*in vitro*) asterisk. The current location of the applied spot of light is indicated with a filled blue circle. The schematic movement of the tip of the spiral wave, as it is anchored to the location of the light spot at previous time points, is indicated in each frame by means of dashed red (*in silico*) and white (*in vitro*) lines. The direction of dragging is indicated in panel (A) with red arrows. In our studies, we terminated figure-of-eight-type reentry by dragging 2 spiral cores towards each other to make them collide and annihilate. a.u., arbitrary units. A movie demonstrating AAD control (with eventual termination) of a figure-of-eight type reentry is presented in Movie 3.

Figure 4 (B1-6) (see also Movie 3) show successful experimental (*in vitro*) validation of our *in silico* findings, following the same termination protocol. When the figure-of-eight type reentry comprises two spirals of opposite chirality that do not rotate exactly in phase, the strategy should be to capture the cores of the pair of spirals with light spots of unequal sizes, so as to compensate for the difference in phases, at the very first step of the control method. A representative example of such a scenario is presented in the Figure 4-figure supplement 1.

In order to terminate reentry characterized by multiple phase singularities, we try different approaches. Figure 5 (A1-7) and (B1-7) (see also Movie 4) illustrate two examples of such attempts *in silico* with reentry characterized by three and seven phase singularities, respectively.

With three spiral cores, we follow a strategy which is a combination of the cases presented in Figures 4 and 2 that is we capture all three cores (Figure 5A2), drag them toward each

4

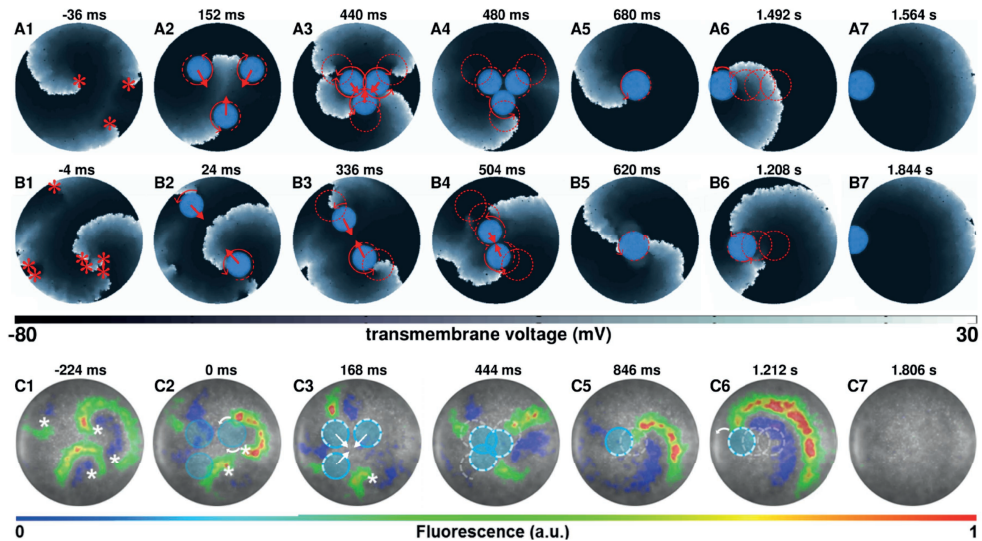


Figure 5. AAD control of multiple spiral wave cores in favor of termination of complex reentrant patterns. Panels (A) and (B) show representative *in silico* voltage maps of the drag-to-termination process for stable reentrant activity with three and seven phase singularities, respectively. Panel (C) shows representative *in vitro* voltage maps of the drag-to-termination process for stable reentrant activity with four phase singularities. Number and the position of the light spots, indicated with blue filled circles, are strategically applied to first capture the existing spiral waves, and then drag them to termination, following the same principle as in Figure 2 (A5-6) and (B5-6). In the process, it is possible to reduce the complexity of the reentrant pattern through annihilation of some of the existing phase singularities by new waves emerging from the location of the applied light spot. The schematic movement of the tip of the spiral wave, as it is anchored to the location of the light spot at previous time points, is indicated by means of dashed red (white) lines *in silico* (*in vitro*), and the direction of dragging is illustrated with red (white) arrows. Movie 4 shows a movie of computer simulations demonstrating AAD control of complex reentrant patterns with three and four spiral waves, in favor of their eventual termination. Movie 5 shows the same process, *in vitro*, but for stable reentry with four-phase singularities. (Time $t=0$ ms denotes the moment when the light is applied).

other (Figure 5A3), reduce complexity via annihilation of two colliding phase singularities (Figure 5A4–5), and drag the remaining spiral core to termination via collision of its phase singularity with the unexcitable boundary (Figures 5A6–7). However, with higher complexity, there is no unique optimal approach that leads to the termination of reentry. In the example presented in Figure 5 (B1–7), we rely on reducing the complexity of the reentrant pattern itself, via strategic application of two light spots, prior to the actual dragging process. New waves emerging from the locations of the applied light spots interact with the existing electrical activity in the monolayer to produce new phase singularities, which collide with some of the preexisting ones to lower the complexity of the reentrant pattern. With reduced complexity, we drag the spiral cores toward each other, till they merge to form a single two-armed spiral, anchored to the applied light spot. We then drag this spiral to the boundary of the monolayer causing its termination. A similar strategy applied *in vitro* enabled successful termination of a complex reentry pattern characterized by four phase singularities. This is illustrated in Figure 5 (C1–7). At the instant when the first set of light spots is applied, reentry is characterized by four phase singularities (Figure 5C1). Note that, of the four phase singularities, two coincide with the locations of two of the applied light spots and two are located away from the third light spot (Figure 5C2). These first two phase singularities anchor immediately to the applied light spots. However, the other two interact with the new wave generated by the third applied light spot and reduce to one phase singularity, which remains free (unanchored) (Figure 5C3). When the next set of light spots are applied (in a complex pattern of three overlapping circles), this phase singularity displays attraction to the new light spot, thus effectively producing a three-armed spiral (Figure 5C4). Finally, when the complex light pattern is replaced by a smaller circular spot of light, the three-armed spiral loses two of its arms through interaction with the emergent new wave from the location of the applied light spot (Figure 5C5). The single spiral can then be dragged to termination (Figures 5C6–7) as in Figure 2.

Taken together, our results show that core positions of spiral waves can be strategically manipulated with the help of optogenetics to establish direct spatiotemporal control over a highly nonlinear system. We demonstrate that application of well-timed and spaced light pulses can result in successful dragging of a spiral wave from one location to another within a monolayer, along any desired path and even to cause its termination. Spiral wave dragging can also be employed to terminate complex reentrant patterns characterized by multiple phase singularities, through appropriate AAD control. However, the probability of its occurrence is subject to two key parameters: (i) *sized* and (ii) drag angle ($\Delta\theta$).

DISCUSSION

Spiral waves occur in diverse natural excitable systems, where they impact the functioning of the system in a beneficial or detrimental manner. Given their dynamic and unpredictable nature, direct control over these nonlinear waves remains a longstanding scientific challenge. While it is an established theory that the properties of the core of a spiral wave determine its overall dynamics,^{9, 10} the corollary that manipulation of spiral wave cores should lead to full

spatiotemporal control over wave dynamics in excitable media, appears to be unexpectedly non-obvious and understudied (see below). In this paper, we prove the aforementioned consequence using the remarkable features of optogenetics. Our study is one of the first to demonstrate the establishment of real-time spatiotemporal control over spiral wave dynamics in spatially extended biological (cardiac) tissue. The only other study that shows effective dynamic spatiotemporal control (as opposed to elimination) of spiral waves is that of.³⁰ However, Burton *et al* use dynamic control to modulate spiral wave chirality, which is markedly different from what we study and prove, namely spiral wave dragging.

4 In this research, we demonstrate a new phenomenological concept to steer spiral waves in excitable media, thereby enabling precise and direct spatiotemporal control over spiral wave dynamics. This so-called AAD control involves a feedback interaction between three fundamental dynamical properties of spiral waves: attraction, anchoring and unpinning. In the past, researchers also employed different kinds of spatiotemporal feedback interactions to control spiral wave dynamics, albeit in non-biological media.³⁴ Their methods, while effective, relied on delivering timed pulses falling in defined phases of the spiral. Although feasible in simple chemical systems, phase-based pulse delivery can be quite challenging in complex biological tissue, where temporal precision is a major subtlety and therefore difficult to achieve. The study by Ke *et al* bypasses this issue by forcing scroll wave filaments to anchor to physical heterogeneities, which can be moved subsequently to steer the waves. However, Ke *et al* demonstrate a process that is continuous in time, as opposed to the discrete nature of our method, which makes it more flexible.¹⁵

Previous studies have explored the concept of spiral attraction in human cardiac tissue.²⁰ According to these findings, the mechanism of attraction of spiral waves to localized heterogeneities is a generic phenomenon, observed among spiral waves in heterogeneous tissue. Some studies show that spiral waves tend to drift to regions with longer rotational periods, that is where the duration of an action potential is longer than elsewhere in the medium.^{20,35,36} This is in consonance with our simulations, where application of a spot of light to a monolayer of excitable, optogenetically modified cardiomyocytes causes the cells in this region to depolarize, bearing a direct influence on the action potential duration of cells in the immediate neighborhood. Once attracted, the spiral anchors to the location of the light spot, thereby making a transition from functional to anatomical reentry. Again, when the light at the current location is switched off and a new location is illuminated, in the next step of the drag sequence, the spiral reverts back to functional reentry, from its anatomical variant. If the new location is such that the spiral core overlaps with the basin of attraction of the optogenetically depolarized area, then it anchors to the new location and makes a transition back to anatomical reentry. Thus, AAD control is associated with repeated alternative transitions between functional and anatomical reentry. However, if the core of the spiral wave does not overlap with the basin of attraction of the next location in the drag sequence, or, if the drag sequence is executed too fast for the spiral to establish a stable core at subsequent new locations, then the spiral detaches, breaks up, or destabilizes without being successfully dragged.

A mechanism, somewhat along the same lines as AAD control, was demonstrated by Krinsky *et al.*,³⁷ using topological considerations. When an existing vortex interacts with a circular wave emerging from a stimulus applied close to the vortex core, they fail to annihilate each other. However, the emergent wave quenches the vortex, resulting in its displacement by the order of half a wavelength. This displacement may occur in any direction, as demonstrated by Krinsky *et al.* In our system, we observe similar emergence of a new (circular) wave from the temporal heterogeneity. This new wave fails to annihilate the existing spiral wave, in line with Krinsky's findings, but leads to the displacement of the core toward the temporal heterogeneity, indicating the existence of a factor of attraction, which determines the direction of drift.

In another study, control of spiral wave turbulence was investigated in a self-regulation system that spontaneously eliminated vortex cores, by trapping the latter with localized inhomogeneities.³⁸ This study used computer simulations and a light-sensitive BZ reaction with a Doppler instability. Movement of a spiral wave along a line of predefined obstacles was also observed by Andreev.³⁹ However, unlike Krinsky *et al* and Guo *et al*, their study uses inactive defects, which do not lead to quenching of the spiral wave. Further topological considerations with respect to movement of spiral waves can be found in the seminal work of Winfree and Strogatz.⁴¹ In our studies of spiral wave dragging with light spots of different sizes (Figure 3), a small-sized spot leads to dragging via a cycloidal trajectory, whereas, a large spot is associated with a linear trajectory. In our subsequent investigations, however, cycloidal trajectories were observed even for large spots. This is because, in the data presented in Figure 3, we investigate dragging at the fastest possible rate. The drag trajectories obtained in that study apply for minimal relocation time ($\tau_{light}=\tau_{min}$, $\tau_{dark}=0$ ms). The larger the value of d , the bigger is the area of light-induced depolarization. Consequently, the higher is the chance for the tip of the spiral wave to fall within the basin of attraction of the illuminated area, causing it to remain anchored to the spot at all times. When the spot of light is moved with $\tau_{dark}=0$ ms and $\tau_{light}=\tau_{min}$, the location of the new light spot forms a composite anchor point in combination with the location of the previous light spot; the effective depolarized region resembles an elongated ellipse, with elongation along the direction of movement of the light spot. This causes the spiral tip to trace a nearly linear path, along the boundary of the elongated ellipse. However, at slower dragging rates, *i.e.* longer τ_{light} , as used in the subsequent studies (Figure 3), the spiral wave gets ample time to execute one or more complete rotations around the region of light-induced depolarization, before being relocated to the next spot. Hence, the cycloidal trajectory at large d . The tendency for the spiral tip to move along a cycloidal trajectory at small d can be explained by the establishment of a very small basin of attraction, which results in an increased demand for τ_{min} . Thus the spiral requires execution of at least one complete rotation around the region of light-induced depolarization before it can relocate to the next spot.

These findings are in consonance with the fundamental view of excitable media as dynamical systems. Based on their experimental, computational and theoretical studies, Zykov *et al*¹⁹ and Nakouzi *et al*¹⁸ reported the involvement of bistability and hysteresis in the transitions from anchoring to unpinning of a wave rotating around an anatomical hole. Bistability, or coexistence of two dynamical attractors in the system, indicates dependence of the outcome of

the transition on initial conditions. In our case, the most important choice of initial conditions can be restricted to the phase of the freely rotating spiral wave or the rigidly anchored reentrant wave. Thus, proper timing of the applied perturbation is crucial regarding the efficacy of control. In this sense our results deceptively remind us of the phenomenon of spiral wave drift, which can be induced by periodic modulation of excitability.¹⁴ However, such drift arises from an interplay between Hopf bifurcation of spiral wave solutions, and rotational and translationally symmetric planar (Lie) groups.⁴¹ In our studies, we rely on completely different nonlinear dynamical phenomena, namely, bistability of the rotating wave solutions and its interplay with spatial and temporal degrees of freedom of the dynamically applied light spot (*i.e.* its position, size, period and timing). This combination gives rise to novel interesting spiral wave dynamics, which opens broad avenues for further theoretical and experimental investigation.

Although apparently straightforward, and, to some extent, predictable on the basis of generic spiral wave theory, our results are not at all obvious. Compared to other systems, such as the BZ reaction, cardiac tissue (i) possesses an inherently irregular discrete cellular structure, underlying the absence of spatial symmetries, (ii) lacks inhibitor diffusion and (iii) has different dimensions. Moreover, since the probability of attraction of a spiral wave to a heterogeneity is determined by the initial conditions and by the strength of successive perturbations, it is not a foregone conclusion that discrete application of light spots outside the core of a spiral wave should always end up in an anchored state. By showing, in cultured cardiac tissue, that spiral wave dynamics can be controlled by targeting the spiral wave core, we have been able to experimentally confirm pre-existing ideas about the behavior of spiral waves in complex systems.

Previous studies also demonstrated alternative methods to ‘control’ spiral-wave dynamics in excitable media, for example, by periodic forcing to induce resonant drift,⁴²⁻⁴⁴ or by periodic modulation of excitability to manipulate spiral tip trajectories.¹⁴ These studies do demonstrate the potential to drive a spiral wave out of an excitable medium, or to force spiral waves to execute complex meander patterns, thereby making landmark contributions to the knowledge of pattern formation or even to cardiac arrhythmia management. However, the principal limitation of these methods is that they are indirect, giving reasonable control over the initial and final states of the system, with little or no control in between. It is herein where lies the advantage of AAD control, which allows precise and complete spatiotemporal control over spiral wave dynamics in two-dimensional excitable media.

Clinical translation

Since we demonstrate AAD control method in a cardiac tissue system, a logical question would be, how to envision the application of this principle to the real heart in order to treat arrhythmias? Currently this topic faces major challenges. The practical application of optogenetics in cardiology is, in itself, a debatable issue. However, with recent advances in cardiac optogenetics,⁴⁵⁻⁴⁹ the future holds much promise. Firstly, we envision the usage of AAD control method in treating arrhythmias that are associated with scroll waves. Since

the penetration depth of light in cardiac tissue is relatively short,⁵⁰ full transmural illumination might be challenging, particularly in ventricles of large mammals like pig, monkey or human. There, AAD control may provide a powerful tool to regulate scroll wave dynamics by epicardial or endocardial illumination. Furthermore, we expect the method to prove most useful when dealing with ‘hidden’ spiral waves, that is spiral waves in remote locations of the heart that are inaccessible by ablation catheters. Ideally, one should build upon the concept introduced by Entcheva and Bub.²⁹ With live spacetime optogenetic actuation of the electrical activity in different parts of the heart, the first step is to detect the location of the instability. Next, one can use a catheter with an in-built LED to attract the scroll wave filament and steer it towards the nearest tissue border for termination. The advantage of this method lies in that one does not require to ablate, and thereby destroy, excitable cardiac tissue, thus avoiding the possibility to create permanent damage to the heart. In addition, as our study demonstrates, anchoring of the spiral core (scroll filament) can occur even if the ‘precise’ location of the core is not identified. Lastly, the discrete nature of our method allows temporal flexibility in steering the spiral core (scroll filament), in that, temporary loss of communication between the catheter and the spiral core will not lead to failure of the technique in general. The reversible nature of the AAD control technique makes it unsuitable for terminating arrhythmias that rely on the establishment of a permanent conduction block as can be produced via conventional catheter ablation.

However, this special feature of AAD may come with certain unique advantages that should be explored in more detail in future studies. For example, in younger patients that are expected to undergo periodic repetitive ablation for termination of reoccurring arrhythmias of unknown origin, the non-destructive nature of AAD may prove to be more desirable than the cumulative widespread destruction of cardiac tissue by radiofrequency or cryoballoon ablation. Alternatively, other methods could be developed and explored for AAD control without the need of optogenetic modification, while still relying on the creation of spatiotemporally controlled heterogeneities for attraction, anchoring and dragging of spiral waves.

In this study, we focus on spiral waves in cardiac excitable media, as these abnormal waves have been associated with lethal heart rhythm disturbances, while their management and termination remain a serious challenge. The insights gained from our results, as well as the AAD control method itself, may not only improve our understanding of spiral wave’s dynamics in favor of restoring normal cardiac rhythm, but also create incentive to explore these principles in other excitable media prone to spiral wave development.

MATERIALS AND METHODS

The electrophysiological properties of neonatal rat atrial cardiomyocytes was modeled according to Majumder *et al.*,⁵¹ whereby, the transmembrane potential V of a single cell evolved in time as follows:

$$dV/dt = - (I_{ion} + I_{stim}) / C_m \quad [1]$$

I_{ion} is the total ionic current, expressed as a sum of 10 major ionic currents, namely, the fast Na^+ current (I_{Na}), the L – type Ca^{2+} current (I_{CaL}), the inward rectifier K^+ current (I_{K1}), the transient outward K^+ current (I_{to}), the sustained outward K^+ current (I_{Ksus}), the background K^+ (I_{Kb}), the background Na^+ (I_{Nab}) and the background Ca^{2+} (I_{Cab}) currents, the hyperpolarization activated funny current (I_{f}), and the acetylcholine-mediated K^+ current ($I_{\text{K,ACh}}$). In two dimensions (2D), these cells were coupled such that V evolved spatiotemporally, obeying the following reaction-diffusion-type equation:

$$\partial V / \partial t = \nabla \cdot (D \nabla V) - [(I_{\text{ion}} + I_{\text{stim}}) / C_m], \quad [2]$$

4

where D is the diffusion tensor. In simple 2D monolayer systems, in the absence of anisotropy, the diffusion tensor takes on a diagonal form with identical elements. Thus D reduced to a scalar in our calculations, with value $0.00012 \text{ cm}^2/\text{ms}$. This resulted in a signal conduction velocity of $22.2 \pm 3.4 \text{ cm/s}$. Furthermore, in 2D, the $I_{\text{K,ACh}}$ was considered to be constitutively active, in consonance with our results from *in vitro* experiments.⁵¹ The optogenetic tool used in the numerical studies was a mutant of Channelrhodopsin 2 (CHR2), adopted from the studies of Boyle *et al.* The parameter set used in our studies was exactly the same as that reported by Boyle *et al.*,⁵² with irradiation intensity 3.0 mW/mm^2 to qualitatively mimic the large photocurrent produced upon illuminating a neonatal rat atrial cardiomyocyte monolayer. In order to be consistent with the *in vitro* experiments, we prepared 10 different simulation domains, composed of neonatal rat atrial cardiomyocytes with 17% randomly distributed cardiac fibroblasts,⁵³ and natural cellular heterogeneity, modelled as per Majumder *et al.*⁵¹ Our statistical studies were performed by taking into consideration, the results obtained from all 10 *in silico* monolayers. In order to demonstrate phenomena such as manipulation of spiral core size and position, we designed several 'illumination' patterns, in the form of a sequence of filled circles of desired radii and projected these patterns on to each of our *in silico* monolayers. Depending on the aim of the study, we adjusted the durations for which the light was applied to the monolayer (*i.e.*, light interval), or kept shut off (*i.e.*, dark interval).

Preparation of CatCh-expressing monolayers

All animal experiments were reviewed and approved by the Animal Experiments Committee of the Leiden University Medical Center and conformed to the Guide for the Care and Use of Laboratory Animals as stated by the US National Institutes of Health. Monolayers of neonatal rat atrial cardiomyocytes expressing the depolarizing ion channel CatCh (Ca^{2+} -translocating channelrhodopsin) were established as previously described.¹⁴ Briefly, the hearts were excised from anesthetized 2-day-old Wistar rats. The atria were cut into small pieces and dissociated in a solution containing 450 U/ml collagenase type I (Worthington, Lakewood, NJ) and $18,75 \text{ Kunitz/ml}$ DNase I (Sigma-Aldrich, St. Louis, MO). The resulting cell suspension was enriched for cardiomyocytes by preplating for 120 minutes in a humidified incubator at 37°C and $5\% \text{ CO}_2$

using Primaria culture dishes (Becton Dickinson, Breda, the Netherlands). Finally, the cells were seeded on round glass coverslips (15 mm diameter; Gerhard Menzel, Braunschweig, Germany) coated with fibronectin (100 µg/ml; Sigma-Aldrich) to establish confluent monolayers. After incubation for 24 hours in an atmosphere of humidified 95% air- 5% CO₂ at 37°C, these monolayers were treated with Mitomycin-C (10 µg/ml; Sigma-Aldrich) for 2 hours to minimize proliferation of the non-cardiomyocytes. At day 4 of culture, the neonatal rat atrial cardiomyocyte monolayers were incubated for 20-24 h with CatCh-encoding lentiviral particles at a dose resulting in homogeneous transduction of nearly 100% of the cells. Next, the cultures were washed once with phosphate-buffer saline, given fresh culture medium and kept under culture conditions for 3-4 additional days.

Optical mapping and optogenetic manipulation

Optical voltage mapping was used to investigate optogenetic manipulation of spiral wave dynamics in the CatCh-expressing monolayers on day 7 of culture by using the voltage-sensitive dye di-4-ANBDQBS (52.5 µM final concentration; ITK diagnostics, Uithoorn, the Netherlands), as described previously.¹⁴ In summary, optical data were acquired using a MiCAM ULTIMA-L imaging system (SciMedia) and analyzed with BrainVision Analyzer 1101 software (Brainvision, Tokyo, Japan). CatCh was locally activated by using a patterned illumination device (Polygon400; Mightex Systems, Toronto, ON) connected to a 470-nm, high-power collimator light emitting diode (LED) source (50 W, type-H, also from Mightex Systems). The PolyLite software (Mightex), was used to control the location and movement of the areas of illumination. Before local optogenetic manipulation, reentry was induced by a light-based S1-S2 cross-field stimulation (n=18). Reentrant waves that were stable for >1 s were exposed to a circular light spot (d=3 mm) at different targeted locations within the monolayer for 200 ms at 0.3 mW/mm².

ACKNOWLEDGMENTS

This study was supported by The Netherlands Organisation for Scientific Research (Vidi grant 91714336) and the European Research Council (Starting grant 716509), both to DAP. Additional support was provided by Ammodo (to DAP and AAFdV). RM would like to thank Dr. Patrick Boyle for discussions. IF would like to thank Cindy Bart and Annemarie Kip for their assistance with the animal experiments and LV production.

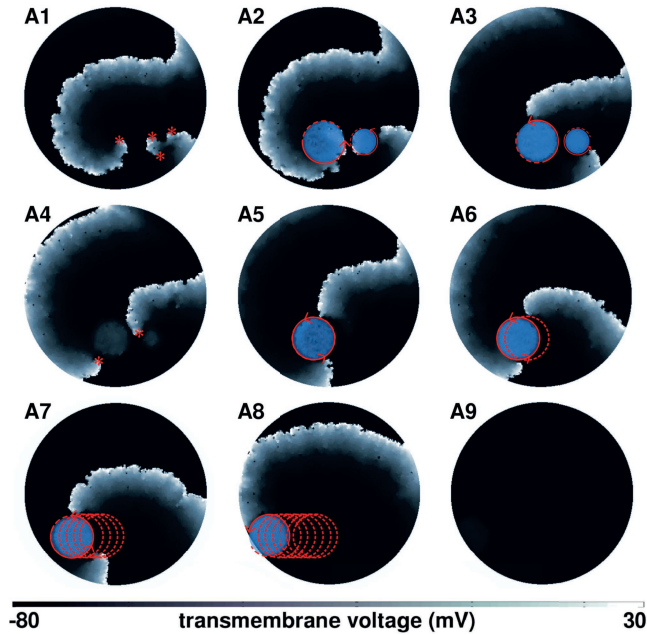
REFERENCES

1. Cross MC, Hohenberg PC. Pattern formation outside of equilibrium. *Reviews of Modern Physics*. 1993; 65:851–1112.
2. Schulman LS, Seiden PE. Percolation and galaxies. *Science*. 1986; 233:425–431.
3. Belousov BP. In: *A periodic reaction and its mechanism* Wiley, New York; 1985.
4. Zhabotinsky AM. A history of chemical oscillations and waves. *Chaos*. 1991; 1:379–86.
5. Kastberger G, Schmelzer E, Kranner I. Social waves in giant honeybees repel hornets. *PLoS ONE*. 2008; 3:e3141.
6. Caspi Y, Dekker C. Mapping out Min protein patterns in fully confined fluidic chambers. *eLife*. 2016; 5:e19271.
7. Karman TV. The Fundamentals of the Statistical Theory of Turbulence. *Journal of the Aeronautical Sciences*. 1937; 4:131–138.
8. Davidenko JM, Kent P, Chialvo DR, Michaels DC, Jalife J. Sustained vortex-like waves in normal isolated ventricular muscle. *Proc Natl Acad Sci USA*. 1990; 87:8785–8789
9. Krinsky VI. Mathematical models of cardiac arrhythmias (spiral waves). *Pharmacol Ther B*. 1978; 3:539–555.
10. Beaumont J, Davidenko N, Davidenko JM, Jalife J. Spiral Waves in Two-Dimensional Models of Ventricular Muscle: Formation of a Stationary Core. *Biophysical Journal*. 1998; 75:1–14.
11. Ermakova EA, Pertsov AM, Shnol EE. On the interaction of vortices in two-dimensional active media. *Physica D: Nonlinear Phenomena*. 1989; 40:185–195.
12. Schebesch I, Engel H. Interacting spiral waves in the oregonator model of the light-sensitive Belousov-Zhabotinskii reaction. *Physical Review E*. 1999; 60:6429–6434.
13. Steinbock O, Schutze J, Muller SC. Electric-field-induced drift and deformation of spiral waves in an excitable medium. *Physical Review Letters*. 1992; 68:248–251.
14. Steinbock O, Zykov V, Muller SC. Control of spiral-wave dynamics in active media by periodic modulation of excitability. *Nature*. 1993; 366:322–324.
15. Ke H, Zhang Z, Steinbock O. Scroll waves pinned to moving heterogeneities. *Physical Review E*. 2015; 91:032930.
16. Davidenko JM, Kent P, Jalife J. Spiral waves in normal isolated ventricular muscle. *Physica D: Nonlinear Phenomena*. 1991; 49:182–197.
17. Ripplinger CM, Krinsky VI, Nikolski VP, Elmov IR. Mechanisms of unpinning and termination of ventricular tachycardia. *Am J Physiol Heart Circ Physiol*. 2006; 291:H184–H192.
18. Nakouzi E, Totz 434 JF, Zhang Z, Steinbock O, Engel H. Hysteresis and drift of spiral waves near heterogeneities: From chemical experiments to cardiac simulations. *Phys Rev E*. 2016; 93:022203.
19. Zykov V, Bordyugov G, Lentz H, Engel H. Hysteresis phenomenon in the dynamics of spiral waves rotating around a hole. *Physica D: Nonlinear Phenomena*. 2010; 239:797 – 807.
20. Defauw A, Vandersickel N, Dawyndt P, Panilov AV. Small size ionic heterogeneities in the human heart can attract rotors. *American Journal of Physiology-Heart and Circulatory Physiology*. 2014; 307:H1456–H1468.
21. Boyden ES, Zhang F, Bamberg E, Nagel G, Deisseroth K. Millisecond-timescale, genetically targeted optical control of neural activity. *Nature Neuroscience*. 2005; 8:1263–1268.
22. Bi A, Cui J, Ma YP, Olshevskaya E, Pu M, Dizhoor AM, Pan ZH. Ectopic expression of a microbial-type rhodopsin restores visual responses in mice with photoreceptor degeneration. *Neuron*. 2006; 50:23–33.
23. Deisseroth K. Optogenetics: 10 years of microbial opsins in neuroscience. *Nature Neuroscience*. 2015; 18:1213–1225.
24. McNamara HM, Zhang H, Werley CA, Cohen AE. Optically controlled oscillators

- in an engineered bioelectric tissue. *Physical Review X*. 2016; 6:031001.
25. Arrenberg AB, Stainier DY, Baier H, Huisken J. Optogenetic control of cardiac function. *Science*. 2010; 330:971–974.
 26. Bruegmann T, Malan D, Hesse M, Beiert T, Fuegemann CJ, Fleischmann BK, Sasse P. Optogenetic control of heart muscle in vitro and in vivo. *Nature Methods*. 2010; 7:897–900.
 27. Jia Z, Valiunas V, Lu Z, Bien H, Liu H, Wang HZ, Rosati B, Brink PR, Cohen IS, Entcheva E. Stimulating cardiac muscle by light: cardiac optogenetics by cell delivery. *Circulation. Arrhythmia and Electrophysiology*. 2011; 4:753–760.
 28. Bingen BO, Engels MC, Schalijs MJ, Jangsangthong W, Neshati Z, Feola I, Ypey DL, Askar SF, Panfilov AV, Pijnappels DA, de Vries AA. Light-induced termination of spiral wave arrhythmias by optogenetic engineering of atrial cardiomyocytes. *Cardiovascular Research*. 2014; 104:194–205.
 29. Entcheva E, Bub G. All-optical control of cardiac excitation: combined high-resolution optogenetic actuation and optical mapping. *The Journal of Physiology*. 2016; 594:2503–2510.
 30. Burton RA, Klimas A, Ambrosi CM, Tomek J, Corbett A, Entcheva E, Bub G.. Optical control of excitation waves in cardiac tissue. *Nature Photonics*. 2015; 9:813–816.
 31. Feola I, Volkens L, Majumder R, Teplenin A, Schalijs MJ, Panfilov AV, de Vries AAF, Pijnappels DA. Localized Optogenetic Targeting of Rotors in Atrial Cardiomyocyte Monolayers. *Circ Arrhythm Electrophysiol*. 2017; 10:e005591.
 32. Mikhailov AS, Showalter K. Control of waves, patterns and turbulence in chemical systems. *Physics Reports*. 2006; 425:79–194.
 33. Mikhailov AS, Loskutov AY. Foundations of synergetics II: Chaos and Noise, vol. 52. Springer Science & Business Media; 2013.
 34. Sakurai T, Mihaliuk E, Chirila F, Showalter K. Design and control of wave propagation patterns in excitable media. *Science*. 2002; 296:2009–2012.
 35. Panfilov AV, Vasiev BN. Vortex initiation in a heterogeneous excitable medium. *Physica D*. 1991; 49:107–113.
 36. Rudenko AN, Panfilov AV. Drift and interaction of vortices in two-dimensional heterogeneous active medium. *Studia Biophysica*. 1983; 98:183–188.
 37. Krinsky V, Plaza F, Voignier V. Quenching a rotating vortex in an excitable medium. *Physical Review E*. 1995; 420 52:2458–2462.
 38. Guo W, Qiao C, Zhang Z, Ouyang Q, Wang H. Spontaneous suppression of spiral turbulence based on feedback strategy. *Phys Rev E*. 2010; 81(056214).
 39. Andreev KV. On the possibility of controlling the motion of spiral waves in a Two-Dimensional lattice of excitable elements with the aid of topological defects. *Technical Physics Letters*. 2005; 31:545–547.
 40. Winfree AT, Strogatz SH. Organizing centres for three-dimensional chemical waves. *Nature*. 1984; 311:611–615.
 41. Wulff C. Bifurcation theory of meandering spiral waves. In: *Nonlinear Physics of Complex Systems* Springer; 1996; 166–178.
 42. Agladze KI, Davydov VA, Mikhailov AS. Observation of a helical wave resonance in an excitable distributed medium. *JETP Lett*. 1987; 45:767–770.
 43. Biktasheva IV, Elkin YE, Biktashev VN. Resonant Drift of Spiral Waves in the Complex Ginzburg-Landau Equation. *J Biol Phys*. 1999; 25:115–127.
 44. Agladze K, Kay MW, Krinsky V, Sarvazyan N. Interaction between spiral and paced waves in cardiac tissue. *American Journal of Physiology-Heart and Circulatory Physiology*. 2007; 293:H503–H513.
 45. Nussinovitch U, Gepstein L. Optogenetics for in vivo cardiac pacing and resynchronization therapies. *Nat Biotechnol*. 2015; 33:750-4.
 46. Crocini C, Ferrantini C, Coppini R, Scardigli M, Yan P, Loew LM, Smith G, Cerbai E, Poggesi C, Pavone FS, Sacconi L. Optogenetics design of mechanically-based stimulation patterns for cardiac defibrillation. *Sci Rep*. 2016; 6:35628.

47. Nyns EC, Kip A, Bart CI, Plomp JJ, Zeppenfeld K, Schalij MJ, de Vries AA, Pijnappels DA. Optogenetic termination of ventricular arrhythmias in the whole heart: towards biological cardiac rhythm management. *Eur Heart J*. 2017; 38:2132–2136.
48. Bruegmann T, Beiert T, Vogt CC, Schrickel JW, Sasse P. Optogenetic termination of atrial fibrillation in mice. *Cardiovascular Research*. 2018; 114:713–723.
49. Boyle PM, Karathanos TV, Trayanova NA. 2018. Cardiac optogenetics. *JACC: Clinical Electrophysiology*. 2018; 4:155–167.
50. Bruegmann T, Boyle PM, Vogt CC, Karathanos TV, Arevalo HJ, Fleischmann BK, Trayanova NA, Sasse P. Optogenetic defibrillation terminates ventricular arrhythmia in mouse hearts and human simulations. *J Clin Invest*. 2016; 126:3894–904.
51. Majumder R, Jangsangthong W, Feola I, Ypey DL, Pijnappels DA, Panilov AV. A Mathematical Model of Neonatal Rat Atrial Monolayers with Constitutively Active Acetylcholine-Mediated K⁺ Current. *PLoS Comp Biol*. 2016; 12:e1004946.
52. Boyle PM, Williams JC, Ambrosi CM, Entcheva E, Trayanova NA. A comprehensive multiscale framework for simulating optogenetics in the heart. *Nat Commun*. 2013; 4.
53. MacCannell KA, Bazzazi H, Chilton L, Shibukawa Y, Clark RB, Giles WR. A mathematical model of electrotonic interactions between ventricular myocytes and fibroblasts. *Biophys J*. 2007; 92:4121–32.

SUPPLEMENTAL MATERIAL



4

Figure S1. AAD control of spiral wave cores to accomplish termination of a complex figure-of-eight type reentry, where the constituting spirals rotate slightly out of phase with each other. A1, Positions of phase singularities of the initial reentrant pattern are marked with red asterisks. A2, Phase correction of spirals by anchoring to light spots of different sizes. A3-5, Formation of a single multi-arm spiral. A6-9, Dragging the multi-arm spiral to termination. In each frame, the current position of the light spot is marked with a filled blue circle. The approximate trajectory of the dragged reentrant pattern is shown with dashed red lines.

Movies

Image processing for *in vitro* movie A: Optical voltage signal was processed with spatial and temporal derivative filters to allow visualization of electrical wave propagation during the application of the light spots.

Image processing for *in vitro* movie B: The data were sampled according to the location of the applied light spot. Next, for each sample set, we obtained the lowest background intensity recorded by the individual pixels over time and constructed a two-dimensional array with these values as elements. Next, we subtracted this array from each frame in the sample set and reassembled the processed datasets to make a complete movie.

Movie S1: Use of AAD control method to drag a spiral wave core along a triangular trajectory *in silico* and *in vitro*. *In vitro* A movie emphasizes the shape of the wavefront. *In vitro* B movie

shows the same data, but processed to show more clearly, what happens during the application of the light spots.

Movie S2: Use of AAD control method to drag a spiral wave core to termination *in silico* and *in vitro*. *In vitro* A movie emphasizes the shape of the wavefront. *In vitro* B movie shows the same data, but processed to show more clearly, what happens during the application of the light spots.

Movie S3: Use of AAD control method to terminate figure-of-eight type of reentry *in silico* and *in vitro*. *In vitro* A movie emphasizes the shape of the wavefront. *In vitro* B movie shows the same data, but processed to show more clearly, what happens during the application of the light spot.

4

Movie S4: Use of AAD control method to terminate complex reentry *in silico*, with 3 (left) and 4 (right) spiral waves.

Movie S5: Use of AAD control method to terminate complex reentry (4 spiral waves) *in vitro*. This movie was obtained with the methodology described above for *in vitro* movie A.





Chapter

OPTOGENETIC MANIPULATION OF ANATOMICAL REENTRY BY LIGHT-GUIDED GENERATION OF A REVERSIBLE LOCAL CONDUCTION BLOCK

Masaya Watanabe*, MD, PhD; Iolanda Feola*, MSc;
Rupamanjari Majumder, PhD; Wanchana Jangsangthong, PhD;
Alexander S. Teplenin, MSc; Dirk L. Ypey, PhD;
Martin J. SchaliJ, MD, PhD; Katja Zeppenfeld, MD, PhD;
Antoine A. F. de Vries, PhD; Daniël A. Pijnappels, PhD

Laboratory of Experimental Cardiology, Department of Cardiology, Heart
Lung Center Leiden; Leiden University Medical Center, the Netherlands.

*equal contribution

5

ABSTRACT

Aims

Anatomical reentry is an important mechanism of ventricular tachycardia, characterized by circular electrical propagation in a fixed pathway. Its current investigative and therapeutic approaches are non-biological, rather unspecific (drugs), traumatizing (electrical shocks) or irreversible (ablation). Optogenetics is a new biological technique that allows reversible modulation of electrical function with unmatched spatiotemporal precision using light-gated ion channels. We therefore investigated optogenetic manipulation of anatomical reentry in ventricular cardiac tissue.

Methods and Results

5 Transverse, 150- μm -thick ventricular slices, obtained from neonatal rat hearts, were genetically modified with lentiviral vectors encoding Ca^{2+} -translocating channelrhodopsin (CatCh), a light-gated depolarizing ion channel, or yellow fluorescent protein (eYFP) as control. Stable anatomical reentry was induced in both experimental groups. Activation of CatCh was precisely controlled by 470-nm patterned illumination, while the effects on anatomical reentry were studied by optical voltage mapping. Regional illumination in the pathway of anatomical reentry resulted in termination of arrhythmic activity only in CatCh-expressing slices by establishing a local and reversible, depolarization-induced conduction block in the illuminated area. Systematic adjustment of the size of the light-exposed area in the reentrant pathway revealed that reentry could be terminated by either wave collision or extinction, depending on the depth (transmurality) of illumination. *In silico* studies implicated source-sink mismatches at the site of subtransmural conduction block as an important factor in reentry termination.

Conclusions

Anatomical reentry in ventricular tissue can be manipulated by optogenetic induction of a local and reversible conduction block in the reentrant pathway, allowing effective reentry termination. These results provide distinctively new mechanistic insight into reentry termination and a novel perspective for cardiac arrhythmia management.

Key Words

Optogenetics, anatomical reentry, tissue culture, optical mapping, computer-based model.

INTRODUCTION

Anatomical reentry represents a common mechanism of heart rhythm disturbances (e.g. ventricular tachyarrhythmias) in structurally damaged myocardium.¹⁻³ Current approaches to investigate, prevent or terminate this reentrant activity rely on (i) global modulation of cardiac electrical function by drug and electrical shock application, or (ii) local modulation of cardiac electrical activity by introducing a permanent conduction block in the pathway of aberrant propagation through local tissue ablation. In general, however, these three approaches are characterized by their relative unspecific, traumatizing and/or irreversible nature, but also by their limited extent to control cardiac electrical function in time and space.⁴⁻⁶ In the past few years, optogenetics has emerged as a unique approach to modulate biological function by combining forced expression of light-sensitive proteins with light-emitting diode (LED) technology for tailored activation of these proteins.^{7, 8} While first introduced in the field of neuroscience, optogenetics is now also proving its potential in cardiac research, especially in cardiac electrophysiological studies. Here, light-gated ion channels are used to modulate cardiac excitability through generation of de- or hyperpolarizing photocurrents in cardiac muscle cells.⁹⁻¹³ In two recent studies, the depolarizing optogenetic tool, ChR2(H143R), was used to terminate ventricular arrhythmias in whole murine hearts. These studies, however, address a different research question with another optogenetic tool than ours and come with rather descriptive insight regarding the underlying anti-arrhythmic mechanisms. In the present study we make use of the controllability that *in situ* models offer to create a model of rat ventricular tachyarrhythmias in which these disturbances are solely based on predefined anatomical reentry. This allowed us to conduct more systematic and detailed studies into the underlying anti-arrhythmic mechanisms of optogenetic interventions. They relied on computer simulations to suggest that Na⁺ channel inactivation based on ChR2-dependent depolarization may be involved in the underlying anti-arrhythmic mechanism. In contrast to other, more conventional approaches, optogenetic control of the electrophysiological properties of cardiomyocytes does allow highly specific and fully reversible modulation of cardiac electrical function with unmatched precision. This is especially true if the light-gated ion channels are activated by programmed patterned illumination, as this will allow superb control of cardiac electrical function in space.¹⁴⁻¹⁷ Given the unique research possibilities offered by optogenetics in combination with patterned illumination and its unexplored effects on anatomical reentrant tachyarrhythmias, we were now interested to determine whether and how optogenetic control of electrical function in the pathway of anatomical reentry could be used to manipulate and terminate anatomical reentrant activity in ventricular cardiac tissue. Cultured rat transverse myocardial tissue slices were used to create a standardized and robust *in situ* model of anatomical reentry, in which the L123C mutant of channelrhodopsin-2 (ChR2) from *Chlamydomonas reinhardtii*, designated Ca²⁺-translocating channelrhodopsin (CatCh), was expressed from a lentiviral vector (LV) and subsequently activated by patterned illumination with 470 nm light. CatCh is more rapidly activated, produces a stronger steady-state current and is approximately 70-fold more sensitive to light stimulation than wild-type ChR2.¹⁸ This distinctive biological approach allowed us

to generate a light-guided, depolarization-induced local conduction block, the presence of which could be tightly controlled in time and space, in any desired area of the tissue slices. This study is the first to demonstrate that such optogenetic manipulation in the pathway of anatomical reentry could terminate the arrhythmic activity, thereby revealing a new mechanism of anatomical reentry termination based on precise, transient and non-destructive modulation of electrical function, *i.e.* without drugs, electrical shocks or tissue damage.

MATERIALS AND METHODS

A detailed description of materials and methods can be found in the Supplementary Material online. All animal experiments were approved by the Animal Experiments Committee of Leiden University Medical Center (LUMC) and done in accordance with the Guide for Care and Use of Laboratory Animals as stated by the US National Institutes of Health.

5

Preparation of transverse rat ventricular tissue slices

After perfusion of the hearts of neonatal Wistar rats with oxygenated phosphate-buffered saline (PBS) containing 10 IU/ml heparin, transverse ventricular tissue slices 150- μ m thick were obtained using a vibratome (VT1200S, Leica Microsystems, Rijswijk, the Netherlands). The slices were kept under culture conditions at 37°C in humidified 95% air-5% CO₂ for 4 days.

Lentiviral gene transfer

The cardiac tissue slices were genetically modified at the day of production by adding concentrated viral vector suspension directly on top of the slices and into the medium under the semi-porous membrane in the presence of 10 μ g/ml diethylaminoethyl-dextran (Carl Roth, Karlsruhe, Germany).

Patch clamp

Patch clamp recordings were performed using an inverted microscope Zeiss Axiovert 35 (Carl Zeiss, Oberkochen, Germany) with an integrated LED-based 470-nm light illumination device (M470L3 collimated LED; Munich, Germany). Patch clamp equipment consisted of a MultiClamp 700B amplifier and a Digidata 1440A A/D converter controlled by commercially available MultiClamp 700B Commander and Clampex v10.3 software (Molecular Devices, Sunnyvale, CA). Perforated patch clamp recordings in current- and voltage-mode were obtained from single neonatal rat ventricular cardiomyocytes expressing CatCh (CatCh-NRVCs)

Integrated system for optical mapping and patterned illumination

The optical mapping system was engineered by integration of a patterned illumination device, the Polygon400 (Mightex Systems, Toronto, ON) to allow recording of electrical activation with the voltage-sensitive dye Di-4-ANEPPS (Life Technologies Europe, Bleiswijk, the Netherlands) and patterned illumination with blue light (470 nm), (Figure S1C). Slices were stimulated either electrically with an epoxy-coated unipolar platinum electrode (FHC, Bowdoin, ME) using

2-ms rectangular pulses of 1.5 V or optically with 10-ms/470-nm light pulses (0.68 mW/mm²), coming from the Polygon400. Reentry was induced by electrical pacing using S1-S2 electrical protocol. After confirmation of the presence of reentrant conduction, slices were exposed to 470-nm LED light for 500 ms using the patterned illumination device.

Numerical Methods

The NRVCs were modeled according to the formulation of Korhonen *et al.*,¹⁹ with adaptations by Hou *et al.*²⁰ The complex intracellular Ca²⁺ diffusion between the sarcolemma and the perinuclear sarcoplasmic reticulum was replaced by a simple Ca²⁺-handling process adopted from tenTusscher *et al.*²¹ Cardiac myofibroblasts were modeled according to the passive formulation of MacCannell *et al.*,²² whereas the empirically derived model of ChR2 (current-enhanced mutant H134R) by Williams *et al.*²³ was used together with the parameter set established by Boyle *et al.*²⁴ to implement optogenetics. Eight confluent monolayer stripes (12.75 × 2.8 mm) were constructed as arrays of 1145 cell sites with 17% myofibroblasts. Each stripe was electrically paced from one side, at a CL of 500 ms, with a 2-ms current stimulus of 100 pA. Wave propagation was then studied in the stripes in the presence of virtual irradiation over a rectangular area 600 μm × 25% or 75% of the transmural width (2.8 mm).

Statistical analysis

Data were expressed as mean ± standard deviation. Comparison between 2 groups was performed with Student's t-test for continuous variables and with the X² test for categorical variables. When data were analyzed across more than 2 variables, analysis of variance (ANOVA) was used. Parameters before and after reentry termination were compared using paired t-tests. To take into account both the number of slices and the number of animals, mixed model of analysis was also performed, when applicable. Differences were considered statistically significant at P<0.05. Statistical analyses were performed with SPSS11.0 for Windows (SPSS, Chicago, IL) and JMP pro 12 for Windows (SAS, Cary, NC).

RESULTS

Electrophysiological effects of CatCh activation

To study the electrophysiological effects of light-mediated CatCh activation, perforated patch clamp experiments were performed on single CatCh-NRVCs. In a previous study from our research group, a 500-ms/470-nm light pulse sufficed to characterize the kinetics of the CatCh-generated photocurrent in atrial cardiomyocytes.²⁵ For this reason, CatCh-NRVCs were exposed to 500-ms blue light pulses in combination with different light intensities to determine the minimum light intensity required to evoke an action potential (AP) and generate a stable voltage plateau during the repolarization phase, *i.e.* prolonged depolarization (Figure S2A). Plotting the mean voltage shift at the end of the 500-ms light pulse against light intensity (n=5 for each condition; Figure S2B) revealed that the prolonged depolarization was characterized by voltage shifts from resting potential of 17.7±20.8 mV for a light intensity of 0.03 mW/mm² to

65.5±4.2 mV for a light intensity of 2.6 mW/mm². Since the maximum voltage shift was already reached at light intensity of 0.65 mW/mm², this light intensity was applied for 5, 50, 500 or 5000 ms to stimulate CatCh-NRVCs. As shown in Figure 1B, the duration of the plateau phase was determined by the duration of the light pulses. Voltage-clamp recordings demonstrated that illumination with 470-nm light for 500 ms induced typical CatCh inward currents at negative holding potential of -40 mV (n=7) (Figure 1C). Peak (I_{pk}) and steady-state (I_{ss}) CatCh photocurrents were 37.9±9.0 and 25.5±5.9 pA/pF, respectively. Moreover, CatCh partially desensitized with a time constant (t_{des}) of 447.6±109.1 ms as determined by a single-exponential fit to the current decay after the peak (Figure 1C). The channel closing time constant (t_{off}), determined by a two-component exponential fit to the current decay after illumination (Figure 1C), was 103.1±26.7 and 965.9±304.8 ms for fast and slow components, respectively. These findings confirmed the presence of a CatCh-generated photocurrent and proof its potential to keep CatCh-NRVCs in a depolarized state.

5

Histological characterization of cardiac tissue slices

Micrographic analyses of transverse neonatal rat ventricular tissue slices revealed that after transduction with the CatCh-encoding LV (CatCh↑ group) or the enhanced yellow fluorescent protein (eYFP)-encoding control vector (eYFP↑ group) (for vector maps, Figure 1A) and 4 days of culture, these slices maintained their gross anatomy, including the presence of both the left and right ventricular lumen (Figure 1D, left panel). In addition, the tissue slices showed the abundant presence of nuclei in a homogenous distribution pattern and, importantly, global transgene expression (Figure 1D, middle and right panel, respectively). Due to the use of the striated muscle-specific MHCK7 promoter, transgene expression was only observed in α -actinin⁺ cells (*i.e.*, cardiomyocytes). Of the cardiomyocytes, 63±13% expressed CatCh, which was mainly localized at the sarcolemma (Figure 1E and F). Immunohistological analysis for sarcomeric α -actinin showed a typical cross-striated expression pattern in both groups, indicating preservation of sarcomeric organization (Figure S3A). Moreover, the gap junction protein connexin43 (Cx43) and the fibroblast marker collagen type 1 (Col1) showed the characteristic staining patterns for these proteins in both the CatCh↑ and eYFP↑ group (Figure S3B and S3C). Immunostaining for cleaved caspase-3 demonstrated lack of apoptotic activity in the large majority of cells (Figure S3D). Cell viability was also investigated by Mitotracker staining for active mitochondria, which showed intense and uniform labeling (Figure S3E).

Electrophysiological characterization of cardiac tissue slices

To investigate their basic electrophysiological properties, such as action potential duration at 80% repolarization (APD_{80}) and conduction velocity (CV), slices were loaded with the voltage-sensitive dye Di-4-ANEPPS and subjected to high-resolution optical mapping while being electrically stimulated at 1-9 Hz. In this study, optical voltage mapping was performed with Di-4-ANEPPS mapping instead of Di-4-ANBDQBS because of a better signal-to-noise ratio and a lack of significant adverse electrophysiological effects (Figure S4). Neither the eYFP↑ slices

Optogenetic termination of anatomical reentry

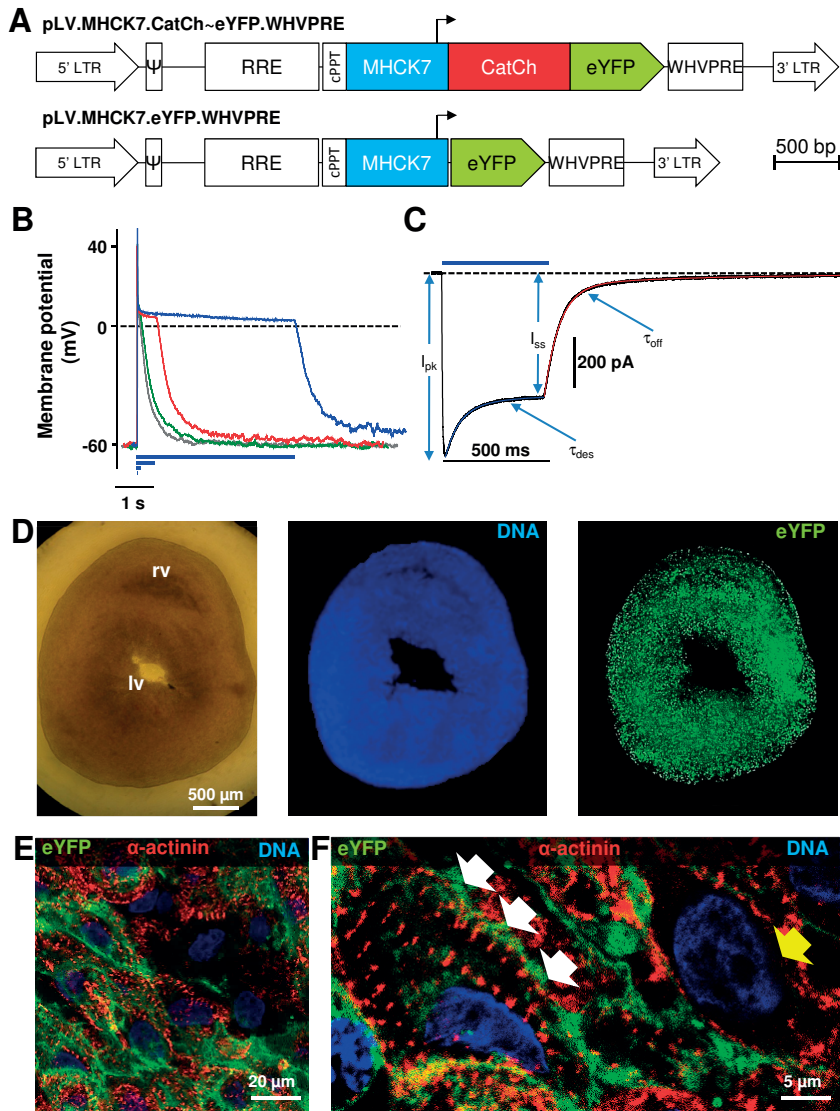


Figure 1. Characterization of CatCh-photocurrent. **A**, Structure of LV shuttle plasmids pLV.MHCK7.CatCh~eYFP.WHVPRE (for generating LV.CatCh~eYFP[↑]) and pLV.MHCK7.eYFP.WHVPRE (to produce LV.eYFP[↑]). 5' LTR: chimeric 5' long terminal repeat containing enhancer and promoter elements of the human cytomegalovirus immediate-early gene and the human immunodeficiency virus type 1 (HIV1) R and U5 regions. Ψ: HIV1 packaging signal. RRE: HIV1 Rev-responsive element. cPPT: HIV1 central polypurine tract and termination site. MHCK7: chimeric striated muscle-specific promoter. CatCh: coding sequence of mutant of the light-gated ion channel Chr2. eYFP: Aequorea victoria enhanced yellow fluorescent protein-coding sequence. WHVPRE: woodchuck hepatitis virus post-transcriptional regulatory element. 3' LTR: wild-type 3' HIV1 LTR. **B**, Representative membrane potential recordings of CatCh-NRVCs upon blue light stimulation at 0.65 mW/mm² for 5, 50, 500 and 5000 ms (n=5). **C**, Typical inward photocurrent evoked at a holding potential of -40 mV by exposure of a CatCh-NRVC to a 500-ms blue light pulse at 0.65 mW/mm² irradiance. **D**, Microscopic images of a slice after transduction with LV.CatCh~eYFP[↑] and 4 days

5

► of culture. Left panel, brightfield image, middle panel, fluoromicrograph showing Hoechst 33342-stained nuclei, right panel, fluorescent micrograph showing CatCh~eYFP expression. (E and F) High magnification images showing CatCh expression at the sarcolemma of α -actinin⁺ cells (*i.e.*, cardiomyocytes; white arrows). As transgene expression was driven by the striated muscle-specific MHCK7 promoter, CatCh was not expressed in α -actinin⁻ cells (yellow arrow) (n=3 slices, 3 rats). lv, left ventricle. rv, right ventricle. bp, base pairs.

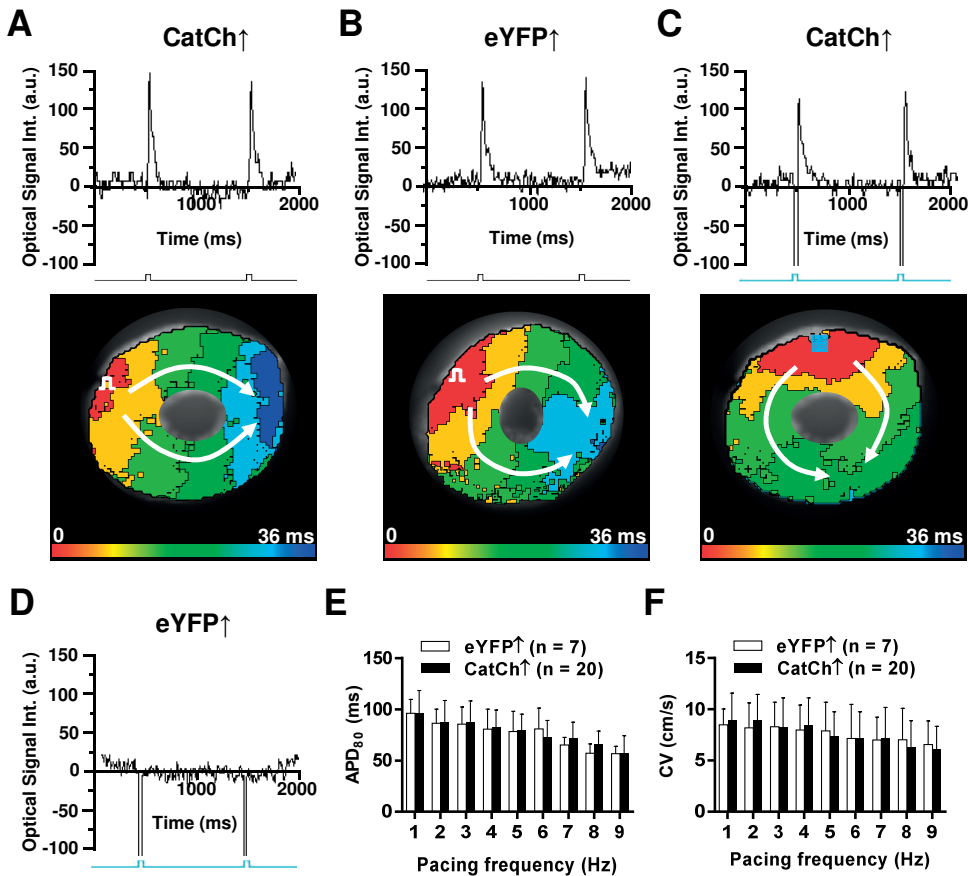


Figure 2. Electrophysiological characteristics of cultured ventricular slices. A and B, Representative optical traces (top) and activation maps (bottom) of CatCh[↑] (A) and eYFP[↑] (B) slice during 1-Hz electrical stimulation. C, Representative optical trace (top) and activation map (bottom) of CatCh[↑] slice following local 10-ms exposure to blue light of 470 nm. D, Typical example of the optical trace resulting from local 10-ms exposure of an eYFP[↑] slice to blue light of 470 nm. E and F, CatCh[↑] (n=20 slices, 9 rats) and eYFP[↑] (n=7 slices, 4 rats) slices display similar APD₈₀ (E) and CV (F) values during electrical stimulation at different pacing frequencies with higher pacing frequencies resulting in shorter APDs and slower conduction by two-way ANOVA. Of note, random effects model also showed no difference between CatCh[↑] and eYFP[↑] slices.

(n=7) nor the CatCh \uparrow slices (n=20) showed spontaneous activity. However, electrical point stimulation evoked APs in all slices in both groups and resulted in bidirectional propagation of the electrical wavefront around the left ventricular lumen followed by its annihilation at the collision site (Figure 2A and 2B). At a pacing frequency of 1 Hz, no significant differences were observed in APD₈₀ or CV between CatCh \uparrow and eYFP \uparrow slices; APD₈₀ was 96 \pm 13 ms vs 96 \pm 22 ms (P=0.43), and CV was 8.9 \pm 2.7 vs 8.4 \pm 1.6cm/s (P=0.99), respectively. As pacing frequency increased from 1 to 9 Hz, the values of these parameters gradually decreased in a similar fashion for both groups (Figure 2E and 2F). From these data, we concluded that there are no major differences in excitability, gap junctional coupling and restitution properties between the CatCh \uparrow and eYFP \uparrow groups. To investigate whether transduction of cardiac tissue slices with CatCh-encoding LV particles resulted in light-gated ion channel activity, these slices were exposed, by patterned illumination, to brief light pulses (10-ms; 470-nm) targeting a 300- μ m square area near the tissue border. As anticipated, APs could be readily evoked by 470-nm light exposure of the CatCh \uparrow slices while optical stimulation of the eYFP \uparrow slices did not produce APs (Figure 2C and 2D). Consistently, following blue light exposure only the CatCh \uparrow slices showed contractions. Together these results indicate that transverse ventricular tissue slices can be derived from neonatal rat hearts and kept in culture for at least 4 days without losing the key anatomical properties and the capability to generate and propagate electrical signals. This culture period suffices to optogenetically modify the cardiac tissue slices with LVs encoding a light-gated depolarizing ion channel, thereby allowing optical control of excitability in these slices.

5

Induction and characterization of anatomical reentry

In order to test the effects of optogenetic manipulation on anatomical reentry, such arrhythmic activity was induced in the cardiac tissue slices by dedicated electrical stimulation according to the so-called extra stimulus S1-S2 protocol.²⁶ The bifurcated wavefront of each S1 stimulus propagated around the left ventricular lumen of the slice and its two parts finally collided at the end of the slice opposite of the pacing electrode (Figure 3A, left activation map). The subsequent S2 stimulus was given at a progressively shorter time interval until unidirectional S2 propagation occurred and reentry was initiated (Figure 3A, middle activation map and right panel of optical records). Typically, reentry was pinned to the left ventricular lumen with activation of the right ventricle following each reentrant cycle (Figure 3A, right activation map). The S1-S2 protocol resulted in sustained reentry in 86% (6 out of 7) and 85% (40 out of 47) of the eYFP \uparrow and CatCh \uparrow slices, respectively (P=0.97, Figure 3B). No significant differences were observed in reentry CL (120 \pm 42 vs 110 \pm 20 ms, P=0.33, Figure 3C), APD₈₀ (56 \pm 14 vs 57 \pm 11 ms, P=0.72, Figure 3D) and CV (3.7 \pm 0.8 vs 4.4 \pm 1.3 cm/s, P=0.23, Figure 3E) between both groups, which suggests that the optogenetic modification itself did not affect either reentry inducibility or key properties of the resulting tachyarrhythmia.

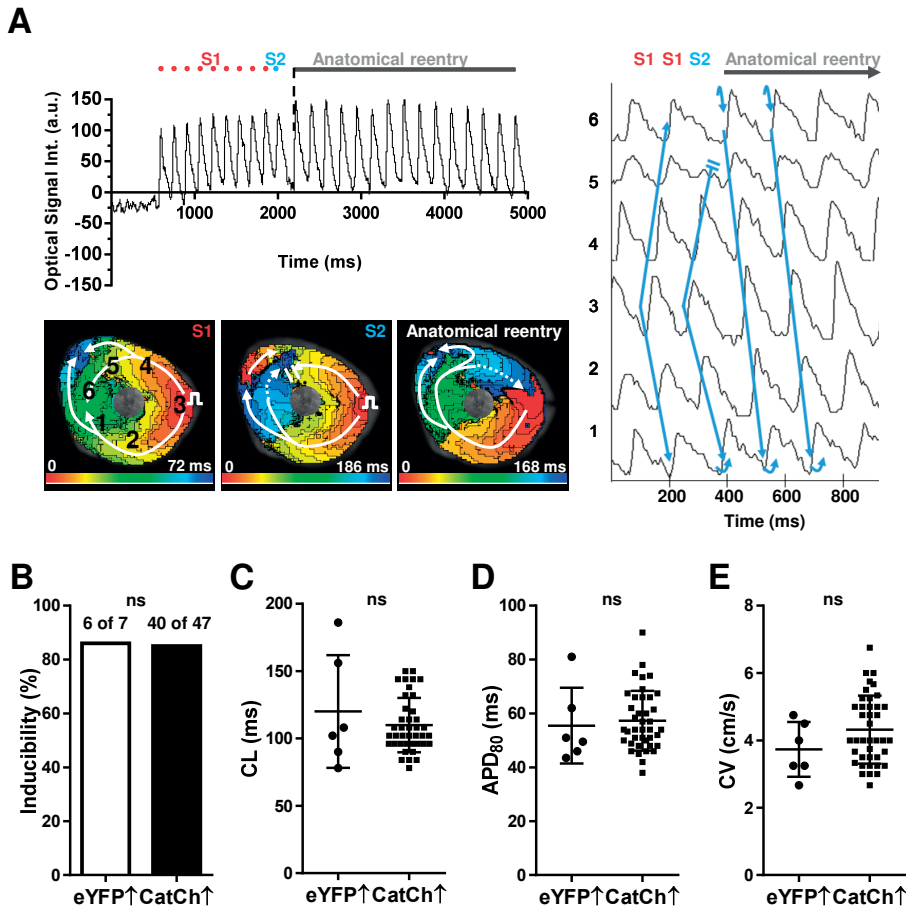


Figure 3. Induction and characterization of anatomical reentry. A, Representative optical trace (left, top) and activation maps (left, bottom) of a CatCh \uparrow slice subjected to S1-S2 electrical stimulation to induce anatomical reentry. The right panel shows enlarged optical traces derived from positions 1 through 6 in the slice at the moment in which anatomical reentry is established. No significant difference was observed in anatomical reentry inducibility (B) between eYFP \uparrow ($n=7$ slices from 4 rats) and CatCh \uparrow ($n=47$ slices from 13 rats) by χ^2 test, nor in the CL (C), APD₈₀ (D) and CV (E) during reentry between groups (6 slices from 4 rats in eYFP \uparrow and 40 slices from 13 rats in CatCh \uparrow) by both student t-test and random effects models.

Effects of global illumination on anatomical reentry

Before testing the effects of illuminating only a local area in the pathway of aberrant conduction (see below), the effects of global illumination on ongoing anatomical reentry were assessed. After the presence of reentry was confirmed by optical mapping, the entire area of the slices was exposed to 470-nm light for a duration of 500 ms, based on CatCh t_{des} (Figure 4A and 4B). Such global illumination terminated reentry in all CatCh \uparrow slices ($n=23$), but none of the eYFP \uparrow slices ($n=6$) ($P<0.01$) (Figure 4C).

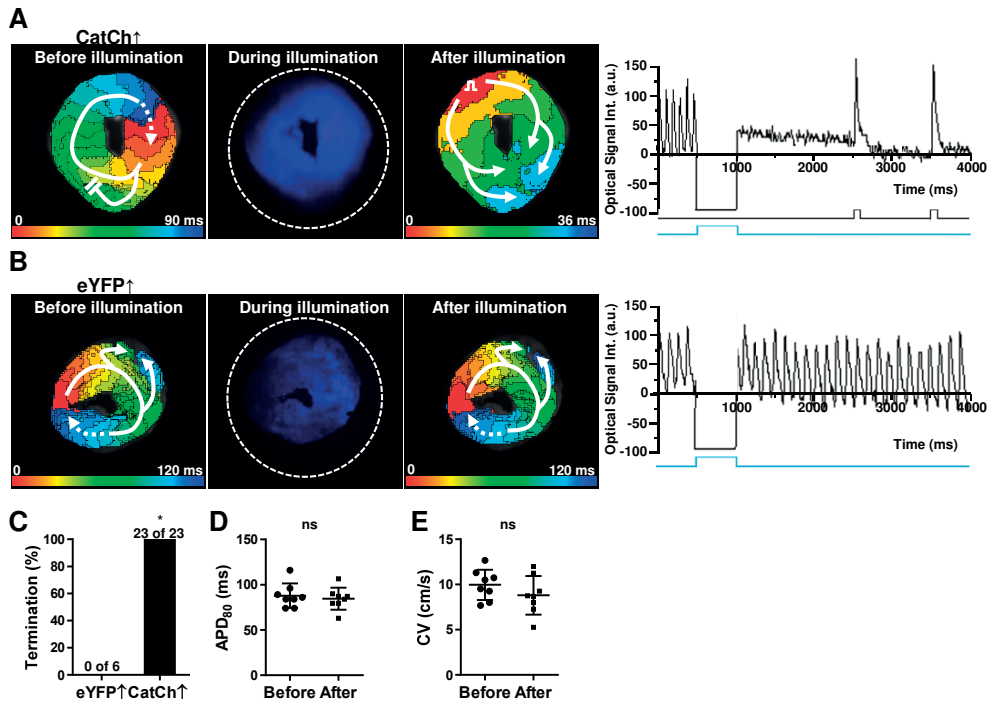


Figure 4. Effects of global illumination on anatomical reentry. A and B, Representative activation maps before and after 500-ms exposure to 470-nm light (left, first and third panels), screen shots taken during the illumination period (left, middle panel) and corresponding optical traces (right) of CatCh \uparrow and eYFP \uparrow slices, respectively. CatCh \uparrow slices showed uniform AP propagation when electrically stimulated at 1 Hz at 1.5 s after illumination (A). Global 470-nm light exposure of eYFP \uparrow slices did not affect reentrant activity (B). C, Incidence of successful anatomical reentry termination in CatCh \uparrow (n=23 slices from 8 rats) and eYFP \uparrow (n=6 slices from 4 rats) slices. Statistical comparison was made using χ^2 test. * $P < 0.001$. No differences were observed in APD₈₀ (D) and CV (E) during electrical stimulation at 1 Hz of CatCh \uparrow slices (n=8 slices from 2 rats) before and after reentry termination using both paired t-test and mixed effect model analysis.

To investigate potential aftereffects of the optogenetic intervention on key electrophysiological properties of the cardiac tissue slices, 1-Hz electrical stimuli were given 1.5 s after global illumination of the CatCh \uparrow slices (n=8) (Figure 4A, right). The APs evoked before and after illumination did not display significant differences in APD₈₀ (87 ± 14 vs 84 ± 12 ms, $P = 0.55$) or CV (10.0 ± 1.7 vs 8.8 ± 2.1 cm/s, $P = 0.13$) (Figure 4D and 4E). These results indicate that anatomical reentry in these cardiac slices could be terminated effectively by global transient light-induced activation of CatCh without compromising subsequent normal electrical activation.

Termination of anatomical reentry by local illumination

Next, the effect of programmed regional illumination of the CatCh \uparrow slices, and therefore local generation of a depolarizing photocurrent, on sustained anatomical reentry was investigated.

First, an area spanning the entire thickness of the myocardium (fully transmural) and 300 or 600 μm in width was illuminated for 500 ms using the patterned illumination device (Figure 5A and 5B). This local activation of CatCh in the pathway of reentrant conduction resulted in 57% (8 out of 14) and 100% (14 out of 14, $P < 0.01$) arrhythmia termination, respectively (Figure 5C). In all cases, arrhythmic activity was terminated by collision of the reentrant wave into the area of CatCh activation-induced temporary conduction block. Of note, in the six cases in which reentry was not terminated, the reentrant CL increased during illumination (Figure 5D). Importantly, re-induction of reentry in 4 of the preparations followed by local illumination of 3 other areas divided over the left ventricular wall again resulted in arrhythmia termination, indicating that this was not a local phenomenon. These data show that not only global illumination but also predefined regional illumination of only a small area of the pathway of reentrant conduction leads to termination of anatomical reentry in optogenetically modified cardiac tissue slices. Activation of CatCh by local transmural illumination resulted in acute generation of a regional and temporary conduction block in which the reentrant wavefront collided, thereby interrupting the reentrant pathway and causing termination of the arrhythmia. After having shown the effects on anatomical reentry of a reversible conduction block spanning the full transmural thickness of a cardiac tissue slice, the anti-arrhythmic potential of subtransmural illumination was investigated. We hypothesized that subtransmural illumination would cause local narrowing of the pathway of reentrant wave conduction, thereby creating a so-called isthmus (Figure 6A and 6B).

The width of the illuminated area was fixed at 600 μm , while its transmurality (*i.e.* depth) was gradually increased from $\frac{1}{4}$, $\frac{1}{2}$, $\frac{3}{4}$ till 1 (*i.e.* full transmural) resulting in a systematic narrowing of the isthmus until it was no longer present. As shown in Figure 6C, reentry could be terminated in all 4 situations but the success rate of termination increased from 2 (10%), 5 (24%), 9 (43%) to 21 (100%) out of 21 slices with an increase in transmurality of illumination from $\frac{1}{4}$, $\frac{1}{2}$, $\frac{3}{4}$ to 1, respectively.

Analysis of the dynamics of the reentrant wavefront during illumination showed that in cases of failed arrhythmia termination, the wavefront passed through the isthmus, thereby allowing reentry to continue (Figure 6A).

Of note, the CLs of the reentrant circuits that could not be terminated increased during illumination (Figure 6D), indicating that optogenetic manipulation of anatomical reentry could also slow down the ongoing reentrant tachyarrhythmia. In case of termination, however, the wavefront entered the isthmus and faded away (*i.e.* wave extinction), while the remainder of the wavefront collided directly into the light-induced conduction block (Figure 6B). Reentry termination occurred at the site of illumination with the exception of two cases (Figure 6E), in which conduction became slower after passing the illuminated area and eventually stopped, thereby still resulting in arrhythmia termination. Together these results demonstrate that light-guided generation of a local and reversible conduction block, which is only partially obstructing the pathway of reentrant conduction, may result in arrhythmia termination. Whether the temporary isthmus between the ventricular lumen and the area of reversible conduction block allowed conduction of reentrant waves depended on its width. By narrowing

Optogenetic termination of anatomical reentry

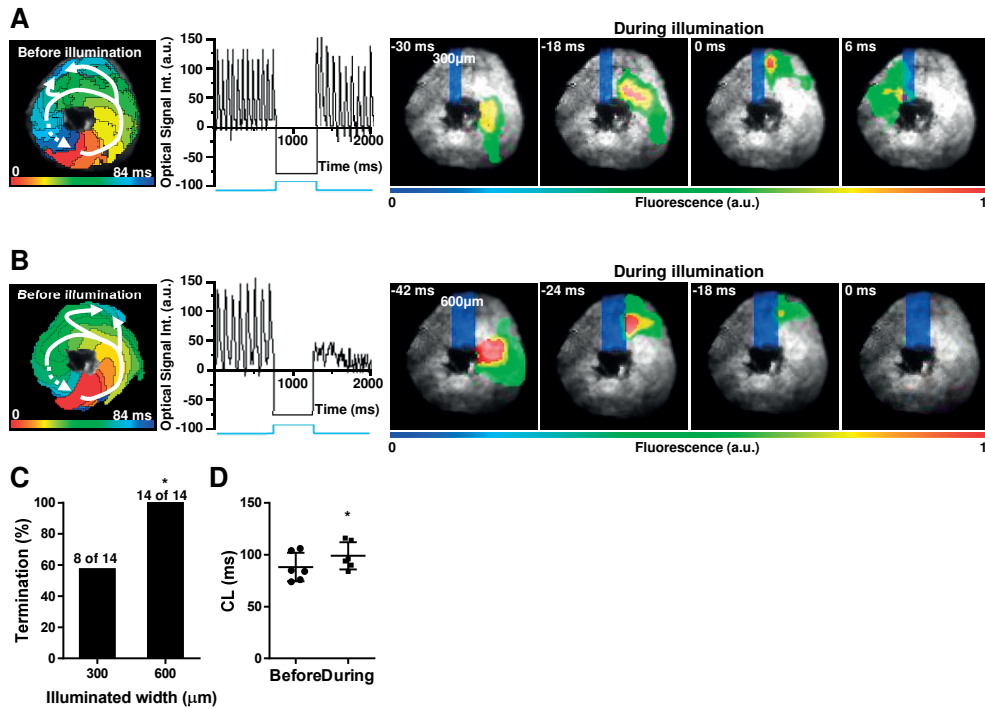


Figure 5. Reentry termination by local transmural illumination of CatCh⁺ slices. **A** and **B**, Typical activation maps confirming the presence of anatomical reentry before 500-ms exposure to 470-nm light (left), traces showing the optical signal before and after illumination (middle) and wave propagation during light exposure (right four panels). Example of a reentrant activation wavefront passing through a light-exposed transmural area 300 μm in width (**A**). Example of successful reentry termination when the width of the light-exposed transmural area is increased to 600 μm (**B**). **C**, The success rate of light-induced anatomical reentry termination depends on the width of the illumination area. Statistical comparison was made using χ^2 test. * $P < 0.01$ ($n = 14$ slices from 5 rats). **D**, Passage of reentrant circuits through the 300-μm wide transmural illuminated area slightly but significantly increased their CL. * $P < 0.05$ using both paired t -test and mixed effect model analysis ($n = 6$ slices from 4 rats).

this isthmus via deeper transmural illumination, reentrant conduction more often faded away causing arrhythmia termination. These findings suggest that a so-called electrical source-sink mismatch at the temporary isthmus could play an important role in the mechanism of reentry termination. In other words, narrowing the isthmus would lead to an increase in source-sink mismatch and thereby raise the chance of AP propagation failure at the isthmus.

In silico studies into the mechanisms underlying block of propagation

To study the role of electrical source-sink relationships in block of AP propagation caused by local subtransmural illumination, computer simulations were performed. If mismatches between source and sink play an important role, their functional modulation (from mismatch to match and vice versa) should change the experimental outcome (from continued propagation

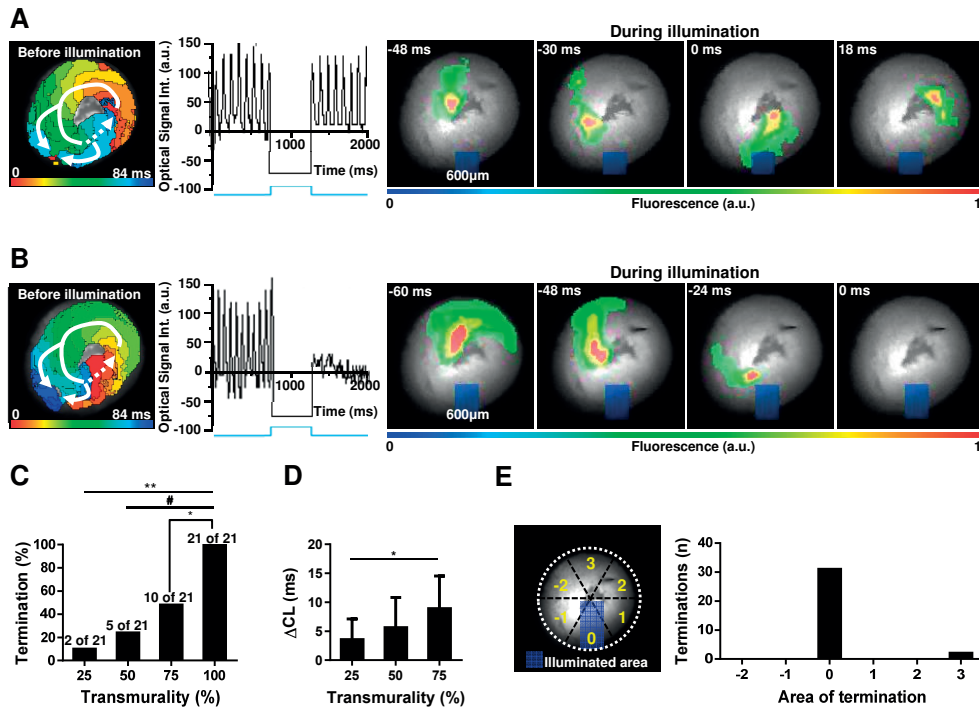


Figure 6. Reentry termination by local subtransmural illumination of CatCh⁺ slices. **A** and **B**, Representative activation maps confirming the presence of anatomical reentry before 500-ms exposure to 470-nm light (left), traces showing the optical signal before and after illumination (middle) and wave propagation during light exposure (right four panels). Example of unsuccessful reentry termination following illumination of a 600- μ m wide area spanning 25% of the total width of the myocardial wall (**A**). Example of successful reentry termination in a CatCh⁺ slice by illumination of a 600- μ m wide area spanning 50% of the total width (**B**). **C**, The success rate of light-induced anatomical reentry termination shows a positive correlation with the extent of transmurality of the 600- μ m wide light-exposed area. * $P < 0.001$ vs 75%, # $P < 0.001$ vs 50%. ** $P < 0.001$ vs 25% using χ^2 test ($n = 21$ slices from 10 rats). **D**, Increases in transmurality of illumination result in larger increases in reentry CL during failed optogenetic arrhythmia termination. * $P < 0.05$ 75% vs 25% using one-way ANOVA with post-hoc Bonferroni's test. Similarly, random effects one-way ANOVA showed significant difference ($P < 0.001$). **E**, Analysis of the incidence of reentry termination in different parts of the slice (equal-sized segments -2, -1, 0, 1, 2, 3) showing that reentry termination rarely occurs outside of the illuminated area (*i.e.* segment 0).

to conduction block and vice versa). For these studies, we created virtual NRVC monolayer strips of 12.75×2.8 mm, in which Chr2 was uniformly incorporated into the cardiomyocytes, thereby mimicking the area of interest in the cultured cardiac tissue slices. Left-sided electrical stimulation of the strip resulted in uniform AP propagation towards the other side of the strip (Figure 7A, left panel). Next, the light-sensitive ion channels were activated by *in silico* illumination of a rectangular central area of $600 \mu\text{m} \times 25\%$ or 75% of the total strip width (Figure 7A, right panels). After creation of a functional conduction block by illuminating 25% of the total strip width, 37.5% of the strips showed 1:1 propagation of the evoked electrical signal

to the right side of the strip, whereas 62.5% showed 1:2 propagation, thus no complete block (Figure 7B). In contrast, illumination of 75% of the total width resulted in complete block of AP propagation at the site of illumination in all strips and in all cases (Figure 7C). The voltage distribution in the strips around this site confirmed the generation of a functional conduction block through depolarization.

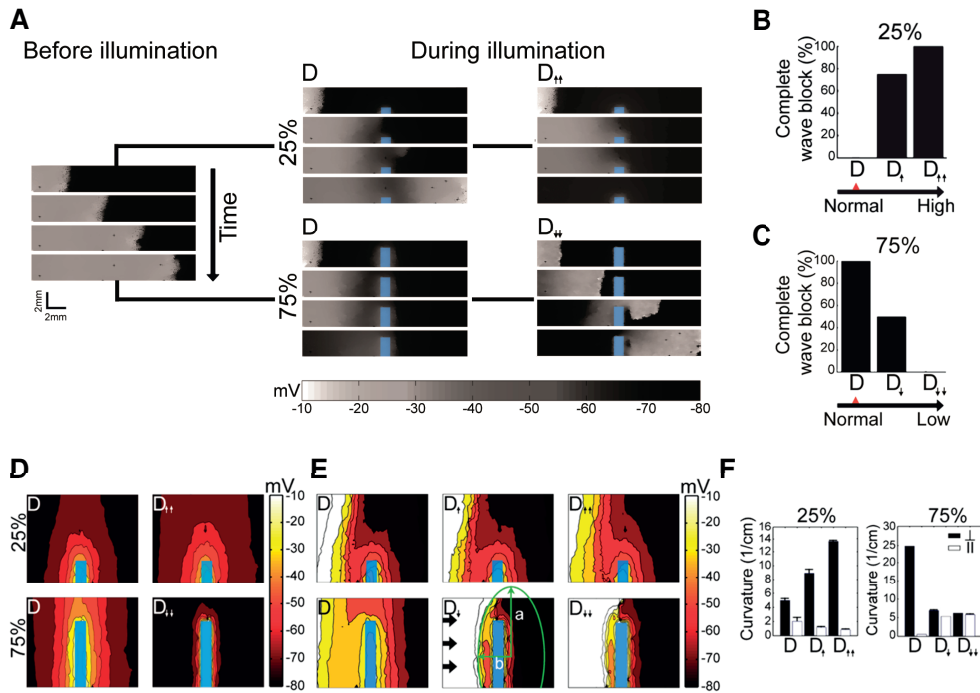


Figure 7. *In silico* study into the mechanism underlying block of AP propagation caused by partial obstruction of the conduction pathway. **A**, Propagation of APs evoked by electrical stimulation through 2.8-mm wide strips containing ChR2-expressing cardiomyocytes before (left) and during (right) illumination. When 25% of the total strip width (upper right panels) with normal intercellular coupling (D) is illuminated, APs propagate successfully through the isthmus, while propagation is blocked with 2-fold increased intercellular coupling (D_↑). When 75% of the total strip width (lower right panels) with normal intercellular coupling (D) is illuminated, propagation is blocked following conduction slowing. Decreasing the intercellular coupling 25-fold (D_↓) enables wave propagation through the isthmus. **B** and **C**, Quantification of successful complete blockage of AP propagation at different levels of intercellular coupling and illumination of 25% (**B**) or 75% (**C**) of the total strip width. **D**, Voltage distribution in the depolarization gradients formed around illuminated rectangles covering 25% (upper panels) and 75% (lower panels) of the total strip width with normal (D, left panels) or increased and decreased (D_↑ and D_↓, right panels) intercellular coupling in the absence of electrical stimulation. **E**, Visualization of voltage around the area of illumination at the instant when the wave impinges on the light-exposed area. By increasing the intercellular coupling the wavefront becomes increasingly concave, while decreasing leads to straightening of the wavefront. **F**, Quantification of longitudinal curvature (||, b/a2) and transverse curvature (⊥, a/b2) of the wavefront impinging on light-exposed rectangles covering 25% (left) or 75% (right) of the total strip width. a, major radius. b, minor radius.

5

This area was characterized by a gradient of membrane potentials ranging from -20 mV in the center to -30 mV at the border of the illuminated area and to -70 mV in the most distal affected region outside of the illuminated area (Figure 7D, left frames). In areas with potentials \geq -45 mV, fast Na⁺ channels were no longer available for excitation, causing the area of light-induced conduction block to extend well beyond the illuminated region. In addition, conduction slowing was observed in the regions with membrane potentials ranging between -45 mV and -65 mV, and therefore with a limited availability of fast Na⁺ channels. Once established, such conduction block and partially depolarized neighboring regions seem to favor failure of AP propagation at the site of illumination. The degree to which depolarization extended into the areas surrounding the illuminated zone was tested in CatCh \uparrow slices through optical mapping with Di-4-ANBDQBS. The CatCh \uparrow slices were electrically stimulated at a frequency of 7-9 Hz prior and during illumination of a 600- μ m-wide rectangular area of 25 or 75% transmural. The gradient in depolarization was assessed by comparing the AP amplitude, before and during illumination, in 3 different spots at increasing distance from the targeted area. This comparison supported the results of the *in silico* study by showing that the optical signal amplitude was most strongly reduced (\sim 50%) in the spot closest to the area of illumination (Figure 8).

To investigate whether electrical source-sink relationships are indeed a key factor underlying block of propagation at the site of illumination, and hence reentry termination, this relationship was modulated in a stepwise manner. Intercellular coupling, or gap junctional conductance, is considered to be an important determinant of passive voltage spread.²⁷ We therefore varied the mathematical coefficient of voltage diffusion (*D*), which biophysically correlates with gap junctional conductance, to study its effects on AP propagation at the site of conduction block. For strips in which only 25% of the total width was illuminated, a 1.5-fold increase in *D* (*D* \uparrow) led to full conduction block in 75% of the strips (Figure 7B), while 12.5% showed 1:2 capture and 12.5% exhibited 1:3 propagation to the right side of the strips. Increasing *D* 2-fold (*D* $\uparrow\uparrow$), resulted in complete failure of propagation at the site of block in all cases (Figure 7B). Such improved gap junctional conductance increased the spatial spread of the depolarization gradients and consequently increased the size of the inexcitable area, further reducing the opportunities for wave propagation (Figure 7E, *D* \uparrow and *D* $\uparrow\uparrow$). A quantitative analysis of the curvature of the incoming wavefront showed that as conductance increased, the ratio (*r*) of longitudinal

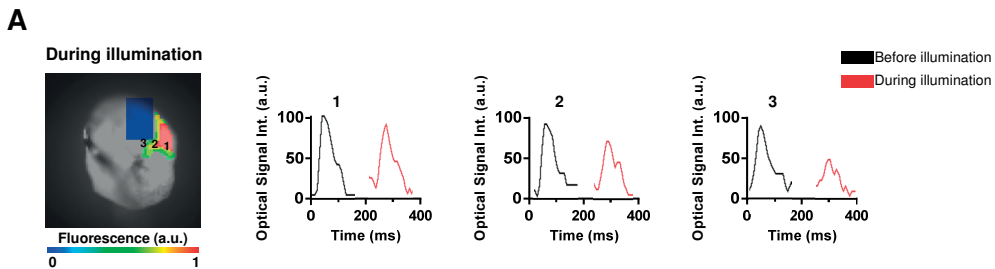


Figure 8. Assessment of depolarization gradient *in vitro*. Optical signal traces from spots 1-3, with 1 being furthest away from the targeted area, before (black) and during (red) illumination (*n*=8 slices from 6 rats).

curvature (*i.e.*, curvature along the direction of propagation) to transverse curvature (*i.e.*, curvature perpendicular to the direction of propagation) decreased from 0.408 to 0.133 and 0.064 for D, D \uparrow and D $\uparrow\uparrow$, respectively (Figure 7F, left). A 12.5- and 25-fold decrease in D (D \downarrow and D $\downarrow\downarrow$, respectively), however, resulted in opposite effects, *i.e.* a drop in the percentage of strips showing failure of propagation at the site of partial conduction block (Figure 7C), a decrease in the spatial spread of the depolarization gradients (Figure 7E, D \downarrow and D $\downarrow\downarrow$), an increase in r from 0.022 to 0.768 and 0.934 for D, D \downarrow and D $\downarrow\downarrow$ (Figure 7F, right), and more often continuation of propagation. Taken together, these results indicate that generation of a conduction block that is partially obstructing the pathway of propagation and thereby leaving a narrow isthmus, could indeed result in failure of such propagation through local formation of temporary source-sink mismatches.

DISCUSSION

Anatomical reentry is a key mechanism of potentially lethal heart rhythm disturbances in structural heart disease, and is characterized by AP propagation around a fixed anatomical obstacle. The mechanisms involved in the interruption and therefore termination of anatomical reentry have been mainly ascribed to global temporary modulation of electrophysiological properties through the application of drugs, electrical shocks and/or local permanent modulation of cardiac electrical activity through tissue ablation at critical sites. Here, we investigated optogenetic manipulation of anatomical reentry in cultured ventricular tissue slices. We consider the results as a proof-of-principle demonstration that such arrhythmia could be optogenetically terminated. The mechanism involved in the interruption of the anatomical reentry, as described in our study, is based on the temporary inhibition of excitability in only a specific part of the reentrant pathway via optogenetic modification and patterned illumination technology. As a result, a functional and reversible conduction block is created in this pathway, thereby preventing continuation of reentry and allowing normal activation to resume. Our data regarding optogenetic control of excitability are in line with previous studies. Bruegmann *et al*⁹ showed that prolonged illumination of cardiomyocytes expressing wild-type ChR2 resulted in a significant and sustained upward shift in membrane potential. As a result of this light-induced depolarization, the cardiomyocytes can no longer be electrically activated thereby producing a functional conduction block. While light-gated cation channels are mostly used as excitatory tools for optical pacing by generating brief supra-threshold depolarizing stimuli, here we show, by single-cell patch clamping in combination with optical voltage mapping of cardiac tissue slices, that their prolonged activation produces a depolarizing current of sufficient strength and duration to allow inhibition of excitation. In their groundbreaking paper, Arrenberg *et al*²⁸ were the first to demonstrate that activation of a light-gated chloride pump, resulting in a hyperpolarizing photocurrent, could also inhibit electrical activity in cardiac tissue. In a recent study by Nussinovitch *et al*,¹² a light-gated hyperpolarizing proton pump was used to inhibit electrical activity in cardiomyocytes cultured on multi-electrode array culture dishes. Whether the results of our study depend on the specific use of CatCh, or may be obtained with other

light-gated depolarizing or hyperpolarizing tools as well, remains to be determined. However, certain differences can be expected, especially given the important contribution that the depolarization gradients in the proximity of the illuminated area seem to have in terminating anatomical reentry. While several prior studies reported optogenetic control over cardiac tissue excitability,⁹⁻¹³ in general, the anti-tachyarrhythmic potential of optogenetics remains relatively poorly studied. In a previous study we investigated the effects of global activation of CatCh on spiral wave tachyarrhythmias in monolayers of atrial cardiomyocytes.²⁵ The resulting depolarizing photocurrent caused drifting of the spiral waves, leading to critical collision and thereby termination of these waves. In more recent studies, the anti-arrhythmic potential of ChR2(H143R), another depolarizing optogenetic tool, has been explored in whole murine hearts. Here, Bruegmann *et al*²⁹ and Crocini *et al*³⁰ have shown that optogenetic manipulation of ventricular arrhythmias may lead to their termination. They relied on computer simulations to suggest that Na⁺ channel inactivation based on ChR2-dependent depolarization may be involved in the underlying anti-arrhythmic mechanism. In the present study, we make use of a controllable *in situ* model of ventricular tachyarrhythmias in which these disturbances are solely based on pre-defined anatomical reentry, thereby allowing more systematic and detailed studies into the underlying anti-arrhythmic mechanisms of optogenetic interventions. Here, patterned illumination was used to generate a transmural conduction block with a width of 600 μ m in the pathway of reentry, which resulted in arrhythmia termination in all slices and in all cases. Under these conditions, the reentrant waves were apparently not able to penetrate the illuminated area deep enough via electrotonic conduction to activate the cardiomyocytes at the other side of the functional conduction block and reentry was therefore terminated at once. Of note, such optogenetic termination of an anatomical reentry is based on a fully reversible functional conduction block leaving no tissue damage or electrical dysfunction. Even more interestingly were our experiments in which the conduction block did not fully obstruct the reentrant pathway, but was leaving a narrow isthmus between the two non-illuminated transmural areas of myocardial tissue. Here, the outcome was directly determined by the width of the isthmus, showing more often reentry termination at the site of illumination with further narrowing of the isthmus. From a mechanistic point of view, we showed, through a set of complementary *in silico* and *in situ* studies, extension of a gradient in depolarization from the illuminated area into the isthmus. The *in silico* data revealed that the membrane potential was ranging from -20 mV in the center to -30 mV at the border of the illuminated area and -70 mV in the most distal region (Figure 7D, left frames). In line with these results, the *in situ* data showed a strong reduction (~50%) of the optical signal amplitude in the spot closest to the area of illumination (Figure S5A), thereby indeed suggesting the presence of a graded decrease in excitability. Generation, by patterned illumination, of a transmural conduction block with a width of 600 μ m in the pathway of reentry, resulted in arrhythmia termination in all slices and in all cases. Under these conditions, the reentrant waves were apparently not able to penetrate the illuminated area deep enough via electrotonic conduction to activate the cardiomyocytes at the other side of the functional conduction block and reentry was therefore terminated at once. Of note, such optogenetic termination of an anatomical reentry is based on a fully reversible functional

conduction block leaving no tissue damage or electrical dysfunction. Even more interestingly were our experiments in which the conduction block did not fully obstruct the reentrant pathway, but was leaving a narrow isthmus between the two non-illuminated transmural areas of myocardial tissue. Here, the outcome was directly determined by the width of the isthmus, showing more often reentry termination at the site of illumination with further narrowing of the isthmus. This result suggested that local electrical source-sink mismatches resulted in reentry termination, because such mismatches are known to block AP propagation. Earlier work from, among others, Cabo *et al.*,³¹ Fast *et al.*³² and Rohr *et al.*,²⁷ identified a crucial role for gap junctional coupling in determining these source-sink relationships, with a stronger effect on the load than source for a certain degree of uncoupling. Hence, upon partial uncoupling, electrical signals are able to propagate from a narrow area to a wider area, while initially their propagation stopped at the site of expansion. Our *in silico* study provides novel insight into this matter by showing that enhanced gap junctional conductance increased the spread of depolarization gradients around the illuminated area, thereby expanding the area of effective functional conduction block and reducing the curvature of the entering wavefront. This reduction in curvature was associated with insufficient depolarizing force at the isthmus, giving rise to source-sink mismatch and resulting in propagation failure (Figure 7). This finding is in line with earlier work of Rohr *et al.*,²⁷ which assessed the role of wavefront curvature in AP propagation at suddenly expanding areas of cardiac tissue.

Study limitations and translational considerations

The *in situ* model presented in this study is based on cultured transverse slices of neonatal rat ventricular myocardium and allowed standardized and systematic studies into optogenetic manipulation of anatomical reentry. Slices from the adult rat heart might be more relevant in terms of translation potential, but the requirement of 4 days in culture to allow sufficient CatCh expression together with the fact that cultured cardiac tissue slices from adult rats degenerate much more quickly than those of newborn rats^{33, 34} led us to employ neonatal rat hearts. The electrophysiological properties of neonatal rat hearts differ to some extent from those of adult hearts. Neonatal rat hearts, for instance, have weaker Na⁺ and repolarizing currents and Cx43 is distributed not only at the intercalated discs but also along the cell borders.³⁵⁻³⁸ Hence, the absolute values as reported in our study should be interpreted keeping these differences in mind, although we believe that the overall conclusion remains valid. Furthermore, the model used in our study allowed us to induce a single pre-defined and stable reentrant wave, which was anchored to the left cardiac lumen. In the diseased whole heart, however, these circuits are often fixed to a much more heterogeneous substrate consisting of, for example, highly fibrotic regions with complex shapes and distribution patterns. Because of this structural heterogeneity in diseased hearts, multiple circuits can be maintained and, as a consequence, the identification of the most critical isthmus might be more challenging as its presence could change in time. For this reason, pathologically more relevant and more complex models are needed to assess the translational value of the novel concept of reentry termination “brought to light” in this study.

Another potential hurdle to the clinical translation of our findings might be the current challenge to illuminate a sufficiently large mass of myocardium (*i.e.* beyond the epi- or endocardial surface) in order to produce a photocurrent strong enough for anatomical reentry termination. Although our study shows that full transmural illumination is indeed the most effective way to terminate anatomical reentry, it also reveals that subtransmural illumination could lead to arrhythmia termination. We are, however, aware of the fact that many more studies are needed to assess the therapeutic relevance of our findings, and we therefore consider these data as proof-of-principle for optogenetic termination of anatomical reentry. Such future experiments should include, for example, various gradients and shapes of illumination to better mimic those illumination patterns that can be expected from epi- or endocardial illumination. Indeed, it is known that tissue penetration of 470-nm light is rather poor.^{9, 39} Zaglia *et al* confirmed that the intensity of such light applied at the epicardial surface, decreases by 80% when reaching areas of myocardium at a depth of 300 μm .⁴⁰ There are, however, several means by which the penetration of light might be improved in order to reach deeper, if this would be needed for effective termination of anatomical reentry in larger hearts, as those of humans. These include the use red-shifted optogenetic tools, such as other ChR2 variants,^{41, 42} in combination with, for example, elastic integumentary membranes equipped with multiple $\mu\text{-LEDs}$ ⁴³ or implantation of injectable hardware-free $\mu\text{-LEDs}$ inside the myocardium.⁴⁴ In addition, more in-depth investigation is needed into the optimal combination of specific light-gated ion channels and illumination protocols with regard to the particular substrate of the arrhythmia, *e.g.* its composition and location. For example, substrates located closer to myocardial surfaces might be more suited for optogenetic targeting than those located deeper in the tissue.

Conclusions

In summary, our data indicate that optogenetic modification of cultured transverse slices of rat myocardial tissue, followed by patterned illumination of a pre-defined area in these slices, allows this area to directly act as a fully reversible functional conduction block shaped by light. Hence, the presence of this block can be tightly controlled in time and space in any desired region of the slice, thereby allowing such a block to be generated in the pathway of anatomical reentry. Depending on the size of the conduction block (*i.e.* the width of the isthmus), reentrant waves are either slowed or halted at the site of illumination. Although our study illustrates that full transmural illumination is the most effective way of anatomical reentry termination, it also shows that this is not absolutely required for termination in our model. This is an important finding, both conceptually (*i.e.* optogenetically induced source-sink mismatches) and practically (*i.e.* no absolute need for full transmural illumination). Computer modeling studies suggest that so-called electrical source-sink mismatches play a crucial role in the mechanism responsible for reentry termination by creating light-induced depolarization gradients that partially obstruct the conduction pathway. The light-guided generation of regional, temporary and reversible conduction block in viable cardiac tissue slices provides a distinctively novel approach to manipulate and terminate anatomical reentry. Thus our data do not only provide novel mechanistic insight into optogenetic control of cardiac electrical function in ventricular

tissue, but that they may also initiate more research into innovative, biology-driven strategies for cardiac arrhythmias therapies.

FUNDING

This work was supported by the Netherlands Organisation for Scientific Research [NWO, Vidi grant 91714336 to D.A.P.]. Additional support was provided by Ammodo [D.A.P. and A.A.F.d.V.] and the Japanese Society of Electrocardiology [Research fellowship 2013 to M.W.].

ACKNOWLEDGMENTS

We thank Cindy Schutte-Bart (Department of Cardiology, LUMC) for assistance with the animal experiments, Stefan Michel (Department of Molecular Cell Biology, LUMC) and Maaïke Vreeswijk (Department of Human Genetics, LUMC) for their help in preparing the cardiac tissue slices and Annemarie Kip (Department of Cardiology, LUMC) for LV production.

CONFLICT OF INTEREST

None.

REFERENCES

1. Hsia HH, Marchlinski FE. Electrophysiology studies in patients with dilated cardiomyopathies. *Card Electrophysiol Rev.* 2002; 6:472-81.
2. Josephson ME, Horowitz LN, Farshidi A, Kastor JA. Recurrent sustained ventricular tachycardia. 1. Mechanisms. *Circulation.* 1978; 57:431-40.
3. Josephson ME, Almendral JM, Buxton AE, Marchlinski FE. Mechanisms of ventricular tachycardia. *Circulation.* 1987; 75:III41-7.
4. Connolly SJ, Dorian P, Roberts RS, Gent M, Bailin S, Fain ES, Thorpe K, Champagne J, Talajic M, Couto B, Gronefeld GC, Hohnloser SH, Optimal Pharmacological Therapy in Cardioverter Defibrillator Patients I. Comparison of beta-blockers, amiodarone plus beta-blockers, or sotalol for prevention of shocks from implantable cardioverter defibrillators: the OPTIC Study: a randomized trial. *JAMA.* 2006; 295:165-71.
5. Moss AJ, Greenberg H, Case RB, Zareba W, Hall WJ, Brown MW, Daubert JP, McNitt S, Andrews ML, Elkin AD. Long-term clinical course of patients after termination of ventricular tachyarrhythmia by an implanted defibrillator. *Circulation.* 2004; 110:3760-5.
6. Stevenson WG, Soejima K. Catheter ablation for ventricular tachycardia. *Circulation.* 2007; 115:2750-60.
7. Ambrosi CM, Klimas A, Yu J, Entcheva E. Cardiac applications of optogenetics. *Prog Biophys Mol Biol.* 2014; 115:294-304.
8. Entcheva E. Cardiac optogenetics. *Am J Physiol Heart Circ Physiol.* 2013; 304:H1179-91.
9. Bruegmann T, Malan D, Hesse M, Beiert T, Fuegeman CJ, Fleischmann BK, Sasse P. Optogenetic control of heart muscle in vitro and in vivo. *Nat Methods.* 2010; 7:897-900.
10. Nussinovitch U, Shinnawi R, Gepstein L. Modulation of cardiac tissue electrophysiological properties with light-sensitive proteins. *Cardiovasc Res.* 2014; 102:176-87.
11. Nussinovitch U, Gepstein L. Optogenetics for in vivo cardiac pacing and resynchronization therapies. *Nat Biotechnol.* 2015; 33:750-4.
12. Nussinovitch U, Gepstein L. Optogenetics for suppression of cardiac electrical activity in human and rat cardiomyocyte cultures. *Neurophotonics.* 2015; 2:031204.
13. Park SA, Lee SR, Tung L, Yue DT. Optical mapping of optogenetically shaped cardiac action potentials. *Sci Rep.* 2014; 4:6125.
14. Bovetti S, Fellin T. Optical dissection of brain circuits with patterned illumination through the phase modulation of light. *J Neurosci Methods.* 2015; 241:66-77.
15. Packer AM, Roska B, Hausser M. Targeting neurons and photons for optogenetics. *Nat Neurosci.* 2013; 16:805-15.
16. Papagiakoumou E. Optical developments for optogenetics. *Biol Cell* 2013;105 :443-64.
17. Reutsky-Gefen I, Golan L, Farah N, Schejter A, Tsur L, Brosh I, Shoham S. Holographic optogenetic stimulation of patterned neuronal activity for vision restoration. *Nat Commun* 2013;4:1509.
18. Kleinlogel S, Feldbauer K, Dempski RE, Fotis H, Wood PG, Bamann C, Bamberg E. Ultra light-sensitive and fast neuronal activation with the Ca(2)+-permeable channelrhodopsin CatCh. *Nat Neurosci.* 2011; 14:513-8.
19. Korhonen T, Hanninen SL, Tavi P. Model of excitation-contraction coupling of rat neonatal ventricular myocytes. *Biophys J.* 2009; 96:1189-209.
20. Hou L, Deo M, Furspan P, Pandit SV, Mironov S, Auerbach DS, Gong Q, Zhou Z, Berenfeld O, Jalife J. A major role for HERG in determining frequency of reentry in neonatal rat ventricular myocyte monolayer. *Circ Res.* 2010; 107:1503-11.
21. ten Tusscher KH, Mourad A, Nash MP, Clayton RH, Bradley CP, Paterson DJ, Hren R, Hayward M, Panfilov AV, Taggart P. Organization of ventricular fibrillation in the human heart: experiments and models. *Exp Physiol.* 2009; 94:553-62.

22. MacCannell KA, Bazzazi H, Chilton L, Shibukawa Y, Clark RB, Giles WR. A mathematical model of electrotonic interactions between ventricular myocytes and fibroblasts. *Biophys J*. 2007; 92:4121-32.
23. Williams JC, Xu J, Lu Z, Klimas A, Chen X, Ambrosi CM, Cohen IS, Entcheva E. Computational optogenetics: empirically-derived voltage- and light-sensitive channelrhodopsin-2 model. *PLoS Comput Biol*. 2013; 9:e1003220.
24. Boyle PM, Williams JC, Ambrosi CM, Entcheva E, Trayanova NA. A comprehensive multiscale framework for simulating optogenetics in the heart. *Nat Commun*. 2013; 4:2370.
25. Bingen BO, Engels MC, Schaliij MJ, Jangsangthong W, Neshati Z, Feola I, Ypey DL, Askar SF, Panfilov AV, Pijnappels DA, de Vries AA. Light-induced termination of spiral wave arrhythmias by optogenetic engineering of atrial cardiomyocytes. *Cardiovasc Res*. 2014; 104:194-205.
26. Kleber AG, Rudy Y. Basic mechanisms of cardiac impulse propagation and associated arrhythmias. *Physiol Rev*. 2004; 84:431-88.
27. Rohr S, Kucera JP, Fast VG, Kleber AG. Paradoxical improvement of impulse conduction in cardiac tissue by partial cellular uncoupling. *Science*. 1997; 275:841-4.
28. Arrenberg AB, Stainier DY, Baier H, Huisken J. Optogenetic control of cardiac function. *Science*. 2010; 330:971-4.
29. Bruegmann T, Boyle PM, Vogt CC et al. Optogenetic defibrillation terminates ventricular arrhythmia in mouse hearts and human simulations. *J Clin Invest* 2016; 126:3894-904.
30. Crocini C, Ferrantini C, Coppini R et al. Optogenetics design of mechanistically-based stimulation patterns for cardiac defibrillation. *Sci Rep*. 2016; 6:35628.
31. Cabo C, Pertsov AM, Baxter WT, Davidenko JM, Gray RA, Jalife J. Wave-front curvature as a cause of slow conduction and block in isolated cardiac muscle. *Circ Res*. 1994; 75:1014-28.
32. Fast VG, Kleber AG. Block of impulse propagation at an abrupt tissue expansion: evaluation of the critical strand diameter in 2- and 3-dimensional computer models. *Cardiovasc Res*. 1995; 30:449-59.
33. Obreztkhikova MN, Sosunov EA, Plotnikov A, Anyukhovskiy EP, Gainullin RZ, Danilo P, Yeom ZH, Robinson RB and Rosen MR. Developmental changes in IKr and IKs contribute to age-related expression of dofetilide effects on repolarization and proarrhythmia. *Cardiovascular research*. 2003; 59:339-50.
34. Antzelevitch C. Are M cells present in the ventricular myocardium of the pig? A question of maturity. *Cardiovascular research*. 1997; 36:127-8.
35. Cordeiro JM, Panama BK, Goodrow R, Zygmunt AC, White C, Treat JA, Zeina T, Nesterenko VV, Di Diego JM, Burashnikov A and Antzelevitch C. Developmental changes in expression and biophysics of ion channels in the canine ventricle. *Journal of molecular and cellular cardiology*. 2013; 64:79-89.
36. Kaneko M, Coppin SR, Fukushima S, Yacoub MH and Suzuki K. Histological Validation of Heart Slices as a Model in Cardiac Research. *Journal of Cell Science & Therapy*. 2012; 3:4.
37. van Kempen MJ, Fromaget C, Gros D, Moorman AF, Lamers WH. Spatial distribution of connexin43, the major cardiac gap junction protein, in the developing and adult rat heart. *Circ Res*. 1991; 68:1638-51.
38. Popa MA and Corotchi MC. An in vitro method for adhesion of fresh adult murine heart slices on Collagen-coated surfaces. *Annals of the Romanian Society for Cell Biology*. 2015; 20:4.
39. Vogt CC, Bruegmann T, Malan D, Ottersbach A, Roell W, Fleischmann BK and Sasse P. Systemic gene transfer enables optogenetic pacing of mouse hearts. *Cardiovasc Res* 2015 May 1; 106:338-43.
40. Zaglia T, Pianca N, Borile G, Da Broi F, Richter C, Campione M, Lehnart SE, Luther S, Corrado D, Miquerol L and Mongillo M. Optogenetic determination of the myocardial requirements for extrasystoles by cell type-specific targeting of ChannelRhodopsin-2. *Proceedings of*

- the National Academy of Sciences of the United States of America. 2015; 112:E4495-504.
41. Lin JY, Knutsen PM, Muller A, Kleinfeld D and Tsien RY. ReaChR: a red-shifted variant of channelrhodopsin enables deep transcranial optogenetic excitation. *Nature neuroscience*. 2013; 16:1499-508.
 42. Prigge M, Schneider F, Tsunoda SP, Shilyansky C, Wietek J, Deisseroth K and Hegemann P. Color-tuned channelrhodopsins for multiwavelength optogenetics. *The Journal of biological chemistry*. 2012; 287:31804-12.
 43. Xu L, Gutbrod SR, Bonifas AP, Su Y, Sulkin MS, Lu N, Chung HJ, Jang KI, Liu Z, Ying M, Lu C, Webb RC, Kim JS, Laughner JI, Cheng H, Liu Y, Ameen A, Jeong JW, Kim GT, Huang Y, Efimov IR and Rogers JA. 3D multifunctional integumentary membranes for spatiotemporal cardiac measurements and stimulation across the entire epicardium. *Nature communications*. 2014; 5:3329.
 44. Kim TI, McCall JG, Jung YH, Huang X, Siuda ER, Li Y, Song J, Song YM, Pao HA, Kim RH, Lu C, Lee SD, Song IS, Shin G, Al-Hasani R, Kim S, Tan MP, Huang Y, Omenetto FG, Rogers JA and Bruchas MR. Injectable, cellular-scale optoelectronics with applications for wireless optogenetics. *Science*. 2013; 340:211-6.

SUPPLEMENTAL MATERIAL

Detailed Methods

Preparation of transverse rat ventricular tissue slices

All animal experiments were approved by the Animal Experiments Committee of Leiden University Medical Center (LUMC) and done in accordance with the Guide for Care and Use of Laboratory Animals as stated by the US National Institutes of Health. Transverse ventricular tissue slices were obtained from neonatal Wistar rats. The 2-day-old rats were anaesthetized by 4-5% isoflurane inhalation and adequate anesthesia was confirmed by the absence of reflexes. After the chest was opened and the inferior vena cava was cut off with scissors, the right atrium was punctured with a 19 gauge needle. The heart was perfused through this needle with pre-warmed and oxygenated phosphate-buffered saline (PBS) containing 10 IU/ml heparin to replace the blood. Subsequently, the heart was excised and stored in ice-cold and pre-oxygenized modified Tyrode's solution (MTS; NaCl 143 mmol/l, KCl 5.4 mmol/l, NaH₂PO₄ 0.3 mmol/l, MgCl₂ 0.5 mmol/l, HEPES 5 mmol/l, CaCl₂ 0.9 mmol/l, glucose 5.5 mmol/l, 2,3-butanedione monoxime 20 mmol/l). Before slicing, the heart was embedded in 4% low melting point agarose (type VII-A; Sigma-Aldrich, St. Louis, MO) dissolved in MTS at 37°C and subsequently fixed to the sample holder of the vibratome (VT1200S, Leica Microsystems, Rijswijk, the Netherlands) using cyanoacrylate-based super glue.¹ The sample was then quickly covered with ice-cold and pre-oxygenated MTS and cut into 150-µm thick tissue slices using Derby extra super stainless double edge razor blades. Each slice was placed onto the semi-porous membrane (0.4 µm pore size) of a PICM0RG50 cell culture insert (Millipore, Amsterdam-Zuidoost, the Netherlands) in a 35-mm diameter Petri dish containing sterilized MTS of room temperature (RT) and gradually warmed to 37°C (Figure S1A and S1B). Next, the MTS was replaced with pre-warmed culture medium Dulbecco's modified Eagle's medium (DMEM; Life Technologies Europe, Bleiswijk, the Netherlands) supplemented with 1% heat-inactivated fetal bovine serum (HI-FBS; Life Technologies Europe), 1× penicillin-streptomycin (Life Technologies Europe), 1× B-27 supplement (Life Technologies Europe) and 5 µM Z-Asp-2,6- dichlorobenzoyloxymethylketone (Santa Cruz Biotechnology, Heidelberg, Germany) and the slice was kept at 37°C in humidified 95% air-5% CO₂ (culture conditions).

Lentiviral gene transfer

The construction of the lentiviral vector shuttle plasmids pLV.MHCK7.CatCh~eYFP.WHVPRE and pLV.MHCK7.eYFP.WHVPRE and the production of the corresponding viral vectors designated LV.CatCh~eYFP↑ and LV.eYFP↑, respectively, have been described previously.² The cardiac tissue slices were placed on a semi-porous membrane and genetically modified at the same day. A concentrated viral vector suspension was added directly on top of the slices with an inoculum consisting of 1 µl of culture medium containing 10 µg/ml diethylaminoethyl-dextran (Carl Roth, Karlsruhe, Germany) and 9 µl of LV suspension. After 30 minutes, the semi-porous membrane was transferred to a culture dish filled with 1 ml medium containing 90 µl LV suspension and diethylaminoethyl-dextran at a final concentration of 1 µg/ml. After 24 h at

37°C in humidified 95% air-5% CO₂, the tissue was washed twice with fresh culture medium and then kept under culture conditions for 4 additional days.

Patch clamp

As reported previously,³ patch clamp recordings were performed under an inverted microscope Zeiss Axiovert 35 (Carl Zeiss AG, Oberkochen, Germany) at 20-23°C using perforated patch clamp technique and a conventional patch clamp equipment consisting of a MultiClamp 700B amplifier and a Digidata 1440A A/D converter (Molecular Devices, Sunnyvale, CA, USA), all connected to a personal computer and driven by commercially available MultiClamp 700B Commander and Clampex v10.3 software (Molecular Devices). Throughout experiments, the current and voltage outputs of amplifier were continuously sampled at intervals of 100 μs and recorded onto personal computer after low-pass filtered at 2-4 kHz with a four-pole Bessel filter. Neonatal rat ventricular cardiomyocytes (NRVCs) were isolated from hearts of 2-day-old Wistar rat pups using collagenase type I (450 U/ml; Worthington, Lakewood, NJ) and DNase I (1,8 U/ml in solution A; Sigma-Aldrich) solution in a shaking water bath at 37°C for 2 × 35 minutes, as described previously.³ Isolated cells were plated on round glass coverslips (15-mm diameter, Thermo Fisher Scientific Gerhard Menzel B.V. & Co. KG, Braunschweig, Germany) coated with fibronectin (Sigma-Aldrich) in 24-well plates (Corning Life Sciences, Amsterdam, the Netherlands) at the density of 15 × 10³ cells/well. Directly after isolation, NRVCs were transduced with LV.CatCh~eYFP↑ by adding the lentiviral vector suspension into the cell suspension. To prevent proliferation of non-cardiomyocytes, 16 hours after plating, cultures were treated for 2 hours with mitomycin-C (10 μg/mL; Sigma-Aldrich). NRVCs expressing CatCh (CatCh-NRVCs) were kept in a humidified incubator at 37 °C and 5% CO₂ and refreshed daily with culture medium consisting of a 1:1 mixture of DMEM (Life Technologies Europe) and Ham's F10 supplemented with 5% HS, penicillin (100 U/ml, Life Technologies) and streptomycin (100 μg/ml, Life Technologies). CatCh-NRVCs were transferred from culture medium to an external cellular solution containing (in mM): 126 NaCl, 11 glucose, 10 HEPES, 5.4 KCl, 1 MgCl₂, and 1.8 CaCl₂ (adjusted to pH 7.40 with NaOH). Approximately within 15-60 minutes after superfusion of external cellular solution, patch clamp experiments were conducted. For CatCh-NRVCs, only solitary cells expressing eYFP were selected for the experiments. The pipettes were fabricated from borosilicate glass capillaries (1.5 mm outer diameter and 1.17 mm inner diameter, Harvard Apparatus, Kent, UK) with a vertical puller (P-30, Sutter Instruments, Novato, CA, USA). CPM-2 coating and polishing microforege (ALA Scientific Instruments, Farmingdale, NY, USA) was employed for fire-polishing to reshape and smooth pipette tips. Pipettes had typical electrical resistances of 2-3 MW in the external cellular solution when filled with the internal solution. Here, an ATP-, GTP and EGTA-free pipette solution containing (in mM): 80 potassium DL-aspartate, 40 KCl, 8 NaCl, 5.5 glucose, 5 HEPES, and 1 MgCl₂ (adjusted to pH 7.20 with KOH) was used to tip-fill patch pipettes, and the same pipette solution containing nystatin (120-200 μg/ml; Sigma-Aldrich) was used to back-fill the pipettes. The giga-ohm seal was formed by continuously applied 10-ms voltage steps from 0 to +5 mV at 10 Hz. After reaching giga-ohm seal, the holding potential was set to -50 mV. The series resistance

was monitored and shown progressively decline. Recordings were started after the series resistance had reached steady state of 15-10 M Ω stable (*i.e.* after 20-30 min). The integrity of the perforated patch was checked during and after recording for every experiments. We noted that the rupture of patch membrane abruptly increased capacitive current, unleashed the pipette solution to diffuse into the cells and caused an irreversible contracture because a specific chelator for calcium EGTA was absence. Therefore, we discarded those cells that showed sudden appearance of the capacitive current or the irreversible contracture under the microscope to ensure reliability of recordings. Cell capacitance (C_m) was calculated from capacitive transient currents evoked during 5 mV steps from a holding potential of -50 mV and electrically removed with amplifier. To minimize voltage error and fetch the adequacy of the voltage-clamp, pipette series resistance was routinely monitored and electrically compensated by >75%. The estimated liquid-junction potential of 11 mV were corrected.

To investigate light induced voltage shift and photo current, we integrated the inverted microscope Zeiss Axiovert 35 (Carl Zeiss AG) with a blue light illumination device M470L3 collimated light-emitting diode (LED) light sources for microscopy driven by the T-Cube LED driver (Thorlabs GmbH, Munich, Germany). The LED based illumination system was controlled by STG4002 2-channels stimulus generator and MC_Stimulus program (Multi Channel Systems MCS GmbH, Reutlingen, Germany) to generate light pluses with various light intensities and durations. A precise 500-ms light pulse at various intensities was employed to determine the minimum light intensity needed for action potential generation with a stable voltage shift. The minimum light intensity (0.65 mW/mm²) at which light stimulus induced action potential with a stable voltage shift was taken as the threshold for investigating prolonged light stimulation induced action potentials, followed by prolonged depolarization. Subsequently, the same minimum light intensity was also used to characterize photo current in CatCh-NRVCs. At holding potential of -40 mV, peak currents (I_{pk}), steady-state current (I_{ss}), desensitization time constant (t_{des}) and channel closing time constant (t_{off}) were determined from photo current recordings during 500-ms light pulse.

Immunohistology

At day 5 of culture, slices were fixed with 4% buffered formaldehyde (Added Pharma, Oss, the Netherlands) for 30 minutes at RT, washed three times with PBS and permeabilized by incubation for 15 minutes at RT with 0.1% Triton-X100 in PBS. Next, slices were incubated overnight at 4°C with antibodies directed against sarcomeric α -actinin (mouse IgG1; Sigma-Aldrich, A7811), Col1 (rabbit IgG; Abcam, Cambridge, MA, ab292), Cx43 (rabbit Ig; Sigma-Aldrich, C6219) or active caspase-3 (rabbit IgG; Abcam, ab2303). All primary antibodies were diluted 1:200 in PBS + 1% FBS (Life Technologies Europe). The day after, slices were washed three times with PBS, incubated for 4 hours at 4°C with the corresponding Alexa Fluor 568-conjugated secondary antibodies (Life Technologies Europe; 1:400 dilution in PBS + 5% FBS) and again washed three times with PBS. For staining of mitochondria, slices were incubated with MitoTracker Red CMXRos (Life Technologies Europe) at a concentration of 200 nM for 30 minutes at 37°C. Subsequently, slices were fixed with 4% buffered formaldehyde and

washed three times with PBS. Nuclear staining was performed at RT with 10 mg/ml Hoechst 33342 (Life Technologies Europe) in PBS and followed by a single wash with PBS. Finally, slices were mounted in Vectashield mounting medium (Vector Laboratories, Burlingame, CA) on top of glass slides. Images were acquired with a confocal laser scanning microscope (LSM 710; Zeiss Nederland, Sliedrecht, the Netherlands). For quantification of CatCh⁺ cells, images were taken at 63× magnification from 7 different areas in the CatCh[↑] slice (n=3 slices, 3 rats) using the confocal microscope Leica TCS SP8 X WLL (Leica Microsystems, Rijswijk, the Netherlands).

Integrated system for optical mapping and patterned illumination

The optical mapping system was engineered to allow recording of electrical activation with the voltage-sensitive dye di-4-ANEPPS (Life Technologies Europe) and patterned illumination with blue light (470 nm) (Figure S1C). To this end, a patterned illumination device, the Polygon400 (Mightex Systems, Toronto, ON) was connected through a cube containing a blue light-specific dichroic mirror (reflect 350-500 nm; pass >513 nm, FF506-Di03-25x36, Semrock, Rochester, NY) to the cube for di-4-ANEPPS and the MiCAM ULTIMA-L imaging system (SciMedia, Costa Mesa, CA). The cube for di-4-ANEPPS contained an excitation filter (pass 525±25 nm, FF03-525/50-25, Semrock), a dichroic mirror (reflect 520-560 nm; pass >600 nm, custom made, SciMedia) and an emission filter (pass >590 nm, custom made, SciMedia). For optical mapping with Di-4-ANBDQBS (52.5 μM final concentration), the cube contained an excitation filter (pass 650±27 nm, FF01-650/54-27, Semrock), a dichroic mirror (reflect 350-676 nm; pass 695-950 nm, FF685-Di02-25 × 35, Semrock) and an emission filter (pass >715 nm, FF01-715/LP-25, Semrock). The Polygon400 is a device based on digital micromirrors that in combination with the custom-made software Polylite (Mightex Systems), allows projection of any shape directly onto the living sample. The light from a high-power LED source (470 nm, 50 W, type-H, Mightex Systems) is guided through a liquid light guide to the Polygon400, reflected by the dichroic mirror and finally projected onto the sample through a 5× objective lens (Leica Microsystems, Wetzlar, Germany). Using this particular setup, it was possible to illuminate a maximal area of 1.78 × 3.1 mm with a pixel resolution of 3.6 μm.

Optical mapping

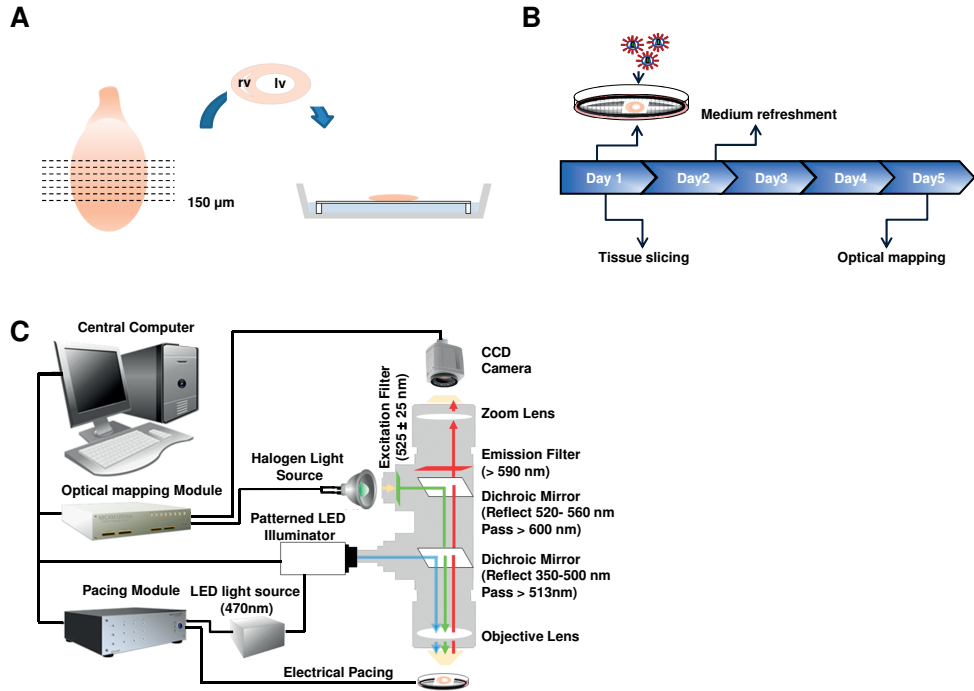
Optical voltage mapping was employed to assess the functional consequences of CatCh-generated photocurrents in transverse ventricular tissue slices kept for 5 days under culture conditions. Electrical activity was visualized using the voltage-sensitive dye di-4-ANEPPS. On day 5 of culture, slices were incubated for 30 min at 37°C with pre-oxygenized MTS containing 1.8 instead of 0.9 mmol/l CaCl₂ (MTS⁺) and 12.5 mmol/l di-4-ANEPPS. Next, slices were washed with pre-oxygenized MTS⁺ of 37°C and transferred to another cell culture insert in a Petri dish with warm MTS⁺. Subsequently, optical mapping was performed at 37°C. To prevent drying of the slice surface, no more than 2 slices were placed on the same inserts and mapping experiments typically did not exceed 30 min. Optical voltage signals were analyzed using BrainVision Analyzer 1103 software (Brainvision, Tokyo, Japan). As measure of APD the period

between the time point of maximal upstroke velocity and 80% repolarization (APD_{80}) was taken. Slices were stimulated either electrically with an epoxy-coated unipolar platinum electrode (FHC, Bowdoin, ME) using 2-ms rectangular pulses of 1.5 V or optically with 10-ms 470-nm light pulses, coming from the Polygon400, at the maximum input voltage tolerated by the system (irradiance 0.68 mW/mm²). A specialized stimulus generator (STG 2004) with corresponding software (MC Stimulus II; both from Multichannel Systems, Reutlingen, Germany) was used to perform both electrical and optical stimulation. Reentry was induced by electrical pacing using a 9-beat driving train with a basic CL of 100-150 ms and a single extrastimulus of 20-80 ms. After confirmation of the presence of reentrant conduction, slices were exposed to 470-nm LED light for 500 ms using the patterned illumination device at 0.68 mW/mm². For baseline shift adjustment during illumination, several filters were applied, which allowed interpretation of signals 30 ms after initiation of local light exposure.

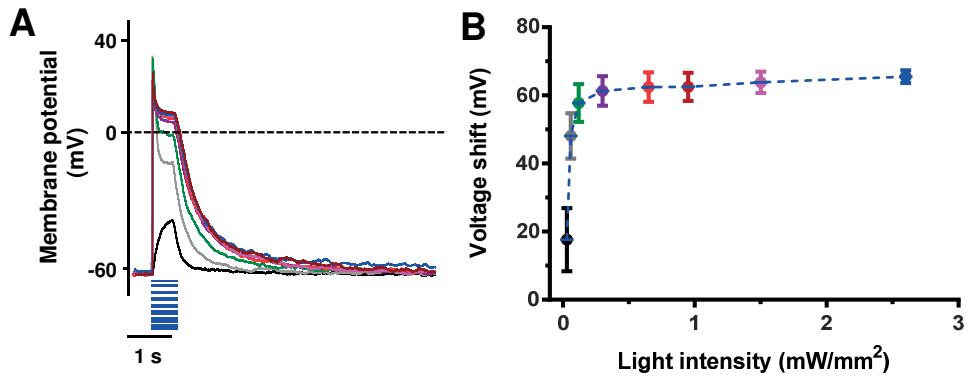
Numerical Methods

The neonatal rat ventricular cardiomyocytes were modeled according to the formulation of Korhonen *et al.*,⁴ with adaptations by Hou *et al.*⁵ The complex intracellular Ca²⁺ diffusion between the sarcolemma and the perinuclear sarcoplasmic reticulum was replaced by a simple Ca²⁺-handling process adopted from ten Tusscher *et al.*⁶ Cardiac myofibroblasts were modeled according to the passive formulation of MacCannell *et al.*,⁷ whereas the empirically derived model of ChR2 (current-enhanced mutant H134R) by Williams *et al.*⁸ was used together with the parameter set established by Boyle *et al.*⁹ to implement optogenetics. Eight confluent monolayer stripes (12.75 × 2.8 mm) were constructed as arrays of 1145 cell sites with 17% myofibroblasts. Each site was occupied by either a cardiomyocyte or a myofibroblast. The cardiomyocytes in the model coupled electrically to each other via an intercellular coupling coefficient $D=0.001\pm 0.0002$ cm²/ms, which describes the passive diffusion of transmembrane voltage between cells and therefore biophysically correlates with gap junctional conductance.¹⁰ For consistency with *in vitro* experiments, cardiomyocytes exhibiting different electrophysiological properties were modeled using a random number generator to create spatial distributions of probabilities for each ionic current/flux produced by a cardiomyocyte. These probabilities were then used to modulate the maximal channel conductance such that the peak value of the associated current/flux ranged from 50 to 150% of the mean value. The myofibroblasts in the stripes coupled electrically to the cardiomyocytes through a gap junctional coupling coefficient G_{gap} of 0.5 nS/pF.¹¹ The temporal part of the mathematical equation for the transmembrane potential in the two-dimensional stripe model with ChR2-expressing cardiomyocytes and 17% myofibroblasts was solved using the forward Euler method with a time step $\delta t=0.005$ ms. The spatial part was solved using a centered finite differencing scheme and space step $\delta x=\delta y=0.00625$ cm on a 5-point stencil. Each stripe was electrically paced from one side, at a CL of 500 ms, with a 2-ms current stimulus of 100 pA (Figure 7A). Wave propagation was then studied in the stripes in the presence of virtual irradiation over a rectangular area 600 × 25% or 75% of the transmural width (2.8 mm; Figure 7A).

Supplementary Figures

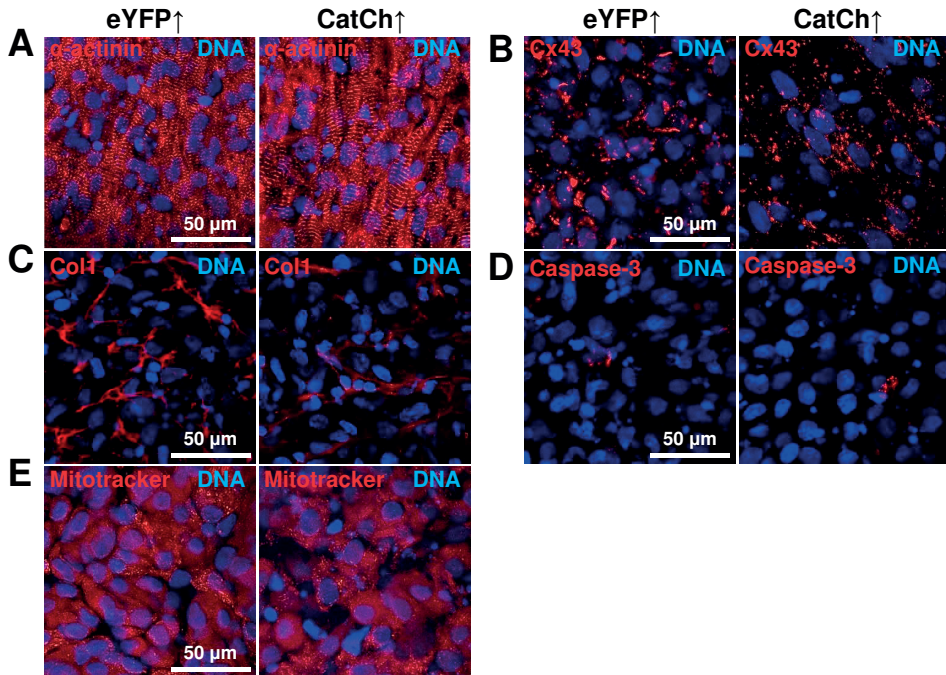


Supplementary Figure 1. Experimental design. A, Transverse ventricular tissue slice preparation. Hearts from 2-day-old neonatal rats were excised and, after flushing out the blood, transverse slices were prepared. Subsequently, the slices were placed onto semi-porous cell culture inserts and maintained for 4 days under culture conditions. B, Experimental timeline. Slices were transduced with LV.eYFP[↑] or LV.CatCh~eYFP[↑] on the day of preparation, while on day 5 of culture, optical mapping or histological analysis was performed. C, Setup of the system used for optical voltage mapping and patterned LED illumination.

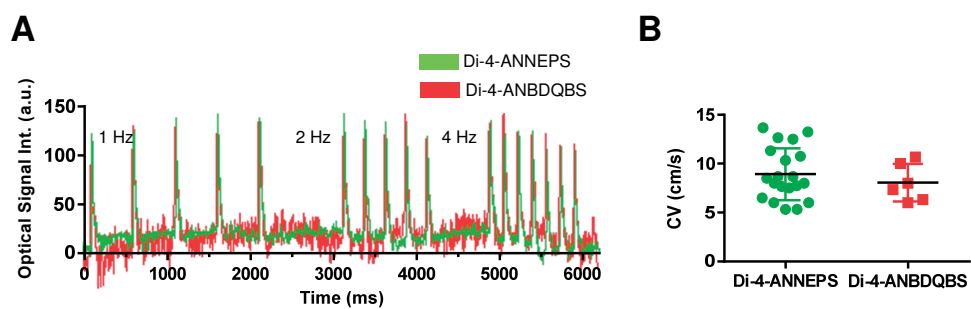


Supplementary Figure 2. Characterization of CatCh light-intensity dependence. B-C, Effect on membrane potential of exposing CatCh-NRVCs to 500-ms blue (470 nm) light pulse of different intensity (n=5).

5



Supplementary Figure 3. (Immuno)histological staining of cultured ventricular slices. The slices were transduced 4 days earlier with LV.eYFP[↑] (left) or LV.CatCh~eYFP[↑] (right) for nuclei (DNA; blue) and α -actinin (A), Cx43 (B), Col1 (C), caspase-3 (D) or Mitotracker (E), all labeled in red (n=3 for both eYFP[↑] and CatCh[↑] slices).



Supplementary Figure 4. Comparison of optical voltage mapping data of electrically stimulated CatCh \uparrow slices that were loaded with Di-4-ANEPPS or Di-4-ANBDQBS. A, Representative optical traces recorded during electrical stimulation at 1, 2, and 4 Hz. B, CVs measured during 1-Hz electrical stimulation showing no significant difference between slices loaded with Di-4-ANEPPS and those loaded with Di-4-ANBDQBS as determined by the unpaired t-test (nDi-4-ANEPPS=20 slices from 9 rats and nDi-4-ANBDQBS=6 slices from 6 rats).

Supplementary References

1. Brandenburger M, Wenzel J, Bogdan R, Richardt D, Nguemo F, Reppel M, Hescheler J, Terlau H, Dendorfer A. Organotypic slice culture from human adult ventricular myocardium. *Cardiovasc Res.* 2012; 93:50-9.
2. Bingen BO, Engels MC, Schalijs MJ, Jangsangthong W, Neshati Z, Feola I, Ypey DL, Askar SF, Panfilov AV, Pijnappels DA, de Vries AA. Light-induced termination of spiral wave arrhythmias by optogenetic engineering of atrial cardiomyocytes. *Cardiovasc Res.* 2014; 104:194-205.
3. Engels MC, Askar SF, Jangsangthong W, Bingen BO, Feola I, Liu J, Majumder R, Versteegh MI, Braun J, Klautz RJ, Ypey DL, De Vries AA, Pijnappels DA. Forced fusion of human ventricular scar cells with cardiomyocytes suppresses arrhythmogenicity in a co-culture model. *Cardiovasc Res.* 2015; 107:601-12.
4. Korhonen T, Hanninen SL, Tavi P. Model of excitation-contraction coupling of rat neonatal ventricular myocytes. *Biophys J.* 2009; 96:1189-209.
5. Hou L, Deo M, Furspan P, Pandit SV, Mironov S, Auerbach DS, Gong Q, Zhou Z, Berenfeld O, Jalife J. A major role for HERG in determining frequency of reentry in neonatal rat ventricular myocyte monolayer. *Circ Res* 2010;107:1503-11.
6. ten Tusscher KH, Mourad A, Nash MP, Clayton RH, Bradley CP, Paterson DJ, Hren R, Hayward M, Panfilov AV, Taggart P. Organization of ventricular fibrillation in the human heart: experiments and models. *Exp Physiol.* 2009; 94:553-62.
7. MacCannell KA, Bazzazi H, Chilton L, Shibukawa Y, Clark RB, Giles WR. A mathematical model of electrotonic interactions between ventricular myocytes and fibroblasts. *Biophys J.* 2007; 92:4121-32.
8. Williams JC, Xu J, Lu Z, Klimas A, Chen X, Ambrosi CM, Cohen IS, Entcheva E. Computational optogenetics: empirically-derived voltage- and light-sensitive channelrhodopsin-2 model. *PLoS Comput Biol.* 2013; 9:e1003220.
9. Boyle PM, Williams JC, Ambrosi CM, Entcheva E, Trayanova NA. A comprehensive multiscale framework for simulating optogenetics in the heart. *Nat Commun.* 2013; 4:2370.
10. Clayton RH, Bernus O, Cherry EM, Dierckx H, Fenton FH, Mirabella L, Panfilov AV, Sachse FB, Seemann G, Zhang H. Models of cardiac tissue electrophysiology: progress, challenges and open questions. *Prog Biophys Mol Biol.* 2011; 104:22-48.
11. Henriquez AP, Vogel R, Muller-Borer BJ, Henriquez CS, Weingart R, Cascio WE. Influence of dynamic gap junction resistance on impulse propagation in ventricular myocardium: a computer simulation study. *Biophys J.* 2001; 81:2112-21.



Chapter

OPTOGENETICALLY-INDUCED MICROFOCI OF OXIDATIVE STRESS INCREASE PROARRHYTHMIC RISK

Iolanda Feola*, MSc; Wanchana Jangsangthong*, PhD;
Alexander Teplenin*, MSc; Martin J. Schalij, MD, PhD;
Dirk L. Ypey, PhD; Antoine A.F. de Vries, PhD; Daniël A. Pijnappels, PhD

Laboratory of Experimental Cardiology, Department of Cardiology, Heart
Lung Center Leiden; Leiden University Medical Center, the Netherlands.

*equal contribution

6

In preparation for submission

ABSTRACT

Introduction

Coronary microvascular dysfunction (CMD) is associated with oxidative stress (OS) and cardiac arrhythmias. However, the mechanisms of these arrhythmias remain obscure. We hypothesized that microfoci of excessive reactive oxygen species (ROS) production lead to local electrophysiological disturbances, thereby increasing pro-arrhythmic risk. To test this hypothesis, we used a unique combination of optogenetics and patterned illumination to precisely control ROS production in time and space.

Methods and results

Neonatal rat ventricular cardiomyocytes (NRVCs) were cultured and transduced with either lentiviral vectors encoding a plasma membrane-bound version of a photo-inducible ROS-generating protein (RGP) called miniSOG or control green fluorescence protein (GFP). ROS generation was induced by 470 nm light irradiation. The effects of ROS on cardiac electrophysiology were evaluated at single-cell and monolayer level. Upon irradiation, ROS levels were significantly increased in NRVCs expressing miniSOG (NRVC-miniSOG). Patch-clamp recordings showed that irradiation-induced changes in electrical activity of NRVC-miniSOG-PM in a time-dependent manner, like depolarization of resting membrane potential, early afterdepolarizations, and sustained depolarization. Optical voltage mapping of NRVC-miniSOG monolayers following irradiation of 0.75-6mm in diameter, circular areas revealed diameter- and time-dependent pro-arrhythmic effects ranging from AP prolongation, conduction slowing to functional conduction block with triggered activity. Importantly, electrical pacing of irradiated NRVC-miniSOG monolayers resulted in tachyarrhythmias sustained by a reentrant circuit anchored to the ROS-induced functional conduction block in 15 out of 60 cultures. None of these effects were observed in control cultures.

Conclusion

This is the first study to reveal a pro-arrhythmic role for microfoci of oxidative stress. Such microfoci lead to disturbances in electrical impulse generation and propagation, thereby enabling formation of reentrant tachyarrhythmias, and providing novel insight into the role of oxidative stress in arrhythmias.

Keywords

Regional oxidative stress, optogenetics, arrhythmias, reentry, optical mapping, patch-clamp.

INTRODUCTION

Coronary microvascular dysfunction (CMD) is characterized by structural¹ or functional² alterations of the inner wall of the coronary pre-arterioles and arterioles that can lead to spasms and decreased blood flow to the heart muscle.^{3,4} Such dysfunction might, therefore, be associated with patchily distributed myocardial ischemia⁵ and consequently with oxidative stress (OS), *i.e.* an overproduction of reactive oxygen species (ROS).^{6,7} Indeed, during an ischemic event, the mitochondria increase the ROS production because of a positive feedback called “ROS-induced ROS release”.⁸ Furthermore, several studies have shown that an additional ROS burst is mainly correlated with the blood reperfusion of the ischemic area.⁹⁻¹⁴ Although it is well known that ROS can give rise to electrophysiological alterations and therefore increase the risk of arrhythmia onset, the pathophysiological progression of such alterations in time and space remain poorly understood due to the lack of dedicated research tools. Indeed, thus far the regional ROS overproduction has been challenging to achieve as well as the investigation of its effects on cardiac electrophysiological properties. In this study, we used a photo-inducible ROS-generating protein (RGP),¹⁵ called miniSOG (mini singlet oxygen generator),¹⁶ and patterned illumination to spatially and temporally control ROS production, by blue-light illumination. Furthermore, miniSOG was targeted to the plasma membrane (PM) of neonatal rat ventricular cardiomyocytes (NRVC) to mimic the ROS release in the vicinity of cardiac ion channels/transporters. Such approach allowed us to investigate whether and how local OS could affect the electrophysiological properties of cardiac cells and thereby induce cardiac arrhythmias.

6

MATERIALS AND METHODS

An expanded Methods section is provided in the Supplemental Material.

In the present study, NRVCs were isolated, cultured and transduced with either lentiviral vectors encoding miniSOG-PM or eGFP-PM (Figure 1A). At day 2-4 post-transduction, ROS overproduction was induced by blue-light (470 nm) illumination and evaluated by fluorescent microscopy imaging, while its effects were investigated via patch-clamp recording and optical-voltage mapping experiments.

RESULTS

Light-induced oxidative stress in miniSOG-PM-NRVCs

ROS generation in NRVCs was assessed by using fluorescent imaging. As shown in Figure 1B and 1C, under normal growth conditions, the ROS level was not different in non-transduced NRVCs (control) and NRVCs expressing miniSOG-PM (miniSOG-PM) and eGFP-PM (eGFP-PM).

To examine whether blue light could contribute to ROS overproduction, miniSOG-PM-NRVCs, eGFP-PM-NRVCs, and control-NRVCs were exposed to blue light for 4 min. Following such illumination, only miniSOG-PM-NRVCs showed significantly increased in ROS production ($P < 0.001$) (Figure 1D and 1E). No significant changes were observed in eGFP-PM-NRVCs and control-NRVCs.

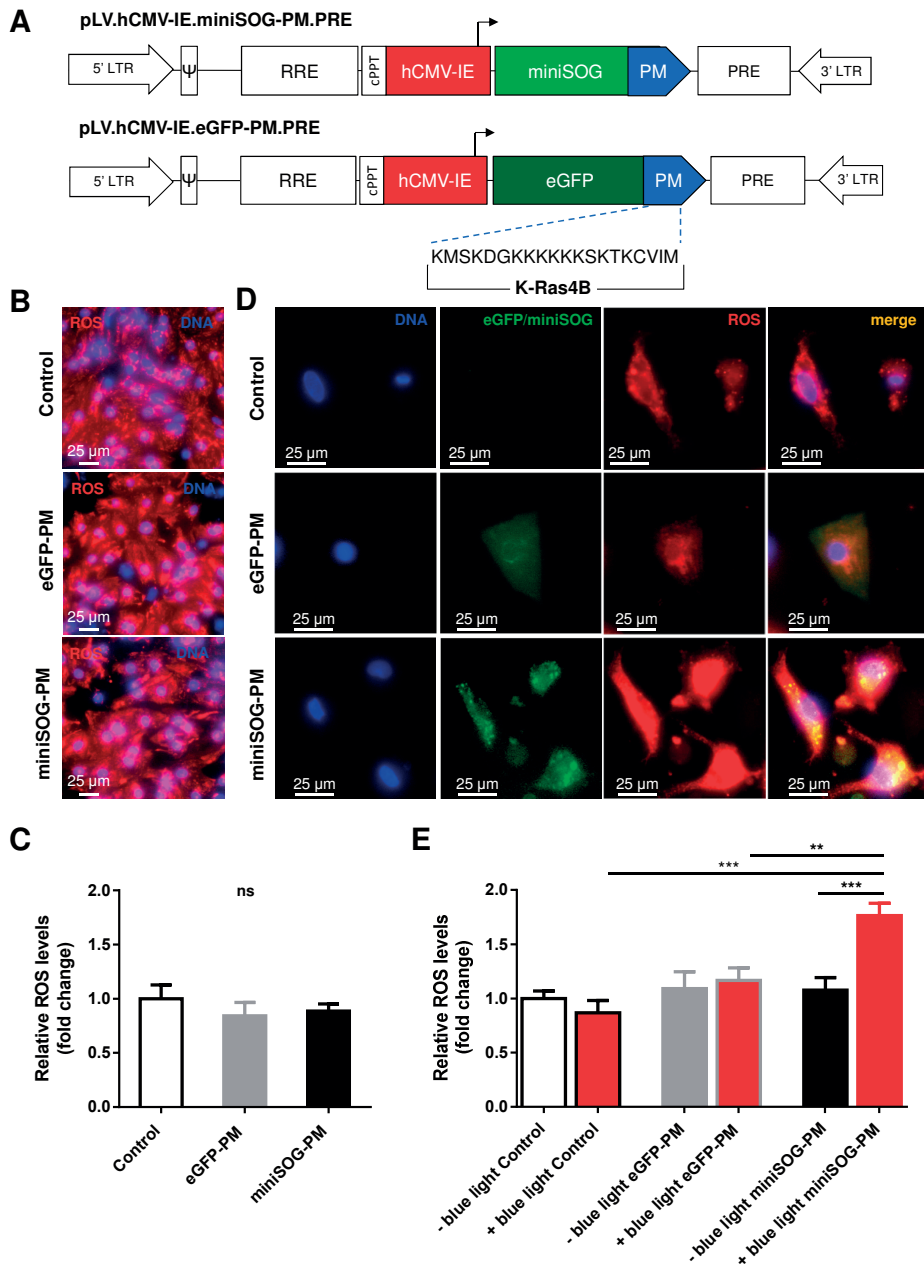


Figure 1. Lentiviral constructs and fluorescence microscopy of NRVCs. **A**, Proviral DNA structure of LV.miniSOG-PM (top) and LV.eGFP-PM (bottom) showing plasma membrane (PM) targeting domain that contains a C-terminal polybasic sequences of the K-Ras4B. The different abbreviations are explained in the paragraph designated 'Plasmid construction and self-inactivating lentiviral vector (SIN-LV) production' of the Supplementary material. **B**, Live-cell fluorescent images of a non-transduced NRVC monolayer (top, control), a LV.eGFP-PM-transduced NRVC monolayer (middle, eGFP-PM), and a LV.miniSOG-PM-transduced NRVC monolayer (bottom, miniSOG-PM) in the absence of 470-nm light. Cells were stained

- for nuclei (DNA; blue) and reactive oxygen species (ROS; red). Scale bar: 25 μm . C, Quantitative analysis of ROS levels detected in monolayers were assessed from red fluorescent signal. Bars show ROS level under normal growth condition (control, white, n=4; eGFP-PM, gray, n=6; miniSOG-PM, black, n=5). D, Live-cell fluorescent images were captured immediately following exposure to 470-nm light for 4 minutes from non-transduced NRVCs (top, control), eGFP-PM-NRVCs (middle, eGFP-PM) and miniSOG-PM-NRVCs (bottom, miniSOG-PM). These cells were stained for nuclei (DNA, blue) and ROS (red) using Hoechst 33342 and CellRox Deep Red reagent, respectively. Scale bar: 25 μm . E, Quantitative analysis of ROS levels detected in cells were assessed from red fluorescent signal. Bar graphs show basis ROS level under normal growth conditions (control, white, n=12; eGFP-PM, gray, n=11; miniSOG-PM, black, n=11). Corresponding filled red bars show ROS level following 470-nm light irradiation (control, n=10; eGFP-PM, n=7; miniSOG-PM, n=16). ** $P < 0.01$ and *** $P < 0.001$.

Electrophysiological characterization of miniSOG-PM-NRVCs

The baseline electrophysiological parameters of miniSOG-PM-NRVCs and eGFP-PM-NRVCs were characterized. First, perforated and whole-cell patch-clamp techniques were used to characterize such parameters in single NRVCs. Figure 2A shows action potentials (APs) recorded in the absence of blue light from a miniSOG-PM-NRVC (black trace) and a eGFP-PM-NRVC (gray trace). Both showed similar spontaneous activity, which is typical of NRVCs.¹⁷ Analysis of mean peak (Figure 2B) and mean steady-state (Figure 2C) total current-voltage (I-V) relationships reveals no difference between miniSOG-PM-NRVCs and eGFP-PM-NRVCs. These results indicate that such genetic manipulation did not change the electrophysiological properties of NRVCs under normal growth conditions.¹⁸

Next, optical-voltage mapping was performed to characterize the electrophysiological properties of eGFP-PM-NRVC and miniSOG-PM-NRVC monolayers. Upon 1-Hz electrical point stimulation, both eGFP-PM-NRVC and miniSOG-PM-NRVC monolayers showed uniform and convex APs propagation from the bipolar pacing electrode (Figure 2H).

No significant differences of action potential duration (APD) and conduction velocity (CV) were observed between eGFP-PM-NRVC and miniSOG-PM-NRVC monolayers; APD₃₀ was 128 \pm 9 ms vs 142 \pm 9 ms ($P=0.28$), APD₅₀ was 165 \pm 12 ms vs 186 \pm 13 ms ($P=0.24$), APD₈₀ was 276 \pm 19 ms vs 275 \pm 16 ms ($P=0.96$), and CV was 19 \pm 0.4 cm/s vs 18 \pm 0.6 cm/s ($P=0.31$). (Figure 2D-G and 2I).

Effect of regional oxidative stress in miniSOG-PM-NRVC monolayers

To evoke regional ROS overproduction in NRVC monolayers, a circular pattern (6 mm diameter) of constant blue light (470nm, 0.3 mW/mm²) was projected to the center of the monolayers for 2, 4 and 6 minutes (Figure 3A and 3B, left). The effects of ROS overproduction on electrophysiological properties were characterized during 1-Hz electrical stimulation. Figure 3B and the Supplementary Table I show that blue-light illumination did not significantly affect the electrical activity of eGFP-PM-NRVC monolayers. In contrast, obvious changes in electrical activity were observed in miniSOG-PM-NRVC monolayers upon blue-light illumination (Figure 3B-E). As shown in Figure 3C, following 2 minutes central illumination and 1-Hz electrical pacing of miniSOG-PM-NRVC monolayers, a significant prolongation in APD was

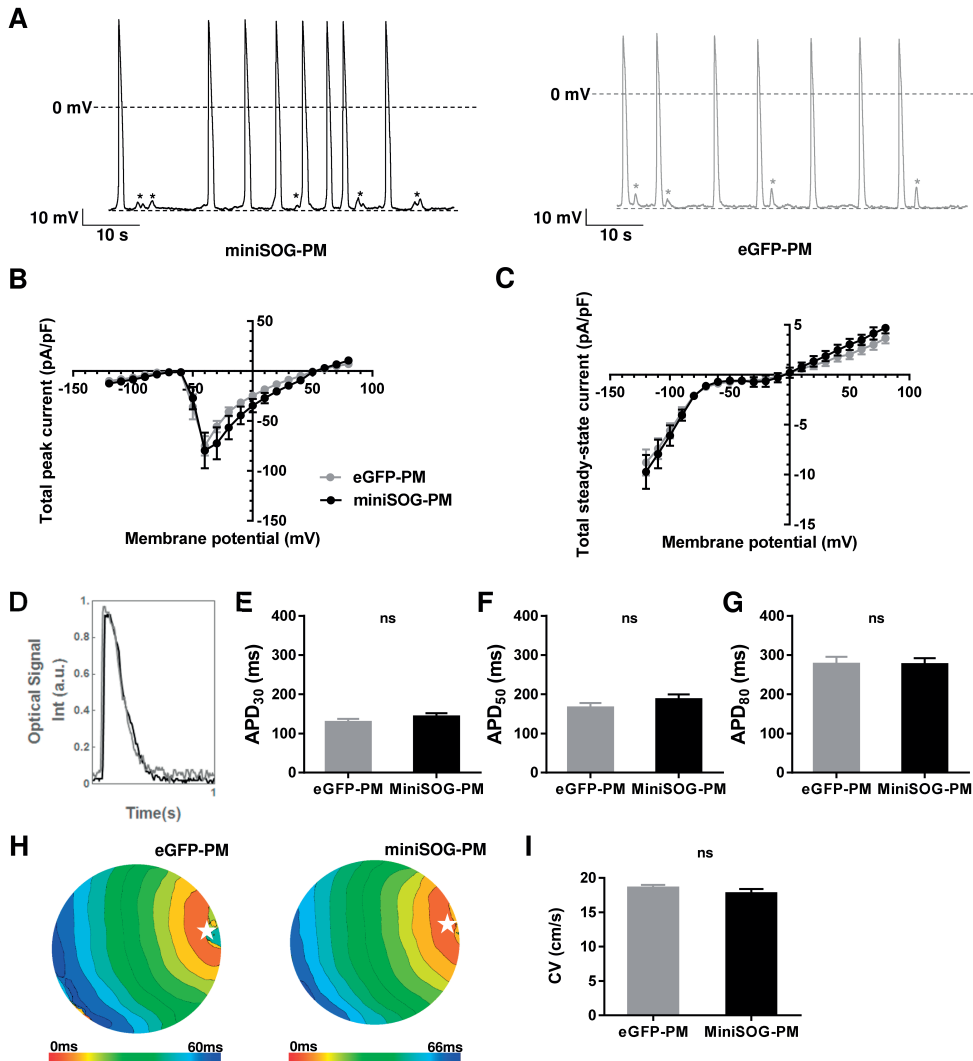


Figure 2. Characterization of single cells and 2-dimensional models of genetically engineered NRVCs. A, typical APs in a miniSOG-PM-NRVC (black) and an eGFP-PM-NRVC (gray). The recordings were obtained by perforated patch-clamp techniques. The voltage-current (I-V) curves of the peak (B) and steady-state (C) current density were expressed as the mean \pm SEM and derived from miniSOG-PM-NRVCs (filled black circle; $n=6$) and eGFP-PM-NRVCs (filled grey circle; $n=8$). B, was obtained from the current amplitudes at the beginning of each voltage steps, and (C) was obtained from steady-state currents at the end of 400-ms test pulses. To record the total membrane currents, 400-ms voltage pulses between -130 and +70 mV were applied in 10 mV increments every 5 s from the holding potential of -90 mV. D, optical signal traces of LV.eGFP-PM-transduced (grey) and LV.miniSOG-PM-transduced (black) NRVC monolayer cultures paced at 1-Hz. Quantification APD₃₀ (E), APD₅₀ (F), and APD₈₀ (G). H, Representative activation maps (6-ms isochrone spacing). I, Assessment of CV by optical-voltage mapping.

observed in the area exposed to blue light (the OS zone) when compared with non-exposed area (non-OS zone); APD_{30} was 161 ± 11 ms vs 304 ± 27 ms ($P < 0.001$), APD_{50} was 188 ± 15 ms vs 344 ± 39 ms ($P < 0.05$), and APD_{80} was 284 ± 25 ms vs 438 ± 50 ms. ($P < 0.05$), $n = 13$. When illumination time was extended to 4 minutes, the ultralong APD was observed in the OS zone of miniSOG-PM-NRVC monolayers during 1-Hz electrical pacing, and ectopic spontaneous activities were noted in 15 of 15 monolayers. As illustrated in Figure 3D, uniform propagation originating from the bipolar pacing electrode was observed during the first stimulus upon 1-Hz electrical pacing. Then, ectopic beats, which originated at a site of the border of the OS zone, initiated propagation, went outward and around the OS zone and terminated at the opposite side of their origin due to the collision of the wavefronts. Of note, the ectopic beats and 1-Hz electrical pacing stimuli were unable to propagate into the OS zone due to its sustained depolarization activity during 6 s data acquisition. Next, following illumination of miniSOG-PM-NRVC monolayers central area, we applied single electrical stimulus and continued monitoring of the depolarization duration of OS zone. Interestingly, we found a variation of the duration of ultralong APD (data not shown). When miniSOG-PM-NRVC monolayers were illuminated for 6 minutes, in addition to spontaneous ectopic activities found in 8 of 15 miniSOG-PM-NRVC monolayers, 7 of 15 of miniSOG-PM-NRVC monolayers exhibited conduction slow in the OS zone during 1-Hz electrical pacing. As shown in Figure 3E, decreased CV was observed in the OS zone. On average CV in the OS zone significantly decreased when comparing to the values before illumination (18 ± 0.4 cm/s vs 8 ± 0.4 cm/s [$P < 0.001$]). In contrast, the average CV in the non-oxidative stress zone did not change following blue-light illumination (18 ± 0.4 cm/s vs 18 ± 0.3 cm/s [$P = 0.7$]).

Additional experiments were conducted to estimate the minimum size of the OS zone needed to give rise to the ectopic phenomena previously described. Figure 4A shows photographs of miniSOG-PM-NRVC monolayers with 0.75-, 1.5- and 3-mm circular patterns of blue light in place.

Following illumination for 6 minutes, ectopic waves and ultra-long APD appeared and spread through the entire monolayer from the oxidative stress zone of 3- and 1.5-mm but not 0.75-mm, Figure 4A and B). Configuration rearrangement did not affect the initiation and propagation of ectopic waves (Figure 4A). Analysis of ectopic incident from 15 miniSOG-PM-NRVC monolayers confirmed that 3-mm circular pattern showed to be the most capable to give rise to spontaneous ectopic beats follow by 1.5-mm circular pattern, whereas the ectopic incident did not appear from 0.75-mm circular one (Figure 4C).

Effect of oxidative stress in single miniSOG-PM-NRVCs

Next, we performed perforated patch-clamp recordings to characterize the effect of OS on electrophysiological changes in single miniSOG-PM-NRVCs and eGFP-PM-NRVCs.

As shown in Figure 5A, which represents similar results from 5 other eGFP-PM-NRVCs, no changes in electrical activity were observed. In contrast, Figure 5B shows that irradiation of a miniSOG-PM-NRVC caused marked changes in electrical activity. We observed the occurrence of changes on second-time scale (14.61 ± 5.28 s; $n = 9$). The rapid progression of changes

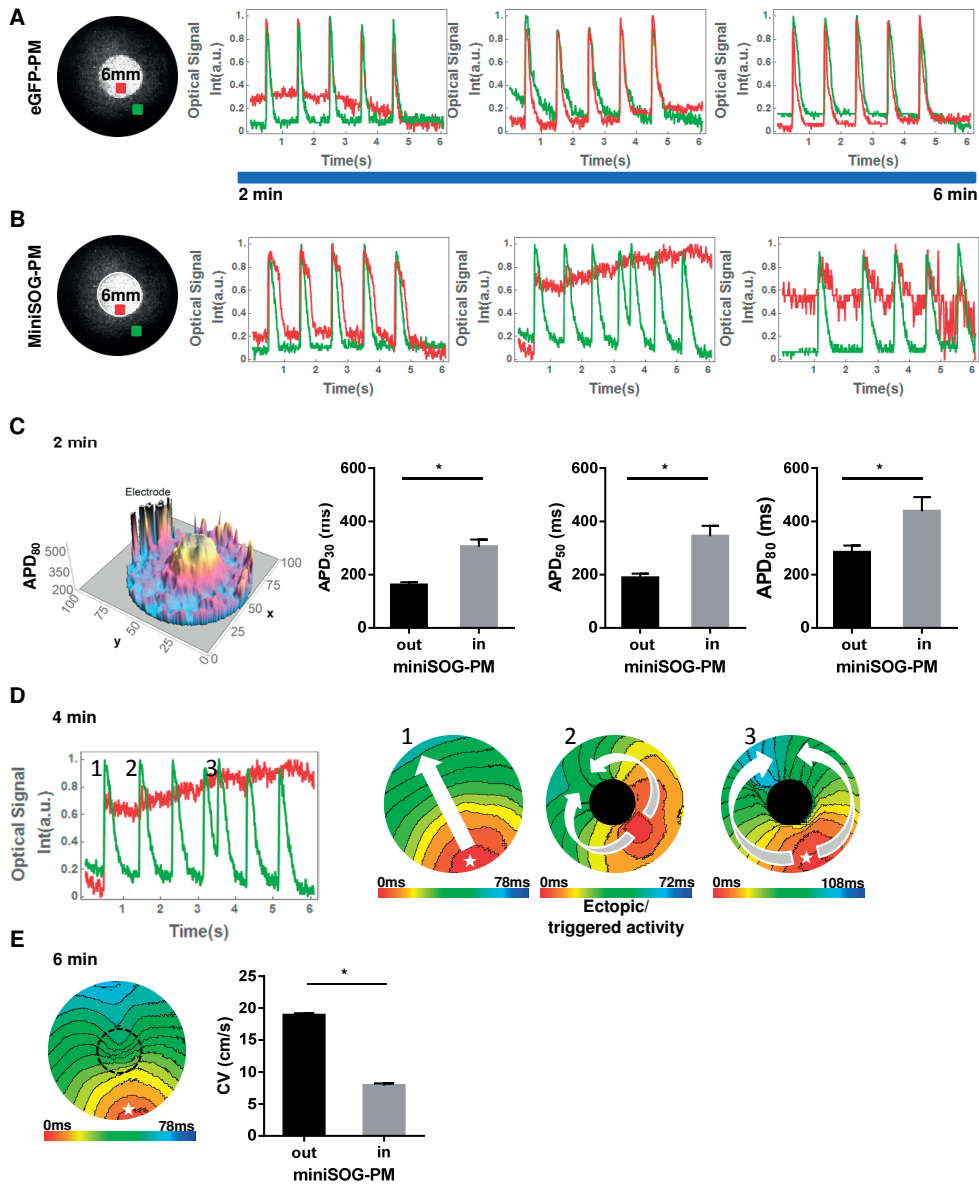
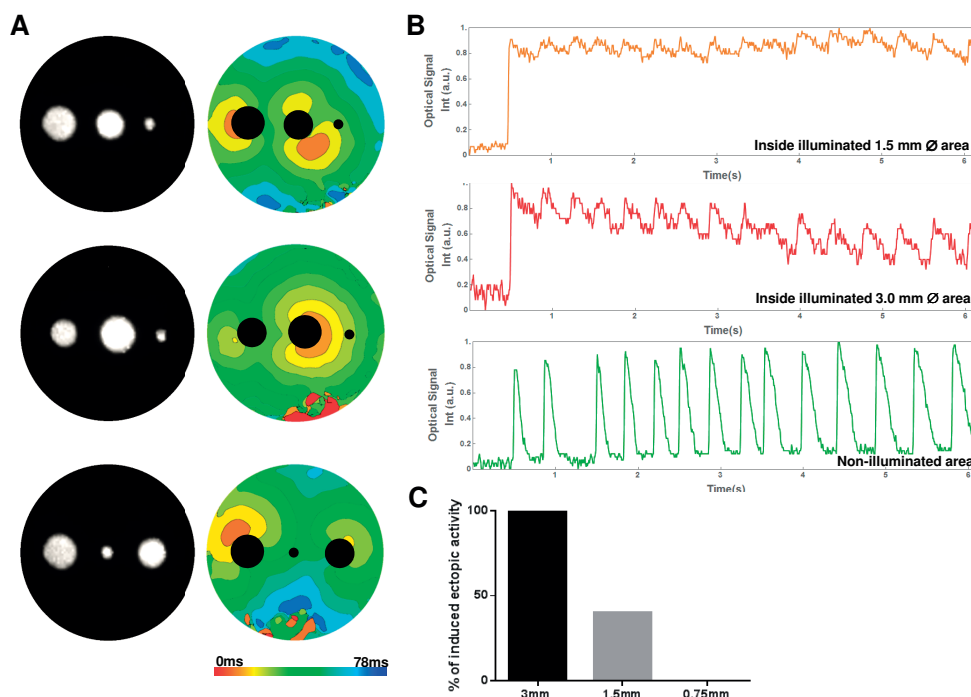


Figure 3. Regional elevated ROS production alters cardiac electrophysiology and leads to disturbances of electrical impulse generation and propagation. A and B, Screenshot of round NRVC monolayers (15-mm-diameter) (left) transduced with LV.eGFP-PM (A) and LV. miniSOG-PM (B), showing a circle and central area (6-mm diameter), which was exposed to 470-nm light. Optical traces (right) show light dosage-dependent effects on the electrical activity. Optical signal traces in green and red are representing non-irradiated and irradiated areas. C, 3-dimensional APD map shows the prolongation occurring only in the circular and central area exposed for 2 minutes to 470-nm light in the miniSOG-PM-NRVC monolayers (left). This map shows bell-shape like distribution of APD values inside OS zone, with the highest APD values in the center of the area. Comparison of APD₃₀, APD₅₀, APD₈₀ between irradiated and non-irradiated areas (right). n=10, *P<0.05. D, Typical optical trace (left) showing the ultra-long APD and triggered beats

▶ occurring when miniSOG-PM-NRVC monolayers were electrically paced at 1Hz after 4 minutes 470-nm light exposure. The activation maps (right) are showing the uniform propagation of the electrical stimulus originating from the bipolar pacing electrode, the triggered ectopic beat originated at a site of the border of the OS zone, and a subsequent electrical stimulus that could be elicited but could not propagate in the OS zone due to the ultralong APD. D, Activation map (left) showing the conduction slowing occurring only in the irradiated area of miniSOG-PM-NRVC monolayers exposed to 470-nm light for 6 minutes (7 out of 15). Comparison of CV between irradiated and non-irradiated area (right). (n=7), *P<0.001.



6

Figure 4. Size threshold of regional elevated ROS area for generation of ultralong APD and ectopic beats in miniSOG-PM-NRVC monolayers. **A**, Screenshot of round NRVC monolayers (15-mm-diameter) showing 3 circular areas under light exposure (3-1.5-0.75 mm diameter) arranged in 3 different configurations (left). **B**, The activation maps are showing that upon 6 minutes irradiation ectopic triggered beats could be originated only from the 3 and 1.5 mm size circular areas. **C**, Optical traces from non-irradiated (green) and irradiated areas, 3 mm in red and 1.5 mm in orange. Red and orange traces show the ultralong APD, the green trace shows ectopic beats. **D**, Comparison of the incidence of ectopic beats originating from the areas with different diameters.

consisted of an initial shift in membrane potential from -73.71 ± 0.78 mV to -66.86 ± 1.30 mV ($n=9$; $P<0.001$), the APD prolongation with the occurrence of early afterdepolarizations (EADs) (Figure 5B, a), and a sustained depolarization (Figure 5B, b). The sustained depolarization began with an AP that strongly depolarized the membrane potential. Then, membrane potential gradually declined on a timescale of minutes to a sustained depolarization between -30 and -10 mV. Similar results were obtained in other 8 miniSOG-PM-NRVCs. These findings suggested

a dose-dependent effect of ROS overproduction to cause a rapid, pronounced and dynamic alteration of electrical activities in response to irradiation time.

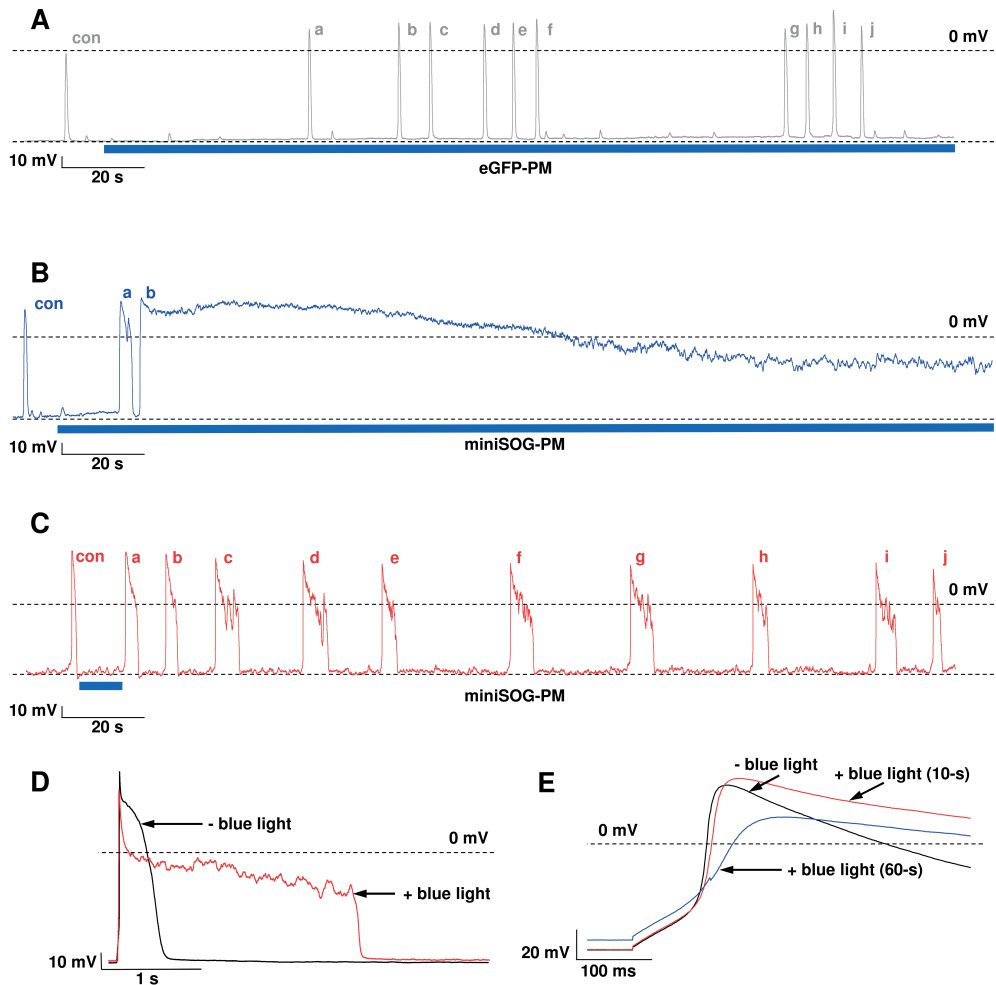
We hypothesized that the longer irradiation of miniSOG-PM-NRVC led to higher amount of ROS production and thereby progressively altering its electrical activity. To test this, we reduced the irradiation time to 10-s. Likewise, Figure 5C shows that brief irradiation of miniSOG-PM-NRVC was capable to markedly lengthen APD and caused the occurrence of EADs before spontaneous recovery of the resting membrane potential (RMP). After 4-5 minutes, AP shortening progressively appeared, as shown in Figure 5C, AP j. Moreover, following irradiation, a subsequent decline in AP amplitude and plateau potential were also observed (Figure 5C and 5D). Whereas, the depolarization of RMP and a sustained depolarization after an AP were not noticed. These findings were similar in 3 other miniSOG-PM-NRVCs.

To further characterize the dosage-dependent effects of ROS on AP alteration, we additionally performed whole-cell recordings in 3 miniSOG-PM-NRVCs.

As shown in Figures 5E, in comparison with the AP recorded in the absence of blue light (black trace), increased ROS overproduction corresponding to irradiation-time not only affected AP amplitude but also reduced AP upstroke velocity, which observed in short (10-s; red trace) and long (60-s; blue trace) irradiation. Moreover, long exposure to blue light caused depolarization of RMP. These results confirmed our findings from perforated-patch recordings and verified the dosage-dependent effect of an elevated ROS to alter cardiac electrical activities.

Since miniSOG is targeted to PM, locally ROS overproduction in the vicinity of cardiac ion channels/transporters can be assumed upon illumination of the miniSOG-PM-NRVCs. Therefore, a possible explanation for the electrophysiological changes could be directly implicated to the effect of ROS on cardiac ion channels/transporters. To investigate this, we performed whole-cell voltage-clamp recording before and after blue-light irradiation in miniSOG-PM-NRVCs to characterize the changes in membrane ionic current. As expected, when a miniSOG-PM-NRVCs was exposed to blue light, excessive ROS was generated and markedly modulated total membrane currents during the voltage-step recording (Supplementary Figure 1). Because the changes in electrical activity induced by ROS were dynamic and occurred very rapid, alterations in the magnitude of whole-cell currents may be expected. Therefore, a ramp protocol that required less time for data acquisition was designed to deliberate current produced by cell over the potentials between -130 mV and +50 mV and introduced to examine 4 miniSOG-PM-NRVCs in order to obtain a quasi-steady-state I-V relationship. This type of plots was used by Qu and Chung to explain the mechanisms underlying the roles of different ionic currents on APD lengthening and EAD genesis in a mathematical model of cardiac myocyte.¹⁹ Figure 6A shows the representative quasi-steady-state currents recorded from a miniSOG-PM-NRVC before (black trace) and after 10-s (red trace) and 60-s (blue trace) blue-light irradiation. The circles in Figure 6A depict the quasi-equilibrium states, where the total outward currents equal to the total inward currents. The black one approximately at -70 mV is the resting potential. The gray and open circles show quasi-equilibrium states at the plateau voltage. In comparison with control (black trace), the quasi-equilibrium state at the plateau voltage is enlarged and occupied longer voltage length following 10-s blue-light irradiation (red trace).

Optogenetic induction of microfoci of oxidative stress



6

Figure 5. Effect of elevated ROS on the electrical activity of single spontaneous beating NRVCs. Perforated patch-clamp technique was employed to record and monitor spontaneous electrical activity of NRVCs for ≥ 4 minutes. **A**, electrical activity of an eGFP-PM-NRVC (eGFP-PM) during continuous irradiation with 470-nm light. The typical action potentials (APs) are observed before (con) and after the start of continuous illumination (a-j). **B**, electrical activity of a miniSOG-PM-NRVC (miniSOG-PM) during continuous illumination with 470-nm light. The rapid progression from a normal AP (con) ranging from the slight resting membrane potential depolarization and lengthening AP duration (APD) with an early afterdepolarization (EAD) (a) to a failure to repolarize (b) are observed. **C**, electrical activity of a miniSOG-PM-NRVC following brief exposure (10-s) to 470-nm light. The following alterations in electrical activity were observed: in a and b, APD prolongation; in c-i, decline in AP amplitude, oscillation in plateau phase with the occurrence of EADs, and prolongation of APD; in j, APD shortening. **D**, the effect of ROS on AP amplitude and plateau potential and APD observed in a miniSOG-PM-NRVC. Black trace illustrates the AP recorded in the absence of 470-nm light, and red trace shows the AP recorded following 470-nm-light illumination. **E**, light dosage-dependent effects on reduction of AP upstroke velocity and amplitude. A miniSOG-PM-NRVC was stimulated by square current pulses (100-pA, 5-ms) to evoke the APs just before (control, black trace) and at two times after the start of 470-nm-light illumination; brief irradiation (10-s, red trace) and continuous irradiation (60-s, blue trace).

Suggesting that elevated ROS significantly alter the inward current, and this current can then act against the unchanged or slightly elevated outward currents to maintain the plateau phase of AP thereby leading to AP lengthening. Since voltage-dependent L-type Ca^{2+} channels ($\text{Ca}_v1.X$) play the main role to generate the inward current during the plateau, elevated ROS may have the effects on $\text{Ca}_v1.X$ gating and thus the window L-type Ca^{2+} current (I_{CaL}).

To examine whether the changes in membrane inward current carried mainly by I_{CaL} could be induced by elevated ROS, we performed voltage-clamp experiments in 5 miniSOG-PM-NRVCs using conventional step-type voltage-clamp protocols. We found that the alteration of the quasi-equilibrium states at the plateau was not only due to the change of I_{CaL} kinetics but also the increase of I_{CaL} (Figure 6B).

Furthermore, some specific changes in another inward current carried by mainly voltage-dependent Na^+ current (I_{Na}) including the alteration in peak current and inactivation kinetics (Figure 6C) were also observed following blue light irradiation. These findings suggest that the presence of late I_{Na} in combination with alteration of window I_{CaL} help the formation of the quasi-equilibrium states at the plateau voltage, which may be responsible for the underlying mechanism of elevated ROS causing ultralong APD and EADs. In addition, when OS was further increased by extending irradiation-time to 60 s, we observed the further alteration of the quasi-equilibrium states. As shown in Figure 6A, blue trace, the lower two quasi-equilibrium states disappear and the only equilibrium state for the upper plateau voltage remains. This indicates the loss of the equilibrium state for the resting potential thereby the membrane voltage cannot decrease to the physiological RMP due to the decline of mainly resting K^+ current (I_{K1}). Moreover, increase in outward current positive to -10 mV and negative shift in holding current were observed. Suggesting the presence of leak current, which favors a failure to repolarize after an AP thereby leading to a sustained depolarization around the remained quasi-equilibrium voltage.

6

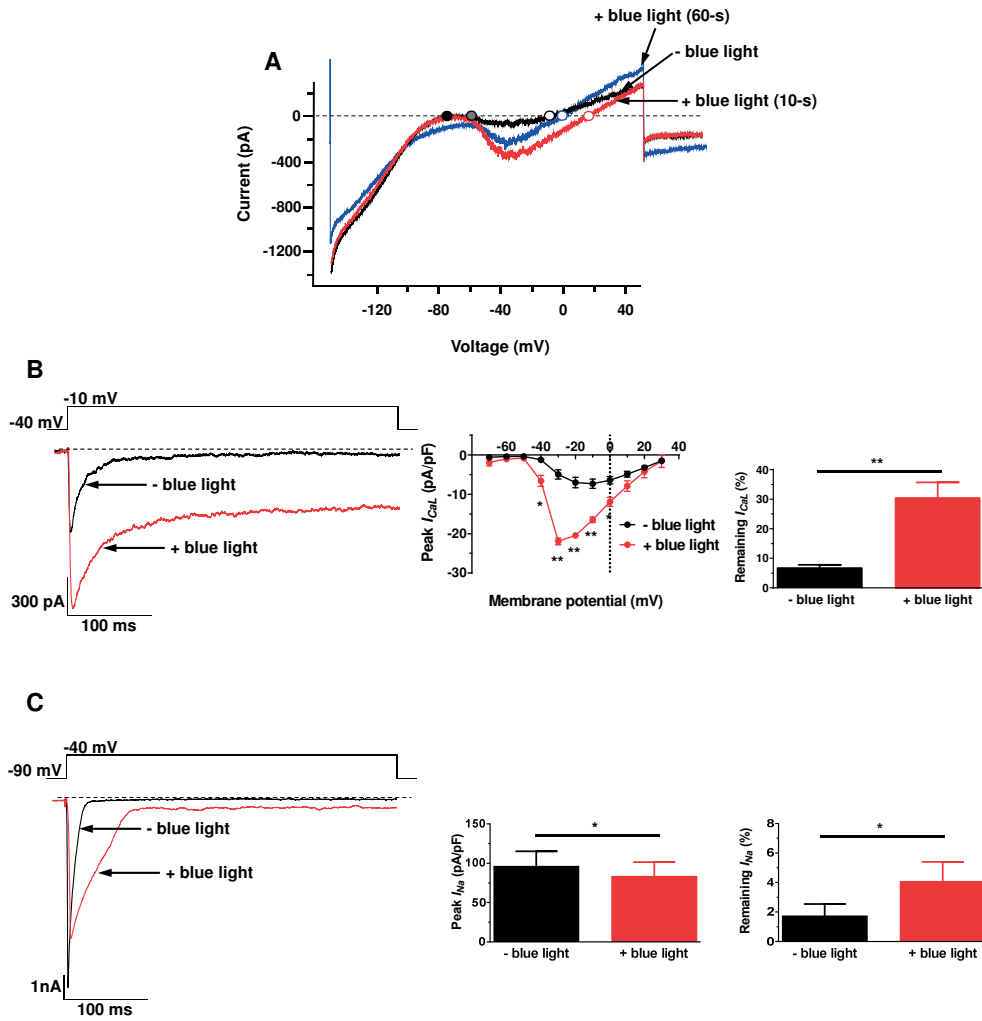
Effect of regional oxidative stress on arrhythmias in miniSOG-PM-NRVC monolayers

Finally, we investigated the effect of the regional OS on arrhythmogenesis in miniSOG-PM-NRVC monolayers. Based on our finding described above, we employed paced beats that developed from the bipolar pacing electrode placed somewhere along the periphery of the monolayer to initiate reentry. Two different strategies to induce reentry, namely, “ectopic stimulation” and “burst pacing” were utilized.

As shown in Figure 7A (left) and 7C (left), for both reentry inducing approaches, first paced beat was capable to uniformly propagate through the entire monolayers. In line with the result as shown in Figure 5D, following first paced beat, sustained depolarization and extremely APD prolongation (2-24 s) were observed in the OS zone. Corresponding optical traces for OS zone (red) and non-OS zone (green) are shown in Figure 7B and 7D.

For ectopic stimulation approach as shown in Figure 7A (middle), we observed the propagation of ectopic beat as described in Figure 3D. Therefore, we applied a properly timed electrical paced beat to face the refractory tail of the ectopic beat leading to developing of

Optogenetic induction of microfoci of oxidative stress



6

Figure 6. Effects of ROS on the quasi-equilibrium states and ionic currents of miniSOG-PM-NRVCs. **A**, the quasi-steady-state I-V curves of a miniSOG-PM-NRVC recorded before (black) and after 10-s (red) and 60-s (blue) blue-light illumination. These I-V curves were evoked by ramping membrane potential between -130 and +50 mV over 8 seconds from holding potential of -90 mV. **B**, Left: current traces representing mainly I_{CaL} recorded from the holding potential (V_h) = -40 mV stepped to -10 mV for 400-ms obtained before (black) and after 10-s (red) blue-light illumination. While performing this recording, I_{Na} I_{CaT} are inactivated by V_h . **B**, Middle: comparison of I-V curves of peak I_{CaL} derived before (black) and after 10-s (red) exposure to blue light, $n=5$. **B**, Right: quantitative analysis of remaining I_{CaL} at 350-ms derived before (black) and after 10 s (red) blue- light illumination, $n=5$. **C**, Left: current traces representing mainly I_{Na} elicited by stepping to -40 mV from a V_h of -90 mV for 400-ms obtained before (black) and after 10-s (red) 470-nm-light illumination. **C**, Middle: quantitative analysis of maximum peak I_{Na} density derived before (black) and after 10-s (red) exposure to blue light, $n=5$. **C**, Right: quantitative analysis of remaining I_{Na} at 350-ms derived before (black) and after 10 s (red) blue-light illumination, $n=5$. * $P<0.05$ and ** $P<0.01$.

uni-directional conduction block, which resulted in the initiation of a ring-like reentrant wave rotating around the OS region (Figure 7A [right]).

For burst pacing approach, following first paced beat, we electrically paced the highest possible frequency that led to 1:1 capture (Figure 7A, middle). Thereby, initiation of ectopic beat was not observed. However, continued high-frequency electrical pacing developed a uni-directional conduction block and successfully induced ring type reentry (Figure 7C [right] a).

As shown in Figure 7E, we induced and observed stable reentry (lasting ≥ 6 s) in 6 out of 30 and 9 out of 30 miniSOG-PM transduced NRVC monolayers by means of ectopic stimulation and burst pacing stimulation, respectively. In addition, we also induced and observed unstable

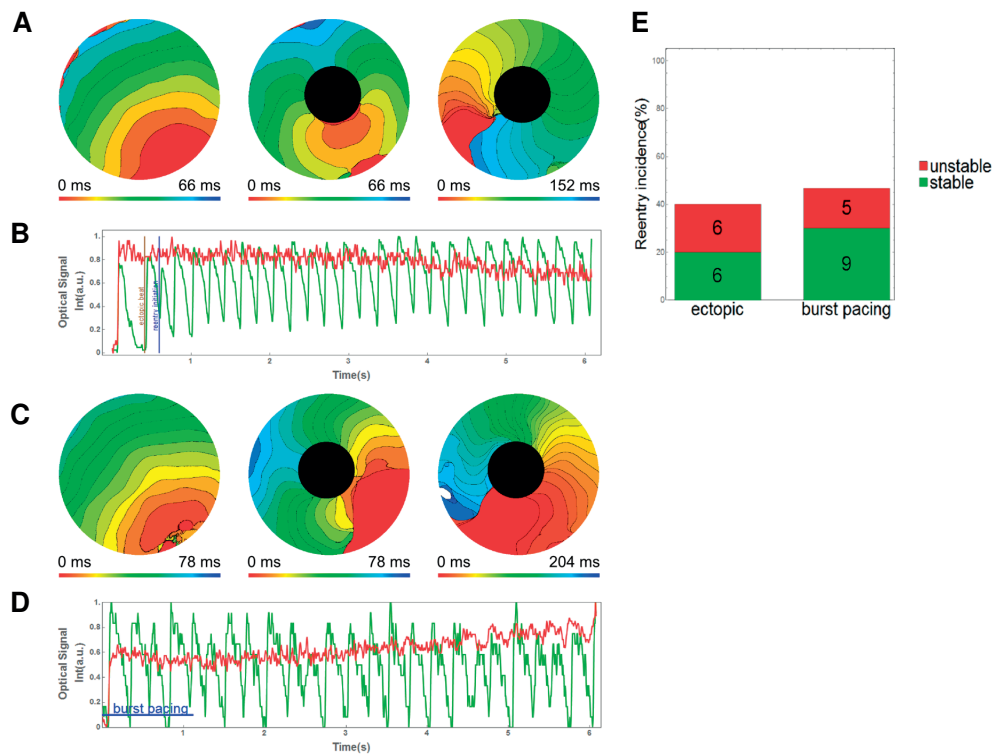


Figure 7. Regional elevated ROS production causes reentry arrhythmias in miniSOG-PM-NRVC monolayers. A and B, Activation maps (A) and optical traces (B) showing the ‘ectopic beat’ protocol employed to induce ring-like reentrant wave rotating around the OS region. After the first electrical stimulus and the consequent triggered ectopic beat, a second electrical stimulus was applied. The proper timing allowed to face the refractory tail of the ectopic beat leading to uni-directional conduction block and reentry establishment. C and D, Activation maps (C) and optical traces (D) showing the ‘burst pacing’ protocol employed to induce ring-like reentrant wave rotating around the OS region. After the first electrical stimulus monolayers were electrically paced at the highest possible frequency that led to 1:1 capture, uni-directional conduction block, and reentry establishment. E, Quantification of stable and unstable reentry initiation for both type of protocols.

or self-terminating reentry episodes (lasting for 2-4 s): 6 for ectopic stimulation and 5 for burst pacing (Figure 7E).

DISCUSSION

Coronary microvascular dysfunction (CMD) is characterized by abnormalities in the coronary blood flow that can lead to myocardial ischemia and therefore to oxidative stress (OS).^{6,7} Such ischemic events are localized in small myocardial areas, *i.e.* patchily distributed in the myocardium.⁵ Furthermore, since those little foci are surrounded by myocardial tissue that is normally functioning, CMD is very difficult to be detected and investigated. In the present study, a photo-inducible ROS-generating protein (RGP),¹⁵ called miniSOG,¹⁶ was used in combination with patterned illumination to create localized areas of OS and investigate whether and how those areas could induce electrophysiological alterations and thereby increase proarrhythmic risk. One of our main motivations to study the effect of local OS was to improve our understanding of its role in cardiac arrhythmias, in a way that was not possible before.

In our study, optical-voltage mapping and patch-clamp experiments showed that the exposure of miniSOG-PM-NRVC cultures to blue light led to an increased intracellular ROS level that caused electrophysiological changes in a dose-dependent manner.

At single-cell level, we found that increased OS depolarized the membrane, depressed AP amplitude, lengthened APD, caused oscillation in the membrane potential during the plateau, EADs, and repolarization failure. In monolayers, we observed time- and diameter-dependent pro-arrhythmic effects of the OS area ranging from electrophysiological changes (APD lengthening, slowed conduction) to arrhythmogenic consequences (functional conduction block, ectopic beats, reentry). Those alterations have been also described in other studies, where different experimental models were used.²⁰⁻²⁶ However, our approach allowed us to localize OS in areas of different dimensions, which could not be achieved, for instance, by means of global administration of primary ROS or ROS-generating reagents (*e.g.* potassium superoxide, hydrogen peroxide (H₂O₂) and xanthine/xanthine oxidase).

The main ROS in cardiac myocytes exists of free radical species, such as superoxide anion (O₂^{·-}) and hydroxyl radical (·OH), or of nonradical species, such as H₂O₂, ¹O₂ and nitrogen species.²⁷ MiniSOG generates ¹O₂ which is an oxygen molecule with an unpaired electron at the higher orbital. Such property makes ¹O₂ highly reactive and believed to be one of the most damaging species. Furthermore, it is characterized by limited diffusion and lack of selectivity. Because of the aforementioned characteristics, ¹O₂ is capable to react in the immediate vicinity of its generation. Moreover, since ¹O₂ is generated by lipid peroxidation of the plasma membrane via other ROS,^{28, 29} in this study, miniSOG was targeted to the cardiac cell membrane to mimic ¹O₂ natural localization, *i.e.* in the vicinity of cardiac ion channels/transporters. Based on this approach, we can attribute the observed electrophysiological alterations to ROS-induced modification of cardiac ion channels. However, we cannot rule out the effects of ROS on a dramatic increase in intracellular Ca²⁺ [Ca²⁺]_i by an increased diastolic Ca²⁺ leak through enhanced ryanodine receptor (RyR2) open probability, which leads together with dysfunctional

sarcoplasmic reticulum (SR) Ca^{2+} ATPase (SERCA2a) to reduced SR Ca^{2+} load. This coupled with an influx of Ca^{2+} through the damaged sarcolemma would cause an increase in free $[\text{Ca}^{2+}]_i$ which can, in turn, initiate arrhythmias.^{27,30,31} Indeed, our optical mapping of $[\text{Ca}^{2+}]_i$ showed that the $[\text{Ca}^{2+}]_i$ transient was dramatically prolonged following exposure of miniSOG-PM-NRVC monolayers to blue light due to ROS overproduction (Supplementary Figure 2).

MiniSOG has been originally employed in cell ablation experiments because of its toxic effects.^{16,32} To avoid such permanent damage we chose durations of irradiation that led to sub-lethal ROS generation and allowed us to reveal a dose-dependent effect of ROS on cardiac electrophysiological alterations and arrhythmias.

On the basis of single-cell experiments, we found that the electrophysiological alterations might involve specific changes in membrane ionic currents, *i.e.* I_{K1} , I_{Na} , I_{CaL} and nonselective cation current (I_{NSC}). The alterations, such as the positive shift in RMP of ≥ 5 mV and the lengthening in AP duration, might be due to a reduction in resting K^+ current through I_{K1} (Figure 6A, blue trace), which may indicate a decrease in the channel open probability under OS.^{33,34} Furthermore, alterations in amplitude, plateau and repolarization phases of an AP may involve changes in I_{Na} , I_{CaL} , and I_{NSC} , which have been already described to be affected by OS.³⁵ It has been reported that Na^+ channel oxidation not only causes a gradual reduction in I_{Na} , but also results in a slowing of inactivation referred as a late I_{Na} component.^{27,36} Therefore, ROS-enhanced late I_{Na} could contribute to the accumulation of intracellular Na^+ , AP prolongation, EADs, and arrhythmias.^{20,30,36} Although redox modification of $\text{Ca}_v1.X$ modulation still remains a matter of debate since ROS can result both in increased and decreased I_{CaL} , depending on the type, level and location of ROS generation,³⁰ our findings likely replicate redox modifications that lead to an increased in I_{CaL} . This suggests that ROS overproduction can alter biophysical properties of I_{CaL} , resulting in significant alteration of the quasi-equilibrium states at the plateau, thereby promoting AP lengthening and EADs occurrence.¹⁹ These EADs were characterized by oscillations with increasing amplitude towards the end of the AP (Figure 5C). Such increase in amplitude is similar to the observation by Song *et al*, who linked this phenomenon to Ca^{2+} overload, increased I_{CaL} and the leakage of RyR2.³⁷ In our study, we cannot rule out the possibility that stress kinases, like cAMP-dependent protein kinase A (PKA), protein kinase C (PKC), and Ca^{2+} /calmodulin-dependent protein kinase II (CaMKII), can activate both I_{Na} and I_{CaL} by phosphorylation, because all three kinases are subject to ROS-dependent oxidation/activation.^{20,32,33} The sustained depolarization resulted from ROS may be attributed to the activation of I_{NSC} . The activation of this leak current, would be expected to cause a concomitant decline in AP amplitude, plateau potential and delayed repolarization, as observed in Figure 5D. Therefore, given the consequences of ROS-induced electrical alteration following blue light irradiation, we presume that severe activation of I_{NSC} would add to repolarization failure as demonstrated in Figure 5B.

At the monolayers level, we show that miniSOG-PM-NRVC monolayers were characterized by abnormalities in the generation and/or propagation of electrical impulses when regional OS was generated by patterned blue-light illumination.

We show that perturbed AP propagation in miniSOG-PM-NRVC monolayer occurs when the OS zone exhibits extremely APD lengthening or conduction slowing. Here, APD

lengthening is characterized by a quasi-stable depolarized state, lasting from 2 to 24 seconds (data not shown). This is in line with the incidence of ultralong APD and EADs observed at single-cell level. Therefore, the presence of ultralong APD in the OS zone in miniSOG-PM-NRVC monolayer may act as a functional disturbance of cardiac electric impulse propagation (functional conduction block) during sinus rhythm. The slow conduction observed here could be also explained with single-cell data, *i.e.* significant reduction in I_{Na} peak current and shift in RMP. In addition, ROS might play a role in gap junction dysfunction. Indeed, during regional OS, ROS may affect the balance of stress kinases and phosphatases in a way that favors the dephosphorylation of connexin 43 (Cx43), which would result in a decrease in gap junctional conductance, thereby contributing to persistent CV slowing in the OS zone.

Disturbance in AP generation, as shown here, were characterized by abnormal automaticity (ectopic beats) arising from the OS border zone of miniSOG-PM-NRVC monolayers. The regionally confined OS zone was characterized by APD prolongation and EADs, which might depolarize the neighboring cardiomyocytes, localized in the non-OS zone, giving rise to triggered activity. The phenomenon of heterogeneity of APD causing ectopic activity has been described in atrial myocytes by Nattel *et al.*³⁸

In conclusion, this study revealed that microfoci of OS lead to disturbances in both electrical impulse generation (*i.e.* EADs, ectopic beats) and propagation (*i.e.* functional conduction block and slowing), thereby favoring reentrant arrhythmia formation. These results provide novel insight into the role of microsubstrates in arrhythmogenesis, which are substrates still left undetectable, and therefore untreated if present, in the current clinical setting.

6

ACKNOWLEDGMENTS

We thank Cindy Bart (Department of Cardiology, LUMC) for assistance with the animal experiments and Annemarie Kip (Department of Cardiology, LUMC) for LV production.

SOURCES OF FUNDING

This work was supported by the Netherlands Organisation for Scientific Research (NWO, Vidi grant 91714336 to D.A.P.). Additional support was provided by Ammodo (D.A.P. and A.A.F.d.V.).

DISCLOSURES

None.

REFERENCES

1. Opherk D, Zebe H, Weihe E, Mall G, Durr C, Gravert B, Mehmel HC, Schwarz F, Kubler W. Reduced coronary dilator capacity and ultrastructural changes of the myocardium in patients with angina pectoris but normal coronary arteriograms. *Circulation*. 1981; 63:817–825.
2. Richardson PJ, Livesley B, Oram S, Olsen EG, Armstrong P. Angina pectoris with normal coronary arteries: transvenous myocardial biopsy in diagnosis. *Lancet*. 1974; 2:677–680.
3. Camici PG, d'Amati G, Rimoldi O. Coronary microvascular dysfunction: Mechanisms and functional assessment. *Nat.Rev.Cardiol*. 2015; 12:48–62.
4. Anderson RD, Pepine CJ. The coronary microcirculation in stemi: The next frontier? *Eur.Heart J*. 2015; 36:3178–3181.
5. Maseri A, Crea F, Kaski JC, Crake T. Mechanisms of angina pectoris in syndrome X. *J Am Coll Cardiol*. 1991; 17:499–506.
6. Giordano FJ. Oxygen, oxidative stress, hypoxia and heart failure. *J Clin Invest*. 2005; 115:500–508.
7. Lucchesi BR. Free radicals and tissue injury. *Dialogues Cardiovasc Med*. 1998; 3:3–22.
8. Zorov DB, Filburn CR, Klotz LO, Zweier JL, Sollott SJ. Reactive oxygen species (ROS)-induced ROS release: a new phenomenon accompanying induction of the mitochondrial permeability transition in cardiac myocytes. *J Exp Med*. 2000; 192:1001–1014.
9. Hess ML, Manson NH. Molecular oxygen: friend and foe. The role of the oxygen free radical system in the calcium paradox, the oxygen paradox and ischemia/reperfusion injury. *J Mol Cell Cardiol*. 1984; 16:969–85.
10. Park JL, Lucchesi BR. Mechanisms of myocardial reperfusion injury. *Ann Thorac Surg* 1999; 68:1905–12.
11. Kilgore KS, Luchessi B.R. Reperfusion injury after myocardial infarction: the role of free radicals and the inflammatory response. *Clin. Biochem*. 1993; 359–370.
12. Zughuib ME, Tang XL, Sun JZ, Bolli R. Myocardial reperfusion injury: fact or myth? A 1993 appraisal of a seemingly endless controversy. *Ann. New York Acad. Sci*. 1994; 723:218–228.
13. Ambrosio G, Tritto I. Reperfusion injury: experimental evidence and clinical implications. *Am. Heart J*. 1999; 138:S69–S75.
14. Weisfeldt ML, Zweier J, Ambrosio G, Becker LC, Flaherty JT. Evidence that free radicals result in reperfusion injury in heart muscle. *Basic Life Sci*. 1988; 49:911–919.
15. Wojtovich AP, Foster TH. Optogenetic control of ros production. *Redox.Biol*. 2014;2:368–376.
16. Shu X, Lev-Ram V, Deerinck TJ, Qi Y, Ramko EB, Davidson MW, Jin Y, Ellisman MH, Tsien RY. A genetically encoded tag for correlated light and electron microscopy of intact cells, tissues, and organisms. *PLoS.Biol*. 2011; 9:e1001041.
17. Boink GJ, Verkerk AO, van Amersfoort SC, Tasseron SJ, van der Rijt R, Bakker D, Linnenbank AC, van der Meulen J, de Bakker JM, Seppen J, Tan HL. Engineering physiologically controlled pacemaker cells with lentiviral hcn4 gene transfer. *J.Gene Med*. 2008; 10:487–497.
18. Engels MC, Askar SF, Jangsangthong W, Bingen BO, Feola I, Liu J, Majumder R, Versteegh MI, Braun J, Klautz RJ, Ypey DL, De Vries AA, Pijnappels DA. Forced fusion of human ventricular scar cells with cardiomyocytes suppresses arrhythmogenicity in a co-culture model. *Cardiovasc.Res*. 2015; 107:601–612.
19. Qu Z, Chung D. Mechanisms and determinants of ultralong action potential duration and slow rate-dependence in cardiac myocytes. *PLoS One*. 2012; 7:e43587.
20. Ward CA, Giles WR. Ionic mechanism of the effects of hydrogen peroxide in rat ventricular myocytes. *The Journal of Physiology*. 1997; 500:631.

21. Jabr RI, Cole WC. Alterations in electrical activity and membrane currents induced by intracellular oxygen-derived free radical stress in guinea pig ventricular myocytes. *Circulation research*. 1993; 72:1229-1244.
22. Jabr RI, Cole WC. Oxygen-derived free radical stress activates nonselective cation current in guinea pig ventricular myocytes role of sulfhydryl groups. *Circulation research*. 1995; 76:812-824.
23. Tarr M, Valenzano DP. Modification of cardiac action potential by photosensitizer-generated reactive oxygen. *Journal of molecular and cellular cardiology*. 1989; 21:539-543.
24. De Diego C, Pai RK, Chen F, Xie L-H, De Leeuw J, Weiss JN, Valderrábano M. Electrophysiological consequences of acute regional ischemia/reperfusion in neonatal rat ventricular myocyte monolayers. *Circulation*. 2008; 118:2330-2337.
25. Kozhevnikov D, Caref EB, El-Sherif N. Mechanisms of enhanced arrhythmogenicity of regional ischemia in the hypertrophied heart. *Heart rhythm : the official journal of the Heart Rhythm Society*. 2009; 6:522-527.
26. Janse MJ, Van Capelle F, Morsink H, Kléber AG, Wilms-Schopman F, Cardinal R, d'Alnoncourt CN, Durrer D. Flow of "injury" current and patterns of excitation during early ventricular arrhythmias in acute regional myocardial ischemia in isolated porcine and canine hearts. Evidence for two different arrhythmogenic mechanisms. *Circulation Research*. 1980; 47:151-165.
27. Yang KC, Kyle JW, Makielski JC, Dudley SC, Jr. Mechanisms of sudden cardiac death: Oxidants and metabolism. *Circ.Res*. 2015; 116:1937-1955.
28. Miyamoto S, Martinez GR, Medeiros MH, Di MP. Singlet molecular oxygen generated by biological hydroperoxides. *J.Photochem. Photobiol.B*. 2014; 139:24-33.
29. Ambrosio G, Flaherty JT, Duilio C, Tritto I, Santoro G, Elia PP, Condorelli M, Chiariello M. Oxygen radicals generated at reflow induce peroxidation of membrane lipids in reperfused hearts. *J. Clin. Invest*. 1991; 87:2056-2066.
30. Wagner S, Rokita AG, Anderson ME, Maier LS. Redox regulation of sodium and calcium handling. *Antioxid. Redox. Signal*. 2013; 18:1063-1077.
31. Kohler AC, Sag CM, Maier LS. Reactive oxygen species and excitation-contraction coupling in the context of cardiac pathology. *J.Mol.Cell Cardiol*. 2014; 73:92-102.
32. Qi YB, Garren EJ, Shu X, Tsien RY, Jin Y. Photo-inducible cell ablation in caenorhabditis elegans using the genetically encoded singlet oxygen generating protein minisog. *Proc. Natl. Acad. Sci. U.S.A*. 2012; 109:7499-7504.
33. Nakaya H, Takeda Y, Tohse N, Kanno M. Mechanism of the membrane depolarization induced by oxidative stress in guinea-pig ventricular cells. *J.Mol.Cell Cardiol*. 1992; 24:523-534.
34. Shimoni Y, Clark RB, Giles WR. Role of an inwardly rectifying potassium current in rabbit ventricular action potential. *J.Physiol*. 1992; 448:709-727.
35. Carmeliet E. Cardiac ionic currents and acute ischemia: From channels to arrhythmias. *Physiol Rev*. 1999; 79:917-1017.
36. Jeong EM, Liu M, Sturdy M, Gao G, Varghese ST, Sovari AA, Dudley SC, Jr. Metabolic stress, reactive oxygen species, and arrhythmia. *J. Mol. Cell Cardiol*. 2012; 52:454-463.
37. Song Z, Ko CY, Nivala M, Weiss JN, Qu Z. Calcium-voltage coupling in the genesis of early and delayed afterdepolarizations in cardiac myocytes. *Biophysical journal*. 2015; 108:1908-1921.
38. Nattel S. New ideas about atrial fibrillation 50 years on. *Nature*. 2002; 415:219-226.

SUPPLEMENTAL MATERIAL

Detailed Methods

Neonatal Rat Ventricular Myocytes (NRVCs) Isolation and Culture

Animal protocols were reviewed and approved by the Animal Experiments Committee of the Leiden University Medical Center (LUMC) and conformed to the Guide for the Care and Use of Laboratory Animals as stated by the US National Institutes of Health. NRVCs were isolated from hearts of 2-day-old Wistar rat pups as previously described.^{1,2} Isolated cells were plated on round glass coverslips (15-mm diameter, Thermo Fisher Scientific Gerhard Menzel B.V. & Co. KG, Braunschweig, Germany) coating with fibronectin (Sigma-Aldrich, St. Louis, MO, USA) in 24-well plates (Corning Life Sciences, Amsterdam, the Netherlands). Depending on the assay, cell densities of $0.1\text{-}8 \times 10^5$ cells/well were used. To prevent perforation of non-cardiomyocytes, 12-16 hours after plating, cultures were treated for 2 hours with mitomycin-C (10 $\mu\text{g}/\text{mL}$; Sigma-Aldrich) as described previously.²

Plasmid Construction and Self-Inactivating Lentiviral Vector (SIN-LV) Production

SIN-LV shuttle plasmid pLV.hCMV-IE.miniSOG-PM.hHBVPRE, which codes for a plasma membrane-associated version of mini singlet oxygen generator (miniSOG), was constructed by a two-step procedure. In step 1, the miniSOG-coding sequence was extended with the plasma membrane targeting motif of human K-Ras4B by replacing the BglII×EcoRI fragment of plasmid miniSOG-C1 (Addgene, Cambridge, MA, USA, plasmid number: 54821)³ with a linker molecule composed of oligonucleotides 5' GATCCAAGATGAGCAAAGACGGC AAAAAGAAGAAAAAGAAGTCCAAGACAAAAGTGCGTGATCATGTAAAG 3' and 5' AATTCCTTACATGATCACGCACTTTGTCTTGGACTTCTTTTCTTCTTTT GCCGTCTTTGCTCATCTTG 3' (Sigma-Aldrich). The resulting plasmid was designated pminiSOG-PM. In step 2, the 414-bp Eco47III×EcoRI fragment of pminiSOG-PM was blunt-ended with Klenow polymerase and inserted in between the SmaI site and filled-in BsrGI site of pLV.hCMV-IE.IRES.eGFP.hHBVPRE.¹

SIN-LV shuttle construct pLV.hCMV-IE.eGFP-PM.WHVoPRE encodes for a version of the *Aequorea victoria* enhanced green fluorescent protein (eGFP) fused at its carboxy terminus to the plasma membrane targeting motif of human K-Ras4B. The coding sequence of this protein designated eGFP-PM (previously known as GFP-tK);⁴ was inserted as an 870-bp Eco47III×XbaI restriction fragment into the polylinker of pLV.hCMV-IE.MCS.WHVoPRE after digestion of this plasmid with SmaI and XbaI. pLV.hCMV-IE.MCS.WHVoPRE is a derivative of pLV.hCMV-IE.IRES.eGFP.hHBVPRE, in which the DNA segment comprising the encephalomyocarditis virus internal ribosomal entry site (IRES), the eGFP open reading frame and the human hepatitis B virus posttranscriptional regulatory element (PRE) is replaced by the oPRE version of the woodchuck hepatitis virus PRE.⁵ LV shuttle plasmids pLV.hCMV-IE.miniSOG-PM.hHBVPRE and pLV.hCMV-IE.eGFP-PM.WHVoPRE were subsequently used for the production of LV.miniSOG-PM and LV.eGFP-PM particles, respectively, using a previously described procedure. Restriction enzymes and other DNA modifying enzymes were obtained from New England Biolabs (Bioké,

Leiden, the Netherlands) or (Thermo Fisher Scientific, Bleiswijk, the Netherlands). Large-scale plasmid isolation was done with the JETSTAR 2.0 Plasmid Maxiprep kit (Genomed, Löhne, Germany) following the instructions of the manufacturer.

Culture and Genetic Modification/Lentiviral Transduction of NRVCs

SIN-LV suspensions stored in 100 μ L portions at -80°C were gradually thawed on ice prior use. At 4 day after culture initiation, NRVCs cultured on glass coverslips were transduced by adding SIN-LV suspension directly to culture medium. After 24 hours, the inoculum was removed and cells were washed once with phosphate-buffered saline (PBS) and 3 times with culture medium before fresh culture medium was given. Culture medium was refreshed daily for 2 additional days to establish high and stable expression level of eGFP-PM or miniSOG-PM in culture NRVCs. To determine the transduction efficiency, transduced cells were stained for nuclei by incubation them in culture medium containing Hoechst 33342 (Molecular Probes™, Thermo Fisher Scientific) at final concentration of 10 $\mu\text{g}/\text{mL}$. Then, cells were washed 3 times with PBS and later fixed with PBS containing 4% formaldehyde (Merck, Amsterdam, the Netherlands) for 15 min at room temperature (RT). After 3 times washing with PBS, coverslips were mounted in Vectashield mounting medium (Vector Laboratories, Burlingame, CA, USA). Finally, green fluorescent signals were assessed from the images acquired with a digital color camera-equipped fluorescence microscope (Nikon Eclipse 80i, Nikon Instruments Europe, Amstelveen, the Netherlands). For the experimental use, SIN-LVs were applied at doses that resulted in transduction of nearly 100% of NRVCs, without microscopic signs of cytotoxicity.

6

Immunocytology

To characterize our NRVC monolayer cultures, we performed immune fluorescent cell staining of non-transduced NRVCs cultured on glass coverslips. 3 days after plating, cells were fixed with PBS containing 4% formaldehyde (Merck) for 15 minutes at RT, washed 3 times with PBS and permeabilized by incubation for 10 minutes at RT with PBS containing 0.05% Triton-X100 (Sigma-Aldrich). Then wash 3 times with PBS containing 0.1% Tween-20 (Sigma-Aldrich). After washing, samples were incubated with primary antibodies diluted in PBS containing 10% fetal bovine serum (FBS; Sigma-Aldrich) and 1% bovine serum albumins (BSA; Sigma-Aldrich). Antibodies against the following antigens were used: sarcomeric α -actinin to detect cardiomyocytes (1:300; mouse IgG1, clone EA-53; Sigma-Aldrich) and collagen type 1 to identify fibroblastic cell types (1:300; rabbit IgG, polyclonal; Abcam, Cambridge, United Kingdom). After washing 3 times for 5 minutes with PBS containing 0.1% Tween-20, cells were incubated with appropriate Alexa Fluor® 488- or 568-conjugated secondary antibodies (1:500; Molecular Probes™, Thermo Fisher Scientific). Nuclear counterstaining was additionally performed by incubating the cells for 10 minutes at RT with 10 $\mu\text{g}/\text{mL}$ Hoechst 33342. Coverslips were mounted in Vectashield mounting medium. Images were acquired with a digital color camera-equipped fluorescence microscope Nikon Eclipse 80i.

Reactive oxygen species (ROS) labeling

We performed live-cell imaging to detect ROS in native NRVCs (control), NRVCs expressing eGFP-PM (eGFP-PM-NRVCs) and NRVCs expressing miniSOG-PM (miniSOG-PM-NRVCs). To quantify the basic ROS level, CellROX® Deep Red reagent (Molecular Probes™, Thermo Fisher Scientific) was used to assess ROS under normal growth condition (37°C under 5% CO₂) in native NRVCs, eGFP-PM-NRVCs and miniSOG-PM-NRVCs, respectively. CellROX® Deep Red dye is cell-permeable and non-fluorescent in the reduced state; upon oxidation, it exhibits excitation/emission maxima at 640/665 nm. To stain the cells and nuclei, NRVCs were incubated under the normal growth conditions for 30 minutes with CellROX® Deep Red dye and Hoechst 33342 dye at a concentration of 5 µM/ml and 10 µg/ml, respectively. Then, NRVCs were washed three times with pre-warm PBS before colorless culture medium was subsequently replaced. Immediately within 10 minutes, cells were imaged under the normal growth condition by Leica AF6000 LX inverted widefield microscopy system (Leica Microsystems B.V., Eindhoven, the Netherlands) equipped with a Hamamatsu EM-CCD camera through a HCX PL FLUOTAR L 40x/0.6 objective. Images were acquired using an A4 cube for Hoechst (excitation 360/40; emission 470/40), a YFP cube for eGFP/miniSOG (excitation 500/20; emission 535/30) and the DiD filter of a CYD fast filter wheel for ROS (excitation 625; emission 710). To minimize and prevent blue light to induce ROS overproduction during imaging, images acquired by a YFP cube were taken at the least of each acquisition per sample. To assess ROS level following blue-light (470 nm) illumination, 24-well plates containing native NRVCs, eGFP-PM-NRVCs, and miniSOG-PM-NRVCs were placed 0.5 cm above the blue-light source and illuminated for 4 minutes under the normal growth condition. Subsequently, cells were stained and imaged as described above. Here, the used light source is blue (470nm) LUXEON® rebel light emitting diode (LED), mounted on a 20 mm star CoolBase - 70 lm @ 700 mA (Quadica Developments Inc., Brantford, Ontario, Canada). The irradiance of 60 mW/mm² as measured after passing through culture plate and glass coverslip with a calibrated optical power meter PM100D conjugated with a S130C photodiode sensor (Thorlabs GmbH, Munich, Germany) was applied to activate ROS overproduction in this assay. Localization and quantification of fluorescence signals was done using dedicated software (Leica Application Suite [Leica Microsystems] and ImageJ [Rasband, W.S., National Institutes of Health, Bethesda, Maryland, USA])

6

Patch-clamp electrophysiological study

For patch-clamp recordings, NRVCs were transduced with either LV.miniSOG-PM or LV.eGFP-PM. 2-4 days after transducing, measurements were performed at 20-23°C. In brief, cells were transferred from culture medium to an external cellular solution containing (in mM): 126 NaCl, 11 glucose, 10 HEPES, 5.4 KCl, 1 MgCl₂, and 1.8 CaCl₂ (adjusted to pH 7.40 with NaOH). Approximately within 15-60 minutes after superfusion of external cellular solution, patch-clamp experiments were conducted. Only solitary cells observed beating were selected for the experiments to record electrical activities and membrane ionic currents. Signals were amplified and digitized using a conventional patch-clamp equipment consisting of a MultiClamp

700B amplifier and a Digidata 1440A A/D converter (Molecular Devices, Sunnyvale, CA, USA) connected to a personal computer. This patch-clamp equipment was controlled and driven by commercially available MultiClamp 700B Commander and Clampex v10.3 software (Molecular Devices) for Windows. Throughout experiments, the current and voltage outputs of amplifier were continuously sampled at intervals of 100 μ s and recorded onto personal computer after low-pass filtered at 2-4 kHz with a four-pole Bessel filter. The patch pipettes were fabricated from borosilicate glass capillaries (1.5 mm outer diameter and 1.17 mm inner diameter, Harvard Apparatus, Kent, UK) with a vertical puller (P-30, Sutter Instruments, Novato, CA, USA). CPM-2 coating and polishing microforege (ALA Scientific Instruments, Farmingdale, NY, USA) was employed for fire-polishing to reshape and smooth pipette tips. For whole-cell experiments, pipettes had typical electrical resistances of 2-3 MW in the external cellular solution when filled with the internal solution containing (in mM): 80 potassium DL-aspartate, 40 KCl, 8 NaCl, 5.5 glucose, 5 HEPES, 5 EGTA, 1 MgCl₂, 4 Mg-ATP, and 0.1 Na₃-GTP (adjusted to pH 7.20 with KOH). The giga-ohm seal was formed by continuously applied 10-ms voltage steps from 0 to +5 mV at 10 Hz. After reaching giga-ohm seal, the holding potential was set to -50 mV, and the patch membrane was rupture by gentle suction applied to the pipette.⁶ Whole-cell capacitance (C_m) was calculated from capacitive transient currents evoked during 5 mV steps from a holding potential of -50 mV and electrically removed with amplifier. To minimize voltage error and fetch the adequacy of the voltage-clamp, pipette series resistance was routinely monitored and electrically compensated by >75%. The estimated liquid-junction potential of 11 mV was corrected.

To activate ROS overproduction in NRVCs during patch-clamp experiments, blue light (470 \pm 20 nm, 0.3 mW/mm², measured after passing through all filters, optics and coverslips by a calibrated optical power meter PM100D conjugated with S130C photodiode sensor) delivery from a mercury arc lamp was served as light source for single-cell illumination. Activation blue light was coupled into an inverted microscope Zeiss Axiovert 35 (Carl Zeiss AG, Oberkochen, Germany) and modulated by shutter system (Lambda 10; Shutter Instruments).

Perforated patch-clamp technique was employed to record the electrical activities of transduced NRVCs before and after exposure to blue light. Pipette resistances between 4-5 MW were used for this techniques. Here, we adjusted our previously described procedures.¹ In brief, an ATP-, GTP and EGTA-free pipette solution containing (in mM): 80 potassium DL-aspartate, 40 KCl, 8 NaCl, 5.5 glucose, 5 HEPES, and 1 MgCl₂ (adjusted to pH 7.20 with KOH) was used to tip-fill patch pipettes, and the same pipette solution containing nystatin (120-200 μ g/ml; Sigma-Aldrich) was used to back-fill the pipettes. After giga-ohm seal formation, the series resistance was monitored and shown progressively decline. Recordings were started after the series resistance had reached steady state of 15-10 M Ω stable (*i.e.* after 20-30 min). The integrity of the perforated patch was checked during and after recording for every experiment. We noted that the rupture of patch membrane abruptly increased capacitive current, unleashed the pipette solution to diffuse into the cells and caused an irreversible contracture because a specific chelator for calcium EGTA was absence. Therefore, we discarded those cells that showed sudden

appearance of the capacitive current or the irreversible contracture under the microscope to ensure reliability of recordings.

Optical-Voltage Mapping

Propagation of action potentials was investigated in monolayer cultures of NRVCs plated out onto 15-mm round glass coverslips in 24-well plates (Corning) at a cell density of 8×10^5 cells per well. Three to four days of culture, the monolayers were transduced with lentiviral vectors encoding either miniSOG-PM or eGFP-PM. Between day 8 to day 9, cultures were optically mapped using voltage-sensitive dye di-4-ANEPPS (Molecular Probes™, Thermo Fisher Scientific) as described previously.^{1,2} In brief, cultures without structural inhomogeneities as judged by light microscopy were selected for staining. Cultures were incubated with culture medium containing 8 $\mu\text{mol/L}$ di-4-ANEPPS for under the normal growth condition for 10 ± 5 minutes. Subsequently, pre-warm color less DMEM/HAMS F10 (Gibco™, Thermo Fisher Scientific) mixed in a 1:1 ratio medium (serum-free) were replaced the culture medium containing dry. Next, the electrical activities of monolayer cultures were examined at 37°C. Each mapping experiments normally did not exceed 30 minutes per 24-wells plate. Excitation light ($e_{\text{ex}} = 525 \pm 25$ nm) was delivered by a halogen arc-lamp (MHAB-150W, Moritex Corporation, San Jose, CA, USA) through epi-illumination. Fluorescent emission light passed through a dichroic mirror and a long-pass emission filter (>590 nm) and was focused onto a 100x100 pixels CMOS camera (Ultima-L, SciMedia, Costa Mesa, CA, USA) by a 1.6x converging lens (Leice, Wetzlar, Germany). This resulted in a spatial resolution of 160 $\mu\text{m}/\text{pixel}$ and a field of view of 16 by 16 mm. Spontaneous or stimulated electrical activity was recorded for 6-24 seconds at 6ms exposure time per frame. Data analysis was performed with specialized software (Brainvision Analyze 1101, Brainvision Inc, Tokyo, Japan) after pixels signals were averaged with 8 of its nearest neighbors to minimize noise-artifacts. Conduction velocity (CV), maximal optical action potential upstroke (dF/dT_{max}), maximal action potential downstroke velocity (dF/dT_{min}), action potential duration until 30%, 50% and 80% repolarization ($\text{APD}_{30, 50 \text{ and } 80}$) were determined at ≤ 1 Hz at six different locations equally distributed throughout the culture and averaged before inclusion in further analyses. Spatial dispersion of repolarization was defined as the maximal difference in APD_{80} within a culture and was determined at activation frequencies of ≤ 1 Hz. 3D APD distribution maps, regional APD distribution histograms were plotted using custom Wolfram Mathematica software. In order to build activation maps, videos were equalized in oscillation amplitude per pixel, filtered with 3-pixel kernel Gauss 2d filter using custom ImageJ-based program. Then activation maps were built using standard Brainvision software.

Patterned illumination

Existing optical mapping setup was conjugated with computer-controlled digital micro-mirror device (DMD)-based, the Polygon 400, (P/N: DSI-G-000; Mightex Systems, Toronto, Ontario, Canada), to enable patterned illumination system (Supplementary Figure 3). 470-nm light from 3 watt high-power LED from LED source (LCS-0470-50-22; Mightex Systems) was projected

on DMD surface via liquid light guide (LLG-03-59-340-0800-1; Mighttix Systems). Reflection from DMD surface was projected and focused on the sample through a custom-built dichroic mirror (reflect 520-560 nm; pass >600 nm, Scimedia Ltd, Costa Mesa, CA, USA) and an objective lens (1x). The constant 470-nm light intensity in the sample plane (0.3 mW/mm²) was used in combination with various illumination time depending on experimental protocols. Light intensity was measured using S130C photodiode sensor by P100D optical power meter.

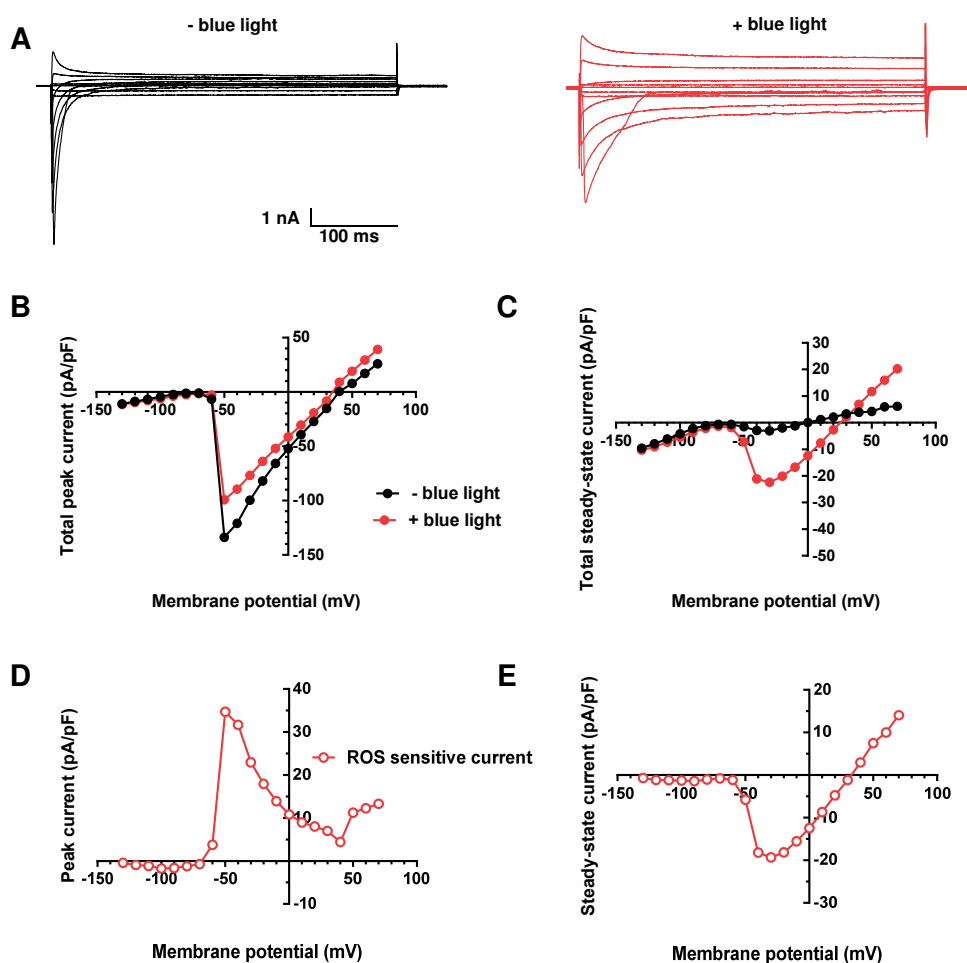
Data analysis and statistics

For off-line analysis, the data stored on personal computers were analyzed by pClamp V10.3 (Molecular Devices), BV analyze V13.12.20 (Brainvision Analyze 1101), and Graph Pad Prism software version 6 (GraphPad Software, Inc., La Jolla, CA). Unless otherwise stated, data were reported as mean \pm standard error of mean (SEM). Statistical comparison of the same groups under control and experimental conditions was performed by both paired and unpaired Student's *t*-test. Statistical comparison of several groups to a control group was performed by oneway ANOVA followed by Turkey's post-test. Significant differences were determined at the $P < 0.05$ level, unless specified. Statistical significance was expressed as follows: *: $P < 0.05$, **: $P < 0.01$, ***: $P < 0.001$. The term *n* refers to the number of experiments.

Supplemental References

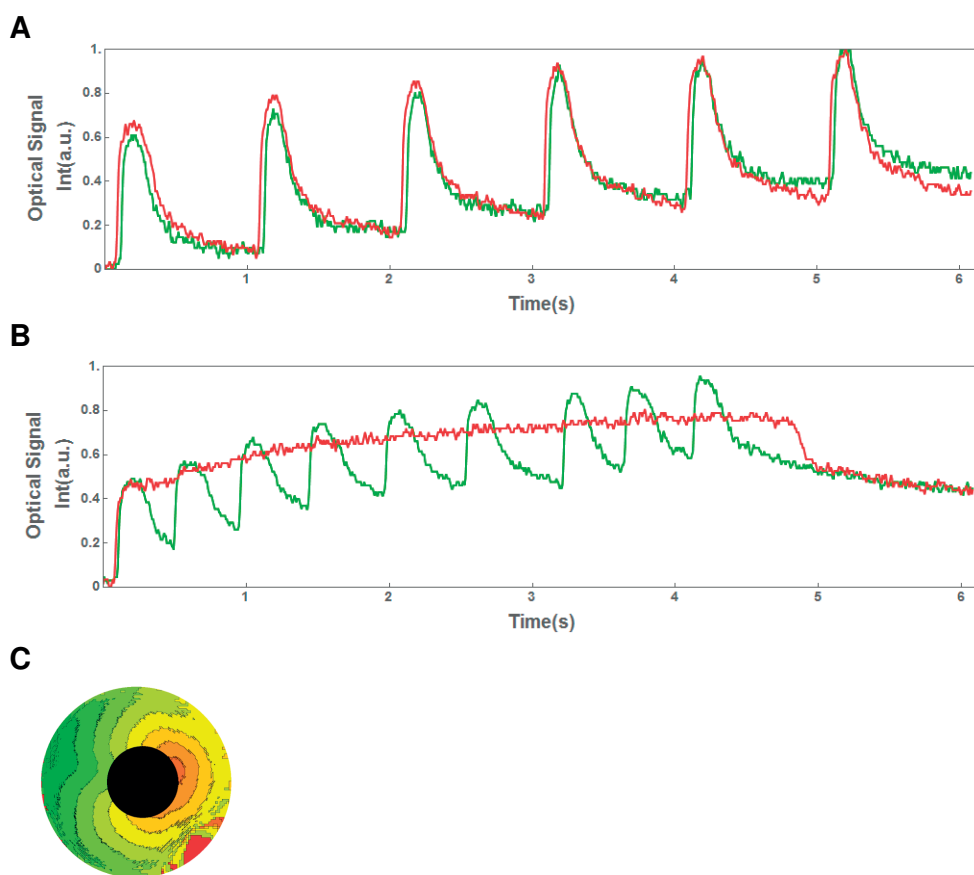
1. Engels MC, Askar SF, Jangsanthong W, Bingen BO, Feola I, Liu J, Majumder R, Versteegh MI, Braun J, Klautz RJ, Ypey DL, De Vries AA, Pijnappels DA. Forced fusion of human ventricular scar cells with cardiomyocytes suppresses arrhythmogenicity in a co-culture model. *Cardiovasc Res.* 2015; 107:601-12.
2. Askar SF, Ramkisoensing AA, Schaliy MJ, Bingen BO, Swildens J, van der Laarse A, Atsma DE, de Vries AA, Ypey DL, Pijnappels DA. Antiproliferative treatment of myofibroblasts prevents arrhythmias in vitro by limiting myofibroblast-induced depolarization. *Cardiovasc Res.* 2011; 90:295-304.
3. Shu X, Lev-Ram V, Deerinck TJ, Qi Y, Ramko EB, Davidson MW, Jin Y, Ellisman MH, Tsien RY. A genetically encoded tag for correlated light and electron microscopy of intact cells, tissues, and organisms. *PLoS Biol.* 2011; 9:e1001041.
4. Apolloni A, Prior IA, Lindsay M, Parton RG, Hancock JF. H-ras but not K-ras traffics to the plasma membrane through the exocytic pathway. *Mol Cell Biol.* 2000; 20:2475-87.
5. Schambach A, Bohne J, Baum C, Hermann FG, Egerer L, von LD, Giroglou T. Woodchuck hepatitis virus post-transcriptional regulatory element deleted from X protein and promoter sequences enhances retroviral vector titer and expression. *Gene Ther.* 2006; 13:641-5.
6. Li C. A reliable whole cell clamp technique. *Adv Physiol Educ.* 2008; 32:209-11.

Supplemental Figures

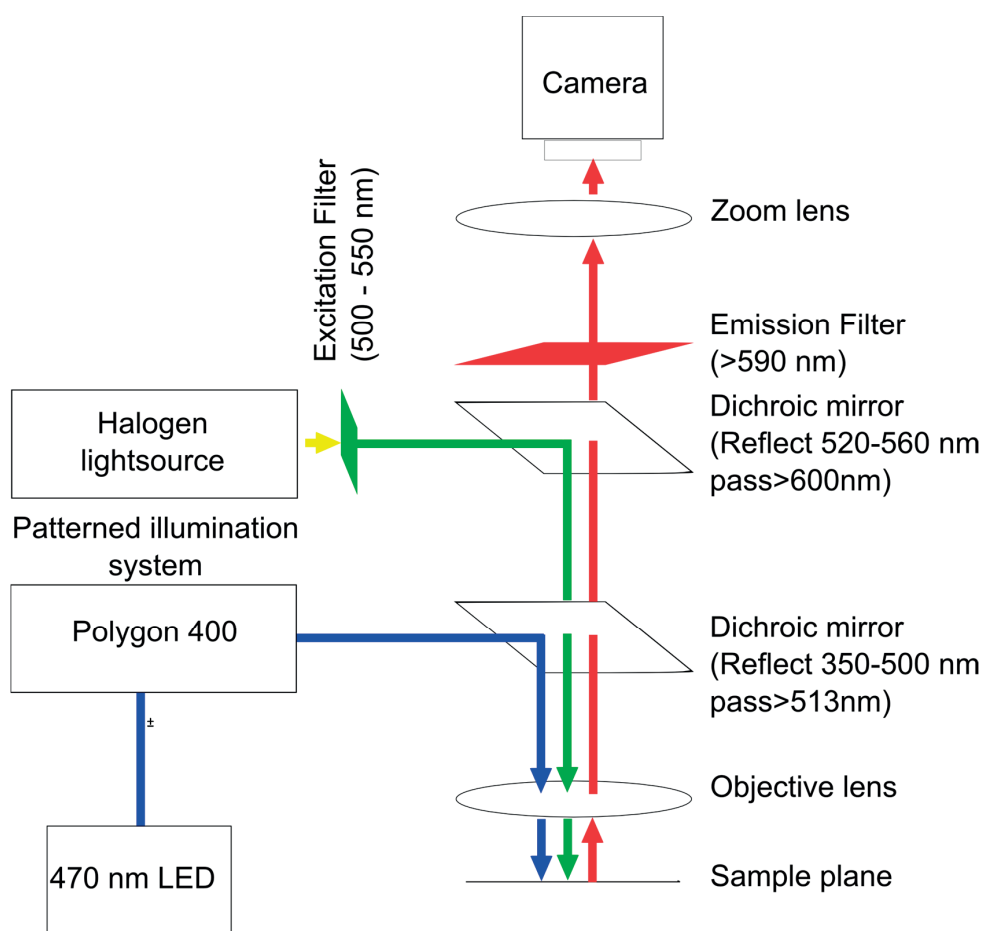


6

Supplementary Figure 1. Effects of ROS on total membrane currents of miniSOG-PM NRVC. The representative total membrane currents (A) of a miniSOG-PM-NRVC were obtained immediately after gaining the cell access (black trace) and after 10-s 470-nm-light illumination (red trace) by performing whole-cell voltage-clamp using 400-ms stepped pulses between -130 and +70 mV from a holding potential of -90 mV. The I-V relationships derived from (A) are shown in (B) for peak currents and C for steady-state currents. Filled black circles represent the control condition in the absence of 470-nm light. Filled red circles represent the OS condition when this cells was exposed to blue light for 10 s. The differences between the peak (D) and steady-state (E) currents before and after blue-light illumination are plotted against the membrane potential (open red circle). These I-V curves reveals ROS-sensitive current component, which is active upon exposure to blue light.



Supplementary Figure 2. Regional elevated ROS production disrupts calcium dynamics in miniSOG-PM-NRVC monolayers, leading to formation of quasistable calcium elevated level inside irradiated area and ectopic activity. A, Rhod2-AM optical-calcium traces during 1Hz electrical stimulation before irradiation shows baseline calcium dynamics. Red trace – central area, green trace – periphery area. B, Calcium transients were elicited by single electrical stimulus after illumination of the central area. Illuminated area (red trace) exhibits elevated calcium level lasting for 5 s. Ectopic activity (green trace) was initiated from the area of calcium elevation (OS zone). C, Typical example of ectopic beat propagation originated from OS zone.



6

Supplementary Figure 3. Optical mapping and patterned illumination setup scheme. Experimental setup includes blue (470-nm) LED light source connected via light-guide to computer controlled DMD-based patterned illumination device (Polygon 400). Computer-generated patterns were projected on sample plane via reflection from dichroic mirror (513 nm pass) and focusing by objective lens. Halogen light source was bandpass filtered at 500-550 nm and dichroic mirrors for fluorescence excitation. Fluorescence signal went through emission filter (> 590 nm) to the camera.

Supplementary Table 1. Electrical physiological parameters in eGFP-PM upon 470-nm-light exposure. APD₃₀, APD₅₀, APD₈₀ and CV inside (in) and outside (out) the irradiated area (6 mm \varnothing) after 2 (n=10), 4 (n=10), and 6 (n=10) minutes upon 470-nm-light exposure. No significant differences were observed.

	2 minutes		4 minutes		6 minutes	
	out	in	out	in	out	in
APD (ms)	133±13	153±16	123±12	149±14	152±24	223±32
APD ³⁰ (ms)	170±17	190±21	148±16	177±17	188±30	260±28
APD ⁵⁰ (ms)	289±27	306±30	229±30	254±30	278±30	339±31
CV ⁸⁰ (cm/s)	18±0,7	19±0,8	18±0,9	18±1	19 ±0,5	19±0,4





Chapter

SUMMARY, CONCLUSIONS AND
FUTURE PERSPECTIVES

7



The general introduction of this thesis, **Chapter I**, describes how electrical signals originate and propagate in a healthy heart and how disturbances of these two properties can lead to cardiac arrhythmias. Furthermore, the current anti-arrhythmic strategies are listed, while more attention is focalized on gene therapy and optogenetics. **Chapter II** describes how monolayers of neonatal rat atrial cardiomyocytes (aCMCs) are optogenetically modified with lentiviral (LV) particles encoding for the depolarizing ion channel CatCh (Ca²⁺-permeable channelrhodopsin). In this chapter, a detailed and precise narration of different processes is presented, going from the isolation of aCMCs, the production of the LV particles, the use of such particles to optogenetically modify the aCMCs, to finally the demonstration, via optical voltage mapping, that the CatCh-expressing aCMC monolayers were responding to global blue light illumination with synchronous elicitation of an action potential. In **Chapter III**, we used the *in vitro* model described in **Chapter II**, *i.e.* CatCh-expressing aCMC monolayers, to investigate on the mechanisms of termination of rotor-guided ablation, *i.e.* a new ablation strategy that recently has emerged in clinical settings. In this study, CatCh was specifically and precisely activated by patterned illumination. Such precise control in space and time allowed us to first induce a stable rotor and secondly to study its termination by optogenetically blocking electrical activation at or near the rotor core region by using circular or linear shapes of illumination. We found that localized optogenetic targeting of rotors in atrial monolayers could both stabilize and destabilize rotors. However, termination required a line of conduction block that from the core region was reaching at least one unexcitable boundary. The beauty of such approach inspired us to continue our research and investigate on spiral wave dynamics. Indeed, in this study, which is described in **Chapter IV**, we also used CatCh-expressing aCMC monolayers and patterned illumination. Here, we describe a unique method to control spiral wave cores in time and space that we called AAD control (Attract-Anchor-Drag). This method relies on i) attraction, ii) anchoring of a spiral wave tip to a temporal heterogeneity (*i.e.* a reversible conduction block that is created close to the spiral core), and iii) dragging to a new, yet predefined location. This process allowed to move the spirals along any desired trajectory and to terminate them when dragged towards an inexcitable boundary or towards other spirals. The *in vitro* experiments were complemented by *in silico* simulations that demonstrated precise and robust spatiotemporal control over spiral wave cores in a wide range of parameters. Application of light spots of different sizes, *i.e.* different diameter (d) showed that a small-sized spot led to dragging via a cycloidal trajectory, whereas, a large spot was associated with a linear trajectory. Indeed, when the large light spots were moved at the fastest rate, the effective depolarized region resembled an elongated ellipse and caused the spiral tip to remain anchored to the boundary of the pattern, which was linear. However, at slower dragging rates, *i.e.* longer light exposure, the spiral wave executed one or more complete rotations around the region of light-induced depolarization, before being repositioned to the next illuminated spot. Hence, spots with larger size can also follow a cycloidal trajectory. Furthermore, the location of the spot of light, the location of the spiral tip, and the direction of drift played an important role in spiral wave dragging. The dragging, indeed, was observed most efficiently when the spot of light was applied sufficiently close to the location of the spiral tip and within an angular spread in the direction of drift of the spiral core. In **Chapter V**, optogenetic

termination of anatomical reentry was investigated in a more complex *in vitro* model, *i.e.* 150- μm thick slices derived from neonatal tissue ventricular slices. The slices were genetically modified with CatCh-encoding LV particles. Here, patterned illumination was used to locally activate CatCh and thereby to induce a local and reversible conduction block in the pathway of reentry. Generation of a transmural conduction block with a width of 600 μm in the re-entrant pathway always led to arrhythmia termination. In this case, the reentrant waves were not able to enter the illuminated area and reentry was therefore immediately terminated. When the conduction block did not fully obstruct the reentrant pathway the outcome was dependent on the width of the isthmus. In these cases, reentry was often terminated at the site of illumination with further narrowing of the isthmus. From a mechanistic point of view, we showed, through a set of complementary *in silico* and *in situ* experiments, that the illuminated area was characterized by an extension into the isthmus of a gradient in depolarization. The *in silico* data revealed that the membrane potential was ranging from -20 mV in the center to -30 mV at the border of the illuminated area and -70 mV in the most distal region. In line with these results, the *in situ* data showed a strong reduction ($\sim 50\%$) of the optical signal amplitude in the spot closest to the area of illumination, thereby suggesting the presence of a graded decrease in excitability.

Since the optogenetic toolbox contains not only light-gated ion channel, we exploited a different optogenetic tool, a ROS-generating protein (RGP), called miniSOG (mini singlet oxygen generator), in combination with patterned illumination to quantitatively, spatially and temporally control ROS production in monolayers of neonatal rat ventricular myocytes (NRVMs). This combination allowed to assess ROS effects on arrhythmogenicity. In **Chapter VI**, we show that microfoci of increased ROS production in myocardial monolayers can promote local disturbances in electrical impulse generation and propagation, leading to ectopic activity, functional conduction block, and reentrant arrhythmias.

In conclusion, the experiments presented in this thesis show how the simplicity of an *in vitro* model might be the key towards a better understanding of complex matters, such as mechanisms of cardiac arrhythmias initiation and termination. In all these experiments optogenetics played a crucial role. Catch was expressed in cardiac tissue allowing the possibility for i) global and local light-pacing, ii) light-dependent induction of a single spiral wave, iii) spiral wave termination when a line of block reaches from the core region to at least one unexcitable boundary, and finally iv) spiral wave dynamics control in space and time, while miniSOG was expressed to show how microfoci of increased ROS production could lead to cardiac arrhythmias by creating disturbances in electrical impulse generation and propagation.

PERSPECTIVES OF OPTOGENETIC APPLICATIONS IN CARDIAC RESEARCH

As shown throughout this thesis, the scientific research in the field of cardiology has been revolutionized by the introduction of optogenetics. In the last eight years, several research groups have shown light-excitation of cardiac myocytes. Arrenberg *et al* used light to pace zebrafish hearts expressing ChR2. They showed that brief optical stimuli were able to evoke

action potentials and therefore modify the beating frequency.³ In the same year, similar effects were also shown *ex vivo* by pacing with light the intact hearts of ChR2(H134R) transgenic adult mice and *in vitro* by pacing the cardiomyocytes isolated from these transgenic hearts.⁴ Opto-pacing was also possible when rodent cardiomyocytes were genetically modified by using viral vector technology, *i.e.* AAV for *in-ex vivo* and LV for *in vitro* applications.⁴⁻⁶ In those eight years, instead, fewer scientific contributions have emerged on light-inhibition of electrical activity. Light-gated chloride pump activation, resulting in a hyperpolarizing photocurrent, was used to inhibit electrical activity in zebrafish cardiomyocytes.³ Light-gated hyperpolarizing proton pump and natural chloride-conducting channelrhodopsin were used to suppress electrical activity in cardiac culture, by their expression in cardiac fibroblast or direct expression in cardiomyocytes, respectively.^{3,7,8} Depolarizing or hyperpolarizing optogenetic tool can also be used to shape an action potential. Their activation can lead, indeed, to action potential prolongation or shortening, respectively.⁹ Furthermore, recently, in addition to those aforementioned applications, the ability to optogenetically terminate tachyarrhythmias has been first shown *in vitro*¹⁰⁻¹² and secondly in the whole rat and mouse hearts expressing light-gated ion channels.¹³⁻¹⁵ However, the clinical translation of such optogenetic applications might encounter various challenges and might need further development and optimization of optogenetic tools, light delivery and in gene transfer technology. A first step in understanding the mechanism and the requirements for optogenetic defibrillation in patients was done by using a patient-specific computational model of post-myocardial infarction.¹³ In this study, Boyle *et al* have shown that mechanistically optogenetic termination was mediated by transmural depolarization of the myocardium that led to a temporal conduction block due to sodium channels unavailability. Regarding the requirements, they have shown that blue light attenuation through the human ventricular thick wall could be an obstacle for successful termination. Termination occurred only when a red-shifted optogenetic tool was used. Accordingly, also *in vitro* assays have shown that tissue penetration of 470-nm light is rather poor. Zaglia *et al* confirmed that the intensity of such light applied at the epicardial surface decreases by 80% when reaching areas of myocardium at a depth of 300 μm . As suggested, to improve light penetration, red-shifted optogenetic tools, such as other ChR2 variants,^{15, 17} could be used and furthermore combined with, for example, elastic integumentary membranes equipped with multiple $\mu\text{-LEDs}$ ¹⁸ or implantation of injectable hardware-free $\mu\text{-LEDs}$ inside the myocardium.¹⁹ In addition, the particular substrate of the arrhythmia, *e.g.* its composition and location in time and space, has to be considered for the selection of specific light-gated ion channels and illumination protocols.

In conclusion, the studies presented in this thesis provide novel mechanistic insight into optogenetic control of cardiac electrical functions. Thereby, these studies might contribute to a better understanding of the mechanisms of cardiac arrhythmias initiation and termination, and may lead to new, pain-free, and biology-driven strategies for cardiac arrhythmias therapies.

REFERENCES

1. Entcheva, E. Cardiac optogenetics. *Am J Physiol Heart Circ Physiol*. 2013; 304:1179-1191.
2. Ambrosi CM, Klimas A, Yu J, Entcheva E. Cardiac applications of optogenetics. *Prog Biophys Mol Biol* 2014; 115:294-304.
3. Arrenberg AB, Stainier DY, Baier H, Huisken J. Optogenetic control of cardiac function. *Science*. 2010; 330:971-4.
4. Bruegmann T, Malan D, Hesse M, Beiert T, Fuegemann CJ, Fleischmann BK, Sasse P. Optogenetic control of heart muscle in vitro and in vivo. *Nat Methods* 2010; 7:897-900.
5. Nussinovitch U, Gepstein L. Optogenetics for in vivo cardiac pacing and resynchronization therapies. *Nat Biotechnol*. 2015; 33:750-4.
6. Vogt CC, Bruegmann T, Malan D, Ottersbach A, Roell W, Fleischmann BK and Sasse P. Systemic gene transfer enables optogenetic pacing of mouse hearts. *Cardiovasc Res*. 2015; 106:338-43.
7. Nussinovitch U, Gepstein L. Optogenetics for suppression of cardiac electrical activity in human and rat cardiomyocyte cultures. *Neurophotonics*. 2015; 2:031204.
8. Govorunova EG, Sineshchekov OA, Spudich JL. *Proteomonas sulcata* ACR1: a fast anion channelrhodopsin. *Photochem. Photobiol*. 2016; 92:257-63
9. Park SA, Lee SR, Tung L, Yue DT. Optical mapping of optogenetically shaped cardiac action potentials. *Sci Rep*. 2014; 4:6125.
10. Bingen BO, Engels MC, Schalij MJ, Jangsangthong W, Neshati Z, Feola I, Ypey DL, Askar SF, Panfilov AV, Pijnappels DA, de Vries AA. Light-induced termination of spiral wave arrhythmias by optogenetic engineering of atrial cardiomyocytes. *Cardiovasc Res*. 2014; 104:194-205.
11. Watanabe M, Feola I, Majumder R, Jangsangthong W, Teplenin AS, Ypey DL, Schalij MJ, Zeppenfeld K, de Vries AA, Pijnappels DA. Optogenetic manipulation of anatomical re-entry by light-guided generation of a reversible local conduction block. *Cardiovasc Res*. 2017; 113:354-66.
12. Feola I, Volkens L, Majumder R, Teplenin A, Schalij MJ, Panfilov AV, de Vries AAF, Pijnappels DA. Localized Optogenetic Targeting of Rotors in Atrial Cardiomyocyte Monolayers. *Circ Arrhythm Electrophysiol*. 2017; 10:e005591.
13. Bruegmann T, Boyle PM, Vogt CC et al. Optogenetic defibrillation terminates ventricular arrhythmia in mouse hearts and human simulations. *J Clin Invest*. 2016; 126:3894-904.
14. Crocini C, Ferrantini C, Coppini R et al. Optogenetics design of mechanically-based stimulation patterns for cardiac defibrillation. *Sci Rep*. 2016; 6:35628.
15. Nyns EC, Kip A, Bart CI, Plomp JJ, Zeppenfeld K, Schalij MJ, de Vries AA, Pijnappels DA. Optogenetic termination of ventricular arrhythmias in the whole heart: towards biological cardiac rhythm management. *Eur Heart J*. 2017; 38:2132-2136.
16. Lin JY, Knutsen PM, Muller A, Kleinfeld D and Tsien RY. ReaChR: a red-shifted variant of channelrhodopsin enables deep transcranial optogenetic excitation. *Nature neuroscience*. 2013; 16:1499-508.
17. Prigge M, Schneider F, Tsunoda SP, Shilyansky C, Wietek J, Deisseroth K and Hegemann P. Color-tuned channelrhodopsins for multiwavelength optogenetics. *The Journal of biological chemistry*. 2012;287:31804-12.
18. Xu L, Gutbrod SR, Bonifas AP, Su Y, Sulkin MS, Lu N, Chung HJ, Jang KI, Liu Z, Ying M, Lu C, Webb RC, Kim JS, Laughner JJ, Cheng H, Liu Y, Ameen A, Jeong JW, Kim GT, Huang Y, Efimov IR and Rogers JA. 3D multifunctional integumentary membranes for spatiotemporal cardiac measurements and stimulation across the entire epicardium. *Nature communications*. 2014; 5:3329.
19. Kim TI, McCall JG, Jung YH, Huang X, Siuda ER, Li Y, Song J, Song YM, Pao HA, Kim RH, Lu C, Lee SD, Song IS, Shin G,

Summary, conclusions and future perspectives

Al-Hasani R, Kim S, Tan MP, Huang Y, Omenetto FG, Rogers JA and Bruchas MR. Injectable, cellular-scale optoelectronics with applications for wireless optogenetics. *Science*. 2013; 340:211-6.



Chapter

SAMENVATTING
LIST OF PUBLICATIONS
ACKNOWLEDGMENTS
CURRICULUM VITAE

8



SAMENVATTING

De algemene introductie van dit proefschrift, **Hoofdstuk I**, beschrijft hoe elektrische impulsen ontstaan, zich voort geleiden in een gezond hart en hoe verstoringen in deze hiervan kunnen leiden tot hartritmestoornissen. Bovendien worden de huidige anti-aritmische strategieën benoemd, het leeuwendeel van de aandacht zal echter liggen bij gentherapie en de optogenetica. **Hoofdstuk II** beschrijft hoe monoculturen van atriale neonatale ratten cardiomyocyten (aCMCs) optogenetisch worden gemodificeerd met lentivirale (LV) deeltjes, die coderen voor het depolariserende ionkanaal CatCh (Ca^{2+} -permeabele 'channelrhodopsin'). In dit hoofdstuk wordt een gedetailleerde uiteenzetting gegeven van de verschillende stappen, beginnend bij de isolatie van aCMCs, gevolgd door de productie van de LV-deeltjes, het gebruik van deze deeltjes om de aCMCs optogenetisch te modificeren en uiteindelijk 'optical voltage mapping' om aan te tonen dat de CatCh gemodificeerde aCMC monoculturen reageren op belichting met algemeen blauw licht, uiteindelijk resulterend in het ontstaan van een synchrone actiepotentialiaal. In **Hoofdstuk III** gebruikten we het *in vitro* model beschreven in Hoofdstuk II, namelijk de aCMC monoculturen met de expressie van CatCh, om onderzoek te doen naar de mechanismen verantwoordelijk voor het termineren middels 'rotor-guided ablation', een nieuwe ablatie strategie die recent is voortgekomen uit de klinische praktijk. In deze studie werd CatCh specifiek en nauwkeurig geactiveerd door middel van belichting middels een patroon. Deze uiterste nauwkeurige controle in ruimte en tijd stelde ons in beginsel in staat om een stabiele rotor te induceren, gevolgd door het bestuderen van zijn terminatie middels optogenetische blokkade elektrische impuls rondom de rotor kern door middel van cirkelvormige of lineaire belichtings patronen. We ontdekten dat lokale optogenetische targeting in atriale monoculturen zowel kon zorgen voor rotor stabilisatie als destabilisatie. Echter voor terminatie was een lijn, resulterend in een voortgeleidings blok, noodzakelijk die reikte vanuit de 'core region' naar tenminste een niet exciteerbare grens. De pracht van deze benadering inspireerde ons om het onderzoek voort te zetten en de 'spiral wave dynamics' verder uit te diepen. Als vervolg hierop, zoals beschreven en gepresenteerd in **Hoofdstuk IV**, gebruikten we ook aCMCs monoculturen met Catch-expressie en patroon belichting. Hierin beschrijven we een unieke methode om controle uit te oefenen op de 'spiral wave cores' in tijd en plaats, dit wordt ook wel AAD (Aantrekken-Verankeren-Slepen) genoemd. Deze methode is gebaseerd op i) aantrekking, ii) verankering van een spiral wave tip naar een tijdelijke heterogeniteit (*d.w.z.* een omkeerbaar voortgeleidings blok dichtbij de 'spiral wave core') en iii) het 'dragen' naar een nieuwe, reeds gedefinieerde locatie. Met dit proces kunnen de 'spirals' over elk gewenst traject worden geleid en uiteindelijk getermineerd wanneer ze naar een 'inexcitable boundary' of andere 'spirals' worden gedirigeerd. De *in vitro* proeven werden aangevuld met *in silico*-simulaties die een nauwkeurige en robuuste spatiotemporele controle van de 'spiral wave cores' aantonen onder verschillende condities. Het gebruik van lichtpunten met verschillende groottes, *d.w.z.* verschillende diameter (d), toonde dat een punt met kleine afmeting leidde tot 'dragging' via een cycloïdale baan, terwijl een grote punt geassocieerd was met een lineaire baan. Inderdaad, toen de grote lichtpunten met de hoogste snelheid werden bewogen, leek het effectieve gedepolariseerde gebied op een

langwerpige ellips en zorgde ervoor dat de 'spiral tip' verankerd bleef aan de grens van lineaire patroon. Echter, bij langzamere sleep snelheden, *d.w.z.* een langere belichtingstijd, voerde de 'spiral wave' één of meer complete rotaties uit rondom het middels licht gedepolariseerde gebied, alvorens deze opnieuw werd gepositioneerd naar de volgende verlichte plek. Derhalve kunnen p unten meteen grotere afmeting ook een cycloïdaal traject volgen. Bovendien speelden de locatie van het lichtpunt, de locatie van de 'spiral tip' en de richting van het 'dragging' een belangrijke rol bij het 'spiral wave dragging'. Het 'draggen' werd was het meest efficiënt wanneer de lichtpunt dicht genoeg bij de locatie van de 'spiral tip' was en binnen de 'angular spread' in de drift richting van de 'spiral core'. In **Hoofdstuk V**, werd optogenetische terminatie van anatomische reentry onderzocht in een meer complex *in vitro* model, *d.w.z.* 150 µm dikke plakjes verkregen uit neonataal ventriculair weefsel. De plakjes werden genetisch gemodificeerd met CatCh-coderende LV-deeltjes. Hier werd patroon belichting gebruikt om CatCh lokaal te activeren om daarmee een lokaal en reversibel voortgeleidings blok te creëren in de baan van de reentry. Het genereren van een transmuraal voortgeleidings blok met een breedte van 600 µm in de baan van de e-entry leidde altijd tot beëindiging van de aritmie. In dit geval waren de 'reentry waves' niet in staat om het belichte gebied te betreden en daarmee werd de reentry onmiddellijk beëindigd. In het geval dat het voortgeleidings blok de baan van reentry niet volledig blokkeerde, was de uitkomst afhankelijk van de breedte van de isthmus. In deze gevallen werd de reentry meestal beëindigd rondom de belichting plek middels het verder vernauwen van de isthmus. Vanuit mechanistisch oogpunt toonden we, door middel van een complementaire reeks *in silico* en *in situ* experimenten, aan dat het belichtingsoppervlak werd gekarakteriseerd door een uitbreiding in de isthmus middels een 'gradient in depolarization'. De *in silico*-gegevens toonden dat de membraanpotentialia varieerde van -20 mV in het midden tot -30 mV aan de rand van het belichte gebied en -70 mV in de meer perifere gebieden. In lijn met deze resultaten toonden de *in situ*-data een sterke reductie (~ 50%) van de optische signaalamplitude op het punt dat het dichtst bij het belichtings gebied lag, daarmee suggestief voor een graduele afname in exciteerbaarheid. Omdat de optogenetic toolbox niet alleen een light-gated ion kanaal bevat hebben we ook een ander optogenetische tool geëxploreerd. Dit was een ROS-generating protein (RGP) genaamd miniSOG (mini singlet oxygen generator) die in combinatie met patroon belichting resulteerde in kwantitatieve, ruimtelijke en temporele controle over de productie van ROS in monoculturen van neonatale ventriculaire ratten cardiomyocyten (NVRMs). Deze combinatie maakte het mogelijk om de ROS effecten op aritmogeniciteit te bestuderen. In **Hoofdstuk VI** laten we zien dat microfoci met verhoogde ROS-productie in myocardiale monoculturen kunnen leiden tot lokale verstoringen in de elektrische impuls generatie en voortgeleiding, resulterend in ectopische activiteit, een functioneel voortgeleidings blok alsmede reentry aritmieën.

Concluderend laten de experimenten in dit proefschrift zien hoe de eenvoud van een *in vitro* model de sleutel kan zijn voor een beter begrip van meer complexe zaken, zoals de mechanismen verantwoordelijk voor de initiatie en terminatie van hartritmestoornissen. Bij al deze experimenten speelde optogenetica een cruciale rol. Catch werd tot expressie gebracht in hartspierweefsel en maakte het daarmee mogelijk om i) globaal en lokaal met licht te pacen, ii)

Samenvatting

een licht afhankelijke enkele 'spiral wave' te induceren, iii) 'spiral wave' te termineren wanneer een blokkerende lijn van de 'core region' naar op z'n minst één niet exciteerbaar gebied loopt, en ten slotte iv) controle over 'spiral wave dynamics' in tijd en ruimte, terwijl miniSOG tot expressie kwam om te laten zien hoe microfoci met toegenomen ROS productie kunnen leiden tot cardiale aritmieën door het creëren van verstoringen bij de elektrische impuls generatie en voortgeleiding.

LIST OF PUBLICATIONS

Full papers

*Equal contribution

Majumder R*, **Feola I***, Teplenin A, de Vries AAF, Panfilov AV, Pijnappels DA. Optogenetics enables real-time spatiotemporal control over spiral wave dynamics in an excitable cardiac system. *eLife*. 2018; 7pii: e41076.

Feola I, Volkens L, Majumder R, Teplenin A, Schalij MJ, Panfilov AV, de Vries AAF, Pijnappels DA. Localized Optogenetic Targeting of Rotors in Atrial Cardiomyocyte Monolayers. *Circ Arrhythm Electrophysiol*. 2017; 10pii: e005591.

Watanabe M*, **Feola I***, Majumder R, Jangsongthong W, Teplenin AS, Ypey DL, Schalij MJ, Zeppenfeld K, de Vries AA, Pijnappels DA. Optogenetic manipulation of anatomical reentry by light-guided generation of a reversible local conduction block. *Cardiovasc Res*. 2017; 113:354-366.

Feola I, Teplenin A, de Vries AA, Pijnappels DA. Optogenetic Engineering of Atrial Cardiomyocytes. *Methods Mol Biol*. 2016; 1408:319-31.

Majumder R, Jangsongthong W, **Feola I**, Ypey DL, Pijnappels DA, Panfilov AV. A Mathematical Model of Neonatal Rat Atrial Monolayers with Constitutively Active Acetylcholine-Mediated K⁺ Current. *PLoS Comput Biol*. 2016; 12:e1004946.

Bingen BO, Engels MC, Schalij MJ, Jangsongthong W, Neshati Z, **Feola I**, Ypey DL, Askar SF, Panfilov AV, Pijnappels DA, de Vries AA. Light-induced termination of spiral wave arrhythmias by optogenetic engineering of atrial cardiomyocytes. *Cardiovascular Res*. 2014; 104:194-205.

Engels MC, Askar SF, Jangsongthong W, Bingen BO, **Feola I**, Liu J, Majumder R, Versteegh MI, Braun J, Klautz RJ, Ypey DL, De Vries AA, Pijnappels DA. Forced fusion of human ventricular scar cells with cardiomyocytes suppresses arrhythmogenicity in a co-culture model. *Cardiovascular Res*. 2015; 107:601-612.

Bingen BO, Askar SF, Neshati Z, **Feola I**, Panfilov AV, de Vries AA, Pijnappels DA. Constitutively active acetylcholine-dependent potassium current increases atrial defibrillation threshold by favoring post-shock re-initiation. *Sci Rep*. 2015; 5:15187.

Letters

Feola I, Volkens L, Majumder R, Teplenin A, SchaliJ MJ, Panfilov AV, de Vries AAF, Pijnappels DA. Response by Feola et al to Letter Regarding Article, “Localized Optogenetic Targeting of Rotors in Atrial Cardiomyocyte Monolayers”. *Circ Arrhythm Electrophysiol*. 2018; 11:e006130.

Presented abstracts (Selection)

Feola I, Watanabe M, Teplenin AS, SchaliJ MJ, Zeppenfeld K, Ypey DL, de Vries AAF, Pijnappels DA. Local light exposure terminates anatomical reentry in optogenetically modified transverse rat ventricular tissue slices. Oral presentation during Young Investigator Award at *Rembrandt Symposium 2015*.

Jangsangthong W, **Feola I**, Teplenin AS, SchaliJ MJ, de Vries AAF, Pijnappels DA. Microfoci of oxidative stress increase pro-arrhythmic risk as revealed by patterned illumination of optogenetically engineered myocardial cultures. Poster presentation at *HRS Conference 2016*.

Feola I, Watanabe M, Teplenin AS, SchaliJ MJ, Zeppenfeld K, Ypey DL, de Vries AAF and Pijnappels DA. Optogenetic termination of anatomical reentry in rat myocardial slices. Oral presentation at *EHRA EUROPACE – CARDIOSTIM 2017*.

Feola I, Volkens L, Majumder R, de Vries AAF, Pijnappels DA. Optogenetic ablation of spiral wave arrhythmias by creating light lesions. Oral presentation during Young Investigator Award at *EHRA EUROPACE – CARDIOSTIM 2017*.

Feola I, Majumder R, de Vries AAF, Panfilov AV, Pijnappels DA. Optogenetic manipulation of atrial spiral wave trajectory in space and time: capture, drag and terminate. Poster presentation at *HRS Conference 2018*.

ACKNOWLEDGMENTS

In my journey towards this dissertation, many people have contributed to my personal and scientific development. First, I would like to express my gratitude to my supervisors, Prof. Schaliĳ, Daniël and Twan, since without their support I would not have been able to conclude this chapter of my life. Twan, thank you for your scientific input and guidance. Daniël, thank you for believing in me, for your support and for always challenging me. Sometimes it has not been easy to cope with the pressure, but this experience has shaped me into who I am today.

My special thanks go to Minka, Cindy, Margreet, Zeinab, Jia, Arti, Marc, Yoke, Masaya, Sasha, Annemarie, Rupa, Emile, Linda, Niels, Pim, Magda, Sven, and Juan. They have supported me when things were not going as planned and celebrated with me the happy moments. Thank you, guys! Minka, thank you for your availability in solving each and every problem. Cindy and Annemarie, thank you for helping with cloning, viral vector production and isolation of cardiomyocytes. Margreet, thanks for your advice and for performing the best western blot with anti-GFP antibody. Zeinab and Prof. Ypey, thank you for your time in teaching and explaining. Jia, thank you for sharing every step of this journey. Arti, thank you for your wise scientific advice. Yoke, thank you for the time spent together in and outside the “dark room”, where your company and the good music made everything easier. Masaya, thank you for your kindness, your time and dedication. Sasha and Rupa, thank you for the great collaboration, it has been a pleasure to discuss scientific matters with you. Linda, thank you for your scientific support by performing patch-clamp experiments. Niels, Emile, and Pim, as very typical Dutch people, you are very direct. Initially, I thought that was a bit rude, and maybe sometimes it is, but sometimes it is also necessary. Thank you for showing that to me. Pim, thank you for helping with the Dutch translation of the summary. Magda, I hoped I had met you before. Thank you for your amazing support in this last period. Juan and Sven, it was a pleasure and fun to share the office with you. Magda and Sasha, finally, thank you for accepting to be my paranims.

Furthermore, I would like to thank Harald for giving me the possibility to come to his laboratory during my master, and Selina for teaching me everything I know about working in a laboratory. Thanks also to Saïd and Brian for their initial input on cardiac electrophysiology.

Valeria, Luca, Nicoletta, and Bob thank you for your friendship, the dinners, the parties and all the moments that we have shared together. The Netherlands has been a better place with you in our life. Thank you also for making me aunty of Thomas and Elisa.

Thanks to my family, family-in-law and all my far-away friends. Your funny messages and your happy news (weddings and babies) have always given me a reason to smile. Special thanks go to the 'Italia-IOlanda', the 'Castelnuovo's club', the 'poli e dintorni' and the 'NL-CH' groups. Irma, thank you for accepting the important task of finalizing the cover of this thesis, that was a special gift. Gloria, we had different experiences but we shared the same emotions. Thank

Acknowledgments

you for showing to me how important it is to follow your dreams. Ala, you are one of the most wonderful creatures I have ever met. Thank you for your unconditional support.

Andrew, you are my special Aussie cousin. Thank you for your love. Your words have always encouraged me. Thanks aunt Lucia and uncle Franco, your availability and your constant presence in mum's life have made me less worried.

Francesco, often I think that maybe your life would have been different if you would have left and I would have stayed. We will never know that, but I hope, with all my heart, you will find your happy dimension. Thank you for supporting my choices.

Mum, it is very difficult to express with words my gratitude to you. You have made so many sacrifices for our happiness. Thank you for being such an inspiring example!

Guido, you are my home, my soul mate. Your support has been really important in this journey. After a bad day, I was often not easy going, but you tried and tried again until I started to smile again. Thank you for being there. Those last 2 years have been even more challenging for us. May the future gift us with the possibility to share more time together, full of adventures and experiences that will make us happy.

Finally, I would like to thank the little warrior that is inside me for never letting me give up.

CURRICULUM VITAE

Iolanda Feola was born on May 20th, 1987 in Vallo della Lucania, Italy. After finishing high school in 2006 she left her little town and moved to Parma where she started her academic journey. She obtained her bachelor's degree in Biotechnology in 2009. Three years later she obtained her master's degree in Medical, Veterinary and Pharmaceutical Biotechnology. During her bachelor, she performed her first internship at the Department of Neuroscience, at University of Parma, under the guidance of prof. R. Tirindelli and dr. L. Silvotti. During her master, she won the Erasmus scholarship that allowed her to move to The Netherlands. There, she spent her six-month internship at the Department of Molecular and Cell Biology at Leiden University Medical Center under the supervision of dr. H. Mikkers and S. Van Leeuwen. In 2013, she started her PhD training in the laboratory of experimental cardiology, Department of Cardiology, under the supervision of prof. dr. M.J. Schalij, dr. D.A. Pijnappels and dr. A.A.F. de Vries. During her training, she investigated the underlying mechanisms of cardiac arrhythmias by using optogenetics to precisely control, in time and space, the electrical properties of cardiac cells. The work performed during her training is presented in this thesis.

AWARDS

- 2017 Diploma in recognition of the best original work. EHRA Europepace-Cardiostim Conference.
- 2017 Runner-up during the Young Investigator Award competition. EHRA Europepace-Cardiostim Conference.
- 2015 Best Oral Presentation Award. Rembrandt Conference of Cardiovascular Science.
- 2010 Erasmus scholarship from the University of Parma to perform an internship abroad.